Computational Investigations at the Gas—Surface Interface: Organic Surface Oxidation and Hydrolysis of Chemical Warfare Agents and Simulants

Robert C. Chapleski, Jr.

Dissertation submitted to the faculty of the
Virginia Polytechnic Institute and State University
in partial fulfillment of the requirements for the degree of

DOCTOR OF PHILOSOPHY
in
Chemistry

Diego Troya, Chair
John R. Morris, co-Chair
Alan R. Esker
T. Daniel Crawford

March 24, 2017
Blacksburg, Virginia

Keywords: heterogeneous, atmospheric, chemical warfare agents, surfaces, oxidants, computational

Computational Investigations at the Gas—Surface Interface: Organic Surface Oxidation and Hydrolysis of Chemical Warfare Agents and Simulants

Robert C. Chapleski, Jr.

ABSTRACT

Motivated by recent experiments in gas—surface chemistry, we report our results from computational investigations of heterogeneous systems relevant to atmospheric chemistry and protection against chemical weapons. To elucidate findings of ultra-high vacuum experiments that probe the oxidation of carbon-carbon double bonds on model surfaces, we used electronic structure and QM/MM methods to study the reaction of ozone with C_{60}-fullerene and the products of nitrate addition to a vinyl-terminated self-assembled monolayer. In the first system, we followed a reaction pathway beginning with primary ozonide formation through the formation of stable products. Theoretical vibrational spectra were used to identify a ketene product in prior experimental work. Next, through the construction of a multilayer model for the initial addition product of a nitrate radical to a chain embedded within a self-assembled monolayer, we report theoretical spectra that are consistent with experimental results. We then examined the fundamentals of the hydrolysis mechanism for nerve agents by a catalyst of interest in the development of filtration materials for chemical-warfare-agent defense. By following the gas—surface reaction pathway of the nerve agent Sarin on the Lindqvist polyoxoniobate $Cs_8Nb_6O_{19}$, we determined that the rate-limiting step is the transfer of a proton from an adsorbed water molecule to the niobate surface, concomitant with the nucleophilic addition of the nascent hydroxide to the phosphorus atom in Sarin. Our results support a general base hydrolysis mechanism, though high product-adsorption energies suggest that thermal treatment of the system is required to fully regenerate the catalyst. We report similar mechanisms for the simulants dimethyl methylphosphonate and dimethyl chlorophosphate, though the latter may serve as a better simulant in studies of this type. Finally, an investigation of Sarin hydrolysis with solvated $Cs_8Nb_6O_{19}$ shows an increase in the rate-limiting barrier relative to the gas—surface system, revealing the role of Cs counterions in the reaction. Then, we further increased explicit solvation to model the homogeneous solution-phase reaction, finding a different mechanism in which a water molecule adds to phosphorus in the rate-limiting step and protonation of the niobate surface occurs in a subsequent barrierless step. By examining the rate-limiting barrier for protonation, we suggest that specific base hydrolysis is also likely in the homogeneous system.

Computational Investigations at the Gas—Surface Interface: Organic Surface Oxidation and Hydrolysis of Chemical Warfare Agents and Simulants

Robert C. Chapleski, Jr.

GENERAL AUDIENCE ABSTRACT

Phenomena that occur where gases meet the surfaces of solids or liquids find relevance in several arenas. In the lower atmosphere, reactions between oxidative gases such as ozone or nitrate on the surface of organic particulates cause these particles to grow and change, contributing to smog and harmful effects to human health. Using computational modeling, we can describe these reactions with atomic-level detail. In the first channel of research presented in this dissertation, we report results that provide insight into these environmental reactions. Then, we change our focus towards an understanding of the reactions that lead to the decontamination of chemical warfare agents on the surface of a transition metal oxide catalyst. Again with computational modeling, we follow reaction pathways as a nerve agent or less harmful simulant reacts with the surface of this material. The entire body of this work—that of atmospheric relevance and that towards an understanding of catalytic deactivation of toxic compounds—emphasizes a strong synergy with experimental efforts. Our work is motivated by a desire to understand experimental results, and the calculations we perform influence the design of future experiments.

for Mom

in loving memory of Dad and Grandpa

Acknowledgments

As my journey through graduate school comes to a close, I am honored with the opportunity to acknowledge those individuals without whom my progress would not be possible.

First and foremost, I thank my fiancé, Stephen Lindamood, for his support and encouragement over the past four years. He is my rock.

Next, I express my gratitude to my family, especially my parents: Karen and Ken Schulden, and Bob and Lynn Chapleski. They provided me with a strong foundation and constant aid in so many ways.

My list of thanks would be incomplete if I did not mention those teachers with whom I have worked over the course of my educational career, especially Fran Meeks, who knew 20 years ago that I would someday be defending a Ph.D. Thesis.

I also send my gratitude to my graduate colleagues and mates in the Morris and Theory Labs, especially Angela Edwards and Yafen Zhang, with whom I celebrated the greatest achievements and overcame the greatest obstacles.

Finally, thanks to my graduate committee, Diego Troya, John Morris, Alan Esker, and Daniel Crawford for the ongoing support and resources. Special thanks to John for helping me find my place in the world of surface science, and to Diego for access to his wellspring of knowledge and experience, endless academic and professional backing, and perpetual vote of confidence.

Table of Contents

List of Figures

List of Tables

Attributions

The work in Chapter 3 of this dissertation has been published previously in the journal *Physical Chemistry Chemical Physics*, with the following reference:

Chapleski, R. C.; Morris, J. R.; Troya, D. *Physical Chemistry Chemical Physics* **2014**, *16*, 5977.

In this multi-author work, Robert Chapleski performed calculations related to primary ozonide formation as reported in Figures 3.2 and 3.4, Pathway A in Figure 3.5 and Figure 3.7, decomposition of the primary ozonide as shown in Figures 3.8 and 3.9, and reactions with a second ozone molecule, shown in Figures 3.10 through 3.12. He also contributed to the construction of the manuscript. John Morris provided experimental spectra reported in Figure 3.2 and 3.7, as well as a great deal of insight from experiments. He also contributed to the construction of the manuscript. Diego Troya performed method validation calculations with CCSD(T) QM:QM methods, as reported in Figure 3.1, as well as spectral calculations for di-POZ systems as shown in Figure 3.4, and electronic structure calculations for full loading of C_{60}, reported in Figure 3.5, Pathway B. He also contributed to the construction of the manuscript.

The work in Chapter 5 of this dissertation has also been published, in *The Journal of Physical Chemistry C*, with the following reference:

Chapleski, R. C.; Musaev, D. G.; Hill, C. L.; Troya, D. *The Journal of Physical Chemistry C* **2016**, *120*, 16822.

In this multi-author work, Robert Chapleski performed verification calculations along all reaction pathways, provided insight into the structures of stationary points from previous calculations, and contributed to the construction of the manuscript. Djamaladdin Musaev and Craig Hill provided insight into the reaction mechanism as well as the polyoxoniobate. They also contributed to the construction of the manuscript. Diego Troya performed electronic structure calculations for reaction pathways and contributed to the construction of the manuscript.

Publications

Rowe, J. M.; Hay, J. M.; Maza, W. A.; Chapleski Jr., R. C.; Soderstrom, E.; Troya, D.; Morris, A. J. Systematic Investigation of Anthracene-Dicarboxylic Acids. *Journal of Photochemistry and Photobiology A: Chemistry* **2017**, *337*, 207.

Chapleski Jr., R. C.; Musaev, D. G.; Hill, C. L.; Troya, D. Reaction Mechanism of Nerve-Agent Hydrolysis with the $Cs_8Nb_6O_{19}$ Lindqvist Hexaniobate Catalyst. *The Journal of Physical Chemistry C* **2016**, *120*, 16822.

Chapleski Jr., R. C.; Zhang, Y.; Troya, D.; Morris, J. R. Heterogeneous Chemistry and Reaction Dynamics of the Atmospheric Oxidants, O_3, NO_3, and OH, on Organic Surfaces. *Chemical Society Reviews* **2016**, *45*, 3731.

Radzinski, S. C.; Foster, J. C.; Chapleski Jr., R. C.; Troya, D.; Matson, J. B. Bottlebrush Polymer Synthesis by Ring-Opening Metathesis Polymerization: The Significance of the Anchor Group. *Journal of the American Chemical Society* **2016**, *138*, 6998.

Chapleski Jr., R. C.; Morris, J. R.; Troya, D. A Theoretical Study of the Ozonolysis of C_{60}: Primary Ozonide Formation, Dissociation, and Multiple Ozone Additions. *Physical Chemistry Chemical Physics* **2014**, *16*, 5977.

Zhang, Y.; Chapleski Jr., R. C.; Lu, J. W.; Rockhold, T. H.; Troya, D.; Morris, J. R. Gas-surface Reactions of Nitrate Radicals with Vinyl-terminated Self-assembled Monolayers. *Physical Chemistry Chemical Physics* **2014**, *16*, 16659.

Wang, Q.; Chapleski Jr., R.C., Plonka, A. M.; Gordon, W. O.; Guo, W.; Nguyen-Phan, T. D.; Sharp, C. H.; Marinkovic, N. S.; Senanayake, S. D.; Morris, J. R.; Hill, C. L.; Troya, D.; Frenkel, A. I. Atomic-Level Dynamics of Polyoxoniobates during DMMP Decomposition. *Scientific Reports* **2017**, Accepted.

Chapter 1
Introduction, Motivations, and Background

Thesis Statement

The objective of this research is to develop a fundamental understanding of specific gas—surface reactions that occur in the atmosphere as well as on the surface of certain metal-oxide catalysts using computational approaches. Along with providing a primary understanding of reaction kinetics and dynamics, computational methods allow for the interpretation of theoretical data, which can elucidate the results of experimental efforts.

1.1 Introduction and Objectives

An appreciation of reactions that occur at the gas—surface interface is essential not only for an understanding of phenomena that occur in the atmosphere, but also on the surfaces of solid catalysts that show promise for the deactivation of chemical warfare agents.

Particulates containing unsaturated organic compounds are prevalent in the troposphere and have been shown to be highly reactive towards atmospheric ozone and nitrate. Both of these oxidants have been shown to add across the double bonds in unsaturated compounds. Model surfaces, such as those provided by C_{60} fullerene and a vinyl-terminated self-assembled monolayer, allow for the positioning of a double bond precisely at the gas—surface interface in order to probe the fundamentals of reaction of a surface-bound double bond with ozone and nitrate. Recent experimental efforts probed these reactions in an ultrahigh vacuum environment,[1,2] raising questions that could be addressed through computational efforts.

The Lindqvist polyoxoniobate ($Cs_8Nb_6O_{19}$) has also shown promise as a catalyst for the degradation of chemical warfare agents. In a recent small-angle x-ray study, a hydrolysis mechanism was proposed for this system.[3] However, atomistic details, including the dynamics of the catalytic reaction, as well as the kinetics (to reveal the rate-limiting step), were left largely unexplained. Further, towards the development of materials for use as coatings and filters capable of deactivating nerve agents, the Lindqvist polyoxoniobate has been largely unexplored as a degradation catalyst in the solid phase.

In order to provide fundamental insight into each of these arenas and to support recent experimental data, this research will focus on three objectives:

1. Refine the mechanism of surface-bound alkene oxidation by ozone and nitrate.
2. Delineate the hydrolysis mechanism of nerve agents and simulants on the surface of a Lindqvist polyoxoniobate.
3. Elucidate the results of experimental spectra for the gas—surface reactions described herein.

To fulfill these objectives, several computational approaches were used including ab initio and molecular mechanics methods. A computational approach not only allows for the probing of reactions that may be difficult to evaluate experimentally due to location (e.g., in the troposphere) or potential hazards to human health (e.g., risks of chemical warfare agent exposure), but also can provide meaningful interpretation to experimental data such as spectral features.

The remainder of this chapter will provide the motivation and background for the research being described in this dissertation. we begin with motivations to investigate surface reactions relevant to tropospheric chemistry and chemical warfare agent degradation. Then, we will describe concepts and experimental approaches that are fundamental to an understanding of gas—surface interfacial chemistry.

1.2 Motivations

1.2.1 Atmospheric Surface Oxidation

There are two general ways that organic particles make their way into the atmosphere. Biogenic and anthropogenic processes can emit soot and organic aerosols,[4-6] and volatile organics can adsorb onto the surfaces of solid particles.[7,8] As such, organic particulates can reach concentrations up to 15 $\mu g/m^3$.[9,10] Once in the atmosphere, the surfaces of these particles can be oxidized by reactive gases such as ozone and nitrate. As a result, particles can grow and change, with large-scale effects. These particulate changes can alter the balance of incoming and outgoing light from the sun,[11,12] and excessive oxidation of volatile organics can lead to smog formation.[13]

For a more in-depth discussion of gas—surface oxidation reactions of atmospheric organic surfaces, the reader is referred to our review article published on the topic.[14]

1.2.1.1 Reactions with Ozone

Gas-phase ozone (O_3) has been shown to add across the double bonds of unsaturated and aromatic organic surfaces, leading to the formation of a surface-bound primary ozonide.[15-18] This unstable moiety can lead to further reactions and particulate changes.[19] Several studies have related the reactive uptake of ozone on an organic surface to the positioning of the double bond; much greater uptake was noted for those surfaces where the saturation is positioned at the gas—surface interface than for a double bond submerged below the surface of the particle.[20-22]

Most research involving the oxidation of saturated organics by ozone has been performed in atmospheric conditions, in the presence of background gases which can have a significant effect on the reaction pathway. For example, at low relative humidity, chains of a vinyl-terminated self-assembled monolayer (Chapter 4) adjacent to one another reacted, leading to aggregation, following exposure to ozone. At high relative humidity, aggregation did not occur, leading to the proposal of an alternate reaction mechanism in the presence of water.[19]

Because background gases can clearly play a role in the ozonolysis of organic surfaces, groups have begun to perform experiments in ultra-high vacuum environments. As such, background gases are removed, so the fundamental aspects of the reaction can be probed. Lu et al. scattered a molecular beam of ozone from a vinyl-terminated self-assembled monolayer in ultra-high vacuum, finding contrasting mechanisms depending on the incident energy of the scattered molecules.[23] At low incident energies, the Langmuir-Hinshelwood mechanism is implicated, and at high energies, the Eley-Rideal is more likely (vide infra).

Furthermore, Davis et al.[1] probed the changes on a C_{60} fullerene surface during ozone exposure in ultra-high vacuum using reflection-absorption infrared spectroscopy (RAIRS, vide infra). After long exposure times, an infrared band appears around 2200 cm^{-1}. To help elucidate the source of this band, we performed vibrational spectra calculations using ab initio theory for the reaction of ozone with the surface of a C_{60} fullerene cage. Further, we are able to show how the C_{60} surface changes as a result of reactions with ozone. This work is described in Chapter 3.

1.2.1.2 Reactions with Nitrate

Like ozone, nitrate radicals (NO_3) have also been shown to add to an unsaturated site on an organic surface.[24-29] Alternatively, nitrate can abstract a hydrogen atom from a molecule in a competing reaction step. In nitrate reactions with organic surfaces, the role of surface reactions was found to be minor in surfaces for which a slow hydrogen abstraction step appears in the

reaction mechanism; nitrate was able to diffuse into the bulk before reacting. Conversely, on unsaturated surfaces, fast nitrate addition increases the role of the surface in the overall reaction, as a nitrate radical will react with the first double bond it encounters.[28,30,31] Thus, a much greater reactive uptake was found for an alkene-terminated self-assembled monolayer than an alkane-terminated one.[24,25]

Both the nitrate addition and hydrogen abstraction pathways described in previous studies have been shown to be influenced by background gases.[24] As with ozone, ultra-high vacuum studies enable experimentalists to probe the fundamentals of reactions of nitrate with organic surfaces in the absence of background gases. Zhang et al. investigated the reaction of nitrate with a vinyl-terminated self-assembled monolayer in ultra-high vacuum.[2] Using RAIRS, they were able to postulate that nitrate adds to the terminal carbon atom in a self-assembled monolayer chain. Using electronic structure and QM/MM methods (Chapter 2), we were able to aid in the assignment of vibrational modes essential to their analysis. Further, we used high-level electronic structure calculations to rule out a possible competing hydrogen abstraction step in the reaction. In Chapter 4, we describe our efforts and results in great detail.

1.2.2 Chemical Warfare Agents and Decontamination

The first modern use of chemical agents as a weapon of mass destruction dates back to WWI, where chlorine and phosgene gases were dispersed on the battlefield and carried through the air, killing thousands of Allied troops.[32] Since then, the family of chemical warfare agents has grown to include many different types of compounds, each with its own deleterious effects on the human body.

There are several classes of chemical warfare agents, including blister agents, choking agents, and nerve agents. Blister agents, or vesicants, include sulfur and nitrogen mustard gases. Exposure to these compounds may result in chemical burns and irritation of the mucosal membranes. Choking agents such as chlorine gas and phosgene cause a buildup of fluid in the lungs, eventually leading to suffocation.

Nerve agents include substances such as Tabun (GA), Sarin (GB), Soman (GD), Cyclosarin (GF), and methylphosphonothiolic acid (VX). The primary mechanism of action of nerve agents is through inhibition of the acetylcholinesterase enzyme.[33-35] Under normal conditions, this enzyme breaks down excess concentrations of the neurotransmitter acetylcholine at neuromuscular junctions and in chemical synapses. Nerve agents chemisorb to a serine site in

acetylcholinesterase, thus preventing acetylcholine breakdown. As acetylcholine is implicated in the activation of muscular tissue, a buildup of this neurotransmitter resulting from acetylcholinesterase inhibition leads to continuous muscular stimulation and hyperactivity. As such, death from nerve agent exposure typically results from suffocation resulting from the inability to control muscles involved in breathing.

Since their initial use over one hundred years ago, the threat of these harmful compounds has not been eliminated. Chemical weapons attacks in Syria,[36] Iraq,[37-39] and Japan[40] have been reported, amongst others, within the past 30 years. Instances of exposure such as these highlight the ongoing need for protection from the harmful effects of these agents.

Methods of interest for chemical warfare agent decontamination include physical removal and chemical processes.[41] Physical removal techniques, which isolate an agent, preventing exposure, include flushing an exposed surface (including skin) with water and irreversibly adsorbing an agent onto a substance such as activated charcoal[42] or an adsorptive resin.[43,44] Chemical processes, which decompose an agent into a less toxic compound, include reaction with hydroperoxide,[45,46] oxidation with bleach,[47] alkoxide addition,[48,49] enzymatic degradation,[50,51] halogenation,[52] and hydrolysis.[53-57] Reactive surfaces such as those of metal nanoparticles,[58-61] metal oxides,[62-72] and zeolites[73,74] have also been implicated in chemical warfare agent destruction. Recently, metal-organic frameworks[75-84] and polyoxometalates[3,66,77,85-87] have also shown promise in this area as hydrolysis catalysts.

Experimental efforts continue towards the development of new methods and a fundamental understanding of current methods of chemical warfare agent decontamination. However, most laboratory environments are not equipped to work with the highly toxic class of chemical warfare agents. Thus, the majority of studies implement nontoxic or less toxic chemical warfare agent simulants, which have similar structures and properties to analogous agents while decreasing the threat of bodily harm to experimentalists. For example, the compounds dimethyl methylphosphonate (DMMP) and dimethyl chlorophosphate (DMCP) are commonly used as experimental analogues to the nerve agent Sarin. Figure 1.1 compares the structure of these three compounds. All three molecules share a common organophosphorus framework consisting of a central phosphorus atom bound to both an sp^2-hybridized oxygen atom and an sp^3 oxygen. In Sarin, however, this sp^3 oxygen is a part of an isopropoxy group, and in the two simulants, it is part of a methoxy group. Beyond the O=P-O framework, the phosphorus atom is also bound to

an electronegative atom in all three compounds: a fluorine atom in GB, another methoxy oxygen in DMMP, and a chlorine atom in DMCP. The final moiety bound to the phosphorus atom also differs amongst compounds: a methyl group in Sarin and DMMP, and a second methoxy group in DMCP.

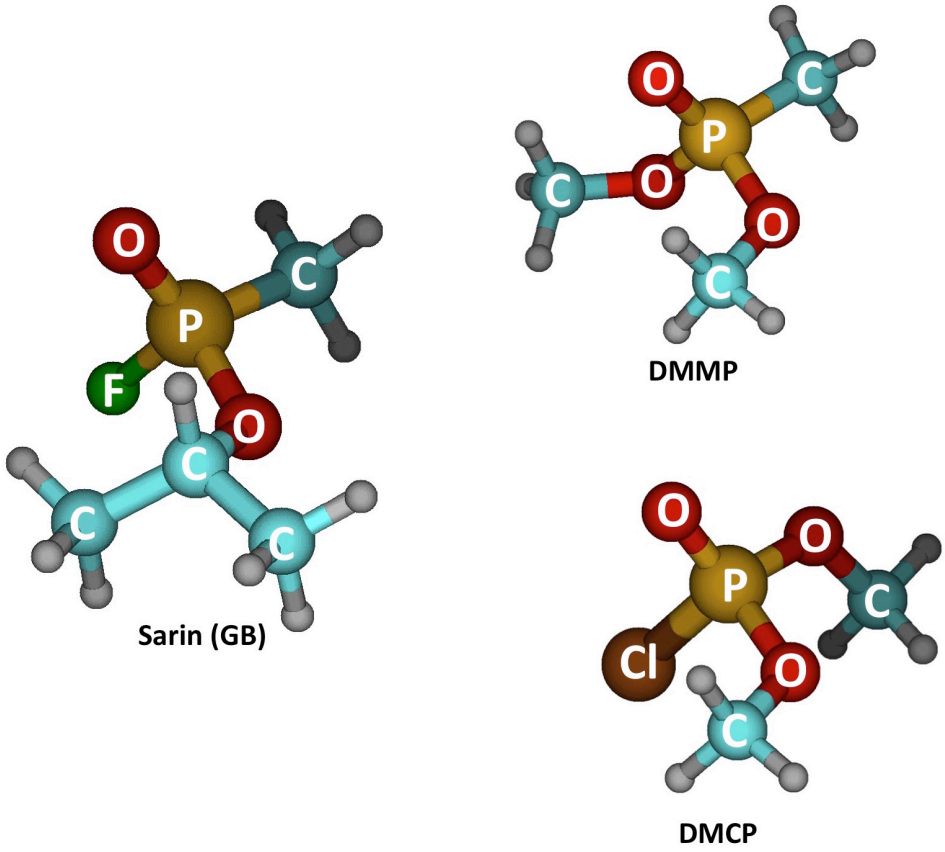

Figure 1.1. Structures of the nerve agent Sarin and simulants dimethyl methylphosphonate (DMMP) and dimethyl chlorophosphate (DMCP).

In this dissertation, several chapters are devoted to our efforts towards an understanding of the fundamental reaction dynamics of the hydrolysis of Sarin and these two simulants adsorbed on the surface of a Lindqvist polyoxoniobate. Thus, not only are we able to describe this reaction for the nerve agent, but we are also able to provide insight into experimental efforts on the same system. In Chapter 5, we describe the mechanism of this reaction for Sarin. In Chapter 6, we proceed with a similar investigation for DMMP. Using Raman and x-ray spectroscopy, experimentalists have investigated DMMP hydrolysis by the same Lindqvist polyoxoniobate as we have constructed for our calculations. Combined, our efforts explain not

only changes that are occurring to the organophosphorus compound during hydrolysis, but also to the niobate. In Chapter 7, we investigate a similar mechanism for DMCP. In addition to facilitating a correlation of results with experimental efforts, studies of multiple compounds in parallel lend themselves to comparison amongst species and evaluation of the simulants for their ability to accurately mimic the properties of the nerve agent. For example, the rate-limiting reaction barrier for DMMP was found to be roughly twice that for GB, while that for DMCP is comparable to GB. Thus, in terms of overall reaction kinetics, DMCP appears to be a better simulant.

1.3 Background

Having described the factors motivating our research, we proceed with an introduction to some of the principles and practices integral to our approach, as well as to gas—surface chemistry in general. After an introduction to the fundamental features of gas—surface reactions, we move into a brief summary of experimental methods with which our computational methods find close synergy.

1.3.1 Key Steps in Gas—Surface Reactions

We begin this section with a discussion the general steps in the reactions that occur at the gas—surface interface.[88] First, a gas molecule is adsorbed onto the surface. Next, adsorbates react, and finally, products desorb. We will now discuss each of these steps in detail.

1.3.1.1 Adsorption

The first step in the interaction of a gas-phase molecule with a larger surface is typically adsorption, in which gas molecules become bound to the surface. Adsorption takes on two forms: physisorption and chemisorption. Physisorption is a consequence of intermolecular interactions between the gas and the surface. As no covalent bonds are formed in physisorption, the electronic structure of the gas molecule remains mostly unchanged, although some distortion is possible in order to facilitate adsorption.

Chemisorption, on the other hand, involves adsorption through the formation of covalent bonds, is much stronger than physisorption, and therefore results in a much stronger interaction between the surface and the adsorbate. Further, there are two general cases of chemisorption. In molecular adsorption, an adsorbed molecule remains intact while chemisorbed. In the primary ozonide of C_{60}, for example (Chapter 3), the O_3 moiety retains both O-O bonds following

chemisorption to the fullerene. Conversely, in dissociative adsorption, bonds are broken in the adsorbate during chemisorption. Methane, for example, has been shown to dissociate upon chemisorption onto nickel surfaces.[89-91]

Sketches of energy with respect to gas—surface distance *r* are shown in Figure 1.2 for physisorption (violet) and chemisorption (green). Note that the physisorption well occurs at larger distances than chemisorption, and has a much shallower well depth. At this point, it is important to note that a physisorbed gas molecule can become chemisorbed, and this transition typically has a barrier, identified in the figure with a double-headed arrow. In this dissertation, an example of physisorption and chemisorption is noted in Chapter 3, in which ozone physisorbs onto C_{60} before chemisorbing. This physisorbed state, identified in the chapter as a van der Waals minimum, must overcome an energy barrier of 0.4 kcal/mol in order for chemisorption to occur (Figure 3.8).

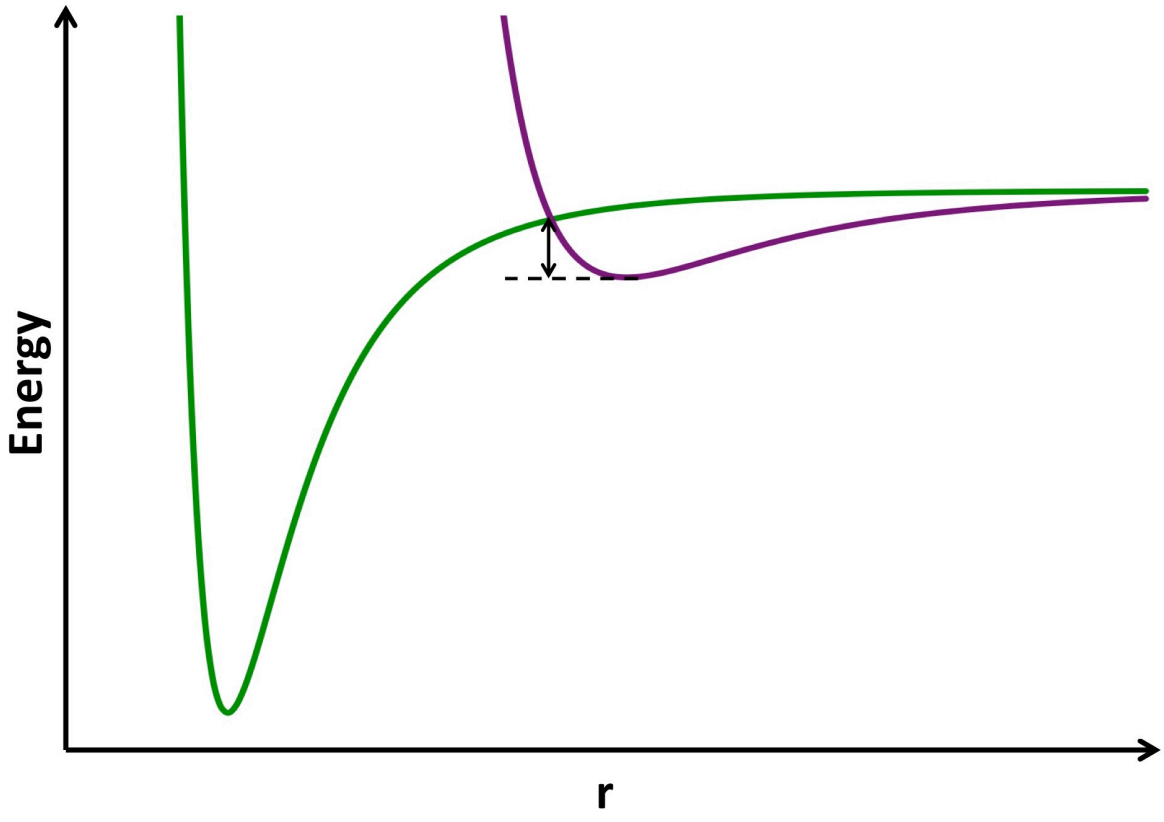

Figure 1.2. A comparison of potential energy sketches for physisorption (violet) and chemisorption (green) of a gas-phase molecule on a surface. The vertical double-headed arrow identifies the physisorption-chemisorption energy barrier.

1.3.1.2 Reaction

Once adsorbed onto the surface, the reaction between the gas and the surface can take place. Surface reactions follow one of two general mechanisms: The Langmuir-Hinshelwood[92] and the Eley-Rideal,[92,93] or a combination thereof.

1.3.1.2.1 The Langmuir-Hinshelwood Mechanism

In the Langmuir-Hinshelwood reaction mechanism, reagents reach thermal equilibrium with the surface upon adsorption.[94,95] Adsorbed reagents then accommodate across the surface until they meet the active site of the surface.[96] That is, they are not physisorbed at a single point on the surface; reagents may diffuse across the surface until they are oriented correctly for reaction. The green scheme in Figure 1.3 illustrates this mechanism, with an adsorbate being accommodated along the surface until it arrives at an active site (red) in the correct orientation. Once the adsorbate meets the active site in the correct orientation and acquires enough energy to overcome the necessary barrier, reaction will occur. As adsorbed reagents have thermalized with the surface, the source of this requisite energy is typically through thermal fluctuations in the surface. In a variation of the Langmuir-Hinshelwood mechanism, a second reagent molecule can also be adsorbed to the surface, and when both adsorbates meet, reaction occurs. At low collision energies, ozone is shown to react with a vinyl-terminated self-assembled monolayer through the Langmuir-Hinshelwood mechanism,[23] as is nitrate.[2]

1.3.1.2.2 The Eley-Rideal Mechanism

In the Eley-Rideal gas—surface reaction mechanism, a gas molecule will react with the surface or with surface-bound adsorbates directly, without accommodating with the surface prior to reaction. Thus, thermal equilibrium is not reached between the gas molecule and the surface, and reaction barriers may be overcome with the incident energy of the colliding gas molecule.[97-99] Reaction can take place between the gas-phase molecule and an active site on the surface or with a surface-bound adsorbate. The yellow scheme in Figure 1.3 illustrates the Eley-Rideal mechanism between a gas molecule and an active site on the surface. At high incident energies, the reaction between ozone and the same vinyl-terminated self-assembled monolayer surface mentioned in the previous paragraph has been shown to follow this mechanism.[23]

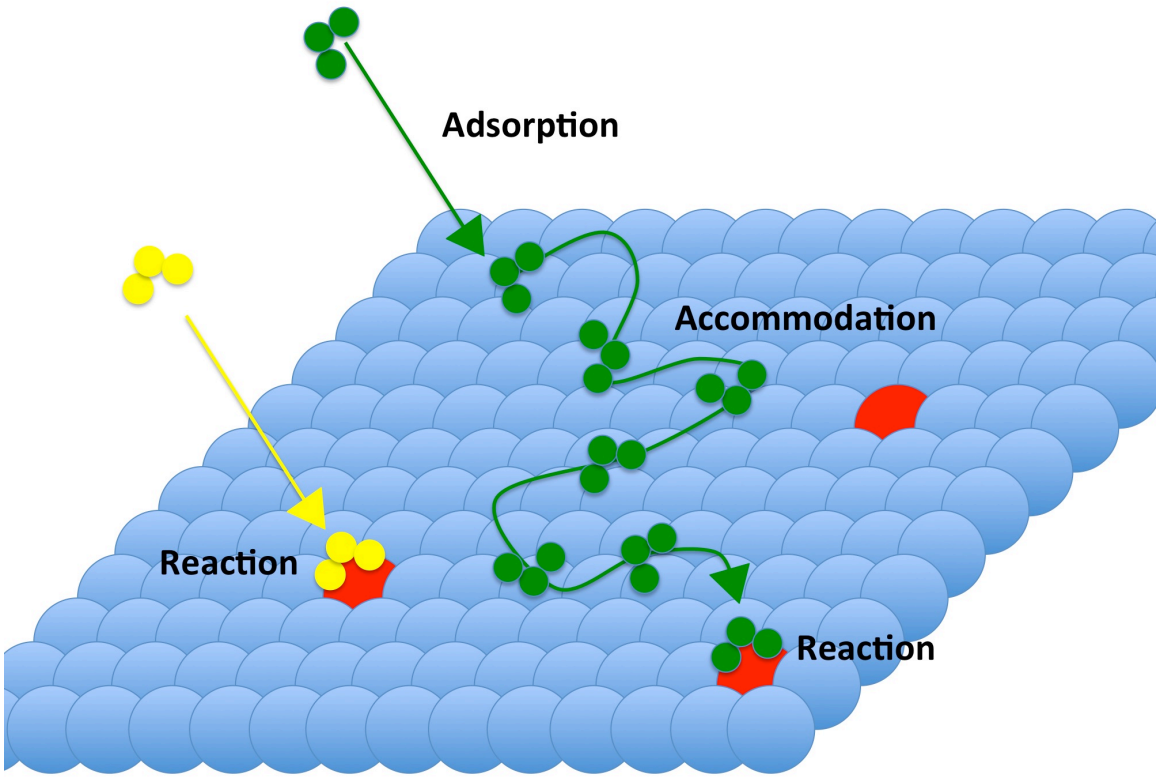

Figure 1.3. An illustration of the Langmuir-Hinshelwood (green adsorbate) and Eley-Rideal (yellow) reaction mechanisms for gas—surface reaction.

1.3.1.3 Desorption

Following reaction, products may remain bound to the surface, either through chemisorption at the reaction site or physisorption. As chemisorbed species are adsorbed much more strongly than physisorbed species (Figure 1.2), much more energy is required for desorption. Physisorbed species accommodate along the surface until they acquire enough energy from thermal fluctuations in the surface to desorb.

In catalytic surfaces such as the Lindqvist polyoxoniobate (Chapters 5-8), desorption is essential to the regeneration of the catalyst. In fact, physisorbed phosphonic acid products remain so strongly bound to the catalyst that we predict that the catalyst is poisoned at the site to which the product is adsorbed; that is, the site is no longer available for future reaction with incident gases. Moreover, while these products are adsorbed, the polyoxoniobate remains protonated—a result of the hydrolysis reaction. In order to fully regenerate the catalyst, the proton must be removed as well.

1.3.2 Experimental Techniques

A large body of the computational research we have undertaken is used to support and elucidate experimental results. Thus, equipped with an understanding of the basic features of a gas—surface reaction, we conclude our Background section with a brief introduction to techniques used to experimentally probe the heterogeneous systems described in the body of this dissertation.

1.3.2.1 Infrared Spectroscopy

According to the harmonic oscillator model,[100] when a molecule absorbs energy in the amount of $h\nu$, a transition from one vibrational energy level to an adjacent energy level occurs. The frequency of the vibration depends on the characteristics of the normal mode of vibration. Further, a given molecule can have several normal modes. Methanol, for example, has 3N-6=12 different vibrational modes. Each of these vibrations has a different frequency, and thus, the energy absorbed to excite each vibration to a higher energy level differs. A source of energy equal in amount to the energy difference between the ground and excited state is required for a specific excitation to occur. The energies required for vibrational excitations generally lie within the range of infrared light; however, not every vibration will be excited by infrared light. In order for a vibrational transition to occur, the net dipole moment of a molecule must change during vibration; that is, the vibration must be IR-active.

An infrared spectrum for a molecule can be generated by plotting all the vibrational frequencies within the molecule along with the corresponding intensity of each transition, which is related to the magnitude of change in dipole moment.

1.3.2.1.1 Reflection-Adsorption Infrared Spectroscopy

Reflection Absorption Infrared Spectroscopy (RAIRS)[101] is a surface-analysis technique that is very sensitive to the orientation of a functional group with respect to the normal of a surface. A RAIRS sample is prepared by adsorbing a thin layer of molecules to a reflective metal substrate. To generate vibrational spectra, infrared light is incident at glancing angles relative to the surface. Light incident upon a surface has a polarization component oriented parallel to the surface and another perpendicular to the surface. The light perpendicular to the surface normal (i.e. parallel to the surface) is phase shifted by about 180°, and therefore tends to destructively interfere with itself upon interaction with the surface. Conversely, the light parallel to the surface normal is shifted by different degrees depending on the incident angle. Thus,

adjusting the angle of incidence can maximize the intensity of constructively interfering light perpendicular to the surface, thereby maximizing its interaction with the matter deposited on the surface and consequently its infrared absorbance. This maximum constructive interference occurs at glancing incident angles, around 85-88° relative to the surface normal, depending on the complex refractive index of the metal substrate.[102]

The intensity of the signal reflected back from the perpendicular-polarized light is related to the dot product of the change in dipole moment and the electric field of the emitted light. Consequently, only the components of the transition dipole moment vector perpendicular to the surface are detectable by RAIRS. This is known as the surface selection rule. Thus, RAIRS is extremely sensitive to orientation of a functional group and its transition dipole relative to a surface.[101] Dipoles perpendicular to the surface are active, but parallel ones are not.

In Chapter 3 of this dissertation, theoretical vibrational spectra (Chapter 2) were calculated for minima along the reaction coordinate for the ozonolysis of C_{60}.[1] These spectra were compared with RAIRS spectra taken in previous experiments in which C_{60} deposited on a gold slide was exposed to ozone in an ultra-high vacuum environment. In Chapter 4, theoretical spectra were calculated for proposed products of nitrate addition to a vinyl-terminated self-assembled monolayer on gold and similarly compared with experimental RAIRS spectra.

1.3.2.2 Raman Spectroscopy

Raman spectroscopy is another technique used to obtain the vibrational spectrum of a molecule. In infrared spectroscopy, the absorption of infrared light is used to inform of vibrational frequencies. Alternatively, in Raman spectroscopy, monochromatic light is scattered from a molecule. As a result of interaction with the molecule, the energy of the light is shifted, and this shift corresponds to the difference in energy between vibrational energy levels. Whereas in infrared spectroscopy, IR activity is based on the change in dipole moment, Raman-active vibrations require a change in the polarizability of a molecule. Polarizability is the ability of a molecule to instantaneously form a dipole as a response to an external field. As the rules differ in infrared and Raman spectroscopy for which vibrations will be active, Raman spectroscopy can be used to probe vibrational modes that may not be present in an infrared spectrum or those that are not well resolved. In Chapter 6, theoretical Raman spectra were compared with experimental Raman spectra for minima along the reaction pathway of DMMP hydrolysis by a Lindqvist polyoxoniobate.

1.3.2.3 X-ray absorption spectroscopy

While infrared methods implement light in the infrared energy range to probe molecular vibrations, x-ray methods use much higher energy light, in the x-ray energy range of the electromagnetic spectrum. This higher energy is typically able to excite inner-shell electrons upon absorption. In the presence of nearby atoms, these exiting electrons scatter from adjacent electron clouds, which affects the intensity at particular energies. Thus, x-ray spectroscopy can be used to describe the nearby environment of an atom in terms of interatomic distances. A specific example of this is EXAFS, or extended x-ray adsorption fine structure spectroscopy.[103] As EXAFS methods are used to probe the local environments of individual atoms, interatomic distances can be calculated from EXAFS spectra.

In Chapter 6, we visualize the changes in interatomic distances in a polyoxoniobate over the course of the DMMP hydrolysis reaction. We further relate the disorder in these distances to protonation of and adsorption of species to the niobate. Armed with the similar ability to report interatomic distances, EXAFS also provides information about structural disorder. As such, we are able to provide insight from electronic structure calculations into EXAFS data taken following experimental exposure of DMMP to a polyoxoniobate.

1.4 Concluding Remarks

In this chapter, we presented our motivations for undertaking the body of research described in this dissertation. The oxidation of organic surfaces in the atmosphere can result in changes in particulate size and composition, resulting in large-scale effects. Though thorough research has been performed previously, questions remain regarding the interaction of atmospheric oxidants with organic surfaces. Thus, we have studied the reaction of ozone with the surface of a C_{60} fullerene molecule, which we report in Chapter 3. We also discuss, in Chapter 4, our work on the addition of nitrate to another model surface—the self-assembled monolayer.

Next, the threat of chemical warfare agents remains a substantial societal issue. Towards the development of materials that can deactivate the highly toxic nature of these compounds, we report our findings for one such material, the Lindqvist polyoxoniobate, and the hydrolysis reaction that occurs when the nerve agent Sarin interacts with its surface (Chapter 5). Here, our computational effort is motivated by the danger of working with this agent in an experimental setting.

Further, compounds that show similar chemistry to Sarin are frequently used in experimental settings to help ensure the safety of investigators while informing of fundamental aspects of the reaction with the more dangerous agent. To provide insight to and gain insight from studies which employ nerve-agent simulants, we report our computational studies of hydrolysis of DMMP and DMCP by the same polyoxoniobate surface in Chapters 6 and 7, respectively.

Finally, to transition from the interactions between a gas-phase molecule and a solid surface, we discuss our model for the heterogeneous hydrolysis of gas-phase Sarin with the surface of a polyoxoniobate solution. From structures along this gas—solution reaction pathway, we expand our model into a fully solvated system. This work is reported in Chapter 8.

Before we begin with specific heterogeneous reaction systems, however, we shall devote Chapter 2 to a discussion of the computational methods employed in these studies.

1.5 References

(1) Davis, E. D.; Wagner, A.; McEntee, M.; Kaur, M.; Troya, D.; Morris, J. R. *The Journal of Physical Chemistry Letters* **2012**, *3*, 3193.

(2) Zhang, Y.; Chapleski, R. C.; Lu, J. W.; Rockhold, T. H.; Troya, D.; Morris, J. R. *Physical Chemistry Chemical Physics* **2014**, *16*, 16659.

(3) Kinnan, M. K.; Creasy, W. R.; Fullmer, L. B.; Schreuder-Gibson, H. L.; Nyman, M. *European Journal of Inorganic Chemistry* **2014**, *2014*, 2361.

(4) Simoneit, B. R. T. T. *Journal of atmospheric chemistry*, *8*, 251.

(5) Graedel, T. E.; Hawkins, D. T.; Claxton, L. D. *Atmospheric Chemical Compounds: Sources, Occurrence, and Bioassay*; Academic Press, 1986.

(6) Standley, L. J.; Simoneit, B. R. T. *Environmental Science & Technology* **1987**, *21*, 163.

(7) Donaldson, D. J.; Anderson, D. *The Journal of Physical Chemistry A* **1999**, *103*, 871.

(8) Gill, P. S. *Reviews of geophysics (1985)* **1983**, *21*, 903.

(9) Fountoukis, C.; Megaritis, A. G.; Skyllakou, K.; Charalampidis, P. E.; Pilinis, C.; Denier van der Gon, H. A. C.; Crippa, M.; Canonaco, F.; Mohr, C.; Prévôt, A. S. H.; Allan, J. D.; Poulain, L.; Petäjä, T.; Tiitta, P.; Carbone, S.; Kiendler-Scharr, A.; Nemitz, E.; O'Dowd, C.; Swietlicki, E.; Pandis, S. N. *Atmos. Chem. Phys.* **2014**, *14*, 9061.

(10) Jimenez, J. L.; Canagaratna, M. R.; Donahue, N. M.; Prevot, A. S. H.; Zhang, Q.; Kroll, J. H.; DeCarlo, P. F.; Allan, J. D.; Coe, H.; Ng, N. L.; Aiken, A. C.; Docherty, K. S.; Ulbrich, I. M.; Grieshop, A. P.; Robinson, A. L.; Duplissy, J.; Smith, J. D.; Wilson, K. R.; Lanz, V. A.; Hueglin, C.; Sun, Y. L.; Tian, J.; Laaksonen, A.; Raatikainen, T.; Rautiainen, J.; Vaattovaara, P.; Ehn, M.; Kulmala, M.; Tomlinson, J. M.; Collins, D. R.; Cubison, M. J.; Dunlea, J.; Huffman, J. A.; Onasch, T. B.; Alfarra, M. R.; Williams, P. I.; Bower, K.; Kondo, Y.;

Schneider, J.; Drewnick, F.; Borrmann, S.; Weimer, S.; Demerjian, K.; Salcedo, D.; Cottrell, L.; Griffin, R.; Takami, A.; Miyoshi, T.; Hatakeyama, S.; Shimono, A.; Sun, J. Y.; Zhang, Y. M.; Dzepina, K.; Kimmel, J. R.; Sueper, D.; Jayne, J. T.; Herndon, S. C.; Trimborn, A. M.; Williams, L. R.; Wood, E. C.; Middlebrook, A. M.; Kolb, C. E.; Baltensperger, U.; Worsnop, D. R. *Science* **2009**, *326*, 1525.

(11) Finlayson-Pitts, B. J.; Pitts Jr, J. N. *Chemistry of the upper and lower atmosphere: theory, experiments, and applications*; Academic press, 1999.

(12) Etheridge, D. M.; Steele, L. P.; Francey, R. J.; Langenfelds, R. L. *Journal of Geophysical Research: Atmospheres* **1998**, *103*, 15979.

(13) ; Canadian Council of Ministers of the Enviroment: Ottawa, Ontario, Canada.

(14) Chapleski, R. C.; Zhang, Y.; Troya, D.; Morris, J. R. *Chemical Society Reviews* **2016**, *45*, 3731.

(15) Tiwari, A. J.; Morris, J. R.; Vejerano, E. P.; Hochella, M. F.; Marr, L. C. *Environmental Science & Technology* **2014**, *48*, 2706.

(16) Liu, Y.; Liggio, J.; Li, S.-M.; Breznan, D.; Vincent, R.; Thomson, E. M.; Kumarathasan, P.; Das, D.; Abbatt, J.; Antiñolo, M.; Russell, L. *Environmental Science & Technology* **2015**, *49*, 2806.

(17) Miet, K.; Le Menach, K.; Flaud, P. M.; Budzinski, H.; Villenave, E. *Atmospheric Environment* **2009**, *43*, 3699.

(18) Gonzalez-Labrada, E.; Schmidt, R.; DeWolf, C. E. *Physical Chemistry Chemical Physics* **2007**, *9*, 5814.

(19) McIntire, T. M.; Scott Lea, A.; Gaspar, D. J.; Jaitly, N.; Dubowski, Y.; Li, Q.; Finlayson-Pitts, B. J. *Physical Chemistry Chemical Physics* **2005**, *7*, 3605.

(20) Vieceli, J.; Ma, O. L.; Tobias, D. J. *The Journal of Physical Chemistry A* **2004**, *108*, 5806.

(21) Gonzalez-Labrada, E.; Schmidt, R.; DeWolf, C. E. *Chemical Communications* **2006**, 2471.

(22) Wadia, Y.; Tobias, D. J.; Stafford, R.; Finlayson-Pitts, B. J. *Langmuir* **2000**, *16*, 9321.

(23) Lu, J. W.; Fiegland, L. R.; Davis, E. D.; Alexander, W. A.; Wagner, A.; Gandour, R. D.; Morris, J. R. *The Journal of Physical Chemistry C* **2011**, *115*, 25343.

(24) Gross, S.; Bertram, A. K. *Journal of Geophysical Research: Atmospheres* **2009**, *114*, n/a.

(25) Knopf, D. A.; Mak, J.; Gross, S.; Bertram, A. K. *Geophysical Research Letters* **2006**, *33*, n/a.

(26) Lee, L.; Wooldridge, P.; Nah, T.; Wilson, K.; Cohen, R. *Physical Chemistry Chemical Physics* **2013**, *15*, 882.

(27) Knopf, D. A.; Forrester, S. M.; Slade, J. H. *Physical Chemistry Chemical Physics* **2011**, *13*, 21050.

(28) Shiraiwa, M.; Pöschl, U.; Knopf, D. A. *Environmental Science & Technology* **2012**, *46*, 6630.

(29) Moise, T.; Talukdar, R. K.; Frost, G. J.; Fox, R. W.; Rudich, Y. *Journal of Geophysical Research: Atmospheres* **2002**, *107*, AAC 6.

(30) Shiraiwa, M.; Pfrang, C.; Pöschl, U. *Atmos. Chem. Phys.* **2010**, *10*, 3673.

(31) Shiraiwa, M.; Garland, R. M.; Pöschl, U. *Atmos. Chem. Phys.* **2009**, *9*, 9571.

(32) Ilchmann, K.; Revill, J. *Science and Engineering Ethics* **2014**, *20*, 753.

(33) Friboulet, A.; Rieger, F.; Goudou, D.; Amitai, G.; Taylor, P. *Biochemistry* **1990**, *29*, 914.

(34) Albaret, C.; Lacoutière, S.; Ashman, W. P.; Froment, D.; Fortier, P.-L. *Proteins: Structure, Function, and Bioinformatics* **1997**, *28*, 543.

(35) Shih, T.-M.; Kan, R. K.; McDonough, J. H. *Chemico-Biological Interactions* **2005**, *157–158*, 293.

(36) In *Science* 2013.

(37) Black, R. M.; Clarke, R. J.; Read, R. W.; Reid, M. T. J. *Journal of Chromatography A* **1994**, *662*, 301.

(38) Okumura, T.; Ariyoshi, K.; Hitomi, T.; Hirahara, K.; Itoh, T.; Iwamura, T.; Nakashima, A.; Motomura, Y.; Taki, K.; Suzuki, K. *Toxin Reviews* **2009**, *28*, 255.

(39) Chao, L. L.; Rothlind, J. C.; Cardenas, V. A.; Meyerhoff, D. J.; Weiner, M. W. *NeuroToxicology* **2010**, *31*, 493.

(40) Tsuchihashi, H.; Katagi, M.; Nishikawa, M.; Tatsuno, M. *Journal of Analytical Toxicology* **1998**, *22*, 383.

(41) Jang, Y. J.; Kim, K.; Tsay, O. G.; Atwood, D. A.; Churchill, D. G. *Chemical Reviews* **2015**, *115*, PR1.

(42) Jenkins, R. A.; Buchanan, M. V.; Merriweather, R.; Ilgner, R. H.; Gayle, T. M.; Watson, A. P. *Journal of Hazardous Materials* **1994**, *37*, 303.

(43) Council, N. R. *Strategies to Protect the Health of Deployed U.S. Forces: Force Protection and Decontamination*; The National Academies Press: Washington, DC, 1999.

(44) Beaudry, W. T.; Wagner, G. W.; Richard Ward, J. *Journal of Molecular Catalysis* **1992**, *73*, 77.

(45) Khan, M. A. S.; Kesharwani, M. K.; Bandyopadhyay, T.; Ganguly, B. *Journal of Molecular Structure: THEOCHEM* **2010**, *944*, 132.

(46) Kesharwani, M. K.; Khan, M. A. S.; Bandyopadhyay, T.; Ganguly, B. *Theoretical Chemistry Accounts* **2010**, *127*, 39.

(47) Bjarnason, S.; Mikler, J.; Hill, I.; Tenn, C.; Garrett, M.; Caddy, N.; Sawyer, T. *Human & Experimental Toxicology* **2008**, *27*, 253.

(48) DeBruin, K. E.; Tang, C. I. W.; Johnson, D. M.; Wilde, R. L. *Journal of the American Chemical Society* **1989**, *111*, 5871.

(49) Yang, Y.-C.; J. Berg, F.; L. Szafraniec, L.; T. Beaudry, W.; A. Bunton, C.; Kumar, A. *Journal of the Chemical Society, Perkin Transactions 2* **1997**, 607.

(50) Russell, A. J.; KAAR, J. L.; BERBERICH, J. A. In *Frontiers of Engineering: Reports on Leading-Edge Engineering from the 2003 NAE Symposium on Frontiers of Engineering*; National Academies Press: 2004, p 77.

(51) Augustinsson, K.-B.; Heimburger, G. *Acta Chem Scand* **1954**, *8*, 1533.

(52) Morales-Rojas, H.; Moss, R. A. *Chemical Reviews* **2002**, *102*, 2497.

(53) Farquharson, S.; Inscore, F. E.; Christesen, S. In *Surface-Enhanced Raman Scattering*; Springer: 2006, p 447.

(54) Gustafson, R. L.; Martell, A. E. *Journal of Physical Chemistry* **1963**, *67*.

(55) Ward, J. R.; Yang, Y.-C.; Wilson Jr, R. B.; Burrows, W. D.; Ackerman, L. L. *Bioorganic Chemistry* **1988**, *16*, 12.

(56) Daniel, K. A.; Kopff, L. A.; Patterson, E. V. *Journal of Physical Organic Chemistry* **2008**, *21*, 321.

(57) Šečkutė, J.; Menke, J. L.; Emnett, R. J.; Patterson, E. V.; Cramer, C. J. *The Journal of Organic Chemistry* **2005**, *70*, 8649.
(58) Smentkowski, V.; Hagans, P.; Yates Jr, J. *J. Phys. Chem.;(United States)* **1988**, *92*.
(59) Hegde, R. I.; Greenlief, C. M.; White, J. M. *The Journal of Physical Chemistry* **1985**, *89*, 2886.
(60) Guo, X.; Yoshinobu, J.; Yates, J. T. *The Journal of Physical Chemistry* **1990**, *94*, 6839.
(61) Henderson, M. A.; White, J. M. *Journal of the American Chemical Society* **1988**, *110*, 6939.
(62) Praveen Kumar, J.; Prasad, G. K.; Ramacharyulu, P. V. R. K.; Garg, P.; Ganesan, K. *Materials Chemistry and Physics* **2013**, *142*, 484.
(63) Verma, A. K.; Srivastava, A. K.; Singh, B.; Shah, D.; Shrivastava, S.; Shinde, C. K. P. *Chemosphere* **2013**, *90*, 2254.
(64) Mitchell, M. B.; Sheinker, V. N.; Cox Jr, W. W.; Hardcastle, K. *The Journal of Physical Chemistry C* **2011**, *115*, 11514.
(65) Janos, P.; Kuran, P.; Kormunda, M.; Stengl, V.; Grygar, T. M.; Dosek, M.; Stastny, M.; Ederer, J.; Pilarova, V.; Vrtoch, L. *Journal of Rare Earths* **2014**, *32*, 360.
(66) Mizrahi, D. M.; Saphier, S.; Columbus, I. *Journal of hazardous materials* **2010**, *179*, 495.
(67) Chen, D. A.; Ratliff, J. S.; Hu, X.; Gordon, W. O.; Senanayake, S. D.; Mullins, D. R. *Surface Science* **2010**, *604*, 574.
(68) Motamedhashemi, M. Y.; Egolfopoulos, F.; Tsotsis, T. *Journal of membrane science* **2011**, *376*, 119.
(69) Saxena, A.; Srivastava, A. K.; Singh, B.; Goyal, A. *Journal of hazardous materials* **2012**, *211*, 226.
(70) Štengl, V.; Grygar, T. M.; Opluštil, F.; Němec, T. *Journal of hazardous materials* **2012**, *227*, 62.
(71) Sato, K.; Hirakawa, T.; Komano, A.; Kishi, S.; Nishimoto, C. K.; Mera, N.; Kugishima, M.; Sano, T.; Ichinose, H.; Negishi, N. *Applied Catalysis B: Environmental* **2011**, *106*, 316.
(72) Štengl, V.; Bludska, J.; Opluštil, F.; Němec, T. *Materials Research Bulletin* **2011**, *46*, 2050.
(73) Knagge, K.; Johnson, M.; Grassian, V. H.; Larsen, S. C. *Langmuir* **2006**, *22*, 11077.
(74) Williamson, C. J.; O'Brien, P. *Journal of Materials Chemistry* **1994**, *4*, 565.
(75) Katz, M. J.; Mondloch, J. E.; Totten, R. K.; Park, J. K.; Nguyen, S. T.; Farha, O. K.; Hupp, J. T. *Angewandte Chemie International Edition* **2014**, *53*, 497.
(76) Wang, S.; Bromberg, L.; Schreuder-Gibson, H.; Hatton, T. A. *ACS applied materials & interfaces* **2013**, *5*, 1269.
(77) Ma, F.-J.; Liu, S.-X.; Sun, C.-Y.; Liang, D.-D.; Ren, G.-J.; Wei, F.; Chen, Y.-G.; Su, Z.-M. *Journal of the American Chemical Society* **2011**, *133*, 4178.
(78) Peterson, G. W.; Wagner, G. W. *Journal of Porous Materials* **2014**, *21*, 121.
(79) DeCoste, J. B.; Browe, M. A.; Wagner, G. W.; Rossin, J. A.; Peterson, G. W. *Chemical Communications* **2015**, *51*, 12474.
(80) Troya, D. *The Journal of Physical Chemistry C* **2016**, *120*, 29312.

(81) Moon, S.-Y.; Wagner, G. W.; Mondloch, J. E.; Peterson, G. W.; DeCoste, J. B.; Hupp, J. T.; Farha, O. K. *Inorganic Chemistry* **2015**, *54*, 10829.
(82) DeCoste, J. B.; Peterson, G. W. *Chemical Reviews* **2014**, *114*, 5695.
(83) López-Maya, E.; Montoro, C.; Rodríguez-Albelo, L. M.; Aznar Cervantes, S. D.; Lozano-Pérez, A. A.; Cenís, J. L.; Barea, E.; Navarro, J. A. R. *Angewandte Chemie International Edition* **2015**, *54*, 6790.
(84) Plonka, A. M.; Wang, Q.; Gordon, W. O.; Balboa, A.; Troya, D.; Guo, W.; Sharp, C. H.; Senanayake, S. D.; Morris, J. R.; Hill, C. L.; Frenkel, A. I. *Journal of the American Chemical Society* **2017**, *139*, 599.
(85) Guo, W.; Lv, H.; Sullivan, K. P.; Gordon, W. O.; Balboa, A.; Wagner, G. W.; Musaev, D. G.; Bacsa, J.; Hill, C. L. *Angewandte Chemie International Edition* **2016**, *55*, 7403.
(86) Okun, N. M.; Tarr, J. C.; Hilleshiem, D. A.; Zhang, L.; Hardcastle, K. I.; Hill, C. L. *Journal of Molecular Catalysis A: Chemical* **2006**, *246*, 11.
(87) Gall, R. D.; Hill, C. L.; Walker, J. E. *Chemistry of materials* **1996**, *8*, 2523.
(88) Davis, M. E.; Davis, R. J. *Fundamentals of chemical reaction engineering*; Courier Corporation, 2012.
(89) Ceyer, S. T. *Annual Review of Physical Chemistry* **1988**, *39*, 479.
(90) Shibuta, Y.; Arifin, R.; Shimamura, K.; Oguri, T.; Shimojo, F.; Yamaguchi, S. *Chemical Physics Letters* **2013**, *565*, 92.
(91) Hamza, A. V.; Madix, R. *Surface science* **1987**, *179*, 25.
(92) Langmuir, I. *Transactions of the Faraday Society* **1922**, *17*, 607.
(93) Ertl, G. *Surface Science* **1994**, *299*, 742.
(94) McCabe, J.; Abbatt, J. P. D. *The Journal of Physical Chemistry C* **2009**, *113*, 2120.
(95) Rettner, C. T.; Auerbach, D. J. *Science-AAAS-Weekly Paper Edition-including Guide to Scientific Information* **1994**, *263*, 365.
(96) Graham, J. D.; Roberts, J. T. *The Journal of Physical Chemistry* **1994**, *98*, 5974.
(97) Brass, S. G.; Ehrlich, G. *The Journal of Chemical Physics* **1987**, *87*, 4285.
(98) Beck, R. D.; Maroni, P.; Papageorgopoulos, D. C.; Dang, T. T.; Schmid, M. P.; Rizzo, T. R. *Science* **2003**, *302*, 98.
(99) Smith, R.; Killelea, D.; DelSesto, D.; Utz, A. *Science* **2004**, *304*, 992.
(100) Atkins, P.; Friedman, R. **2005**.
(101) Greenler, R. G. *J. Chem. Phys.* **1966**, *44*, 6.
(102) Greenler, R. G. *Journal of Vacuum Science and Technology* **1975**, *12*, 1410.
(103) Newville, M. *Reviews in Mineralogy and Geochemistry* **2014**, *78*, 33.

Chapter 2
Applied Computational Methods in Investigations of Reactions at the Gas—Surface Interface

In this chapter, we describe the computational approaches used to investigate the heterogeneous gas—surface systems described in this dissertation. We begin with electronic structure calculations, through the basic scope of Hartree-Fock theory. After describing this method and how it is used to calculate molecular energy, we highlight its shortcomings and go on to discuss density functional theory, and how it attempts to remedy what is lacking from of Hartree-Fock theory.

With an understanding of how energy is calculated in both of these methods, we continue our discussion with geometry optimization and vibrational frequency calculations, eventually tying together these two concepts to verify the nature of a stationary point. Next, we describe the intrinsic reaction coordinate method and how it can further verify a transition state by linking it to its adjacent minima.

We end the chapter with an introduction to molecular mechanics and its applicability to much larger systems than can be treated with electronic structure calculations. Considering the approximations that must be made in the name of treating a large system, we conclude by considering QM/MM methods as a compromise between accuracy and efficiency for large systems where results from a high-level approach is desired.

2.1 Electronic Structure Calculations

2.1.1 The Schrödinger Equation and Hamiltonian Operator

A main goal of computational chemistry is to describe the electronic motions and energy of a molecular system. This can be accomplished by solving the electronic Schrödinger equation (Equation 2.1) for a given molecular geometry.[1]

$$\hat{H}\Psi = E\Psi \tag{2.1}$$

where E is the energy of the molecule, $\hat{H}$ denotes the Hamiltonian operator, and Ψ is the molecular wavefunction. The individual terms of the Hamiltonian operator are identified in Equation 2.2, and each term is expanded in Equation 2.3. Note: for simplicity and convenience,

atomic units are commonly used in theoretical chemistry,[2] and these units will be used in the equations presented in this section on electronic structure calculations.

$$\hat{H} = \hat{T}_N + \hat{T}_e + V_{NN} + V_{ee} + V_{eN} \tag{2.2}$$

$$\hat{H} = -\sum_{A}^{nuc} \frac{1}{2m_A} \nabla_A^2 - \sum_{i}^{e^-} \frac{1}{2} \nabla_i^2 + \sum_{A>B}^{nuc} \frac{Z_A Z_B}{R_{AB}} + \sum_{i>j}^{e^-} \frac{1}{r_{ij}} - \sum_{A}^{nuc} \sum_{i}^{e^-} \frac{Z_A}{r_{iA}} \tag{2.3}$$

The first two terms in the Hamiltonian represent the kinetic energy of nuclei and electrons, $\hat{T}_\mathrm{N}$ and $\hat{T}_\mathrm{e}$; and the last three terms represent the potential energies of internuclear and interelectronic repulsion as well as electron-nuclear attraction: V_NN, V_ee, and V_eN, respectively. In Equation 2.3, capital *A* and *B* identify individual nuclei, and lowercase *i* and *j* represent individual electrons. Z_A is the atomic number of nucleus *A* with mass m_A, *R* represents internuclear distance, and *r* represents interelectronic (r_ij) or electron-nuclear (r_iA) distance. Finally, ∇^2 represents the Laplacian operator, given as $\nabla^2 = \frac{\partial^2}{\partial x^2} + \frac{\partial^2}{\partial y^2} + \frac{\partial^2}{\partial z^2}$ for a set of spatial coordinates *x*, *y*, and *z*.

2.1.2 The Born-Oppenheimer Approximation

In order to determine the electronic structure of a molecule, certain reasonable approximations are commonly made, for the sake of mathematical solvability and computational efficiency. The first of those approximations is the Born-Oppenheimer approximation—that the nuclei can be treated with fixed coordinates.[3] Since the mass of the electron is roughly 1800 times less than that of a proton, the electrons move on a much shorter timescale, thus justifying this approximation. In the Hamiltonian operator, as a result of fixed nuclear coordinates, $\hat{T}_\mathrm{N}$ becomes zero, and V_NN becomes a constant which is simply added to the electronic energy solution to the Schrödinger equation. The Schrödinger equation, modified to include this electronic Hamiltonian, $\hat{H}_\mathrm{el}$, is given in Equation 2.4.

$$\hat{H}_{el} \Psi_{el}(\vec{r}; \vec{R}) = E_{el}(\vec{R}) \Psi_{el}(\vec{r}; \vec{R}) \tag{2.4}$$

Resulting from application of the Born-Oppenheimer approximation, the wavefunction $\Psi(\vec{r}; \vec{R})$ now describes the electrons with a vector $\vec{r}$ which includes three spatial coordinates and one spin coordinate for each electron in a field of fixed nuclear charges with spatial coordinates for each nucleus denoted collectively by the vector $\vec{R}$.

2.1.3 Hartree-Fock Theory

2.1.3.1 Slater Determinants

Despite the Born-Oppenheimer approximation, the electronic Schrödinger equation becomes impossible to solve exactly for multi-electronic systems. To simplify the mathematics a bit more, a further approximation can be made that the Schrödinger equation can be solved by describing the electronic wavefunction as a single Slater determinant. That is,

$$\Psi^{HF}(\vec{x}_1, \vec{x}_2, \ldots, \vec{x}_N) = \frac{1}{\sqrt{N!}} \begin{vmatrix} \chi_1(\vec{x}_1) & \chi_2(\vec{x}_1) & \cdots & \chi_N(\vec{x}_1) \\ \chi_1(\vec{x}_2) & \chi_2(\vec{x}_2) & \cdots & \chi_N(\vec{x}_2) \\ \vdots & \vdots & \ddots & \vdots \\ \chi_1(\vec{x}_N) & \chi_2(\vec{x}_N) & \cdots & \chi_N(\vec{x}_N) \end{vmatrix} \tag{2.5}$$

where N is the total number of electrons, $\vec{x}_\mathrm{i}$ represents the three spatial and one spin coordinate for a single electron i, and χ_i represents individual electronic orbitals.

2.1.3.2 Hartree-Fock Energy

Implementing the above two approximations: the Born-Oppenheimer approximation and expression of a wavefunction (Ψ^{HF}) as a single Slater determinant, Hartree-Fock theory attempts to solve the electronic Schrödinger equation.[4,5] During this process, orbitals χ_i are selected so as to minimize the calculated electronic energy of the molecule, E_el. In doing so, this theory invokes the Variational principle, which states that the ground-state energy of a molecule is always lower than the expectation value of the Hamiltonian operator, $\widehat{H}_\mathrm{el}$. Thus, the lower the energy resulting from a set of χ_i, the closer in energy the calculated E_el will be to the actual ground-state electronic energy of a molecule. The expectation value of the Hamiltonian, and thus the Hartree-Fock energy (E^{HF}), is calculated using Equation 2.6:

$$E^{HF} = \int (\Psi^{HF})^* \, \widehat{H}_{el} \, \Psi^{HF} \, d\tau \tag{2.6}$$

where $(\Psi^{\mathrm{HF}})^*$ is the complex conjugate of Ψ^{HF}, and integration is taken over all space.

At this point, it becomes useful to introduce the concepts of one- and two-electron operators. The one-electron Hamiltonian $\hat{h}(i)$, defined in Equation 2.7, includes the one-electron kinetic energy term for electron i and the term for electron-nuclear attraction between all nuclei and electron i:

$$\hat{h}(i) = -\frac{1}{2}\nabla_i^2 - \sum_A^{nuc} \frac{Z_A}{r_{iA}} \tag{2.7}$$

A separate, two-electron term, includes electron-electron repulsions between electron *i* and another electron *j*:

$$V(i,j) = \frac{1}{r_{ij}} \tag{2.8}$$

Using these one-electron and two-electron operators, the electronic Hamiltonian for a molecule then becomes:

$$\hat{H}_{el} = \sum_{i}^{e^-} \hat{h}\,(i) + \sum_{i>j}^{e^-} V(i,j) + V_{NN} \tag{2.9}$$

and the electronic Hartree-Fock energy becomes:

$$E^{HF} = \sum_{i}^{e^-} < i|\hat{h}|i > + \frac{1}{2}\sum_{i,j}^{e^-} < ij|ij > - < ij|ji > + V_{NN} \tag{2.10}$$

The bracketed terms in Equation 2.10 are given in Dirac notation[6] and can be expanded following the relations for generic orbitals p, q, r, and s, and operator $\hat{O}$:

$$< p|q > \equiv \int \chi_p^*(\vec{x}_1)\chi_q(\vec{x}_1)\, d\vec{x}_1 \tag{2.11}$$

$$< p|\hat{O}|q > \equiv \int \chi_p^*(\vec{x}_1)\hat{O}\chi_q(\vec{x}_1)\, d\vec{x}_1 \tag{2.12}$$

$$< pq|rs > \equiv \int d\vec{x}_1 \int d\vec{x}_2\, \chi_p^*(\vec{x}_1)\chi_q^*(\vec{x}_2)\frac{1}{r_{12}}\chi_r(\vec{x}_1)\chi_s(\vec{x}_2) \tag{2.13}$$

In Equation 2.10, the $< ij|ij >$ term gives the Coulomb repulsion between electrons 1 and 2 in orbitals *i* and *j*, respectively. $< ij|ji >$ is denoted the exchange term and is a consequence of the Pauli exclusion principle[7] and the expression of the wavefunction as a Slater determinant.

2.1.3.3 Orbital Calculation

Having described how E^{HF} is calculated, we now turn our attention to the method in which orbitals are selected to yield the minimum possible energy. Equation 2.14 shows the use of a Lagrangian function[8] to achieve this minimization.

$$\mathcal{L}[\{\chi_i\}] = E^{HF}[\{\chi_i\}] - \sum_{ij} \varepsilon_{ij}(< i|j > - \delta_{ij}) \tag{2.14}$$

where $\mathcal{L}[\{\chi_i\}]$ specifies the Lagrangian as a function of all orbitals χ_i, ε_{ij} denote undetermined multipliers, and δ_{ij} is the Kronecker delta (δ_{ij}=1 if i=j; δ_{ij}=0 otherwise), which enforces orthonormality of the orbitals.

If orbital χ_i is changed slightly to some $\chi_\mathrm{i} + \delta\chi_\mathrm{i}$ in Equation 2.14, a resulting $\delta\mathcal{L}[\{\chi_\mathrm{i}\}]$ can be expanded. Setting $\delta\mathcal{L}[\{\chi_\mathrm{i}\}]$ to zero ensures a minimum of the Lagrangian function and consequently a minimum E^{HF}. When $\delta\mathcal{L}[\{\chi_\mathrm{i}\}]$ is set to zero, the resulting relation can be derived:

$$[\hat{h}(\vec{x}_1) + \sum_j \hat{J}_j(\vec{x}_1) - \hat{K}_j(\vec{x}_1)]\,\chi_i(\vec{x}_1) = \sum_j \varepsilon_{ij}\,\chi_j(\vec{x}_1) \tag{2.15}$$

which includes a Coulomb repulsion term, $\hat{J}_\mathrm{j}(\vec{x}_1)$:

$$\hat{J}_j(\vec{x}_1) = \int d\vec{x}_2 |\,\chi_j(\vec{x}_2)|^2 \frac{1}{r_{12}} \tag{2.16}$$

and an exchange term, $\hat{K}_\mathrm{j}(\vec{x}_1)$:

$$\hat{K}_j(\vec{x}_1) = \int d\vec{x}_2\,\chi_j{}^*(\vec{x}_2)\chi_i(\vec{x}_2)\frac{1}{r_{12}} \tag{2.17}$$

2.1.3.4 Self-Consistent Field

The operator on the left-hand side of Equation 2.15 which acts on $\chi_\mathrm{i}(\vec{x}_1)$ is known as the Fock operator, $\hat{F}(\vec{x}_1)$. The Fock operator can be used to obtain orbital functions χ_i and their corresponding orbital energies ε_i:

$$\hat{F}(\vec{x}_1)\chi_i(\vec{x}_1) = \varepsilon_i\chi_i(\vec{x}_1) \tag{2.18}$$

where ε_i is a diagonal element of the matrix ε_ij. A complication with this eigenvalue equation is the inclusion of χ in the Fock operator. χ is an eigenfunction obtained through the use of $\hat{F}$, but $\hat{F}$ uses χ in its $\hat{J}$ and $\hat{K}$ terms. To work around this, an initial guess set of χ is used to obtain $\hat{J}$, $\hat{K}$, and $\hat{F}$, initially. This initial $\hat{F}$ is then used to generate a new set of χ, which is then used to obtain new $\hat{F}$ and subsequently χ. This process is repeated until the values of χ converge to within a given limit. This process of reiterating $\hat{F}$ and χ is known as the Hartree Fock Self-consistent Field (SCF) procedure.

2.1.3.5 The Hartree-Fock-Roothan Method

Extending this procedure a bit further, the Hartree-Fock-Roothan[9,10] method begins with a pre-selected set of one-electron basis functions, $\tilde{\chi}_\mu$, used to describe a molecular orbital X_i when scaled by a set of constants C:

$$\mathrm{X}_i = \sum_{\mu=1}^{k} C_{\mu i}\, \tilde{\chi}_\mu \tag{2.19}$$

These constants provide a linear combination of the basis functions supplied by the basis set and are optimized during the SCF procedure. Combined, these scaled basis functions describe the molecular orbital. This optimization process is called the linear combination of atomic orbitals (LCAO) technique. Although this name may imply that basis functions are centered on atomic nuclei, this is not necessarily true. Even more importantly, basis set selection is highly dependent upon the molecular system of interest. This will be discussed to more depth later in this chapter.

Key approximations of Hartree-Fock theory include the Born-Oppenheimer approximation and the description of the wavefunction as a single Slater determinant. Whereas these can potentially affect the accuracy of energies calculated using this method, the largest source of error lies in the fact that electron correlation is unaccounted for. For example, the Coulomb exchange energy for each electron is calculated by treating all the other electrons collectively, contributing towards a mean field of charge that interacts with the electron of interest. Thus, the dependence of this energy on the instantaneous behavior of another specific electron is neglected.

2.1.4 Density Functional Theory

Density functional theory (DFT) methods attempt to remedy the lack of electron correlation inherent to Hartree-Fock while solving the Schrödinger equation in a similar fashion. At a similar computational cost to the Hartree-Fock method, DFT methods have been shown to yield much more accurate results when it comes to ground-state molecular structure, theoretical spectra, and reaction enthalpy calculations.

As opposed to a wavefunction as in Hartree-Fock, DFT uses electron density, $\rho(\vec{r})$, to calculate the molecular energy. Whereas the wavefunction is a function of four coordinates (three spatial and one spin) for each electron, electron density is a function of three spatial coordinates, immediately reducing the mathematical complexity of solving the Schrödinger equation.

Hohenberg and Kohn initially proved that energy is a functional of electron density; given a function that describes electron density throughout space, electronic energy can be calculated. Further, they showed that, like Hartree-Fock Theory, DFT methods are variational; that is, the correct ground-state density can be obtained through minimization of energy obtained

with the density functional.[11] The form of this functional, and thus the means by which energy is approximated from the density function varies from one DFT method to the next.

2.1.4.1 The Density Functional

The density functional for electronic energy is typically divided into terms for electronic kinetic energy, electron-electron interaction energy, and electron-nuclear attraction energy, as shown in Equation 2.20. This is analogous to the electronic Hamiltonian operator in Hartree-Fock Theory.

$$E[\rho(\vec{r})] = T[\rho(\vec{r})] + E_{ee}[\rho(\vec{r})] + E_{eN}[\rho(\vec{r})] \tag{2.20}$$

To solve for the electron kinetic energy term, $T[\rho(\vec{r})]$, Kohn and Sham[12] treated individual electrons as non-interacting with one another. Instead, electrons are considered to interact with an average charge field of all the other electrons. This is much the same as in Hartree-Fock theory, which does not include explicit electron correlation. Thus, kinetic energy can be calculated using orbitals, as in Hartree-Fock. The Kohn-Sham DFT electronic kinetic energy operator, $\hat{T}_s$, is given in Equation 2.21, in which each electron is in an orbital ϕ_i:

$$\hat{T}_s = \sum_{i}^{e^-} < \phi_i \left| -\frac{1}{2}\nabla_i^2 \right| \phi_i > \tag{2.21}$$

$\rho(\vec{r})$ can be calculated from the occupied orbitals used in the above equation:

$$\rho(\vec{r}) = \sum_{i}^{occ.orbitals} |\phi_i(\vec{r})|^2 \tag{2.22}$$

Electron-electron interaction energy, $E_{\mathrm{ee}}[\rho(\vec{r})]$, similar to that in Hartree-Fock Theory, contains terms for Coulomb repulsion and electron exchange. The Coulomb repulsion term, $J[\rho(\vec{r})]$, is derived through the consideration of two interacting electron density distributions, $\rho(\vec{r})$ and $\rho(\vec{r}')$ over a distance of $\vec{r} - \vec{r}'$:

$$J[\rho(\vec{r})] = \frac{1}{2}\int\int \frac{\rho(\vec{r})\rho(\vec{r}')}{|\vec{r} - \vec{r}'|} d\vec{r} d\vec{r}' \tag{2.23}$$

The final term in the functional, $E_{\mathrm{eN}}[\rho(\vec{r})]$, gives the electron-nuclear attraction energy. This term is defined in Equation 2.24 and is very similar to the V_{eN} term in the Hamiltonian operator.

$$E_{eN}[\rho(\vec{r})] = -\sum_{A}^{nuc} \int \frac{Z_A \rho(\vec{r})}{|\vec{R}_A - \vec{r}|} d\vec{r} \tag{2.24}$$

Whereas the analogous term in the Hamiltonian takes a double sum over all nuclei and electrons, the electron-nuclear attraction functional term sums over all nuclei and integrates over all possible points with electron density. In Equation 2.24, $\left|\vec{R}_A - \vec{r}\right|$ is the distance between a point in space where density is being probed and a given nucleus A.

2.1.4.2 Exchange and Correlation

So far, we have described the electronic kinetic, Coulomb repulsion, and electron-nuclear attraction contribution terms in the energy density functional equation (Equation 2.20). The contribution due to electron exchange from the electron-electron interaction must still be considered. A correction resulting from the fact that explicit electron-electron interactions are neglected in the Kohn-Sham kinetic energy functional is also required. This correction is commonly referred to as electron correlation. In practice, approximations of exchange ($E_{\mathrm{X}}[\rho(\vec{r})]$) and correlation ($E_{\mathrm{C}}[\rho(\vec{r})]$) functionals set apart one density functional from another, and are typically summed into a single term in the density functional, $E_{\mathrm{XC}}[\rho(\vec{r})]$. Thus,

$$E_{XC}[\rho(\vec{r})] = (T[\rho(\vec{r})] - T_s[\rho(\vec{r})]) + (E_{ee}[\rho(\vec{r})] - J[\rho(\vec{r})]) \tag{2.25}$$

To summarize the terms contributing to the DFT calculation of energy, Equation 2.20 can be rewritten as:

$$E[\rho(\vec{r})] = T_s[\rho(\vec{r})] + E_{eN}[\rho(\vec{r})] + J[\rho(\vec{r})] + E_{XC}[\rho(\vec{r})] \tag{2.26}$$

2.1.4.3 Kohn-Sham SCF Method

The calculation of the Kohn-Sham kinetic energy requires orbitals occupied by electrons. Similar to the Hartree-Fock method, these orbitals can be obtained using a SCF procedure. In the SCF procedure for Kohn-Sham DFT, the one-electron operator $\hat{h}_{\mathrm{KS}}$ is used, which includes kinetic energy and effective potential terms:

$$\hat{h}_{KS} = -\frac{1}{2}\nabla^2 + V_{eff} \tag{2.27}$$

The effective potential, V_{eff}, on the electron includes the attraction between that electron and all nuclei, the field of all other electrons, and corrections due to exchange and correlation:

$$V_{eff}(\vec{r}) = V_{eN}(\vec{r}) + \int \frac{\rho(\vec{r})'}{|\vec{r} - \vec{r}'|} + V_{XC}(\vec{r}) \tag{2.28}$$

where

$$V_{XC}(\vec{r}) = \frac{\delta E_{XC}[\rho(\vec{r})]}{\delta[\rho(\vec{r})]} \tag{2.29}$$

With the one-electron Kohn-Sham operator, orbitals can be calculated as eigenfunctions of Equation 2.30:

$$\hat{h}_{KS}\phi_i = \varepsilon_i\phi_i \tag{2.30}$$

The above equation is solved iteratively to convergence in order to generate occupied orbitals, ϕ_{i}, and energies, ε_{i}. Electron density can then be calculated using Equation 2.22. Further, as in the implementation of Hartree-Fock-Roothan theory,[9,10] an appropriate basis set can be specified and scaled by a corresponding set of constants in order to describe molecular orbitals. In this common case, the value of the constants is optimized in the SCF procedure.

2.1.4.4 Types of Density Functionals

2.1.4.4.1 Local-Density Approximation Functionals

The calculation of the first three terms on the right-hand side of Equation 2.26 are straightforward and typically do not vary across various DFT functionals. However, as there is no single definitive form for exchange and correlation functionals, approximations are commonly made in the $E_{\mathrm{XC}}[\rho(\vec{r})]$ term. In the local-density approximation (LDA),[11] the exchange-correlation energy at some position $\vec{r}$ can be computed from the density at that position. The LDA exchange functional, $E_{\mathrm{X}}[\rho(\vec{r})]$, is defined as:

$$E_X{}^{LDA}[\rho(\vec{r})] = -\frac{3}{4}\left(\frac{3}{\pi}\right)^{1/3}\int \rho^{4/3}(\vec{r})\, d\vec{r} \tag{2.31}$$

This approximation is derived through the treatment of electron density as a uniform electron gas, with equal electron density at all points in space. To date, there is no correlation functional derived analytically from the uniform electron gas model. However, several research groups have fitted numerical LDA correlation functionals from the results of quantum Monte Carlo calculations.[13] Examples include the VWN ,[14] PZ81,[15] CP,[16] and PW92[17] functionals.

2.1.4.4.2 Generalized Gradient Approximation and Meta-GGA Functionals

Because LDA functionals assume uniform electron density everywhere, they tend to overestimate exchange-correlation energy. In an attempt to account for non-homogeneous electron density, the generalized gradient approximation (GGA) assumes that E_{XC} depends not only on $\rho(\vec{r})$ but also on its derivative. There are various forms of both exchange and correlation functionals that implement GGA. A common GGA exchange functional is B88,[18] and correlation functionals include PW91[19] and LYP.[20] Meta-GGA functionals extend GGA functionals by incorporating a dependence of the functional on the second derivative of density, along with the

dependence on density and its gradient as seen in GGA functionals. The M06-L density functional[21] is a representative example.

The M06-L density functional, used in our work with polyoxoniobates (Chapters 5-8), was chosen for its good performance with both main group and transition metal chemistry as well as organometallic and noncovalent interactions.[21] Noncovalent interactions, as we will discuss in detail, play an integral role in the energetics of the hydrolysis of organophosphorus nerve agents by Lindqvist polyoxoniobates. One drawback to the Minnesota group of functionals such as M06-L is the higher sensitivity to the integration grid than is normally used in electronic energy calculations.[22] Integration grids vary by the number of points per atom used to calculate numerical integrals. In the Gaussian suite of software,[23] an ultrafine grid uses 99 radial shells per atom, and 590 angular points per shell, for a total of 58,410 integration points per atom. Comparatively, a superfine integration grid uses 175 radial shells for first row atoms and 250 shells for atoms in the second row and above, and each shell has 974 angular integration points. Results of integration-grid sensitivity in M06-L can be seen by comparing the reaction energetics for Sarin hydrolysis by $Cs_8Nb_6O_{19}$ using an ultrafine integration grid (Figure 5.2, X-F pathway) to those using a superfine integration grid (Figure 8.1, black trace).

2.1.4.4.3 Hybrid Functionals

Finally, hybrid DFT methods incorporate Hartree-Fock exchange along with exchange and correlation functionals from other sources. Common examples include B3YLP,[24] PBE0,[25,26] and HSE.[27] In B3LYP specifically, the exchange-correlation functional incorporates the LDA exchange functional and the VWN approximation to LDA correlation,[14] as well as B88 exchange,[18] LYP correlation[20] and Hartree-Fock exchange. Individual terms in the B3LYP exchange-correlation functional (E_{XC}^{B3LYP}) have been scaled by three parameters derived from experimental data:

$$E_{XC}^{B3LYP} = E_X^{LDA} + a_0(E_X^{HF} - E_X^{LDA}) + a_X(E_X^{B88} - E_X^{LDA}) + E_C^{LDA} + a_C(E_C^{LYP} - E_C^{LDA}) \quad (2.32)$$

In Equation 2.32, the three experimentally derived parameters, a_0, a_X, and a_C, are 0.20, 0.72, and 0.81, respectively.

In our work with atmospheric systems, we chose the B3LYP hybrid functional, which has generally been shown to provide accurate results in organic systems.[28] Specifically, this functional has successfully been used to calculate the energetics[29,30] and theoretical spectra[31] for

the ozonolysis of aromatic compounds and fullerenes, motivating our choice of this method for C_{60} ozonolysis investigations (Chapter 3). Further, B3LYP has been shown to accurately replicate geometries and vibrational spectra with experimental results for a series of organic nitrates;[32] thus, this density functional was also our primary choice for theoretical spectra calculations of the products of nitrate addition to an unsaturated organic surface (Chapter 4).

2.1.5 Basis Sets

2.1.5.1 Gaussian Basis Sets

In electronic structure calculations, a basis set of functions is typically used and subsequently scaled during an SCF procedure. These one-electron functions are used to build molecular orbitals. Most modern computational chemistry programs use Gaussian functions to describe orbitals. Gaussian functions have the following general form:

$$\phi_{abc}^{Gaussian}(x,y,z) = Nx^a y^b z^c e^{-\zeta r^2} \tag{2.33}$$

where x, y, and z are spatial coordinates, N is a normalization constant, ζ describes the width of the orbital, and r describes the distance of the point with coordinates (x,y,z) from the center of the Gaussian function. a, b, and c are integers used to describe the angular momentum of the orbital. For spherical orbitals, a=b=c=0. For p orbitals, one of these integers is 1, where the remaining two are zero; for example, a p_x orbital has a=1, and b=c=0. d orbitals have two of these integers equal to 1, such as in d_{yz}, with a=0, and b=c=1.

According to the Gaussian Product Theorem, a product of two Gaussian functions equals another Gaussian, facilitating their ease of use in Hartree-Fock and DFT methods which involve a great deal of orbital multiplication. Due to this convenience, Gaussian-type orbitals (GTOs)[33] are used almost universally by computational chemists. This is despite the fact that Slater-type orbitals (STOs),[34] with an exponential r term (instead of the r^2 seen for GTOs) better describe the radial distribution of electron density in hydrogenic atoms. Commonly, a linear combination of Gaussian functions will be used to mimic the shape of an STO. Such orbitals are called contracted Gaussian-type orbitals (CGTOs).

Basis sets vary widely based on how they describe atomic orbitals in an atom. In a minimal basis set, one basis function is used for each atomic orbital. However, the use of more than one basis function per orbital allows for orbital flexibility; the orbital is better able to respond to the presence of another atom. Thus, double-, triple-, and quadruple-, etc., zeta basis sets include two, three, and four basis functions and so on for each atomic orbital, respectively.

Chemists are typically focused on the behavior of valence electrons, requiring a greater number of functions for valence orbitals than for core atomic orbitals. Thus, split-valence basis[35] sets use one set of functions to describe each core atomic orbital and a larger basis for valence orbitals.

2.1.5.2 Pseudopotentials

For heavy atoms with a large number of core electrons, the core electrons can be treated collectively as averaged potentials, or pseudopotentials, instead of with basis functions.[36] This increases computational efficiency, as expensive integrals no longer need to be calculated, without sacrificing much accuracy, as core electrons are not typically affected by changes in chemical bonding. Our work with Lindqvist polyoxoniobates (Chapters 5-8) implements the Lanl2dz pseudopotential and accompanying basis set,[37-39] developed by a team at Los Alamos National Labs, to describe Cs and Nb atoms. This pseudopotential-basis set combination, along with the M06-L density functional, has shown to successfully describe the mechanism of hydrolysis of organophosphorus nerve agents and simulants by a polyoxoniobate catalyst,[40] motivating our choice to use the same set of pseudopotentials, basis functions, and functional for degradation of agents and simulants by $Cs_8Nb_6O_{19}$.

2.1.5.3 Polarization and Diffuse Functions

In the presence of an external field such as that due to a nearby atom, orbitals may shift in shape. The inclusion of flexible polarization functions in a basis set allows for such a response.[41] An s-orbital, for example, is more able to shift if it is mixed with a p-orbital. Also, in systems in which electron density may be found far from the nucleus, such as anionic or van-der-Waals-bound complexes, the inclusion of diffuse functions in basis sets is important to appropriately describe molecular behavior. In diffuse functions, the ζ exponential factor is very small (Equation 2.33), creating very large orbitals.[42]

Specific basis sets are typically made of combinations of basic basis-set elements. For example, the Pople 6-31G(d) is a split-valence double-zeta basis set.[35,43-51] Core orbitals are each described as a CGTO made up of 6 Gaussian functions, and valence orbitals are described by two orbitals: one CGTO made of 3 Gaussians, and one single GTO. Further, as indicated by the (d), this basis set has d polarization functions added to non-hydrogen atoms. Another basis set, 6-31+G, has the same double-zeta split-valence arrangement of electrons but lacks the polarization functions. Instead, as indicated by the +, this basis set includes diffuse s and p functions on non-

hydrogen atoms. A second + would indicate the inclusion of diffuse functions on hydrogen atoms also (i.e., 6-31++G).

2.1.5.4 Dual-Level Calculations

When choosing a basis set for a molecular system, it is important to ensure that the basis set accounts for all the essential features of the system while maintaining computational efficiency. Thus, it is not uncommon to perform geometry optimizations and vibrational frequency calculations (vide infra) using a smaller basis set and correcting the electronic energy of the optimized system with a single-point energy calculation using a larger basis set. This dual-level type of calculation increases the accuracy of an energy calculation while saving a great deal of computational time, as geometry optimizations require the calculation of energy and first derivatives at several points during the process. For example, in Chapters 5-8 in this dissertation, DFT calculations were performed in order to determine the reaction dynamics of Sarin and nerve-agent mimics on transition-metal oxides. For nonmetal atoms, the 6-31G(d,p) basis set was used for geometry optimization and vibrational frequency calculations. Following optimization, the electronic energies of all stationary points were then calculated using the larger 6-31++G(d,p) basis set for nonmetal atoms. As diffuse functions were only included in single-point energy calculations, their effects on electronic energy could be accounted for without recalculating diffuse orbitals at each optimization step; furthermore, as the nature of a stationary point (i.e., a minimum or a transition state) has already been determined through frequency calculations, expensive Hessian matrices are not required for the larger-basis calculations. The energies reported for these calculations reflect the electronic energy calculated with the larger basis set using the geometry optimized with the smaller basis set. Further, reported energies have been corrected by the zero-point energy calculated with the smaller basis set. Of course, underlying dual-level calculations performed in this manner is the approximation that the geometry optimized with the smaller basis set does not vary significantly from that which would be optimized with the larger basis or that any variation is consistent throughout the entire potential energy surface. Finally, under certain circumstances, a dual-level approach can be used with multiple levels of theory. For example, in Chapter 4, a dual-level approach was used in an effort to determine the energy barrier for nitrate addition to a double bond. Using geometries calculated with the B3LYP density functional and the 6-31G(d) basis set, single-point calculations along the reaction coordinate for nitrate addition were performed using other density

functionals, basis sets, and even higher levels of theory, including coupled cluster with single, double, and estimated triple excitations (CCSD(T)).[52-54]

2.1.6 Potential Energy Surfaces

2.1.6.1 Internal Coordinates

Once an appropriate method (or density functional) and basis set are selected, the energy can be calculated for a molecular system. This energy depends upon the spatial orientation of the atoms within the molecule, $\vec{R}$. which can be easily expressed using internal coordinates.

Consider a molecular system composed of two atoms, *A* and *B*, connected by a covalent bond. The geometry of this molecule can be fully described using a single internal coordinate, r_{AB}: the distance between the two atoms. When r_{AB} remains unchanged, translating or rotating *A* and *B* will not affect the energy of the molecular system. Increasing the size of the system, however, requires the incorporation of additional internal coordinates to fully describe the molecule. For the triatomic nonlinear molecule *CDE*, for example, three internal coordinates are required. For example, two coordinates r_{CD} and r_{DE} may be used, to describe the internuclear distances between atoms *C* and *D*, and *D* and *E*, respectively. Considering these two distances, an additional coordinate is required to fully describe the molecule—$\angle CDE$, the angle formed by vectors $\vec{r}_{\mathrm{CD}}$ and $\vec{r}_{\mathrm{DE}}$, with atom *D* at its vertex—for example. As the number of atoms in a molecule increases, so does the number of internal coordinates required to fully describe its geometry. For a nonlinear molecule, 3*N*-5 coordinates are required, where *N* is the number of atoms in the molecule.

With a set of internal coordinates in hand, the energy of a molecular system can be calculated. Of course, varying one or more internal coordinates will vary the calculated energy of the system. To completely represent the dependence of energy on a given set of coordinates, a topological construct called the potential energy surface is used. The inclusion of the "potential" descriptor reflects the dependence of energy upon the relative position of atoms in the system. In a potential energy surface, energy is plotted as a function of each internal coordinate. This is very simple for the diatomic molecule *AB*, which relies on only one internal coordinate. A potential energy surface for *AB* is shown in Figure 2.1. In the figure, energy is plotted with respect to r_{AB}. In the figure, we note that there is a point at which the energy is at a minimum. This is the equilibrium position, with internuclear distance r_{eq}. Beginning at equilibrium position, if the bond connecting *A* and *B* is contracted, that is, if r_{AB} is decreased, an increase in energy is noted

due to repulsions between the atoms. On the other hand, if r_{AB} is increased from r_{eq}, an increase in energy is seen until eventually A and B become so far apart that they cease to interact. Thus, the energy of the system reaches a finite limit as r_{AB} approaches infinity. The difference in energy between the bottom of the potential-energy well and that of separated atoms is given as D_e.

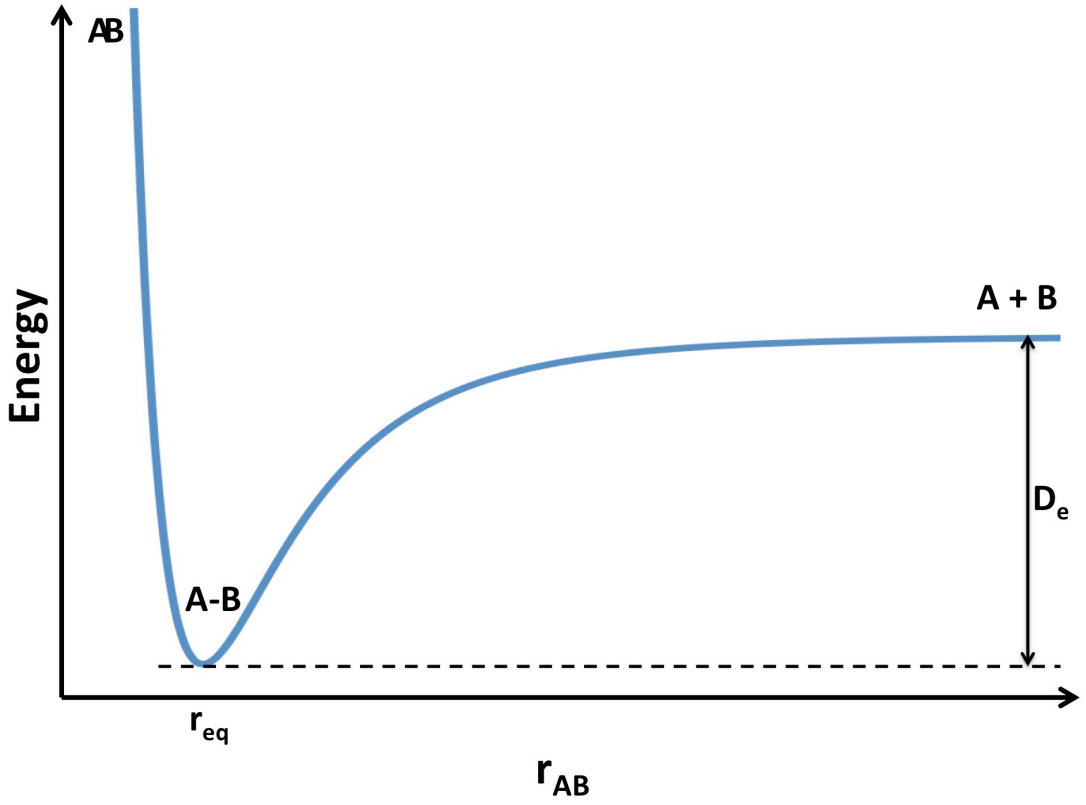

Figure 2.1. Potential energy of molecular system *A-B* as a function of internuclear distance r_{AB}.

Though represented simply for a diatomic molecule, a complete potential energy surface quickly becomes more abstract for larger systems. For triatomic *CDE*, for example, energy depends on three interatomic coordinates; thus, the potential energy plot requires four dimensions: one for each coordinate, and one for energy. Even for a triatomic system, a complete potential energy surface can be difficult, if not impossible, to visualize. However, if one or more coordinates is held invariant, a slice of the surface can be can be plotted as a function of the remaining coordinate. For example, $\angle CDE$ can be fixed as energy is plotted against both

distances r_{CD} and r_{DE}. At a different $\angle CDE$, the same plot may differ substantially. This potential energy surface can be simplified even further, by fixing an additional coordinate such as r_{DE}. Now, the surface is representable by a two-dimensional graph (i.e., energy vs. r_{CD}, with fixed $\angle CDE$ and r_{DE}), similar to that shown in Figure 2.1. This type of potential energy surface, where energy is plotted as a function of one (or a few) coordinates, and the other coordinates are held fixed, is called a rigid potential energy surface. Conversely, energy can be plotted against r_{CD}, and the remaining coordinates can be optimized (vide infra) at each *C-D* distance being sampled. The resulting plot in this case is called a relaxed potential energy surface.

2.1.6.2 Stationary Points and the Reaction Coordinate

A potential energy surface for O_3 is shown in Figure 2.2.[55] Here, energy is plotted as a function of both the O-O-O angle as well as the distance between a terminal oxygen atom and the central oxygen atom in ozone. In this case, both $O_{terminal}$-$O_{central}$ distances are assumed to be the same, and are thus representable on a single axis. As the figure shows, a minimum in the potential energy surface occurs when O-O distance is 1.160 Å and $\angle OOO$ is 120.9° for ozone. Another minimum occurs when $r_{\mathrm{OO}} = 1.316$ Å and $\angle OOO = 60°$ for isoozone. The lowest energy pathway that connects these two minima, defined as the reaction coordinate, is identified by a dashed line in the figure. Moving from one minimum to the other along this pathway, to form isoozone from ozone, for example, an energy barrier must be overcome. This barrier is the difference in energy between the maximum-energy point along along the reaction coordinate and that of the starting geometry, e.g., ozone. The geometry at the maximum is defined as the transition state.

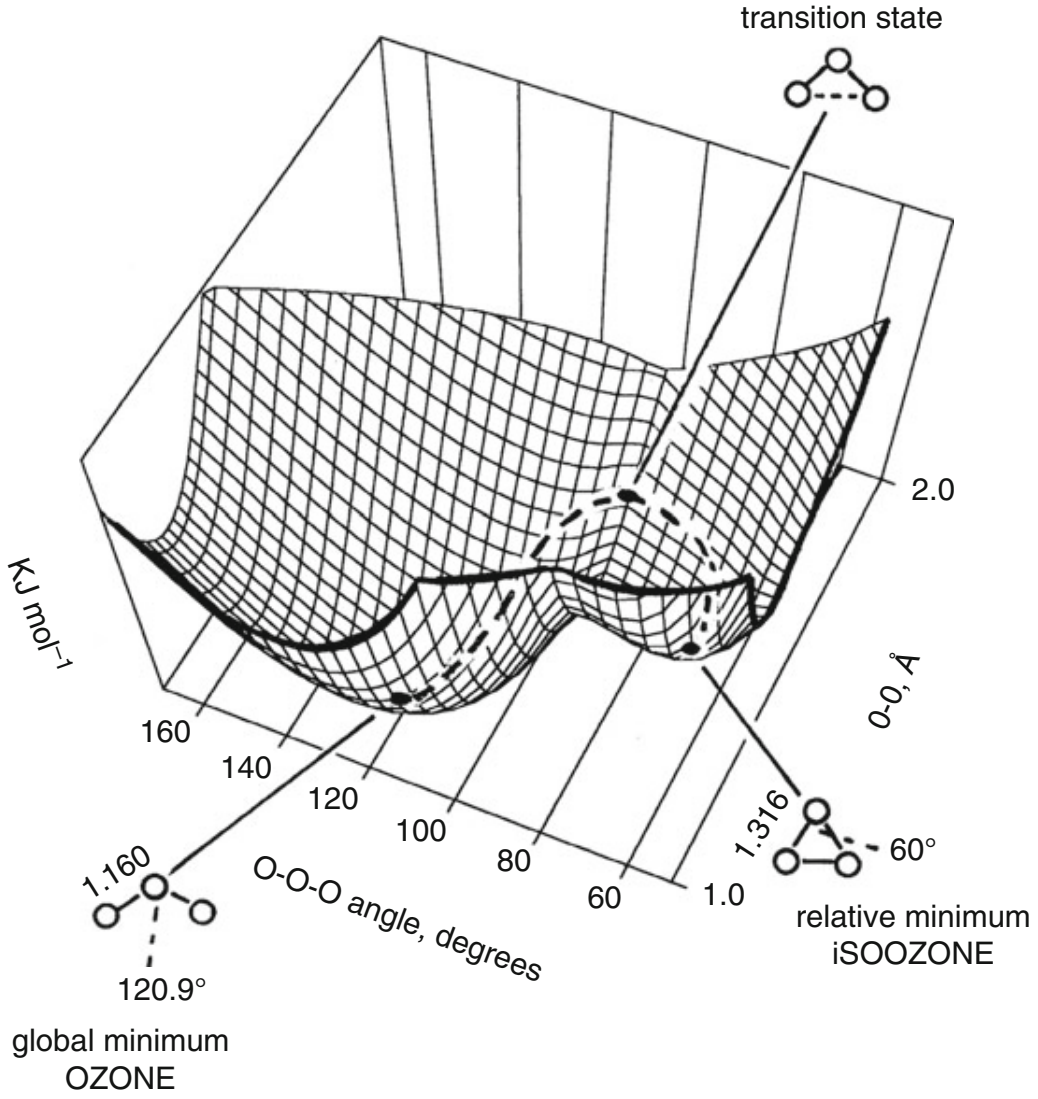

Figure 2.2. The ozone/isoozone potential energy surface (calculated by the AM1 method).[56] The dashed line on the surface is the reaction coordinate. Reprinted (adapted) from Computational Chemistry: Introduction to the Theory and Applications of Molecular and Quantum Mechanics, The Concept of the Potential Energy Surface, 2011, 15, E. G. Lewars, © Springer Science+Business Media B.V. With permission of Springer.

At all three points—the two minima (e.g., ozone and isoozone) and the transition state—the potential energy surface is flat, that is, the partial derivative of the energy with respect to all internal coordinates q_i is zero (Equation 2.34). As such, these minima and maximum are described as stationary points.

$$\frac{\partial E}{\partial q_i} = 0 \tag{2.34}$$

Further, as the points on the potential energy surface corresponding to ozone and isoozone are minima, the second derivative of the energy with respect to all internal coordinates is greater than zero, indicating that the surface is concave up for all coordinates. At the transition state, the second derivative is negative along the reaction coordinate, indicating a maximum. However, as the transition state lies along the lowest energy pathway that connects the two minima, the second derivative of the energy with respect to all other coordinates will be positive (Equation 2.35):

$$\begin{gathered}\text{For a minimum, } \frac{\partial^2 E}{\partial {q_i}^2} > 0. \\ \text{For a transition state, } \frac{\partial^2 E}{\partial q^2} < 0 \text{ along the reaction coordinate, and} \\ \frac{\partial^2 E}{\partial {q_i}^2} > 0 \text{ for all other coordinates.}\end{gathered} \tag{2.35}$$

At this point, it becomes important to note that the reaction coordinate does not necessarily coincide with a single internal molecular coordinate. In the case of the formation of isoozone from ozone, for example, an examination of the geometries along the reaction coordinate shows a decrease in $\angle OOO$ as well as an increase in r_{OO} leading to the transition state, followed by a decrease in r_{OO} leading to the isoozone minimum. Thus, instead of plotting energy as a function of a single internal coordinate, the progress of a chemical reaction is typically depicted by plotting energy as a function of the reaction coordinate. A qualitative sketch of this reaction coordinate graph for the formation of isoozone from ozone is shown in Figure 2.3.

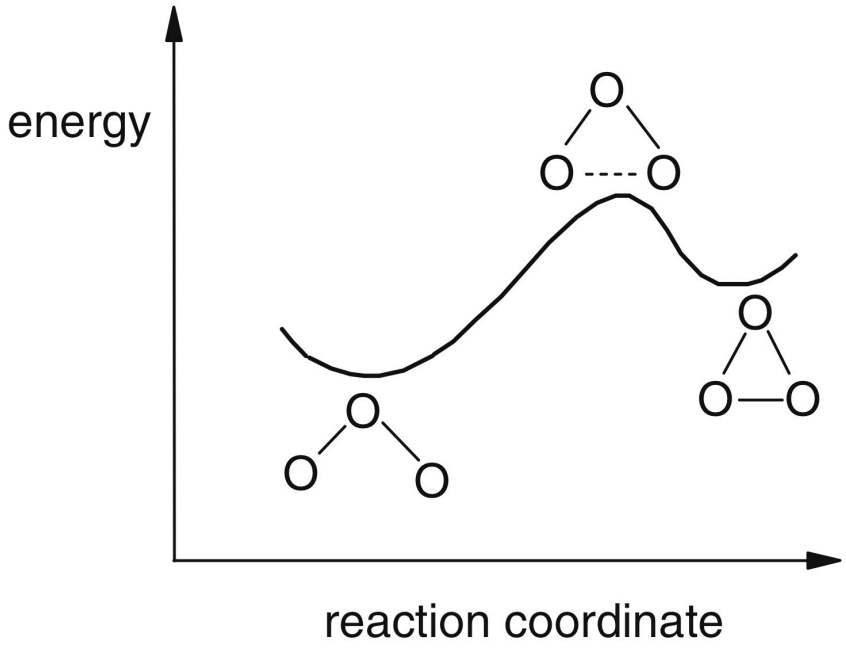

Figure 2.3. A slice through the ozone/isoozone potential energy surface, showing energy as a function of the reaction coordinate. Reprinted (adapted) from Computational Chemistry: Introduction to the Theory and Applications of Molecular and Quantum Mechanics, The Concept of the Potential Energy Surface, 2011, 15, E. G. Lewars, © Springer Science+Business Media B.V. With permission of Springer.

2.1.7 Geometry Optimization

Once an appropriate method (or density functional) and basis set are selected, the energy can be calculated for a given molecular geometry. However, the energy calculation methods described above are only applicable to a fixed set of molecular coordinates, in accordance with the Born-Oppenheimer approximation. The results of these calculations offer no insurance that the molecular arrangement corresponds to a stationary point, wherein the energy is at a minimum or maximum, on the potential energy surface. At these extrema, the gradient of energy, or first derivative with respect to all internal coordinates, is zero. Thus, to reach a stationary point on a potential energy surface, the energy gradient of a molecular system can be minimized by favorably changing the positions of individual atoms. Any algorithm for changing these atomic positions and thus minimizing energy gradients is called geometry optimization.[57]

A simple geometry optimization algorithm is called the method of steepest descent.[58,59] Herein, an initial guess at the geometry is used as input, and the energy is calculated for this

point (e.g., using an SCF method), along with the gradient of the energy. Next, an updated geometry is obtained using Equation 2.36:

$$\vec{R}_{n+1} = \vec{R}_n - \gamma_n \nabla(\mathrm{E}(\vec{R}_n)) \tag{2.36}$$

where $\vec{R}_{\mathrm{n}}$ is the initial geometry, $\vec{R}_{\mathrm{n+1}}$ is the updated geometry, γ_{n} is a scale factor dependent on the size of the gradient (for larger gradients, the difference in geometries between $\vec{R}_{\mathrm{n}}$ and $\vec{R}_{\mathrm{n+1}}$ will be greater), and $-\nabla(\mathrm{E}(\vec{R}_{\mathrm{n}}))$ is the force acting on the molecular system due to the particular arrangement of atoms $\vec{R}_{\mathrm{n}}$. Once the new geometry $\vec{R}_{\mathrm{n+1}}$ is obtained, its energy and gradient are calculated. $\vec{R}_{\mathrm{n+1}}$ is then evaluated against a set of convergence criteria: 1) $\nabla\left(\mathrm{E}(\vec{R}_{n+1})\right) = 0$, 2) $\mathrm{E}(\vec{R}_{n+1}) = \mathrm{E}(\vec{R}_n)$, and 3) $|\vec{R}_{n+1} - \vec{R}_n| = 0$. If all three criteria are met within preset convergence thresholds, the geometry optimization is finished. Otherwise, the process repeats with $\vec{R}_{\mathrm{n+1}}$ as the new initial geometry.

More complex geometry optimization methods are similar to the steepest descent method, varying mainly in the geometry updating step, given in Equation 2.36. In the conjugate gradient method, for example, a history term is incorporated which takes into account the energy gradient at previous iterations of the optimization process. Other optimization algorithms include the Newton-Raphson method and Rational Function Optimization.[57]

It is important to note that optimization methods can be used to converge to any stationary point, be it a minimum or maximum, along a potential energy surface, as all stationary points have zero-energy gradients. Therefore, to verify a minimum has been reached, the second derivative of the energy with respect to a given coordinate is calculated at a stationary point following geometry optimization. If the second derivative is positive, the energy surface is concave up along that coordinate around the stationary point, indicating a local minimum along the coordinate, and if it is negative, the surface is concave down, indicating a local maximum. For a system with more than one coordinate, a Hessian matrix of partial second derivatives with respect to all possible pairs of atomic coordinates is used. A minimum is achieved when all eigenvalues of this matrix are positive. In the case where a negative eigenvalue is obtained at a stationary point, the potential energy surface is at a local maximum along the coordinate yielding the negative eigenvalue.

2.1.7.1 Transition-State Optimization

A transition state is a special case in which the Hessian provides exactly one negative eigenvalue, indicating minima along all coordinates except for one maximum. Thus, in an optimization calculation where a transition state is desired, Hessian matrices must be calculated, which can have a hefty computational expense. In optimizing a transition state, the Hessian matrix is calculated for the initial guess geometry. Ideally, for a good initial guess transition state geometry, there will only be one negative eigenvalue in the matrix, indicating the coordinate to be maximized in energy during optimization while the energy of the entire system is minimized. In the event that there is more than one negative eigenvalue, that which has the largest magnitude will dictate the coordinate along which energy will be maximized. At this point, it becomes evident that a good initial guess geometry is integral to the success of a transition state optimization.

Once the parameter to be maximized has been identified in a transition state optimization, optimization proceeds, and the Hessian matrix is updated using the previous Hessian and gradient from previous points. This method, the Berny Algorithm,[60-65] is much less computationally intensive than calculating a new Hessian after each iteration in the optimization, and it typically results in convergence. If convergence is not reached after a number of optimization cycles, a new Hessian can be generated using a geometry along the optimization process before proceeding. This is only if optimization is indeed proceeding in the desired direction.

2.1.8 Calculation of Theoretical Vibrational Spectra

Following geometry optimization for a molecular system, a theoretical vibrational spectrum can be calculated from that system. Not only can this spectrum verify a minimum or a transition state, as it requires the calculation of second derivatives, but it can also correlate with experimental spectra, informing of spectral features related to the presence of chemical moieties and interactions as well as chemical changes that occur during reaction.

To begin a vibrational frequency calculation, a Hessian matrix is calculated to ensure that a minimum (all positive eigenvalues) or a transition state (exactly one negative eigenvalue) has been reached. Recall that the Hessian is a matrix of the second-order partial derivatives of molecular energy with respect to atomic coordinates, with matrix elements given in Equation 2.37:

$$h_{ij} = \left(\frac{\partial^2 E}{\partial x_i \partial x_j}\right)_{x_i = x_{i_0}, x_j = x_{j_0}} \tag{2.37}$$

where x_i and x_j are individual atomic coordinates in the molecular system. As this Hessian is calculated following geometry optimization, second derivatives are therefore being evaluated with respect to coordinates at energy extrema (e.g., x_{i_0}).

The potential energy of a particular vibration can be expressed as a Taylor-series expansion:

$$V(x) = V_0 + \frac{\partial V}{\partial x}(x - x_0) + \frac{1}{2}\frac{\partial^2 V}{\partial x^2}(x - x_0)^2 + \cdots \tag{2.38}$$

In Equation 2.38, x_0 is the equilibrium position of the oscillator, and V_0 is the energy at that position. As x_0 is a minimum, the derivative of energy at that point will be 0. Further, setting V_0 to 0 and truncating the series after the second-order term results in the expression of Hooke's law for energy, in accordance with the harmonic oscillator model:[66]

$$V(x) = \frac{1}{2}k(x - x_0)^2 \tag{2.39}$$

where k is defined as the force constant, related to the stiffness of the oscillator, obtained by taking the second derivative of the energy with respect to displacement of the oscillator. In a polyatomic system, force constants for vibrations can thus be calculated as eigenvalues of a mass-weighted Hessian matrix (Equation 2.40).

$$K'Q = H'Q \tag{2.40}$$

where K' are the force-constant eigenvalues with eigenvectors Q, and H' is the mass-weighted Hessian with matrix elements h'_{ij}, scaled by the masses of atoms i and j:

$$h'_{ij} = \frac{h_{ij}}{\sqrt{m_i m_j}} \tag{2.41}$$

Extensively, the eigenvectors Q of this matrix provide the normal modes of vibration, q_{ij}, for a molecule. Since the matrix elements have been mass-weighted, the frequency of each normal-mode vibration, ν_{ij}, is simply the square root of the corresponding force-constant eigenvalue k'_{ij}.

Finally, the zero-point vibrational energy can be calculated from the sum of normal-mode vibrational frequencies:

$$ZPE = \frac{1}{2}h\sum_k \nu_k \tag{2.42}$$

where h is Planck's constant, and ν_k are the normal-mode vibrational frequencies. The zero-point vibrational energy results from vibrational motion that occurs at the ground vibrational state; even at a temperature 0 K, vibrational motion occurs—a consequence of Heisenberg's uncertainty principle.[67] To account for this, a zero-point vibrational energy correction (Equation 2.42) is typically included in the energies of stationary points in reaction coordinate graphs as presented in the following chapters.

Recall that the Hessian matrix informs of the concavity of a potential energy surface. Because theoretical vibrational spectra, to which a Hessian is essential, are calculated following geometry optimization, these spectra can inform of the higher-order nature of a stationary point. At a minimum-energy geometry, all Hessian eigenvalues K' will be positive, indicating that the potential energy surface is concave up around the minimum in all dimensions. Exactly one negative Hessian eigenvalue indicates that the potential energy surface is concave up in all dimensions except for one, in which it is concave down. This condition indicates that the corresponding geometry is for a transition state. As the eigenvectors Q correspond to normal modes of vibration, that q_{ij} associated with the negative k'_{ij} value will show motion characteristic of the transition state, such as that leading to breakage and/or formation of a bond.

The calculation of vibrational frequencies we have just described made use of the harmonic oscillator model.[66] Thus, any anharmonic aspects of a real system such as bond breakage and formation have been neglected. Even though he harmonic oscillator shows less deviation from the anharmonic model as a geometry nears a minimum, and the ground-state vibrational motion, which occurs near a minimum, is most often of interest when examining experimental spectra, there are some deviations in calculated frequencies that must be accounted for when comparing theoretical and experimental spectra. Further, approximations in the method used to calculate the energy of a molecule, as described at the beginning of this chapter, may result in further deviations. Typically, multiplying vibrational frequencies by a method-dependent scaling factor ameliorates these deviations. Thus, we have scaled our experimental IR frequencies reported in Chapter 3 for C_{60} ozonolysis and in Chapter 4 for self-assembled monolayer nitrate-addition product accordingly.

Finally, the relative intensities of vibrations in theoretical spectra can be determined through the use of perturbation theory. As discussed in the previous chapter, a vibrational mode is infrared-active if it shows a change in dipole moment due to vibration, and a mode is Raman-

active if it has a change in polarizability. Through use of Taylor series expansions on both the wavefunction and electronic energy, the effects of an applied field on the eigenvalues for dipole moment and polarizability operators can be evaluated to determine the intensity of an IR- or Raman-active transition.[68]

2.1.9 The Intrinsic Reaction Coordinate Method

A vibrational frequency calculation involves the use of a mass-weighted Hessian matrix, H', in an eigenvalue equation. The result of exactly one negative eigenvalue amidst positive eigenvalues indicates that a transition state has been reached. However, there are many possible transition states possible within a molecular system. The intrinsic reaction coordinate method (IRC) is a way to verify that the correct transition state has been optimized; that is, that the transition state does, indeed, lead directly from desired reagent (or intermediate) to product (or intermediate).[69]

This process begins with a transition state geometry (‡), indicated by a negative force constant $k'_{‡}$ resulting from Hessian eigenvector $q'_{‡}$. The coordinates of the geometry are displaced in the direction of $q'_{‡}$ by a small amount. The gradient and Hessian are evaluated at this new point ($‡ + 1$) and the eigenmode $q'_{‡+1}$ indicating negative curvature on the potential energy surface will dictate the vector of displacement. All other coordinates $q'_{ij\neq(‡+1)}$ will be minimized in energy, causing their gradients to be reduced to zero; the only non-vanishing gradient will be that along the direction of $q'_{‡+1}$. The optimization of all other coordinates ensures that the lowest energy path leading from a transition state to a minimum is followed. This process is repeated until all k'_{ij} eigenvalues are positive, indicating that the $q'_{‡+\mathrm{N}}$ vector has entered a region of positive curvature. At this point, the gradient will have its largest component along $q'_{‡+\mathrm{N}}$. As such, $q'_{‡+\mathrm{N}}$ will continue to determine the direction in which the IRC proceeds, and the optimization-re-evaluation process will continue until all gradients are zero, indicating that a minimum has been reached.

The IRC method connects the transition state to a corresponding minimum (e.g., reagents). To connect it to the other minimum (e.g., products), an IRC can be repeated in which the coordinates are displaced in the opposite direction of $q'_{‡}$. Once both minima are obtained, their geometries can be inspected. If desired minima (e.g., reagents and products) have been obtained, the optimized transition state is the corresponding one. Otherwise, a new guess

geometry should be prepared and a transition-state optimization performed. Finally, as geometries are reported for each step along an IRC, changes in geometry can be observed leading from the transition state to an adjacent minimum.

In Chapter 3, we use IRC calculations to verify that transition states corresponded to adjacent minima for the ozonation of C_{60}. In Chapters 5 and 6, through use of IRCs, we tracked changes in interatomic distances around the rate-limiting transition state of Sarin and DMMP hydrolysis by $Cs_8Nb_6O_{19}$ for several different pathways. With these changes, we were then able to relate the synchronicity of the formation and breakage of certain bonds to the relative reaction barriers of each pathway.

2.2 Molecular Mechanics

Due to the presence of multi-electron integrals in Hartree-Fock and DFT, both methods can quickly become intractable as the number of atoms in a molecular system is increased. For larger systems, it is much more practical to treat individual atoms as massed point charges instead of with several Gaussian functions. Further, instead of implementing quantum mechanical operators, subjecting atoms to force fields defined using classical mechanics is an efficient way to describe the collective behavior of as many as millions of atoms at a time. Combined, these two approximations are the foundation of molecular mechanics calculations and allow for the treatment of large molecular systems consisting up to millions of atoms.

2.2.1 Force Fields

In molecular mechanics, the energy of a system can be completely described as a sum of covalent and noncovalent interactions:

$$E = E_{covalent} + E_{noncovalent} \tag{2.43}$$

2.2.1.1 Covalent terms

Covalent energy terms result from contributions of each pair of atoms within a bond, each trio of atoms in a bond angle, and each pair of atoms in a 1,4 spatial relationship, described in terms of their dihedral angle:

$$E_{covalent} = E_{bonds} + E_{angles} + E_{dihedrals} \tag{2.44}$$

The functional form of bonding force field terms can be described using the harmonic oscillator model. Consider two atoms separated by a distance r with an equilibrium distance r_{eq}.

As r deviates from r_{eq}, the energy of the bond increases. A second-order Taylor expansion of energy with respect to r, evaluated at r_{eq}, and defining the energy at r_{eq} as zero leads to:

$$E_{bond} = K_b(r - r_{eq})^2 \tag{2.45}$$

Note that this is very similar to Hooke's Law for energy (Equation 2.39), with ½ factored into the force constant. At this point, it is also important to note that, much as with the calculation of vibrational spectra, since the harmonic oscillator model is being implicated in the definition of force field terms, bond breaking and formation is not accounted for in typical molecular mechanics calculations. Further, this type of calculation works best at bond lengths around r_{eq}, as the harmonic oscillator model shows the best agreement with an anharmonic oscillator at this distance, as described in the previous chapter. In Equation 2.45, two parameters must be specified for each bond: K_b and r_{eq}. These values can be found experimentally or from the results of electronic structure calculations. Keeping the harmonic oscillator approximation in mind, the selection of the appropriate r_{eq} for a given bond is essential to the accurate calculation of energy using molecular mechanics. The collective sum of all bonded interactions within a molecule gives the E_{bonds} term from Equation 2.44:

$$E_{bonds} = \sum_{b}^{bonds} K_b(r_b - r_{eq_b})^2 \tag{2.46}$$

Angle bending terms have a similar functional form to that for bonding terms. The collective angle bending term is given in Equation 2.47:

$$E_{angles} = \sum_{a}^{angles} K_a(\theta_a - \theta_{eq_a})^2 \tag{2.47}$$

Each angle bending term considers three atoms, *A*, *B*, and *C*, with *A* sharing a bond with *B*, and *B* sharing a bond with *C*, thus forming $\angle ABC$, with interior angle θ. As θ deviates from its equilibrium θ_{eq}, the angle bending energy increases for that trio of atoms. To specify each force field term, K_a and θ_{eq_a} are required as input.

The functional form for dihedral angles differs from that for bonds and angle bends, as dihedral rotations are periodic in nature. Consider ethane, with hydrogen atoms H_1 and H_2 on opposite carbon atoms separated in a 1,4 H_1-C-C-H_2 orientation. The dihedral φ between H_1 and H_2 is the angle formed between the two hydrogen atoms as one looks down the C-C bond (as in a Newman projection, Figure 2.1). At $\varphi = 0°, 120°, or\ 240°$, hydrogen atoms are eclipsed, and the

dihedral energy is at a maximum. Conversely, at $\varphi = 60°, 180°, or\ 300°$, the hydrogen atoms are in staggered, with minimal dihedral energy. To account for this periodicity, a sinusoidal functional form can be used to describe the dihedral energy. The collective energy term for all dihedrals in a molecule is given as Equation 2.48:

$$E_{dihedrals} = \sum_{d}^{dihedrals} A_d[1 + \cos(n_d\varphi_d - \gamma_d)] \qquad (2.48)$$

In Equation 2.48, n corresponds to the *n*-fold rotation of the dihedral, $\gamma_d$is an offset angle, and A_d is a fitting parameter that describes the amplitude of the sinusoidal, related to the rotational barrier. For ethane, *n*=3, as shown in Figure 2.4.

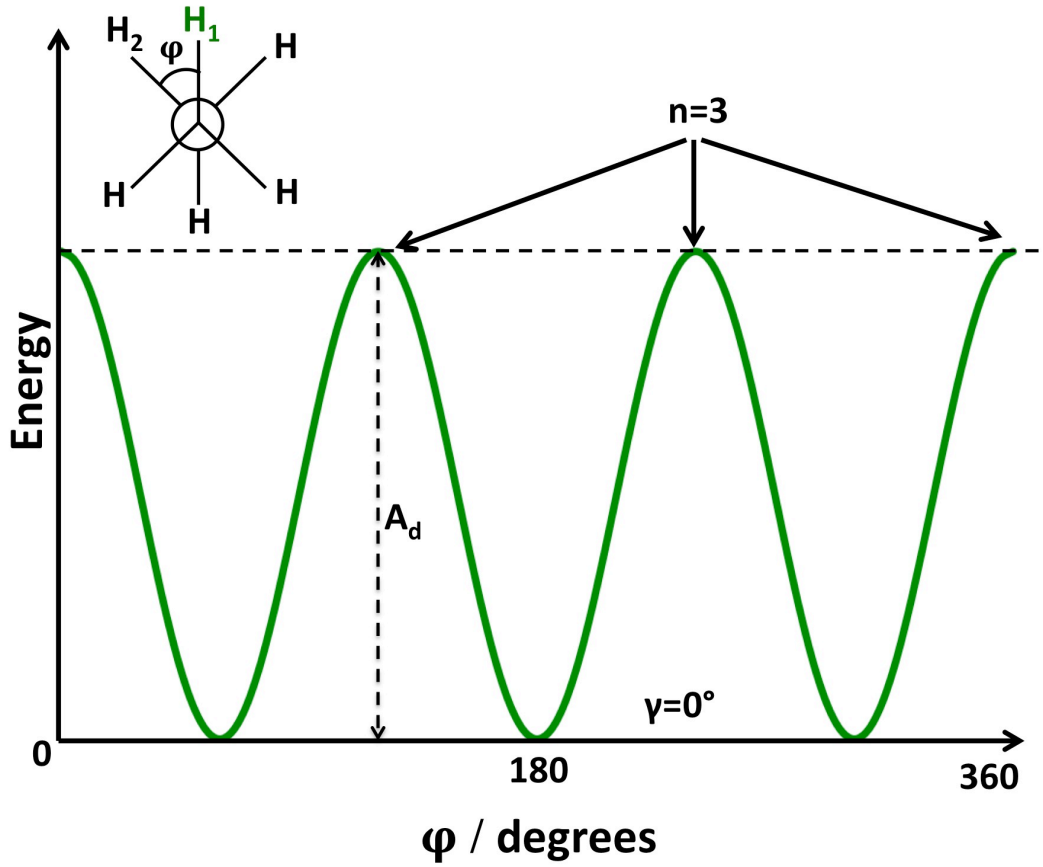

Figure 2.4. Energy with respect to H-C-C-H dihedral angle for ethane, identifying parameters in the functional form for molecular mechanical dihedral angles.

2.2.1.2 Noncovalent Terms

In molecular mechanics, noncovalent interactions are described by two terms: an electrostatic term and a van der Waals term:

$$E_{noncovalent} = E_{electrostatic} + E_{vdW} \tag{2.49}$$

The electrostatic term arises from the fact that each atom has a point charge associated with it. As such, electrostatic interactions between any two atoms with charges q_i and q_j can be calculated with respect to the distance between them, r_{ij}, using Coulomb's Law, similarly to the potential energy terms in the Hamiltonian operator (Equation 2.3). Equation 2.50 gives the functional form for the total electrostatic energy in a molecular mechanics system. Note that a dialectric ε is used instead of the permittivity of free space, ε_0, as these calculations can account for an implicit solvent, if desired.

$$E_{electrostatic} = \sum_{i=1}^{N} \sum_{j=i+1}^{N} \frac{q_i q_j}{4\pi\varepsilon r_{ij}} \tag{2.50}$$

To account for van der Waals interactions, a second term is incorporated into the noncovalent molecular mechanics energy. For bonded atoms, this term is typically only applied to atoms that are more than two covalent bonds apart from one another, as interactions between atoms closer than that are accounted for in bonding terms. The van der Waals term can take many forms, but the most common form is that of the Lennard-Jones potential:[70]

$$E_{Lennard-Jones} = \varepsilon \left[\left(\frac{r_0}{r} \right)^{12} - 2 \left(\frac{r_0}{r} \right)^{6} \right] \tag{2.51}$$

The Lennard-Jones potential is characterized by two terms: an attractive term with $-1/r^6$ dependence on internuclear distance, and a repulsive term with $1/r^{12}$ dependence. These contributions are shown as the red and green traces, respectively, in Figure 2.5. Combined, they give an energy surface (black trace) with a potential well at distance r_0 with energy ε at r_0. The Lennard-Jones potential accurately describes the $-1/r^6$ dependence of distance on van der Waals attractions. However, short-range repulsions have close to exponential dependence. For the sake of computational efficiency, a $1/r^{12}$ term is used instead, as it can be evaluated simply by squaring the $1/r^6$ term. Combined, all Lennard-Jones terms make up the van der Waals interactions contribution to noncovalent molecular mechanics energy:

$$E_{vdW} = \sum_{i=1}^{N} \sum_{j=i+1}^{N} \varepsilon_{ij} \left[\left(\frac{r_{0ij}}{r_{ij}} \right)^{12} - 2 \left(\frac{r_{0ij}}{r_{ij}} \right)^{6} \right] \quad (2.52)$$

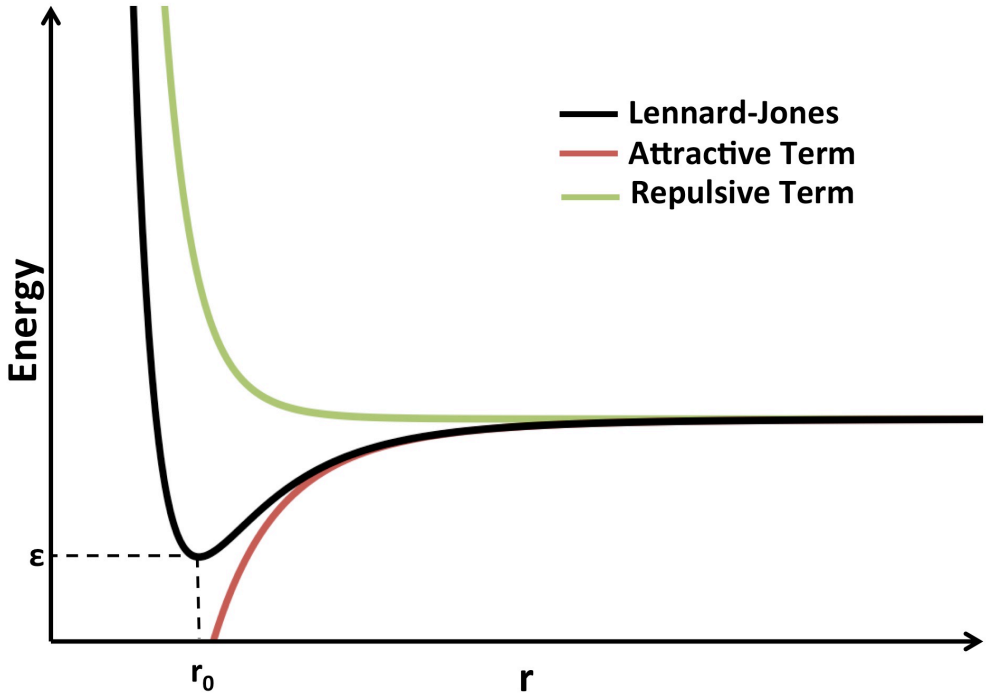

Figure 2.5. Black: The Lennard-Jones potential as a function of interatomic distance, r. Red: Attractive $-2\varepsilon(r_0/r)^6$ contribution to the potential. Green: Repulsive $\varepsilon(r_0/r)^{12}$ contribution.

2.2.2 QM/MM Methods

While molecular mechanics calculations are very economical and can be applied to large systems compared to electronic structure calculations, a major disadvantage to this type of calculations lies in the treatment of each atom as a point charge with mass. Without individual electrons, all intra-atomic contributions to energy such as electronic kinetic energy, electron-nuclear repulsion, and electron-electron repulsion are completely neglected. This makes molecular mechanics a far worse approximation to molecular energy than DFT or even Hartree-Fock, which leave only electron exchange and correlation left to be considered. Furthermore, common forcefields such as AMBER,[71] OPLS,[72,73] and UFF[74] categorize like atoms together as

atom types, assigning each atom of a given type with the same force constant and equilibrium bond length or angle. Thus, there is no differentiation between atoms within a type. All hydrogen atoms in propane, for example, may be assigned the same type, although the environment of those H atoms bound to the central carbon is different from those on the terminal carbon atom. Moreover, molecular mechanics methods as described in this chapter do not allow for bond breaking or bond formation. Thus, any interest in chemical reactions is left to other methods.

Certain aspects of a large molecular system can be described with the accuracy closer to that of electronic structure calculations by treating most of the system with molecular mechanics and a small region of interest with electronic structure methods. This hybrid approach is called quantum mechanics/molecular mechanics (QM/MM).[75-77] In QM/MM calculations, those atoms specified to the QM region are subject to expensive integral calculations required for electronic structure methods. As a result, they can show changes in bonding, and accurate theoretical spectra can be calculated. The remainder of the system is treated with molecular mechanics forcefields. Additionally, interactions between the QM and MM regions are also treated with MM forcefields. As a consequence of treating only a region of interest with QM methods and the remainder of a system with MM force fields, high-quality results can be obtained from a relatively efficient calculation. In Chapter 4, we present a QM/MM approach to calculate the vibrational spectrum of the product of nitrate radical addition to a vinyl-terminated self-assembled monolayer (SAM) chain. In order to examine the effect of including this chain in a SAM, we surrounded it with non-nitrated SAM chains. As we were primarily interested in the vibrational modes of the product chain, we included only that central chain in the QM region, and the rest of the chains in the MM region.

2.3 Concluding Remarks

In this chapter, we described the computational methods that we have used in our investigations of gas—surface reactions. Beginning with Hartree-Fock theory, we outlined the fundamental features of electronic structure calculations. Then, motivated by shortcomings of this theory regarding electron correlation, we moved into density functional theory and the different approaches to calculating exchange and correlation therein. Next, we highlighted approaches to describing orbitals through the use of basis sets.

With an understanding of how electronic energy is calculated, a computational approach to finding a stable geometry through optimization was described, as well as how a Hessian matrix can be used to determine if a stationary point corresponds to a minimum or a transition state. With the Hessian in hand, we then proceeded to explain how theoretical vibrational frequencies are calculated. Finally, we described how to verify that a transition state connects two adjacent minima using the IRC method.

We then moved on to describe how energies of large molecular systems is calculated through molecular mechanics method. These methods use classical force fields, thus introducing approximations. However, it remains possible to obtain information with greater accuracy for large systems through the application of QM/MM calculations.

Throughout this chapter, we made an effort to relate each method to an investigation that we report in future chapters. The rest of this dissertation is dedicated to those investigations. In Chapter 3, we describe our investigations of the ozonolysis of C_{60} using DFT. In Chapter 4, we use QM/MM calculations to obtain theoretical spectra for a SAM chain that has reacted with a nitrate radical. In Chapter 5, the reaction mechanism of Sarin hydrolysis as catalyzed by a Lindqvist polyoxoniobate is described using DFT methods. In Chapters 6 and 7, we continue our efforts with the Lindqvist polyoxoniobate by examining the hydrolysis of nerve-agent simulants DMMP and DMCP. Finally In Chapter 8, we return to Sarin hydrolysis in the presence of a now-solvated catalyst.

2.4 References

(1) Schrödinger, E. *Physical Review* **1926**, *28*, 1049.

(2) Hartree, D. R. *Mathematical Proceedings of the Cambridge Philosophical Society* **2008**, *24*, 89.

(3) Born, M.; Oppenheimer, R. *Annalen der Physik* **1927**, *389*, 457.

(4) Hartree, D. R. *Mathematical Proceedings of the Cambridge Philosophical Society* **1928**, *24*, 89.

(5) Fock, V. *Zeitschrift für Physik* **1930**, *61*, 126.

(6) Dirac, P. A. M. *Mathematical Proceedings of the Cambridge Philosophical Society* **1939**, *35*, 416.

(7) Pauli, W. *Zeitschrift für Physik* **1925**, *31*, 765.

(8) Lagrange, J. L. *Mécanique analytique*; Ve Courcier, 1815.

(9) Roothaan, C. C. J. *Reviews of Modern Physics* **1951**, *23*, 69.

(10) Hall, G. G. *Proceedings of the Royal Society of London. Series A. Mathematical and Physical Sciences* **1951**, *205*, 541.
(11) Hohenberg, P.; Kohn, W. *Physical Review* **1964**, *136*, B864.
(12) Kohn, W.; Sham, L. J. *Physical Review* **1965**, *140*, A1133.
(13) Ceperley, D. M.; Alder, B. J. *Physical Review Letters* **1980**, *45*, 566.
(14) Vosko, S. H.; Wilk, L.; Nusair, M. *Canadian Journal of Physics* **1980**, *58*, 1200.
(15) Perdew, J. P.; Zunger, A. *Physical Review B* **1981**, *23*, 5048.
(16) Cole, L. A.; Perdew, J. P. *Physical Review A* **1982**, *25*, 1265.
(17) Perdew, J. P.; Wang, Y. *Physical Review B* **1992**, *45*, 13244.
(18) Becke, A. D. *Physical Review A* **1988**, *38*, 3098.
(19) Perdew, J. P.; Chevary, J. A.; Vosko, S. H.; Jackson, K. A.; Pederson, M. R.; Singh, D. J.; Fiolhais, C. *Physical Review B* **1992**, *46*, 6671.
(20) Lee, C.; Yang, W.; Parr, R. G. *Physical Review B* **1988**, *37*, 785.
(21) Zhao, Y.; Truhlar, D. G. *The Journal of Chemical Physics* **2006**, *125*, 194101.
(22) Peverati, R.; Truhlar, D. G. *Philosophical Transactions of the Royal Society A: Mathematical, Physical and Engineering Sciences* **2014**, *372*.
(23) Frisch, M. J.; Trucks, G. W.; Schlegel, H. B.; Scuseria, G. E.; Robb, M. A.; Cheeseman, J. R.; Scalmani, G.; Barone, V.; Mennucci, B.; Petersson, G. A.; Nakatsuji, H.; Caricato, M.; Li, X.; Hratchian, H. P.; Izmaylov, A. F.; Bloino, J.; Zheng, G.; Sonnenberg, J. L.; Hada, M.; Ehara, M.; Toyota, K.; Fukuda, R.; Hasegawa, J.; Ishida, M.; Nakajima, T.; Honda, Y.; Kitao, O.; Nakai, H.; Vreven, T.; Montgomery Jr., J. A.; Peralta, J. E.; Ogliaro, F. ß.; Bearpark, M. J.; Heyd, J.; Brothers, E. N.; Kudin, K. N.; Staroverov, V. N.; Kobayashi, R.; Normand, J.; Raghavachari, K.; Rendell, A. P.; Burant, J. C.; Iyengar, S. S.; Tomasi, J.; Cossi, M.; Rega, N.; Millam, N. J.; Klene, M.; Knox, J. E.; Cross, J. B.; Bakken, V.; Adamo, C.; Jaramillo, J.; Gomperts, R.; Stratmann, R. E.; Yazyev, O.; Austin, A. J.; Cammi, R.; Pomelli, C.; Ochterski, J. W.; Martin, R. L.; Morokuma, K.; Zakrzewski, V. G.; Voth, G. A.; Salvador, P.; Dannenberg, J. J.; Dapprich, S.; Daniels, A. D.; Farkas, O.; Foresman, J. B.; Ortiz, J. V.; Cioslowski, J.; Fox, D. J.; Gaussian, Inc.: Wallingford, CT, USA, 2009.
(24) Becke, A. D. *The Journal of Chemical Physics* **1993**, *98*, 5648.
(25) Perdew, J. P.; Ernzerhof, M.; Burke, K. *The Journal of Chemical Physics* **1996**, *105*, 9982.
(26) Adamo, C.; Barone, V. *The Journal of Chemical Physics* **1999**, *110*, 6158.
(27) Heyd, J.; Scuseria, G. E.; Ernzerhof, M. *The Journal of Chemical Physics* **2003**, *118*, 8207.
(28) Tirado-Rives, J.; Jorgensen, W. L. *Journal of Chemical Theory and Computation* **2008**, *4*, 297.
(29) Chu, S. N.; Sands, S.; Tomasik, M. R.; Lee, P. S.; McNeill, V. F. *Journal of the American Chemical Society* **2010**, *132*, 15968.
(30) Hendrickx, M. F. A.; Vinckier, C. *The Journal of Physical Chemistry A* **2003**, *107*, 7574.
(31) Davis, E. D.; Wagner, A.; McEntee, M.; Kaur, M.; Troya, D.; Morris, J. R. *The Journal of Physical Chemistry Letters* **2012**, *3*, 3193.
(32) Gong, X. D.; Xiao, H. M. *Journal of Molecular Structure: THEOCHEM* **2001**, *572*, 213.
(33) Boys, S. F. *Proceedings of the Royal Society of London. Series A. Mathematical and Physical Sciences* **1950**, *200*, 542.

(34) Slater, J. C. *Physical Review* **1930**, *36*, 57.
(35) Ditchfield, R.; Hehre, W. J.; Pople, J. A. *The Journal of Chemical Physics* **1971**, *54*, 724.
(36) Schwerdtfeger, P. *ChemPhysChem* **2011**, *12*, 3143.
(37) Hay, P. J.; Wadt, W. R. *The Journal of Chemical Physics* **1985**, *82*, 270.
(38) Wadt, W. R.; Hay, P. J. *The Journal of Chemical Physics* **1985**, *82*, 284.
(39) Hay, P. J.; Wadt, W. R. *The Journal of Chemical Physics* **1985**, *82*, 299.
(40) Guo, W.; Lv, H.; Sullivan, K. P.; Gordon, W. O.; Balboa, A.; Wagner, G. W.; Musaev, D. G.; Bacsa, J.; Hill, C. L. *Angewandte Chemie International Edition* **2016**, *55*, 7403.
(41) Frisch, M. J.; Pople, J. A.; Binkley, J. S. *The Journal of Chemical Physics* **1984**, *80*, 3265.
(42) Clark, T.; Chandrasekhar, J.; Spitznagel, G. W.; Schleyer, P. V. R. *Journal of Computational Chemistry* **1983**, *4*, 294.
(43) Hehre, W. J.; Ditchfield, R.; Pople, J. A. *The Journal of Chemical Physics* **1972**, *56*, 2257.
(44) Hariharan, P. C.; Pople, J. A. *Theoretica chimica acta* **1973**, *28*, 213.
(45) Hariharan, P. C.; Pople, J. A. *Molecular Physics* **1974**, *27*, 209.
(46) Gordon, M. S. *Chemical Physics Letters* **1980**, *76*, 163.
(47) Francl, M. M.; Pietro, W. J.; Hehre, W. J.; Binkley, J. S.; Gordon, M. S.; DeFrees, D. J.; Pople, J. A. *The Journal of Chemical Physics* **1982**, *77*, 3654.
(48) Binning, R. C.; Curtiss, L. A. *Journal of Computational Chemistry* **1990**, *11*, 1206.
(49) Blaudeau, J.-P.; McGrath, M. P.; Curtiss, L. A.; Radom, L. *The Journal of Chemical Physics* **1997**, *107*, 5016.
(50) Rassolov, V. A.; Pople, J. A.; Ratner, M. A.; Windus, T. L. *The Journal of Chemical Physics* **1998**, *109*, 1223.
(51) Rassolov, V. A.; Ratner, M. A.; Pople, J. A.; Redfern, P. C.; Curtiss, L. A. *Journal of Computational Chemistry* **2001**, *22*, 976.
(52) Bartlett, R. J.; Purvis, G. D. *International Journal of Quantum Chemistry* **1978**, *14*, 561.
(53) Pople, J. A.; Head-Gordon, M.; Raghavachari, K. *The Journal of Chemical Physics* **1987**, *87*, 5968.
(54) III, G. D. P.; Bartlett, R. J. *The Journal of Chemical Physics* **1982**, *76*, 1910.
(55) In *Computational Chemistry: Introduction to the Theory and Applications of Molecular and Quantum Mechanics*; Springer US: Boston, MA, 2003, p 9.
(56) Dewar, M. J. S.; Zoebisch, E. G.; Healy, E. F.; Stewart, J. J. P. *Journal of the American Chemical Society* **1985**, *107*, 3902.
(57) Schlegel, H. B. *Wiley Interdisciplinary Reviews: Computational Molecular Science* **2011**, *1*, 790.
(58) Debye, P. *Annalen der Physik* **1909**, *335*, 57.
(59) Steinmetz, H. L. *Industrial & Engineering Chemistry* **1966**, *58*, 33.
(60) Baker, J. *Journal of Computational Chemistry* **1993**, *14*, 1085.
(61) Peng, C.; Bernhard Schlegel, H. *Israel Journal of Chemistry* **1993**, *33*, 449.
(62) Li, X.; Frisch, M. J. *Journal of Chemical Theory and Computation* **2006**, *2*, 835.
(63) Pulay, P.; Fogarasi, G. *The Journal of Chemical Physics* **1992**, *96*, 2856.

(64) Pulay, P.; Fogarasi, G.; Pang, F.; Boggs, J. E. *Journal of the American Chemical Society* **1979**, *101*, 2550.

(65) Fogarasi, G.; Zhou, X.; Taylor, P. W.; Pulay, P. *Journal of the American Chemical Society* **1992**, *114*, 8191.

(66) Atkins, P.; Friedman, R. **2005**.

(67) Heisenberg, W. *Zeitschrift für Physik* **1927**, *43*, 172.

(68) Siebert, F.; Hildebrandt, P. In *Vibrational Spectroscopy in Life Science*; Wiley-VCH Verlag GmbH & Co. KGaA: 2008, p 11.

(69) Fukui, K. *Accounts of Chemical Research* **1981**, *14*, 363.

(70) Jones, J. E. *Proceedings of the Royal Society of London. Series A* **1924**, *106*, 463.

(71) Cornell, W. D.; Cieplak, P.; Bayly, C. I.; Gould, I. R.; Merz, K. M.; Ferguson, D. M.; Spellmeyer, D. C.; Fox, T.; Caldwell, J. W.; Kollman, P. A. *Journal of the American Chemical Society* **1995**, *117*, 5179.

(72) Jorgensen, W. L.; Maxwell, D. S.; Tirado-Rives, J. *Journal of the American Chemical Society* **1996**, *118*, 11225.

(73) Jorgensen, W. L.; Tirado-Rives, J. *Journal of the American Chemical Society* **1988**, *110*, 1657.

(74) Rappe, A. K.; Casewit, C. J.; Colwell, K. S.; Goddard, W. A.; Skiff, W. M. *Journal of the American Chemical Society* **1992**, *114*, 10024.

(75) Dapprich, S.; Komáromi, I.; Byun, K. S.; Morokuma, K.; Frisch, M. J. *Journal of Molecular Structure: THEOCHEM* **1999**, *461–462*, 1.

(76) Svensson, M.; Humbel, S.; Froese, R. D. J.; Matsubara, T.; Sieber, S.; Morokuma, K. *The Journal of Physical Chemistry* **1996**, *100*, 19357.

(77) Maseras, F.; Morokuma, K. *Journal of Computational Chemistry* **1995**, *16*, 1170.

Chapter 3

Theoretical Study of the Ozonolysis of C_{60}: Primary Ozonide Formation, Dissociation, and Multiple Ozone Additions

Robert C. Chapleski Jr., John R. Morris, and Diego Troya*

Department of Chemistry, Virginia Tech, Blacksburg, VA 24061, USA

* Corresponding author: troya@vt.edu

Abstract

We present an investigation of the reaction of ozone with C_{60} fullerene using electronic structure methods. Motivated by recent experiments of ozone exposure to a C_{60} film, we have characterized stationary points in the potential energy surface for the reactions of O_3 with C_{60} that include both the formation of primary ozonide and subsequent dissociation reactions of this intermediate that lead to C-C bond cleavage. We have also investigated the addition of multiple O_3 molecules to the C_{60} cage to explore potential reaction pathways under the high ozone flux conditions used in recent experiments. The lowest-energy product of the reaction of a single ozone molecule with C_{60} that results in C-C bond breakage corresponds to an open-cage $C_{60}O_3$ structure that contains ester and ketone moieties at the seam. This open-cage product is of much lower energy than the $C_{60}O + O_2$ products identified in prior work, and it is consistent with IR experimental spectra. Subsequent reaction of the open-cage $C_{60}O_3$ product with a second ozone molecule opens a low-energy reaction pathway that results in cage degradation via loss of a CO_2 molecule. Our calculations also reveal that, while full ozonation of all bonds between hexagons in C_{60} is unlikely even under high ozone concentration, the addition of a few ozone molecules to the C_{60} cage is favorable at room temperature.

3.1 Introduction

Pioneer studies of the ozonolysis of unsaturated molecules date back more than a century, with initial investigations focused on the use of ozone to process organics in solution.[1] Though

studies throughout the years have proposed several alternatives for the reaction mechanism, the mechanism originally put forward by Rudolf Criegee has been found to predominate.[2-4] In the Criegee mechanism,[5] the ozone molecule undergoes a concerted cycloaddition to a carbon-carbon double bond. The addition results in the breakage of the π bond between the carbon atoms and the concerted formation of two carbon-oxygen bonds that results in an unstable cyclic molozonide intermediate (the primary ozonide, or POZ). Even though the POZ is an unstable intermediate in the overall reaction mechanism, its thermal stabilization and low-temperature spectroscopic detection have been possible under carefully controlled conditions.[6,7]

Subsequent reactions of the POZ are quite complex and depend on the structure of the unsaturated reactant. Limited spectroscopic evidence of intermediates and their chemistry[7-10] has made theoretical studies paramount to the understanding of the later stages of the ozonolysis reaction mechanism. Naturally, the best-studied ozonolysis reaction using theoretical methods is that of ethylene. CCSD(T) single-point calculations using a split-valence triple-zeta basis set with geometries obtained at the CASSCF level provided a complete description of the connections between the POZ and the various products that can be formed.[11] Following a number of dissociation, decomposition, recombination, and isomerization pathways involving the POZ, a Criegee intermediate carbonyl oxide, and a secondary ozonide, the simplest carbon-containing products that can be formed include CO_2, CO, and formaldehyde. The general mechanism for ozonolysis of small gas-phase alkanes complements what is known for ethylene, and has been reviewed in Refs. 2, 12, and 13.

In contrast with the wealth of information on the ozonolysis of alkenes, much less is known about the processing of organic aromatic molecules by ozone. Examination of kinetic data indicates that the ozonolysis thermal rate constants decrease from ethylene to aromatic compounds.[14] To investigate this trend, Hendrickx and Vinckier[15] used calculations performed at the B3LYP and CCSD(T) levels with the 6-31G** basis set that compared the energetics of the formation of the primary ozonides of ethylene and benzene. The calculated barrier for the addition of ozone to benzene (15.8 kcal/mol) compared favorably to the experimentally determined barrier of 14.6 kcal/mol,[14] and was found to be much larger than that for the reaction with ethylene (3.3 kcal/mol). This comparison of the barriers agrees with the fact that the thermal rate constant for the ethylene reaction is much larger than for the reaction with benzene. The increase in the barrier in going from ethylene to benzene was attributed to the disruption in

benzene aromaticity by the introduction of the ozone moiety. Regarding the reaction energy, the POZ formation with ethylene was found to be about 30 kcal/mol more exothermic than for benzene.

Moving beyond benzene toward polycyclic aromatic hydrocarbons (PAH), Chu et al. performed geometry optimizations and vibrational frequency calculations at the B3LYP/6-31G** level of theory for the addition of ozone to surface-adsorbed anthracene, pyrene, and benzo[a]pyrene.[16] The loss in planarity upon ozone addition as the C atoms undergoing reaction change hybridization from sp^2 to sp^3 was found to be an important factor in the determination of the reaction energy. In effect, the loss of planarity in PAHs that are adsorbed on a surface involves liftoff from the surface, which carries an energetic penalty. For the ozone addition to anthracene, two pathways involving the central ring were examined. The first pathway exhibits addition along a C=C bond, characteristic of the Criegee mechanism. The second pathway is a 1,4 cycloaddition that involves the formation of a bridge-like structure between the carbon atoms that belong exclusively to the central ring in anthracene. This addition is thermodynamically more favorable than addition to a C=C bond.

For surface-adsorbed pyrene, Criegee addition was considered for ozonolysis along C=C bonds in the perimeter of the molecule. For this PAH, the authors went beyond the formation of the primary ozonide and investigated the first steps in the subsequent reaction mechanism. Dissociation of the POZ provided a secondary ozonide of much lower energy than the POZ. Evolution of the secondary ozonide via additional dissociation reactions was not investigated. Finally, the energetics of ozone addition to surface-adsorbed benzo[a]pyrene across selected C=C bonds were found to be strongly dependent upon the degree of planarity of the benzo[a]pyrene moiety in the primary ozonide. Generally, POZ formation favors the least reduction in molecular planarity.

In this work, we make progress in the determination of the mechanism of ozonolysis of C=C double bonds beyond ethylene and PAHs by investigating the reaction of O_3 with the most abundant fullerene, C_{60}. Reactions of ozone with C_{60} have been studied in various solvents,[17-20] and the primary ozonide for C_{60} has been identified using liquid chromatography. Moreover, UV-VIS and NMR spectra for several fullerenes and their oxidation intermediates in solution are available.[21] In certain solvents, ozonolysis of C_{60} and C_{70} fullerenes results in polymeric fullerene oxide formation,[17,19] and analogies have been drawn between these polymeric oxides

and graphitic oxide.[18] Beyond the solution phase, the reactivity of fullerenes with ozone has been investigated mostly using electronic structure calculations. Shang et al.[22] used the AM1 semiempirical Hamiltonian to calculate the energetics of the stationary points along the reaction coordinate for C_{60} ozonolysis. The calculations showed that of the two types of C=C bonds in C_{60} (the one between two hexagons, 6,6, and that between a hexagon and a pentagon, 6,5), addition to the 6,6 bonds was thermodynamically favored. The barrier for POZ formation was found to be 20 kcal/mol, which would indicate a slow process at ambient temperatures. Decomposition of the POZ species ultimately results in an epoxide of $C_{60}O$ stoichiometry after evolution of $O_2(^1\Delta)$. A similar study was reported more recently for C_{70}.[23] Sabirov et al.[24,25] performed theoretical calculations using the PBE functional with a split-valence triple-zeta basis set for the addition of ozone to a range of fullerenes from C_{20} to C_{76}. The authors noted a direct correlation between reaction energy and radius of fullerene curvature at the site of ozone addition, with POZ formation on high-curvature fullerenes leading to larger exothermicity. Further confirming this trend, the energetics of the ozonolysis reaction of C_{70} were investigated in a separate study employing plane-wave DFT techniques.[26] These calculations traced the reaction through the primary ozonide and the Criegee intermediate to epoxide product formation and O_2 release. The most probable sites of ozonolysis were found in this study to also be those with larger curvature on the C_{70} moiety.

In a recent paper, Davis et al.[27] reported the first room-temperature spectroscopic determination of the primary ozonide in O_3 reactions with C_{60} beyond the solution phase. Under ultra-high vacuum (UHV) conditions, a C_{60} film was exposed to pure ozone and the reaction was monitored using reflection-absorption infrared spectroscopy (RAIRS). Comparison of low-exposure IR spectral signatures to B3LYP/6-31G* harmonic frequency calculations of the POZ unequivocally attributed the experimental spectrum to the 6,6 POZ. The calculations showed that, in contrast to prior work on PAHs,[16] ozone addition to a 6,6 bond in C_{60} is barrierless, which follows the expectation of heightened reactivity of the double bond as a result of cage curvature.

The experiments of Davis et al.[27] provided a variety of additional information about the reaction of O_3 with C_{60} that motivates the work we present in this paper. First, while the measured IR spectrum at low ozone exposures agrees well with the calculated spectrum for a single POZ on a 6,6 bond, the possibility exists that more than one POZ can be formed on the

same cage. In this paper, we address whether multiple ozone addition to C_{60} is thermodynamically possible and whether the calculated IR spectra of C_{60} containing more than one POZ agrees with the low-exposure IR measurements. Second, it is well known that the POZ is an intermediate in the ozonolysis of alkenes, and further progress along the reaction coordinate yields more stable products. This was captured in the experiments, as the IR spectrum at longer exposure times changes from that of the POZ to one of products that have strong absorption at ~1800 cm^{-1}, characteristic of C=O moieties. Third, at longer exposures, other less intense IR bands develop in the 2200 cm^{-1} region. The main product of gas-phase fullerene ozonolysis that has been explored in the literature using computational methods so far is the $C_{60}O$ epoxide.[22] As we show below, this product is inconsistent with the experiments, thereby providing additional motivation for the detailed studies of alternative POZ decomposition reactions presented in this paper.

In the following, we first present the details of the calculations. We then show the results of the study of multiple ozone addition to C_{60} and subsequently detail our investigation of the POZ evolution towards low-energy products. Finally, we offer concluding remarks.

3.2 Computational Details

Most of the calculations presented in this work have been carried out with the B3LYP method and the 6-31G* basis set as implemented in the Gaussian09 code.[28] While one ideally would like to use multireference methods to properly take into consideration the biradical character of ozone and of some of the intermediates presented in this paper, such type of calculations have only been possible for the ozonolysis of the smallest alkenes.[11] However, comparison between CASSCF and B3LYP geometries shows that the more inexpensive DFT method provides results that are qualitatively correct.[11] Therefore, DFT methods have been the technique of choice for prior calculations of larger molecules, including PAHs[16] and fullerenes.[22,25,26,29] Additional benchmarks for the performance of the B3LYP/6-31G* method for ozonolysis are provided by studies of the reaction of O_3 with benzene, where high-level energy calculations (CCSD(T) using B3LYP geometries) were compared to the B3LYP results.[15] B3LYP reasonably captured reaction energies and barriers predicted by CCSD(T).

To further test the accuracy of B3LYP/6-31G* calculations, in this work we have carried out single-point hybrid QM:QM calculations at the CCSD(T)/6-311G*:B3LYP/6-31G* level

using the ONIOM formalism[30] for the primary ozonide formation. The high-level layer of these benchmarks, calculated at the CCSD(T)/6-311G* level, corresponds to the ozone molecule and the naphthalene moiety whose central C-C bond is the 6,6 bond to which ozone adds. The rest of the cage is treated at the B3LYP/6-31G* level, and hydrogen-atom links are employed between the two layers. A schematic of the QM:QM partitioning is depicted in Figure 3.1. As we show below, the ONIOM benchmarks agree quite well with the B3LYP/6-31G* estimates of the reaction energetics. This validation is important for our work, as gold-standard CCSD(T) calculations on the entire system will continue to be prohibitive in years to come for some of the molecules calculated in this work, which possess up to 150 non-hydrogen atoms ($C_{60}O_{90}$ stoichiometry) and up to 780 valence electrons.

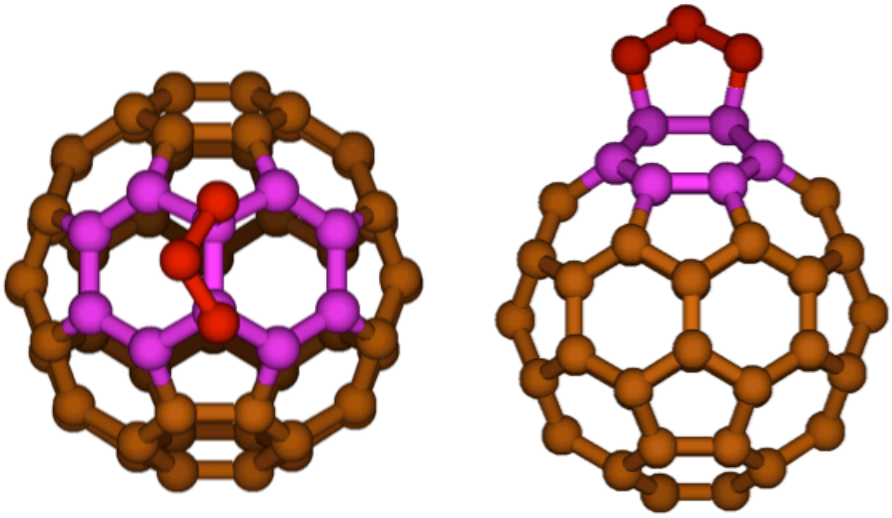

Figure 3.1. Schematic of the partition between QM regions in the hybrid QM:QM CCSD(T)/6-311G*:B3LYP/6-31G* ONIOM calculations. In brown are carbon atoms calculated at the B3LYP/6-31G* level. In pink and red are the carbon and oxygen atoms belonging to the CCSD(T)/6-311G* layer. Chapleski, R. C.; Morris, J. R.; Troya, D. *Physical Chemistry Chemical Physics* **2014**, *16*, 5977. - Published by the PCCP Owner Societies.

The located minima and transition states have been confirmed employing harmonic frequency analysis, and the connections between transition states and minima have been mapped using intrinsic reaction coordinate (IRC) calculations. The calculated IR spectra show B3LYP/6-31G* harmonic frequencies scaled by a factor of 0.96. All of the energies presented below have been zero-point corrected.

3.3 Results

3.3.1 *Primary-ozonide Formation*

The mechanism of POZ formation on C_{60} has been explored in detail in prior work,[22,25] and we provide only a brief review here for the sake of completeness. There are two symmetry-inequivalent types of C-C bonds in C_{60}, those between hexagons, and those between a pentagon and a hexagon. For both sites, the addition of ozone to generate the POZ is highly exothermic, but addition to a 6,6 site is thermodynamically more favorable than to a 6,5 site. The B3LYP/6-31G* zero-point corrected energies are -44.0 and -28.4 kcal/mol, respectively for the 6,6 and 6,5 additions. More importantly, there is also a significant difference in the barriers. Thus, while the zero-point-corrected barrier for 6,6 addition is -2.2 kcal/mol, that for 6,5 addition is 4.3 kcal/mol. The sizeable difference in the barrier translates into a thermal rate constant at room temperature that is orders of magnitude larger for addition to 6,6 than to 6,5, and it suggests exclusive formation of the 6,6 POZ under the experimental conditions of Davis et al.[27] The fact that the barrier for the 6,6 reaction is negative implies a transition state that is below the reagents' asymptote and follows the formation of a pre-transition-state complex formed by long-range van der Waals forces, as has been described before.[25] The energy of the van der Waals minimum is -2.6 kcal/mol at the B3LYP/6-31G* level. We note that the barrier calculated in this work is in stark contrast with the one previously calculated with the lower-level AM1 semiempirical Hamiltonian (+20 kcal/mol),[22] suggesting inaccuracy in the semiempirical Hamiltonian for the transition state of this reaction.

Figure 3.2 shows the IR spectrum measured during exposure of a C_{60} film to 100 L (1 L $=1\text{x}10^{-6}$ Torr·s) of pure ozone (red trace). This spectrum differs from that of C_{60} primarily in the absence of bands at 1428 and 1128 cm^{-1} and the presence of intense absorption at 977 cm^{-1}. In Fig. 3.2a and 3.2b, the experimental spectrum is compared with the calculated ones for the 6,6 and 6,5 POZ, respectively. In addition to the intense band at 977 cm^{-1} in the experiment, two bands of decreasing intensity appear at slightly lower frequencies. The 6,6 calculated spectrum agrees well with the experiment and replicates the peak structure seen around 977 cm^{-1}, with the calculated peaks being consistently shifted by about 20 cm^{-1} toward lower frequencies from the experiment. In contrast, the calculated 6,5 POZ (Fig. 3.2b) does not agree as well with the experiment around 977 cm^{-1}, but more noticeably, it exhibits an intense peak at ~1400 cm^{-1}, which is absent in the measurements. The agreement between the 6,6 POZ calculated spectrum

and the lack of agreement between the 6,5 POZ calculated spectrum and experiment demonstrate that 6,6 POZ formation is exclusive under thermal conditions. Fig. 3.2c shows the calculated IR spectrum of the $C_{60}O$ epoxide proposed as the end product of gas-phase C_{60} ozonolysis in the literature.[22] Clearly, the spectrum recorded in the laboratory under short-time ozone exposure to C_{60} does not support the formation of this product.

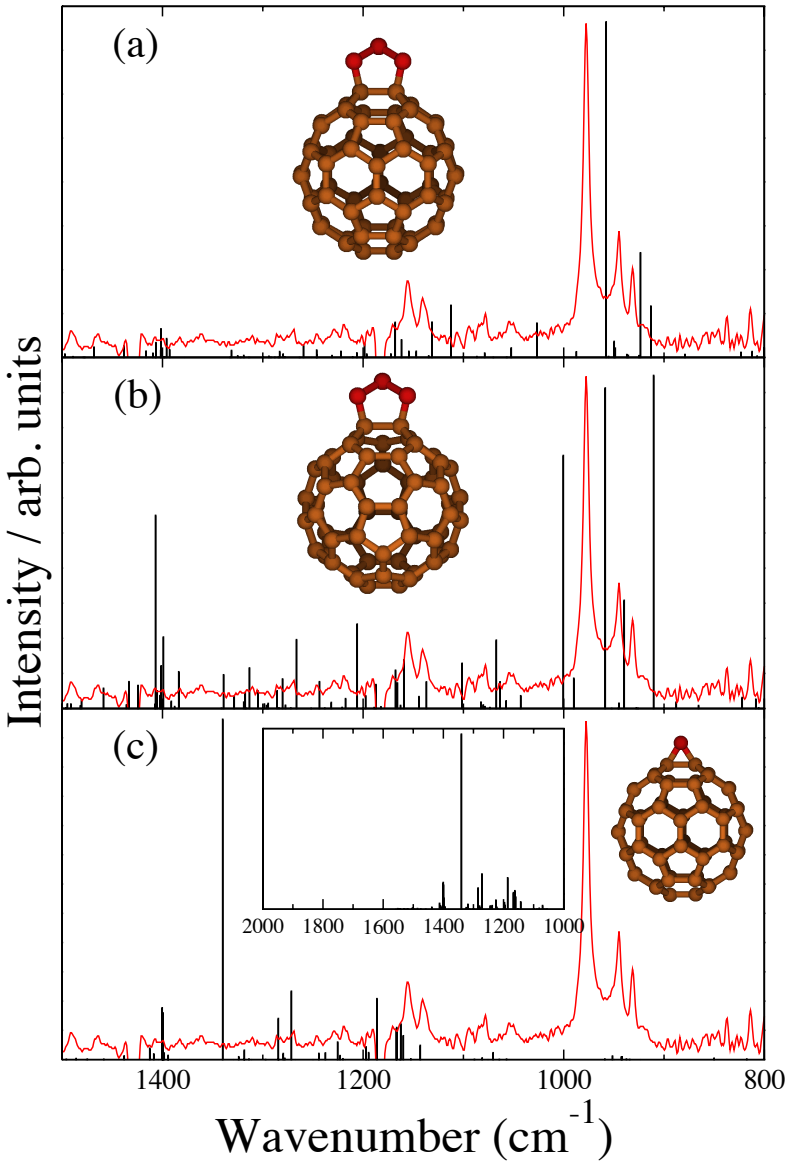

Figure 3.2. Calculated infrared spectra of (a) 6,6 C_{60} POZ, (b) 6,5 C_{60} POZ, and (c) $C_{60}O$ epoxide. The red trace corresponds to the experiments of Ref. 27 after 100 L of ozone exposure to a C_{60} film. The inset in panel (c) shows the calculated IR spectrum of $C_{60}O$ in the 1000-2000 cm^{-1} region. The spectra are normalized to highest peak height. Chapleski, R. C.; Morris, J. R.; Troya, D. *Physical Chemistry Chemical Physics* 2014, *16*, 5977. - Published by the PCCP Owner Societies.

To calibrate the accuracy of the B3LYP/6-31G* combination for the title reaction, we have computed the reaction energies and barrier using higher-level methods as described above. The hybrid QM:QM CCSD(T)/6-311G*:B3LYP/6-31G* calculations provide a reaction energy for the 6,6 POZ formation of -46.2 kcal/mol, which compares well with the B3LYP/6-31G* value (-44.0 kcal/mol). In addition, the B3LYP/6-31G* barrier (-2.2 kcal/mol) is also a good representation of the more accurate hybrid result (-0.5 kcal/mol). These comparisons lend confidence to the use of B3LYP/6-31G* calculations for the rest of this paper.

Because of the large amount of ozone with which the C_{60} film was dosed in the experiment when the spectrum of Fig. 3.2 was obtained (100 monolayers), and because B3LYP/6-31G* predicts that the addition of ozone to C_{60} is barrierless, a question emerges as to whether POZ formation on more than one 6,6 bond of the C_{60} cage can lead to IR spectra that also agree with experiment. Figure 3.3 shows a Schlegel representation of all eight possible double 6,6 POZ isomers that can be formed on C_{60}. The reaction energies for the di-POZ formation (-45.9, -42.1, -40.5, -43.9, -43.4, -42.5, -42.7, and -42.3 kcal/mol for isomers A-H, respectively) are very similar to that of the single POZ (-44.0 kcal/mol), which suggests that the thermodynamics of formation of a second POZ on a C_{60} cage that already possesses one POZ is not significantly affected by the first POZ. Moreover, calculation of the barriers for the formation of the di-POZs A-H (-0.9, -1.3, -1.1, -2.2, -1.8, -1.6, -1.7, and -1.3 kcal/mol, respectively) indicates that the addition of a second POZ to a $C_{60}O_3$ POZ continues to be kinetically favored. This result is especially poignant for the di-POZ A, as in this isomer both primary ozonides reside in nearest-neighbors 6,6 sites. However, as the calculations show, the presence of two POZs in the same hexagon does not significantly affect the energetics of POZ formation.

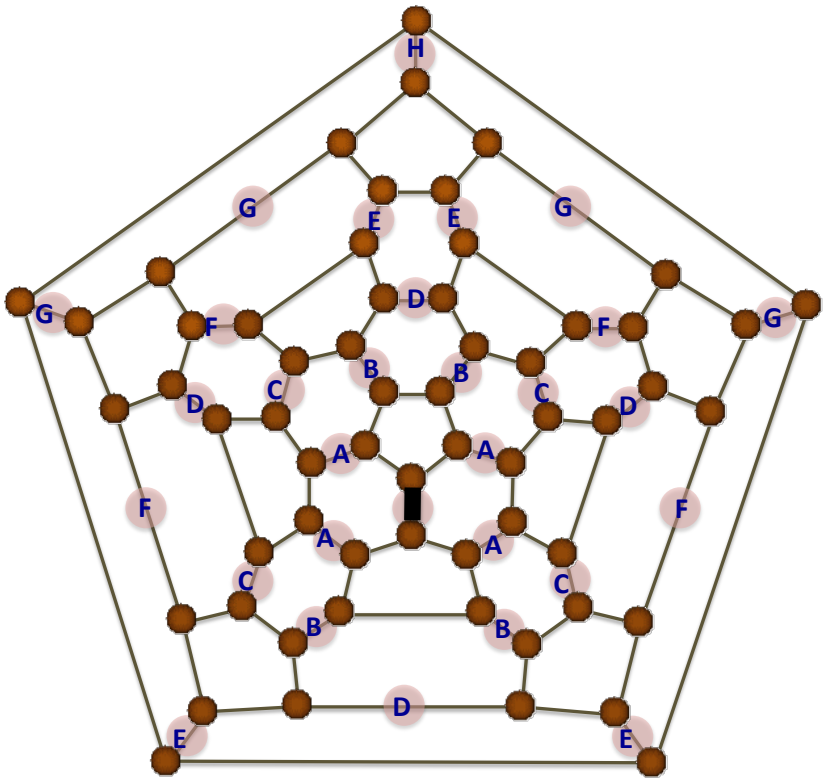

Figure 3.3. Schlegel diagram of C_{60} showing the eight possible symmetry-inequivalent 6,6 di-POZ isomers. The 6,6 bond with black shade represents the location of the first 6,6 POZ. Chapleski, R. C.; Morris, J. R.; Troya, D. *Physical Chemistry Chemical Physics* 2014, *16*, 5977. - Published by the PCCP Owner Societies.

Figure 3.4 shows the calculated IR spectra of some selected di-POZ isomers compared to the spectrum of the single 6,6 POZ (Fig. 3.4a). The IR trace of the di-POZ species in which both ozonides are nearest neighbors (isomer A, Fig. 3.4b) is significantly different from that of the single POZ. Therefore, it seems unlikely that the di-POZ isomer A forms in the low-exposure regime of the study of Davis et al.[27] For other isomers, the differences between the IR spectra of the di-POZ species and the primary ozonide are small enough that we cannot determine unequivocally whether the experimental IR spectrum corresponds to a single POZ, to a species that contains two POZs, or to a combination in which some of the C_{60} molecules in the film contain a single POZ and some others possess two. For instance, even though the IR spectra of di-POZ isomers B and C exhibit more bands in the 977 cm^{-1} region than the single POZ, these bands have a smaller intensity and are sufficiently close to other, more intense peaks to be

enveloped by the broader experimental bands. IR spectra for the rest of the di-POZ isomers not shown in Fig. 3.4 are similar to those of isomers B, C, and H.

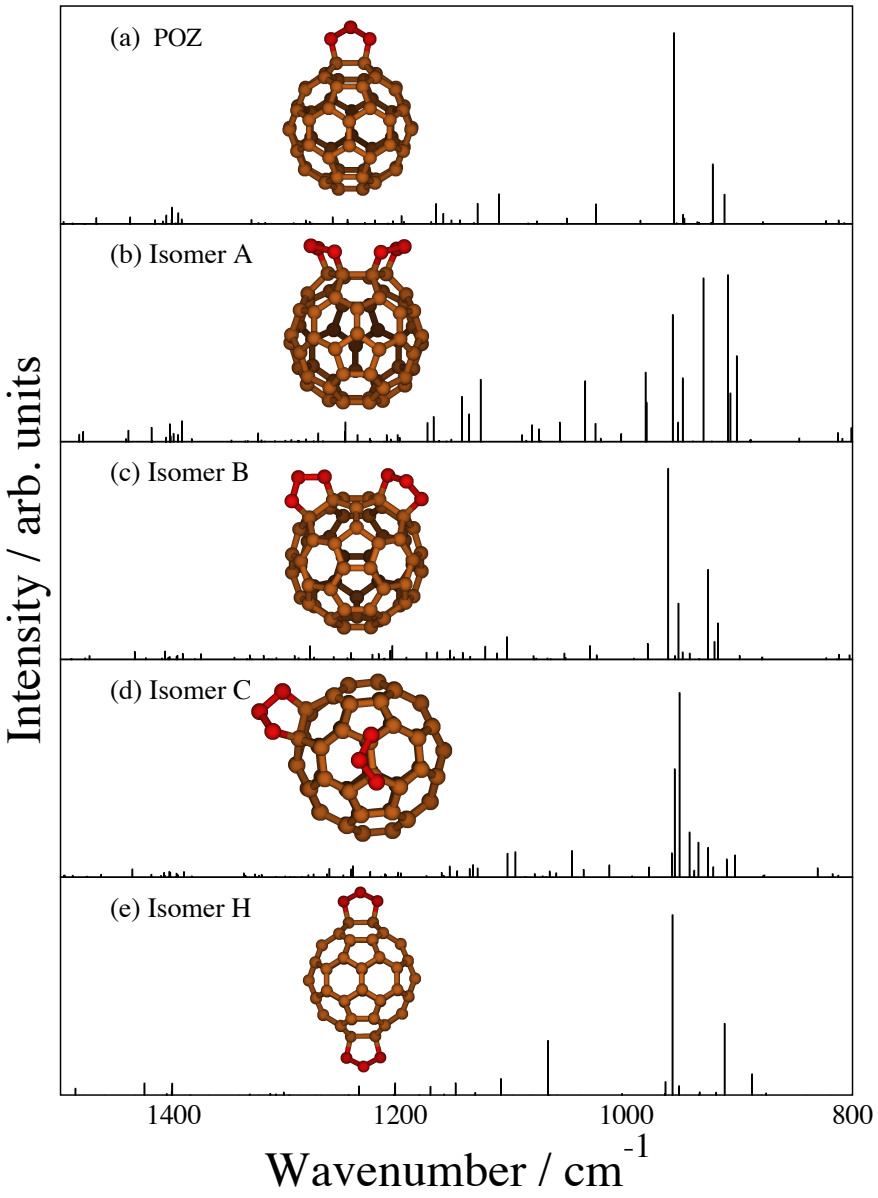

Figure 3.4. Theoretical IR spectra of selected 6,6 di-POZ C_{60} isomers compared to the IR spectrum of the 6,6 POZ (a). Chapleski, R. C.; Morris, J. R.; Troya, D. *Physical Chemistry Chemical Physics* 2014, *16*, 5977. - Published by the PCCP Owner Societies.

Since the calculations of reaction energetics for di-POZ isomers and the data in Fig. 3.4 show that the possibility exists that more than one ozonide could be formed on the C_{60} cage, we have performed a study of POZ formation on all available 6,6 bonds of C_{60}. Thus, starting from the POZ, we have calculated the reaction energy of successive addition of O_3 to the remaining 29 6,6 bonds of C_{60} to form poly-POZ products. Because the number of potential isomers for the tri-, tetra-, etc., adducts quickly becomes intractably large, we have calculated the reaction energy along two exemplary ozonation routes. Figure 3.5 shows the order of formation of primary ozonides along these two routes. Pathway A considers that ozonation occurs in 6,6 sites that are furthest from other 6,6 bonds that already contain a primary ozonide. Along this route, one can generate POZs on 6,6 bonds that are not in the same hexagon up to the 7^{th} addition. Similarly, addition of the 17^{th} ozone molecule and beyond necessitates the placement of three ozonides on the same hexagon. Pathway B considers ozonation that grows from an initial 6,6 bond toward 6,6 bonds that are in the vicinity of the original POZ and then disseminate throughout the entire cage. The plot shown in Figure 3.5 exhibits the zero-point-corrected reaction energy for the $C_{60}O_{3*(n-1)} + O_3 \rightarrow C_{60}O_{3*n}$ reactions, where n, the number of final primary ozonides that the cage contains after the reaction, serves as the abscissa.

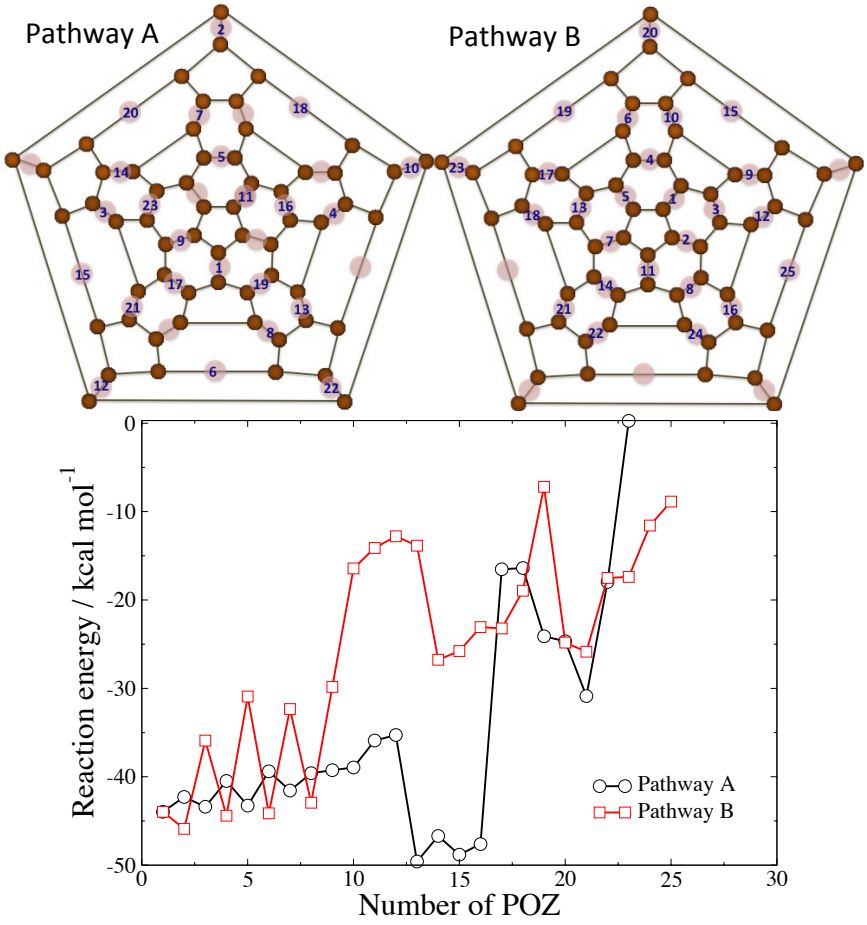

Figure 3.5. (Top) Ozonation pathways. The numbers on 6,6 bonds indicate the order in which primary ozonides are formed on the C_{60} cage for both pathways. (Bottom) Zero-point corrected energies for the $C_{60}O_{3*(n-1)} + O_3 \rightarrow C_{60}O_{3*n}$ (POZ) reactions. Chapleski, R. C.; Morris, J. R.; Troya, D. *Physical Chemistry Chemical Physics* 2014, *16*, 5977. - Published by the PCCP Owner Societies.

As expected, successive ozonation generally leads to increasingly less exothermic processes due to, first, growing repulsion between neighboring POZs, and second, growing cage strain as C atoms undergo sp^2 to sp^3 rehybridization upon addition. Pathway A leads to products that are generally more thermodynamically stable than along pathway B, as the former pathway avoids as much as possible the initial formation of nearest-neighbor ozonides and therefore reduces inter-POZ repulsion and local strain. There are several points of interest along pathway A. First, there is a noticeable increase in the reaction energy for the formation of the 13th ozonide. We attribute the increased exothermicity in this reaction to the release of strain in the vicinity of the bond that undergoes POZ formation. As ozonation proceeds up to the 12th addition, strain is generated

along the bond that undergoes the 13th cycloaddition. Figure 3.6 shows the relevant region of the molecule for reagents and products, where the twist around the C=C bond that forms part of the 13th POZ can be appreciated. The change in hybridization of the C atoms undergoing addition serves to release some of this strain, which leads to an increased exothermicity. Second, there is a sharp decrease in the reaction exothermicity from the 16th to the 17th ozonide. As mentioned above and shown in the Schlegel representation of Figure 3.5, the 17th POZ formation in pathway A is the first that involves the ozonation of all three 6,6 bonds in a hexagon. Both the repulsions between the oxygen atoms in the proximal POZs and the strain generated in the C-atom hybridization change are likely contributors to the destabilization of this molecule.

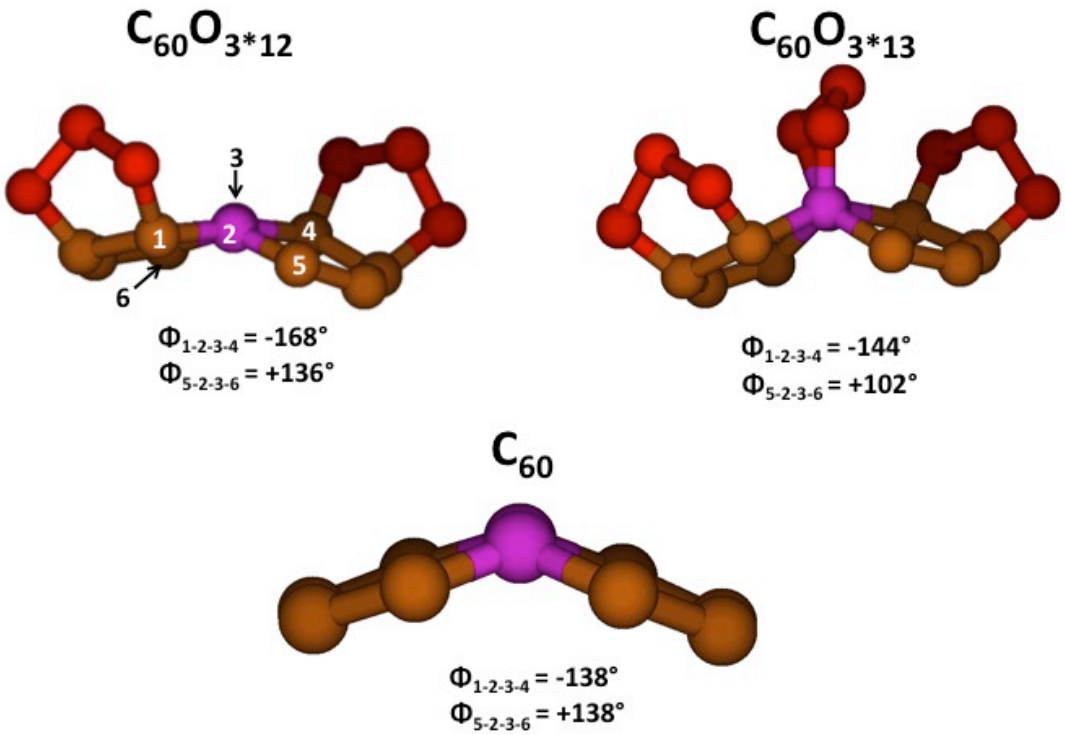

Figure 3.6. Structure of selected atoms in the $C_{60}O_{3*12}$, $C_{60}O_{3*13}$, and C_{60} molecules showing key C-C-C-C dihedral angles. The bond connecting the two carbon atoms that are central to the calculated dihedral angles are shown in pink for clarity. Chapleski, R. C.; Morris, J. R.; Troya, D. *Physical Chemistry Chemical Physics* 2014, *16*, 5977. - Published by the PCCP Owner Societies.

Pathway B represents an ozonation route in which primary ozonides are formed in close proximity to each other. This route is intended to capture a reaction pathway in which an O_3

molecule reacts upon collision adjacent to an existing POZ (i.e. no thermalization and subsequent diffusion occurs). Clustering primary ozonides in the same region of the C_{60} results in less exothermic reactions than pathway A on average, owing to inter-POZ repulsion and the strain generated along the same region of the cage. However, at large loadings (for 17 POZs and above), pathway A and B provide reaction energies that are similar, as at those loadings, repulsion or strain cannot be easily avoided along either route. At large loadings, the reaction energies become less and less negative, suggesting that full ozonation is not favored. In fact, while we tried to optimize the structures of $C_{60}O_{3*n}$ with n up to 30, the larger species (n > 25) did not converge to stable minima.

To further estimate the likelihood of large ozone loading in a single C_{60} cage, we have complemented the analysis of thermodynamic stability shown in Fig. 3.5 by calculating barriers of POZ formation for a few selected ozonation steps. Along pathway B, the barriers for the 1st, 2nd, and 3rd ozonations are -2.2, -0.9, and +3.5 kcal/mol. These barriers indicate that ozonation of the third 6,6 bond of a hexagon is considerably slower at room temperature than addition to a 6,6 bond in a hexagon that is pristine or has only one POZ. Regarding route A, the barrier for the 17th ozonation, which is the first one that completes a hexagon, is as large as 33.9 kcal/mol, strongly suggesting that high loadings are unlikely. To sample intermediate loadings, we have calculated the barrier for addition of the 7th ozone molecule along pathways A and B. These barriers (2.8 and 3.3 kcal/mol for pathways A and B, respectively) are significantly smaller than those found at larger loadings and are of the same size as the one for ozonation of ethylene.[11] Taken together, this analysis of the barriers indicates that full ozonation of C_{60} is highly unlikely under thermal conditions. The formation of a few ozonides is, however, highly exothermic and occurs through small barriers, suggesting the possibility that C_{60} might accommodate reactions with several ozone molecules in high-flux conditions. Figure 3.7 shows the structures of sample poly-POZ species. The IR spectra for these sample poly-POZ species show results similar to those described above for the di-POZ species, in which the main features of the experimental spectrum are borne out by the calculations, but the presence of various POZ on the cage gives rise to additional low-intensity peaks in close proximity to the more intense bands.

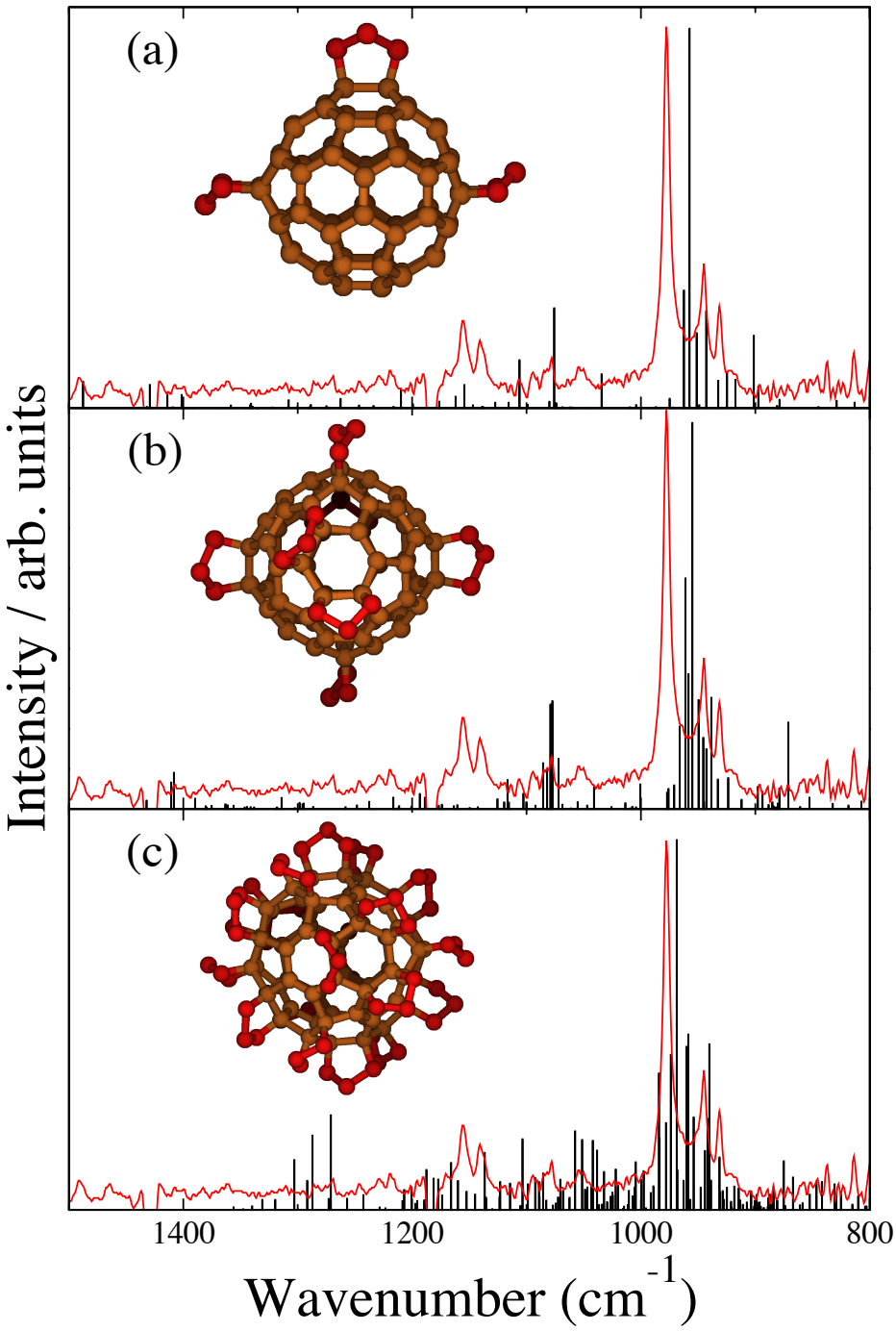

Figure 3.7. Calculated infrared spectra of (a) $C_{60}O_{3*3}$ POZ, (b) $C_{60}O_{3*7}$ POZ, and (c) $C_{60}O_{3*19}$ POZ. The red trace corresponds to the experiments of Ref. 27 after 100 L of ozone exposure to a C_{60} film. The spectra are normalized to highest peak height. Chapleski, R. C.; Morris, J. R.; Troya, D. *Physical Chemistry Chemical Physics* 2014, *16*, 5977. - Published by the PCCP Owner Societies.

3.3.2 Decomposition of the Primary Ozonide

A critical simplification in the examination of the formation of multiple primary ozonides on C_{60} presented above is that the POZ does not decompose prior to addition of subsequent ozone molecules. However, the POZ is known to be short-lived at room temperature, and consequently, an unequivocal characterization of this intermediate outside the solution phase was not accomplished until 2012.[27] We now investigate potential decomposition pathways of a single POZ in an attempt to provide a more complete description of this reaction.

As mentioned above, the experiments of Davis et al.[27] detected the POZ after 100 L exposure. IR spectra recorded at larger exposures and longer reaction times showed the disappearance of the POZ peak around 977 cm^{-1} with simultaneous growth of a broad band at 1700-1900 cm^{-1} (see Fig. 1 of Ref. 27). Prior gas-phase ozonolysis studies of C_{60} have considered the decomposition of the POZ into an epoxide and O_2 as the only reaction pathway,[22] and analogous results have been presented for C_{70}.[23,26] However, as Fig. 3.2c shows, epoxide formation is inconsistent with experimental IR data at short times. Epoxide formation at longer times is also inconsistent with experiment, as the spectrum in the inset of Fig. 3.2c does not show any peaks in the 1700-1900 cm^{-1} region. In search of reaction products that are consistent with the experiment, we have characterized additional stationary points on the POZ decomposition potential energy surface beyond the primary ozonide.

The full reaction pathway, including the POZ formation for completeness, is presented in Figure 3.8, and shows the formation of products that are far more stable than $C_{60}O$ and singlet O_2. Structures of the minima and transition states along the reaction pathway are shown in Figure 3.9, and energetic data are given in Table 3.1. The first step in the decomposition of the POZ (labeled A in Fig. 3.8) is the concerted breakage of the C-C and an O-O bond. Detailed structures of the relevant sections of the molecule are shown in Figure 3.9, where the atoms of the bonds undergoing bond breakage are labeled as 1_C-2_C and $1'_O$-$3'_O$. Following breakage of these bonds, the 1_C-2_C distance increases from 1.61 Å in the POZ to 2.67 Å in the Criegee intermediate B, indicating an opening of the fullerene cage. Rotation of the carbonyl oxide ($2_C2'_O3'_O$) moiety also occurs after the transition state.

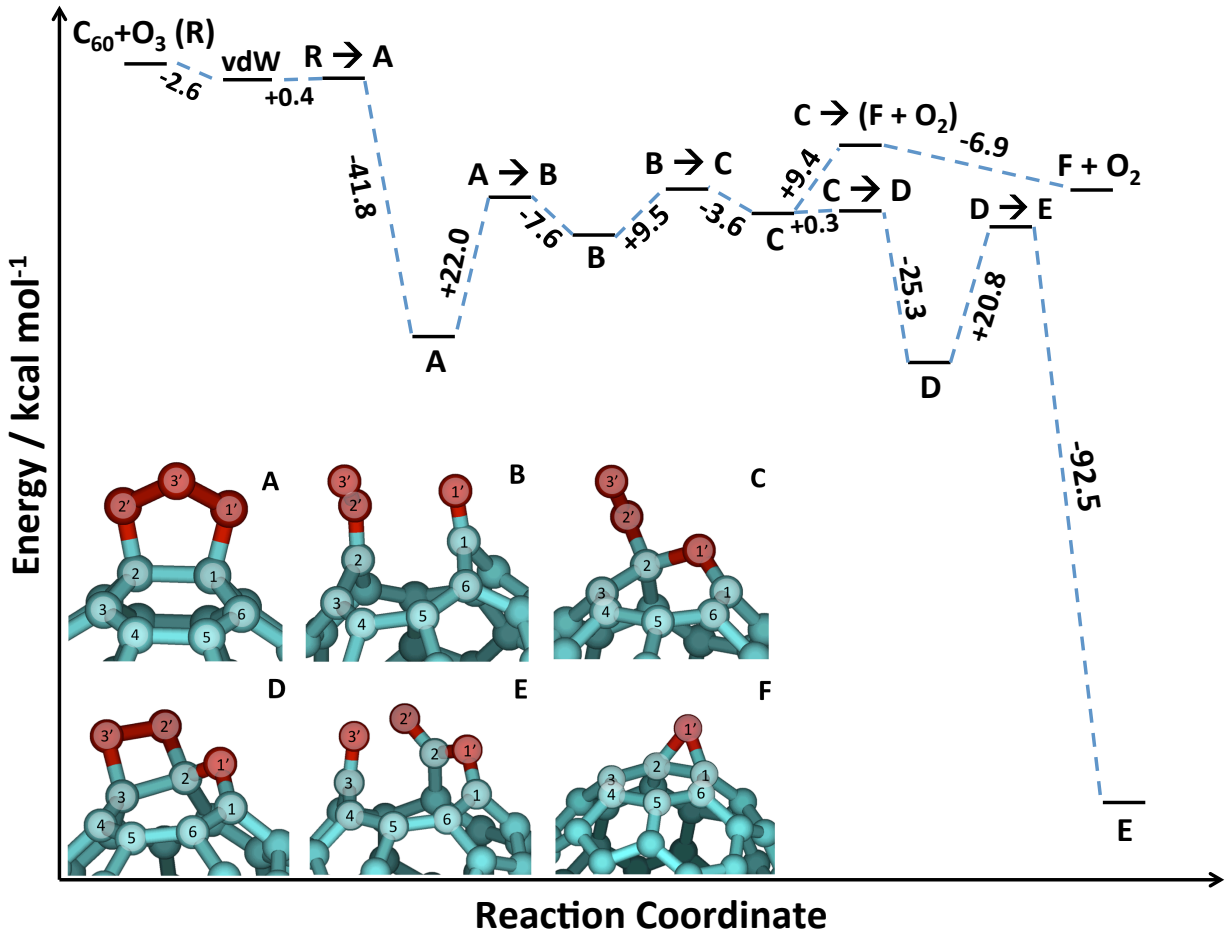

Figure 3.8. B3LYP/6-31G* stationary points on the reaction pathway for addition of one ozone molecule to C_{60} fullerene. Chapleski, R. C.; Morris, J. R.; Troya, D. *Physical Chemistry Chemical Physics* 2014, *16*, 5977. - Published by the PCCP Owner Societies.

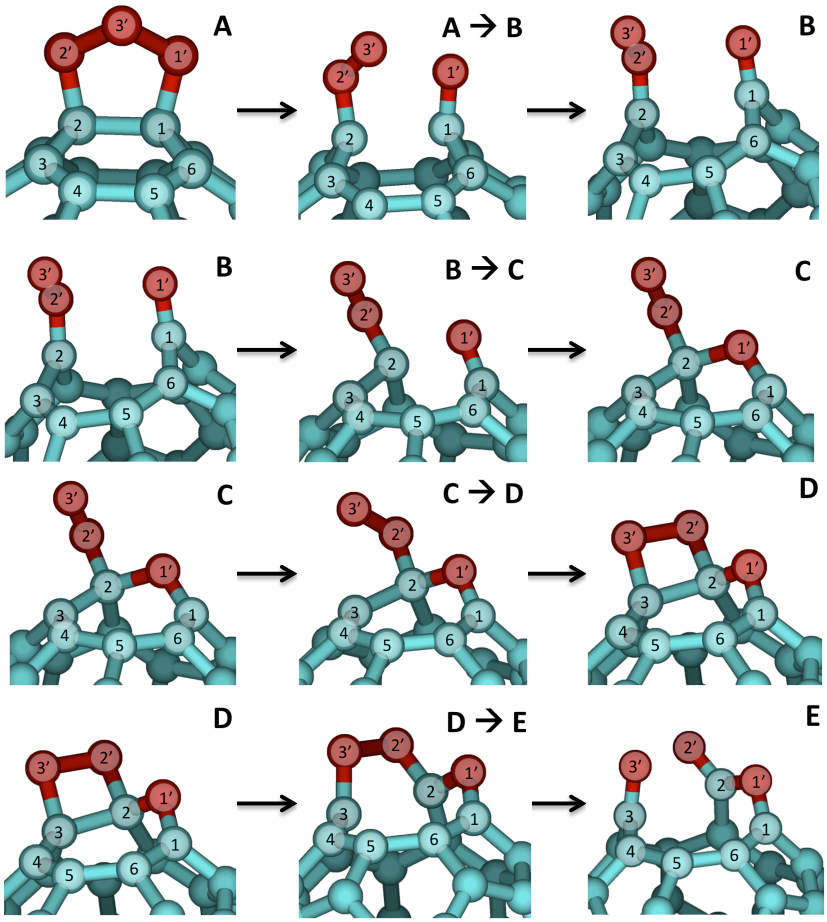

Figure 3.9. Selected regions of optimum structures of minima A-E and transition states between them in the lowest-energy reaction pathway profile of Figure 3.8. Chapleski, R. C.; Morris, J. R.; Troya, D. *Physical Chemistry Chemical Physics* 2014, *16*, 5977. - Published by the PCCP Owner Societies.

Intermediate	Energy	Energy (TS)
$C_{60}+O_3$		
A	-44.0	-2.2
B	-29.6	-22.0
C	-23.7	-20.1
D	-48.7	-23.4
E	-120.3	-27.9
F + O_2	-21.1	-14.2
$C_{60}O_3(E)+O_3$		
G	-50.3	-3.6
H	-68.8	-35.7
J	-184.7	+7.7

Table 3.1. Energies (kcal/mol) of intermediates and transition states leading to them referred to reagents in the $C_{60}+O_3$ and $C_{60}O_3(E)+O_3$ reactions. Energies correspond to zero-point-corrected B3LYP/6-31G* calculations. Chapleski, R. C.; Morris, J. R.; Troya, D. *Physical Chemistry Chemical Physics* 2014, *16*, 5977. - Published by the PCCP Owner Societies.

The Criegee intermediate (B) rearranges to form a bond between $1'_O$ and 2_C that results in a seven-membered oxepin ring (C). Note that the 2_C carbon atom of the carbonyl oxide moiety rehybridizes from sp^2 to sp^3 at the transition state. Subsequent to oxepin ring formation, the O-O moiety bound to 2_C aligns with a C-C bond to form a dioxetane ring (D). This step occurs through a very small barrier (0.3 kcal/mol) and is the first exothermic step following POZ formation. The C-D step also represents the key difference between the pathway for epoxide + O_2 formation described in prior work[22] and the new mechanism that we present here. Contrary to the low barrier and exothermic formation of the dioxetane species D, a much larger barrier of 9.4 kcal/mol must be surmounted from the oxepin species C to produce $C_{60}O$ epoxide and O_2, which are about 30 kcal/mol less thermodynamically stable than product D. Under thermal conditions, the rate of the reaction that yields the epoxide will be about 10^6 smaller than the rate of dioxetane-species formation, thereby explaining the complete absence of a spectral signature for the epoxide product in the experiments of Davis et al.[27]

The final step in the decomposition pathway leads from dioxetane intermediate (D) to ketoester product (E). Animation of the imaginary frequency of the intervening transition state shows the breakage of the bond between 2_C and 3_C. Therefore, the scission of the $2'_O$-$3'_O$ bond that accompanies this step occurs after the transition state, and this has been corroborated by IRC calculations. The high exothermicity of this last step (-71.7 kcal/mol) results from the further opening of the fullerene cage and from the formation of very stable carbonyl and ester moieties at the seam of the opened cage. A noticeable feature of the potential energy surface is that once minimum D has been formed, the reaction to form product E has an energy barrier 4.5 kcal/mol greater than the back-reaction that returns intermediate D into C (towards epoxide product formation). Therefore, under thermal conditions, the forward reaction toward low-energy products will be considerably faster.

Harmonic frequency calculations of the stationary points of the low-energy reaction pathway shown in Fig. 3.8 can be used to provide further insight into the experimental results. As mentioned above, Davis et al.[27] performed RAIRS analysis during the reaction between ozone and C_{60} fullerene in ultra-high vacuum conditions. Concomitant with the disappearance of RAIRS peaks characteristic of the POZ is the formation of an intense, broad infrared band characteristic of C=O stretches in the 1750-1875 cm^{-1} region.[31] This suggests the formation of carbonyl groups following the degradation of the primary ozonide. Of the B-E minima examined in this work, only those with carbonyl moieties yield theoretical vibrational modes with frequencies greater than 1650 cm^{-1}: minimum B exhibits a C=O stretching mode at 1731 cm^{-1}, and product E shows similar stretching modes at 1710 cm^{-1} (ketone) and 1811 cm^{-1} (ester). The fact that the low-energy product E possesses vibrations that absorb IR wavelengths in the range measured by Davis et al. at long reaction times provides confidence to the feasibility of the ozonolysis reaction pathway mapped in this paper.

3.3.3 Reactions with a Second Ozone Molecule

Two additional pieces of experimental information are available from the work of Davis et al. First, at very long exposures (5000 L and beyond), in addition to the carbonyl fingerprints in the IR spectrum, a lower-intensity yet noticeable band appears at about 2200 cm^{-1}. None of the calculated species described so far in this paper can account for that peak. Second, the rate at which ozone reacts with the C_{60} film becomes smaller at high exposures, indicating a substantial change in the C_{60} film that leads to reaction retardation. In addition, earlier solution experiments

have described the appearance of an "ozopolymer" species at high ozone exposures.[19] Taken together, these qualitative experimental results might suggest the degradation of the C_{60} cage to yield a stable, heavily oxidized substrate that does not react readily with additional ozone. The products of the ozonolysis reaction just described lead to an open-cage structure with an oxidized seam, with many available sites for subsequent reaction with additional ozone molecules. Since our calculations of multiple additions of ozone molecules to a single cage indicate that several ozone molecules can add through low barriers, an open question remains about the mechanism of further reactions that lead to further cage degradation.

In the reminder of this paper, we describe a first attempt at characterizing those reactions by investigating the effect of the addition of a second molecule to the end product of the ozonolysis of C_{60} by one ozone molecule. Contrary to our assumption in the calculations presented in Fig. 3.5, we assume that the reaction of ozone to C_{60} leading to the ketoester product E is rapid and that a second ozone molecule does not add to the cage before product E is formed.

From the discussion above, it is clear that there is a large number of 6,6 sites on product E to which a second ozone molecule can add. Because we are interested in pathways that lead to a further opening of the cage, we present here calculations of a pathway that considers the addition of a second ozone molecule to a 6,6 bond belonging to the seam of the open cage. Obviously, this is just one the many possible pathways for the reaction of a second ozone molecule with an oxidized C_{60} cage. The full potential energy profile of the reaction is shown in Figure 3.10, the key regions of the structures of the stationary points are in Figure 3.11, and corresponding energetic data are given in Table 3.1.

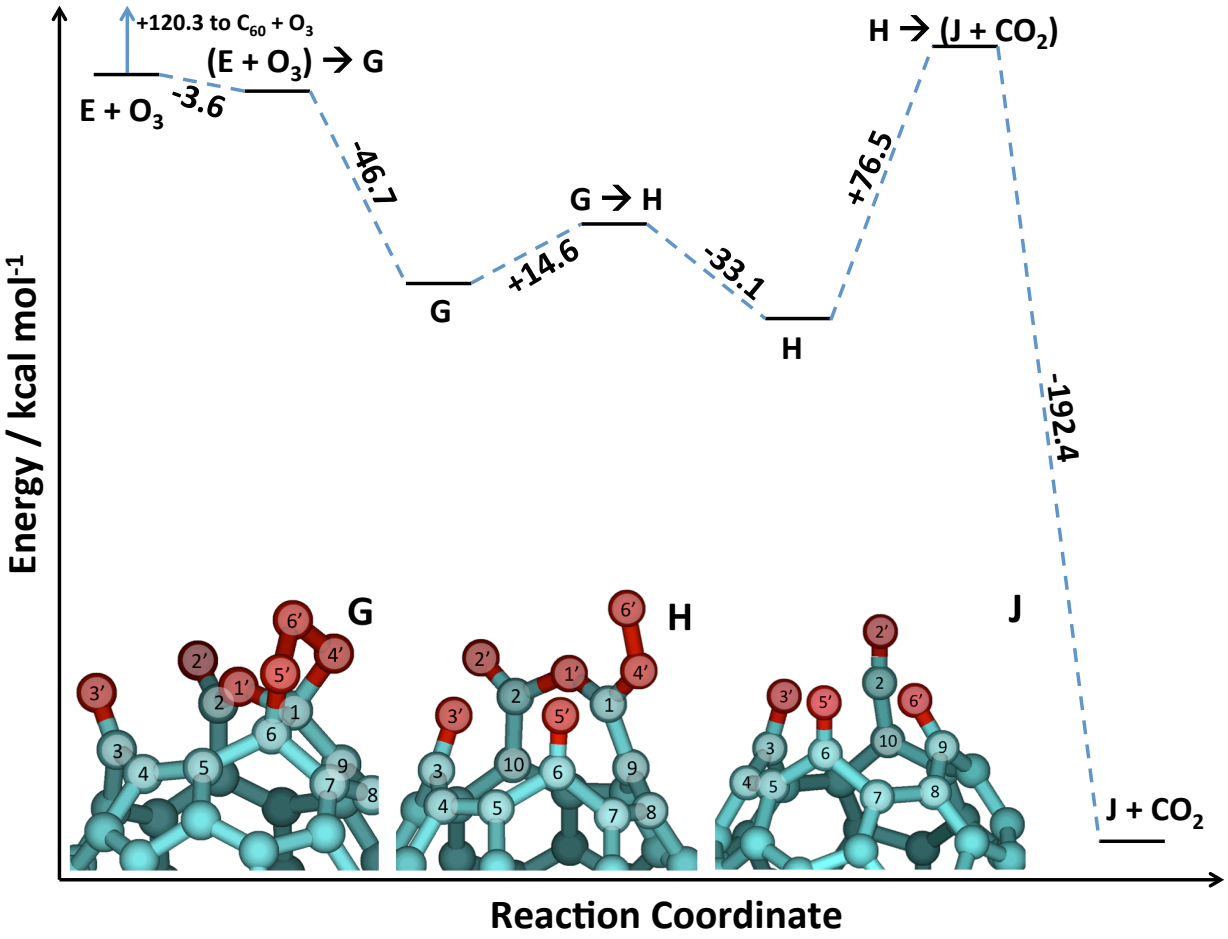

Figure 3.10. B3LYP/6-31G* stationary points on the reaction pathway for addition of a second ozone molecule to product E in Figures 3.8 and 3.9. Chapleski, R. C.; Morris, J. R.; Troya, D. *Physical Chemistry Chemical Physics* 2014, *16*, 5977. - Published by the PCCP Owner Societies.

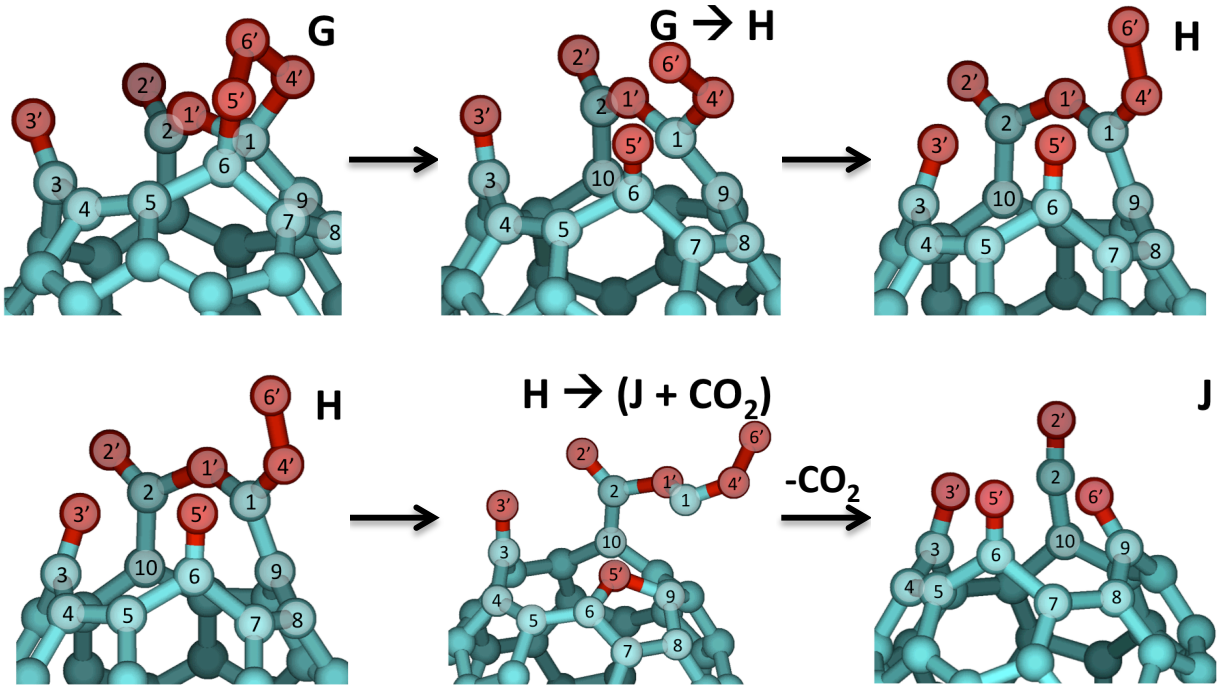

Figure 3.11. Selected regions of optimum structures of minima G-J and transition states between them in the reaction pathway for addition of a second ozone molecule to product E in Figure 3.8. Chapleski, R. C.; Morris, J. R.; Troya, D. *Physical Chemistry Chemical Physics* 2014, *16*, 5977. - Published by the PCCP Owner Societies.

In the specific pathway we follow here, the reaction starts with the addition of a second ozone molecule across the 1_C=6_C bond adjacent to the 1_C-1'$_O$-2_C moiety of product E. Similar to the initial formation of the C_{60} POZ, this reaction has a transition state below the reagents' asymptote. The addition of a second ozone molecule to product E leads to a POZ formation (G). Both the mechanism and the reaction energy (-50.3 kcal/mol) are analogous to the ones described above for POZ formation on a pristine C_{60} cage.

Following the formation of the POZ species G, a concerted exothermic dissociation of the POZ, followed by the rotation of the 6'$_O$-4'$_O$ moiety of the resulting carbonyl oxide, yields species H. Since the original C=C bond to which the second ozone molecule has added belonged to the seam of the open cage, this POZ dissociation leads to a further opening of the fullerene, evidenced by the increase in distance between 1_C and 6_C from 1.60 Å in minimum G to 2.05 Å at the transition state, and ultimately to 3.07 Å in minimum H.

From minimum H, a final complex step leads to product J with concomitant evolution of gaseous CO_2. The step starts with a concerted breakage of the bond between 1_C and 9_C and the formation of a bond between $5'_O$ and 9_C leading to the transition state (Fig. 3.11). This portion of the step leads to the formation of a furan ring at the transition state. After the transition state, several changes in bonding occur, which are shown in the IRC plot that connects this transition state to products J + CO_2 (Figure 3.12). (The energy values reported in Figure 3.12 have not been ZPE-corrected.) The IRC calculation shows that following the transition state, the $1_C4'_O6'_O$ moiety rotates to allow for subsequent bond formation between $6'_O$ and 9_C. Next, the bond is broken between oxygen atoms $4'_O$ and $6'_O$, followed by bond breakage between atoms $5'_O$ and 9_C of the furan ring, and π-bond formation between $5'_O$ and 6_C. The final portion of the step is the scission of the $1'_O$-2_C bond that ultimately leads to gaseous CO_2 accompanied by formation of a ketene moiety at the seam of the cage. To verify that none of these changes result in stable minima prior to products J + CO_2, each structure depicted in Figure 3.12 was subjected to a geometry optimization, and each optimization yielded products J + CO_2. Therefore, the mechanism shown in Figure 3.12 is indeed continuously downhill.

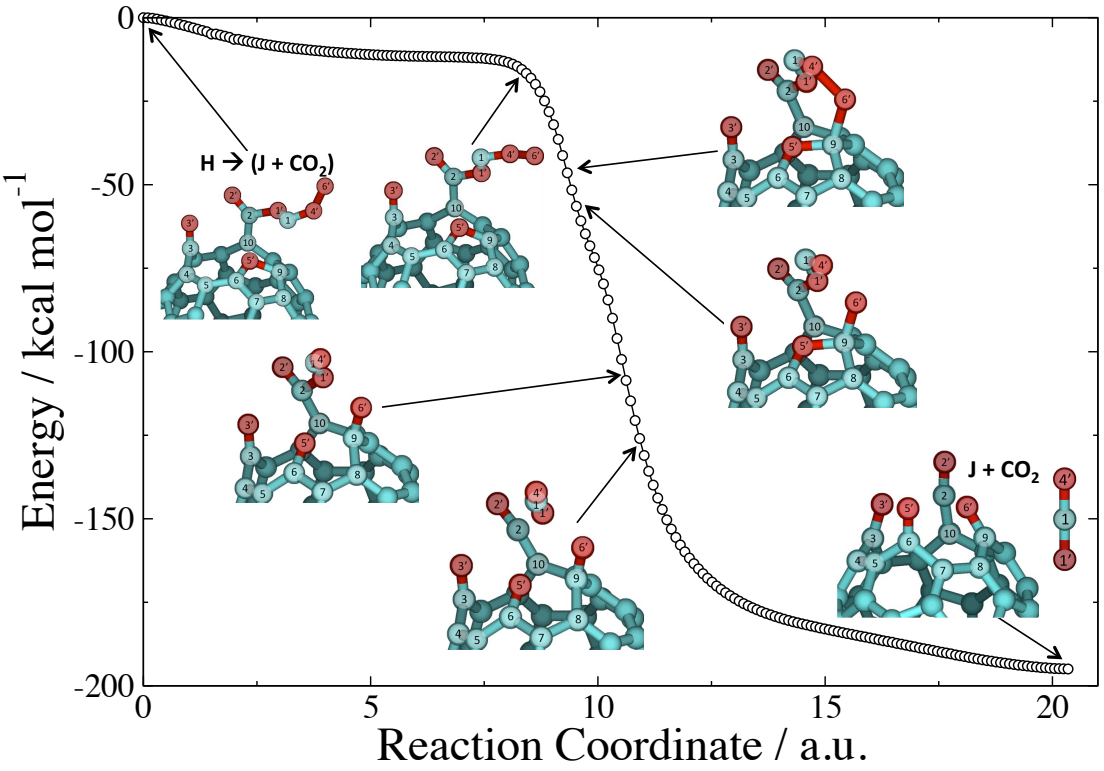

Figure 3.12. B3LYP/6-31G forward IRC calculation connecting the transition state of the H→J+CO_2 step of Figs. 3.10 and 3.11 with products. Chapleski, R. C.; Morris, J. R.; Troya, D. *Physical Chemistry Chemical Physics* 2014, *16*, 5977. - Published by the PCCP Owner Societies.

While the formation of CO_2 and stable carbonyl and ketene products at the seam of the cage leads to a tremendously exothermic last step in the mechanism (-115.9 kcal/mol), the barrier for this step is quite large (76.5 kcal/mol). In fact, this step is clearly the rate-limiting one, as its barrier is 7.7 kcal/mol above the E+O_3 reagents' asymptote. It is therefore unclear whether, under room-temperature conditions, mass loss of the cage occurs at any appreciable rate. While these calculations might trigger further experiments aimed at identifying cage degradation, we can probe the plausibility of product J by comparing calculated and experimental IR signals. As was the case for addition of the first ozone, very few theoretical vibrational modes with frequencies above 1650 cm^{-1} were found for the E→J+CO_2 mechanism, and all of them are carbonyl stretching modes. Furthermore, the asymmetric ketene stretching mode of product J was the only one amongst all the minima with a frequency calculated above 2000 cm^{-1}. This

mode, with a theoretical frequency of 2106 cm^{-1}, is in the region of the low-intensity but broad experimental peak around 2200 cm^{-1} obtained at high levels of ozone exposure. While we cannot unequivocally attribute product J to the experimental spectrum, the agreement between the calculated frequency for this stretch and the experimentally measured IR feature strongly suggests the formation of a ketene moiety. Although the mechanism for ketene formation in the experiment may differ from the one suggested here, this work can serve as a blueprint for future calculations that will explore cage-opening pathways that are possible when a second ozone molecule reacts with a C=C bond different from the one considered here.

3.4 Concluding Remarks

Fullerenes are currently produced by the metric ton, yet little is known about the fate of these carbonaceous materials in the environment, where they are processed by atmospheric oxidizers. In contrast to the wealth of ozonation studies of C_{60} in solution, detailed gas-phase or gas—surface studies are more sparse, and until now have focused on characterizing the first intermediate in the reaction pathway, the primary ozonide, and the $C_{60}O$ epoxide + O_2 products. Drawing motivation from very recent gas—surface UHV experiments, we have carried out an extensive investigation of the C_{60}+O_3 reaction that transcends the formation of the primary ozonide and the $C_{60}O$+O_2 products using electronic-structure methods. We have identified a decomposition pathway of the primary ozonide that is of substantially lower energy than the $C_{60}O$+O_2 products previously reported. This decomposition entails permanent breakage of the C-C bonds in the C_{60} cage that ultimately result in an open-cage structure. The seam of the open cage contains stable ketone and ester moieties, whose IR absorption is consistent with experiments. The new final product of the reaction of ozone with C_{60} is ~100 kcal/mol more stable than the $C_{60}O$+O_2 products, which explains the lack of evidence for the latter products in the measured IR spectra of recent experiments. While studies in which the cage of fullerenes can be opened via solution chemistry abound,[32] the work presented here serves to fill the gap for this type of studies beyond the solution phase.

We have also learned that while ozonation of all 6,6 bonds in C_{60} is unlikely even in high-flux conditions, addition of a few ozone molecules to a single cage is exothermic and occurs over low barriers. With this in mind, we have explored one of the many possible reactions between the ketoester product of the C_{60}+O_3 reaction and a second ozone molecule that adds to a

C=C double bond at the seam of the open cage. The dissociation of the primary ozonide of this addition ultimately leads to a further opening of the cage, mass loss due to CO_2 evolution, and stable ketone and ketene products at the seam that are consistent with IR measurements. Solution studies of extensive ozonation have found evidence of an ozopolymer product whose formation has been postulated to entail the formation of covalent bonds between adjacent C_{60} cages. However, those studies have not been able to determine with certainty whether the fullerenes present an open-cage structure. While understanding the formation of bridges between C_{60} cages during ozonolysis is outside the scope of this paper, the calculations that we show here present pathways for low-energy open-cage structures that might intervene in the solution ozonation studies.

Ultimate proof of C_{60} cage opening due to ozonolysis will be provided by future experimental gas—surface studies. Nevertheless, the possibility that ozone can degrade a C_{60} cage stimulates investigation of the potential release of a range of materials that endohedral fullerenes are known to encapsulate, such as heavy metals.[33] The release of an endohedral fullerene payload upon ozonolysis will be the subject of future theoretical studies.

3.5 Acknowledgments

The support of the National Science Foundation CHE-0547543 and CHE-0948293 is gratefully acknowledged. The authors also acknowledge Advanced Research Computing at Virginia Tech for providing computational resources and technical support that have contributed to the results reported within this paper. URL: http://www.arc.vt.edu

3.6 References

(1) Rubin, M. B. *Helvetica Chimica Acta* **2003**, *86*, 930.
(2) Vereecken, L.; Francisco, J. S. *Chemical Society Reviews* **2012**, *41*, 6259.
(3) Krisyuk, B. E.; Maiorov, A. V. *Russ. J. Phys. Chem. B* **2011**, *5*, 790.
(4) Gadzhiev, O. B.; Ignatov, S. K.; Krisyuk, B. E.; Maiorov, A. V.; Gangopadhyay, S.; Masunov, A. E. *The Journal of Physical Chemistry A* **2012**, *116*, 10420.
(5) Criegee, R. *Angewandte Chemie International Edition in English* **1975**, *14*, 745.

(6) Feltham, E. J.; Almond, M. J.; Marston, G.; Ly, V. P.; Wiltshire, K. S. *Spectrochimica Acta Part A: Molecular and Biomolecular Spectroscopy* **2000**, *56*, 2605.

(7) Coleman, B. E.; Ault, B. S. *The Journal of Physical Chemistry A* **2010**, *114*, 12667.

(8) Su, Y.-T.; Huang, Y.-H.; Witek, H. A.; Lee, Y.-P. *Science* **2013**, *340*, 174.

(9) Taatjes, C. A.; Welz, O.; Eskola, A. J.; Savee, J. D.; Scheer, A. M.; Shallcross, D. E.; Rotavera, B.; Lee, E. P. F.; Dyke, J. M.; Mok, D. K. W.; Osborn, D. L.; Percival, C. J. *Science* **2013**, *340*, 177.

(10) Beames, J. M.; Liu, F.; Lu, L.; Lester, M. I. *Journal of Chemical Physics* **2013**, *138*.

(11) Anglada, J. M.; Crehuet, R.; Bofill, J. M. *Chemistry – A European Journal* **1999**, *5*, 1809.

(12) Johnson, D.; Martson, G. *Chemical Society Reviews* **2008**, *37*, 699.

(13) Donahue, N. M.; Drozd, G. T.; Epstein, S. A.; Presto, A. A.; Kroll, J. H. *Physical Chemistry Chemical Physics* **2011**, *13*, 10848.

(14) Atkinson, R. *Journal of Physical and Chemical Reference Data* **1997**, *26*, 215.

(15) Hendrickx, M. F. A.; Vinckier, C. *The Journal of Physical Chemistry A* **2003**, *107*, 7574.

(16) Chu, S. N.; Sands, S.; Tomasik, M. R.; Lee, P. S.; McNeill, V. F. *Journal of the American Chemical Society* **2010**, *132*, 15968.

(17) Cataldo, F. *Carbon* **2002**, *40*, 1457.

(18) Cataldo, F. *Fullerenes Nanotubes and Carbon Nanostructures* **2003**, *11*, 1.

(19) Cataldo, F.; Heymann, D. *Polymer Degradation and Stability* **2000**, *70*, 237.

(20) Deng, J. P.; Mou, C. Y.; Han, C. C. *Fullerene Science and Technology* **1997**, *5*, 1033.

(21) Heymann, D.; Weisman, R. B. *Comptes Rendus Chimie* **2006**, *9*, 1107.

(22) Shang, Z.; Pan, Y.; Cai, Z.; Zhao, X.; Tang, A. *The Journal of Physical Chemistry A* **2000**, *104*, 1915.

(23) Huang, Y.-S.; Wang, G.-W. *Journal of Molecular Structure: THEOCHEM* **2008**, *860*, 24.

(24) Sabirov, D. S.; Bulgakov, R. G. *Computational and Theoretical Chemistry* **2011**, *963*, 185.

(25) Sabirov, D. S.; Khursan, S. L.; Bulgakov, R. G. *Journal of Molecular Graphics and Modelling* **2008**, *27*, 124.

(26) Bil, A.; Latajka, Z.; Morrison, C. A. *The Journal of Physical Chemistry A* **2009**, *113*, 9891.

(27) Davis, E. D.; Wagner, A.; McEntee, M.; Kaur, M.; Troya, D.; Morris, J. R. *The Journal of Physical Chemistry Letters* **2012**, *3*, 3193.

(28) Frisch, M. J.; Trucks, G. W.; Schlegel, H. B.; Scuseria, G. E.; Robb, M. A.; Cheeseman, J. R.; Scalmani, G.; Barone, V.; Mennuci, B.; Petersson, G. A.; et. al *Gaussian 09, Revision A.1* **2009**.

(29) Sabirov, D. S.; Khursan, S. L.; Bulgakov, R. G. *Russian Chemical Bulletin* **2008**, *57*, 2520.

(30) Dapprich, S.; Komáromi, I.; Byun, K. S.; Morokuma, K.; Frisch, M. J. *J. Mol. Struct. (Theochem)* **1999**, *462*, 1.

(31) Lin-Vien, D.; Colthup, N. B.; Fateley, W. G.; Grasselli, J. G. In *The Handbook of Infrared and Raman Characteristic Frequencies of Organic Molecules*; Lin-Vien, D., Colthup, N. B., Fateley, W. G., Grasselli, J. G., Eds.; Academic Press: San Diego, 1991, p 73.

(32) Vougioukalakis, G. C.; Roubelakis, M. M.; Orfanopoulos, M. *Chemical Society Reviews* **2009**, *39*, 817.

(33) Stevenson, S.; Rice, G.; Glass, T.; Harich, K.; Cromer, F.; Jordan, M. R.; Craft, J.; Hadju, E.; Bible, R.; Olmstead, M. M.; Maitra, K.; Fisher, A. J.; Balch, A. L.; Dorn, H. C. *Nature* **1999**, *401*, 55.

Chapter 4

Products of Gaseous NO_3 Radical Reaction with a Vinyl-Terminated Self-Assembled Monolayer: A QM:MM Vibrational Mode Analysis

Abstract

Motivated by recent experimental results in ultra-high vacuum, we present an investigation in which a possible product of the addition of a nitrate radical to a vinyl-terminated self-assembled monolayer (SAM) chain is explored. The construction of an *in silico* model of this product surrounded by non-reacted chains allowed for the calculation of vibrational frequencies for the product chain in the SAM environment. By comparing the calculated spectra with experimental spectra, we verified that the formation of the product is likely in ultra-high vacuum; that is, that the nitrate radical adds to the terminal carbon atom on the vinyl terminus of the SAM chain. Further, we find that the inclusion of the product chain does not largely affect the frequencies of key nitrate vibrational modes. Finally, we use electronic structure calculations to show that the addition mechanism is more likely than a competing hydrogen-abstraction mechanism.

4.1 Introduction

Zhang et al. performed ultra-high vacuum experiments in which a vinyl-terminated self-assembled monolayer (SAM) was exposed to nitrate radicals generated by the thermal decomposition of N_2O_5.[1] Through the analysis of infrared spectra generated via *in situ* reflection-absorption infrared spectroscopy (RAIRS) as well as X-ray photoelectron spectroscopy, they were able to propose a product resulting from the addition of the nitrate radical to the terminal carbon atom in a vinyl-terminated SAM chain. In order to support these findings, we performed QM:MM calculations on a model system containing several vinyl-terminated alkyl chains in a self-assembled monolayer arrangement. Following model construction and geometry optimization, vibrational mode calculations were aligned with experimental spectra to facilitate product identification. Further calculations explored the possibilities of subsequent radical additions and a competing hydrogen abstraction mechanism.

4.1.1 Self-assembled Monolayers

Self-assembled monolayers (SAMs) are two-dimensional organic assemblies formed by the adsorption of organic molecules onto a metal film or single crystal. [2-5] These organics, typically thiols,[6,7] have a great binding affinity for noble metals such as gold. In solution, SAMs are produced by the dissolution of thiols in a solvent in the presence of a metal substrate. Over time, interactions between the thiolates and metal substrate, as well as between neighboring molecules, lead to arrangement and slow reorganization of thiolate molecules on the substrate eventually into a highly ordered organic layer bound to the substrate.

Due to their highly ordered nature, SAMs facilitate fundamental investigations of heterogeneous reactions with specific surface-bound species. Moreover, through the careful selection of organic molecules, functional groups can be positioned precisely at the gas—surface interface, allowing for fundamental studies of heterogeneous reactions between gas- or solution-phase molecules and the surface-bound functional groups.[4]

Once formed, SAMs can be described in terms of their structural features, illustrated generally in Figure 4.1. The organic layers are bound to a substrate, typically a thin film of metal deposited onto a glass slab. Gold is the most common choice for substrate as it is inert to most organics and easy to obtain. Other common substrate metals are silver, copper, and palladium. The head group (α) is the structural element of the orgnanic that becomes bound to the substrate as the SAM is formed. Sulfur is an ideal head group due to the affinity of alkanethiols for otherwise inert gold. Connected to the head group is the spacer group, commonly a straight-chain alkyl moiety or a polyphenyl chain, which links the head group to the tail group. The tail group (ω) is the moiety which is positioned at the gas—surface interface. These can vary widely amongst a range of organic functional groups.

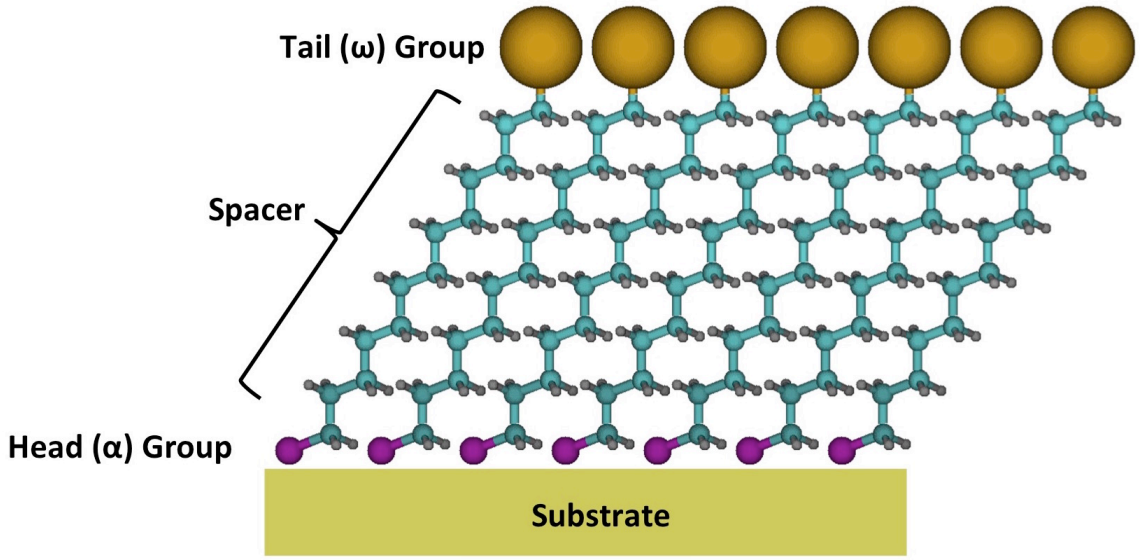

Figure 4.1. Key structural features of a self-assembled monolayer.

In the experimental study by Zhang et al., octadecene thiol was dissolved in a hexane solution along with a polycrystalline gold slide and for 24 hours.[8] The resulting SAM, which consists of 18-carbon chains (16-carbon ethylene linker + 2-carbon vinyl tail group) adsorbed onto the gold substrate via interactions with the sulfur head group, is shown schematically in the left panel of Figure 4.2. Previous work has shown that, in SAMs, alkanethiol chains show hexagonal packing on the substrate with spacing between adjacent head sulfur atoms of 4.97 Å.[3,9]

4.1.2 Nitrate

Beginning with their detection in the troposphere in 1978,[10] nitrate radicals (NO_3) have become of particular interest to atmospheric chemistry due to their reactions with volatile organic compounds, which contributes to their degradation.[11-13] Generated through the reaction of NO_2 with O_3 (Scheme 4.1), nitrate radicals photodissociate rapidly in the daylight (Schemes 4.2 and 4.3).[14,15]

$$NO_2 + O_3 \rightarrow NO_3 + O_2 \quad (4.1)$$

$$NO_3 \xrightarrow{h\nu} NO + O_2 \quad (4.2)$$

$$NO_3 \xrightarrow{h\nu} NO_2 + O \quad (4.3)$$

After sunset, however, NO_3 is highly active in tropospheric chemistry. Primarily through reaction with carbon-carbon double bonds, NO_3 exposure to particles in the atmosphere may lead to changes in particulate properties such as size, and optical scattering and absorption.[16,17] More generally, the reaction of nitrate with volatile organic compounds can facilitate the generation of secondary organic aerosols, a common class of pollutants.[18,19] NO_3 activity is heightened by the decreased concentration of the more oxidative OH at night. However, reactions of NO_3 lead to the formation of OH and HO_2 radicals,[12,20,21] which may oxidize compounds not otherwise reactive to NO_3.

The reaction of nitrate with unsaturated organic compounds has a rich history.[13] Several experimental studies have focused on the reactions of gaseous nitrate with unsaturated organic molecules in order to understand the properties and behavior of this highly relevant atmospheric molecule. Groups have employed relative rate methods to determine rate constants for the reaction of nitrate radicals with straight chain[22,23] and branched alkenes,[22-24] aromatics,[22,25] unsaturated aldehydes,[18,22,23] unsaturated ketones,[26] unsaturated alcohols,[23] and other compounds present in the atmosphere.[27,28] Other studies have been focused on product analysis[29] of these reactions through methods such as FTIR,[30,31] revealing organic nitrates as products. Through both experiment and computational modeling approaches, nitrate exposure has been shown to be the dominant loss process for certain alkene-rich compounds in the atmosphere.[32-34] Three studies investigated the relationship between alkyl chain length and reaction rate with NO_3, finding differing results. While lengthening the carbon chain was not found to affect the reactive rate constant with unsaturated aldehydes,[18] a chain-length dependence on reaction rate was observed for straight-chain[22] and branched alkenes.[24] An additional computational study has shown that increased HOMO energy of alkenes directly relates to reaction rate.[35]

Moving from single-molecule to heterogeneous reactions, the focus of kinetics studies shifts from the reaction rate to the reactive uptake coefficient. This coefficient is described as the ratio of the number of molecules that react with the surface to the number that collide with the surface. Several studies have examined the reactive uptake of NO_3 on liquid[36,37] and amorphous solid organic surfaces.[37-40] Moise et al. found that the NO_3 reactive uptake coefficient for some unsaturated organics decreased upon freezing, while no change was seen for others. This dependence was related to the solubility and diffusion of the NO_3 within the surface.[37] Another study related the structure of an organic surface to the relative contribution of surface and bulk

reactions on NO_3 reactive uptake. In saturated surfaces, for which a slow hydrogen abstraction is the initial step in reaction with NO_3, the contribution of the surface to the overall reaction is minor, as NO_3 is able to diffuse into the bulk before reacting. In unsaturated surfaces, however, a fast addition of NO_3 across a double bond at the surface prevents diffusion into the bulk; thus, reactions the surface dominate the overall reaction rate.[38]

A previous study on the reaction of nitrate with both alkane and terminal alkene SAMs showed that uptake was greater on the model surface than on liquid or solid films. This was due to the positioning of the carbon-carbon double bond at the gas—surface interface, facilitating reaction with gaseous nitrate molecules.[41] However, due to decomposition of products during XPS analysis and during sample transfer between analytic instruments, several expected products were not observed.

Although many investigations have described the reaction of nitrate radicals with both organic molecules and surfaces, several questions remained. For example, in some FTIR studies that identify organic nitrate products,[30,31] specific vibrational mode assignments were not reported. Additionally, several of these products were missing from the previous study on nitrate reactions with SAMs.[41] Thus, Zhang et al. set out to understand more completely the relationship between the structure of organic surfaces and NO_3 reactivity, as well as characterization of reaction products and mechanisms.

In order to describe the fundamentals of the reaction of nitrate with unsaturated organic surfaces, Zhang et al. exposed a vinyl-terminated SAM surface to a flux of nitrate radicals in an ultra-high vacuum environment.[1] The implementation of a SAM allows for the precise positioning of the reactive carbon-carbon double bond at the surface, and ultra-high vacuum reaction conditions prevent reactions with background gases. During exposure, *in situ* time-resolved vibrational RAIRS[42] spectra as well as post-exposure XPS spectra allowed for the monitoring of changes to the surface due to NO_3 exposure. Interpretation of these spectra, using insight from previous studies,[7,41,43-48] lead to the proposal of a terminal organic nitrate (ω-ONO_2) radical product resulting from addition of nitrate to the terminal carbon atom in the vinyl tail group. Figure 4.2 shows the proposed addition scheme.

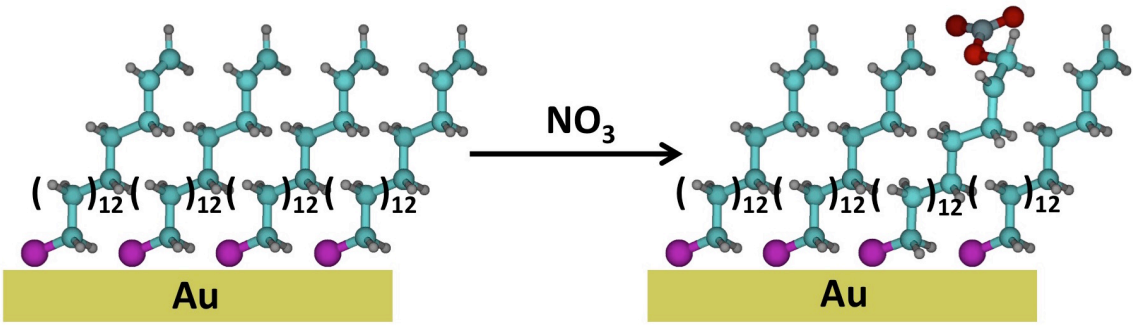

Figure 4.2. Proposed scheme showing addition of a nitrate radical to the terminus of a vinyl self-assembled monolayer chain. Color scheme: C: cyan, H: gray, N: red, O: gray, S: magenta.

4.2 Computational Details and Model Development

To provide further insight into this experiment, we constructed a model system containing several vinyl-terminated alkyl chains in a self-assembled monolayer arrangement. Once fully developed, the geometry of the system was optimized and theoretical vibrational frequencies were calculated the Gaussian09 code.[49] Now, we will describe the system that was used for these calculations.

For computational efficiency, several approximations were made in our model. In the experiment by Zhang et al., linear chains containing 18 carbon atoms each were used. For computational efficiency, our model contains chains of much shorter length. In order to accurately model the experimental spectrum of the nitrate radical product proposed by Zhang et al., single nitrate-terminated alkyl chains of increasing length were constructed and optimized both at the B3LYP/6-31G* and MP2/6-31G* levels of theory, and frequency calculations were performed on the optimized structures. To align theoretical spectra with experimental ones, scaling factors of 0.96 and 0.94 were applied to all frequencies calculated using B3LYP/6-31G* and MP2/6-31G*, respectively.[50] Beginning with the methyl nitrate radical, the chain length was increased by adding methylene groups one at a time. The frequencies of the scissoring ($\delta(\text{-ONO}_2)$), symmetric stretch ($\nu_s(\text{-ONO}_2)$), and asymmetric stretching ($\nu_a(\text{-ONO}_2)$) modes of nitrate all converged to within 10 cm^{-1} for chains with four or more carbon atoms. Figure 4.3 shows the plots of vibrational frequency with respect to carbon chain length for these three modes. With this convergence in consideration, we chose to move forward with chains each containing eight carbon atoms for our model SAM system.

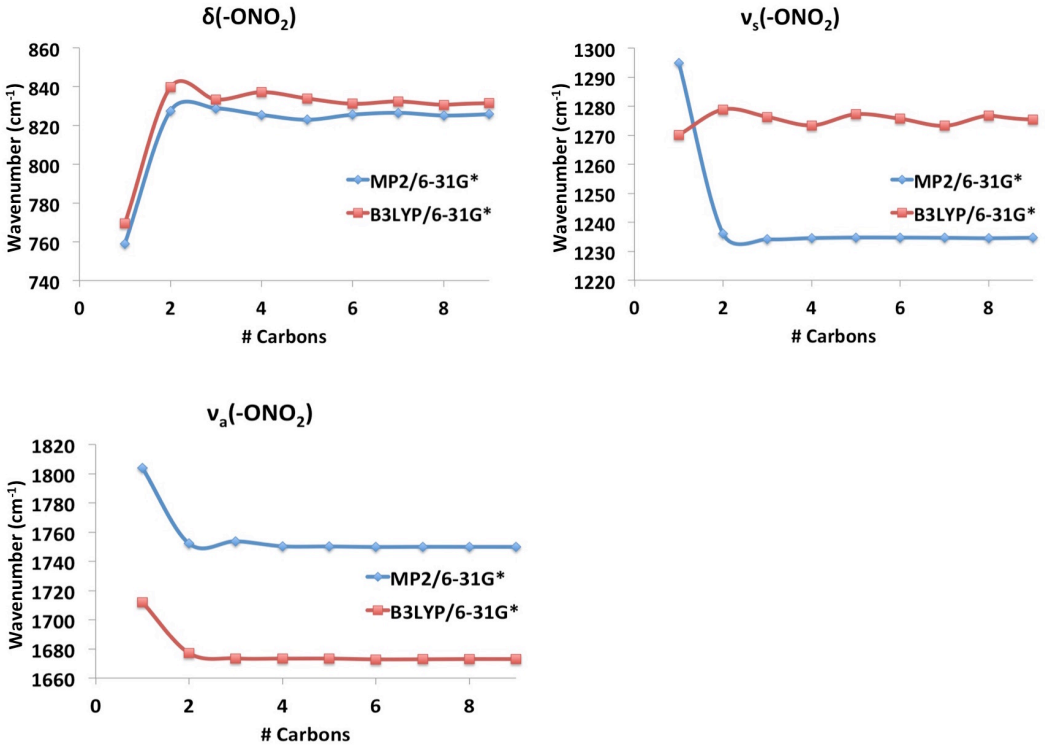

Figure 4.3. Vibrational frequencies of the $–ONO_2$ scissoring (δ), symmetric stretching (ν_s), and asymmetric stretching (ν_a) modes with respect to alkyl chain length for gas-phase alkyl nitrate radical chains. Calculated using MP2/6-31G* (blue) and B3LYP/6-31G* (red). Zhang, Y.; Chapleski, R. C.; Lu, J. W.; Rockhold, T. H.; Troya, D.; Morris, J. R. Physical Chemistry Chemical Physics 2014, 16, 16659. - Reproduced by permission of the PCCP Owner Societies.

In the experiment, octadecene thiol chains were used for the synthesis of the SAM instead of octadecene. As such, S-Au bonds anchor the SAM to the gold substrate. In our computational model SAM, frozen α-CH_3 head groups were used instead of α-SH bound to a substrate. To verify that frozen methyl groups are a sufficient substitute for a bound sulfur group, B3LYP/6-31G* vibrational modes of a single α-SH alkyl chain were compared to those of a single α-CH_3 chain for both reagent ω-vinyl and product ω-nitrate chains. Characteristic frequencies were in both cases found to vary by less than 5 cm^{-1}. Table 4.1 lists these frequencies, compared for $CH_3(CH_2)_5CHCH_2$ and $SH(CH_2)_5CHCH_2$ (reagents), as well as for $CH_3(CH_2)_5CHCH_2ONO_2$ and $SH(CH_2)_5CHCH_2ONO_2$ (products).

Calculated Vibrational Mode	Vibrational Wavenumber (cm^{-1})	
	Reagents	
	α-CH_3	α-SH
ω(=CH_2)	899	901
δ(CH_2)	1482	1480
ν(C=C)	1664	1664
ν_s(CH_2)	2908	2908
ν_a(CH_2)	2957	2962
ν_s(=CH_2)	3028	3029
ν_a(=CH_2)	3103	3105
	Products	
	α-CH_3	α-SH
δ(-ONO_2)	831	831
ν_s(-ONO_2)	1275	1275
ν_a(-ONO_2)	1673	1674

Table 4.1. Selected vibrational modes for α-CH_3 and α-SH variations of the ω-vinyl octene reagent as well as the ω-ONO_2 product of nitrate radical addition to 1-octene. Calculated for a single gas-phase chain using B3LYP/6-31G*. Greek letters are used in the table to describe vibrational motions. ω: out-of-plane deformation, δ: scissoring, ν: stretching, ν_s: symmetric stretching, ν_a: asymmetric stretching. Zhang, Y.; Chapleski, R. C.; Lu, J. W.; Rockhold, T. H.; Troya, D.; Morris, J. R. Physical Chemistry Chemical Physics 2014, 16, 16659. – Reproduced (adapted) by permission of the PCCP Owner Societies.

With frequencies well converged with respect to chain length, alkyl chains with eight carbons each and frozen α-CH_3 groups were chosen for construction of a SAM model. A summary of the approximations made to the SAM chains is shown in Figure 4.4a. To examine the vibrational spectrum of the ω-ONO_2 alkyl radical product chain in the environment of a ω-vinyl SAM, this chain was surrounded by 36 chains of 1-octene in a hexagonal formation (Figure 4.4b). To replicate the arrangement of chains in an alkanethiol SAM, the α-CH_3 groups of these chains were frozen at an interchain distance of 5 Å, such that each chain occupied a surface area of 21.4 $Å^2$.

For further computational efficiency, a multi-level quantum mechanical/molecular mechanical (QM:MM) approach was used for geometry optimization and frequency calculation of our SAM model. The center ω-ONO_2 chain was optimized at the B3LYP/6-31G* (QM) level, while the rest of the system was optimized at the MM level through the application of classical mechanics using universal force field (UFF) terms.[51] Interactions between atoms in the QM and

MM levels were treated at the MM level. To preserve the integrity of this finite-size model, all atoms in the outermost ω-vinyl chains of the model were frozen along with the α-CH_3 carbon atom in each chain. The resulting theoretical SAM model resulting from this partial QM:MM optimization is shown in Figure 4.4b.

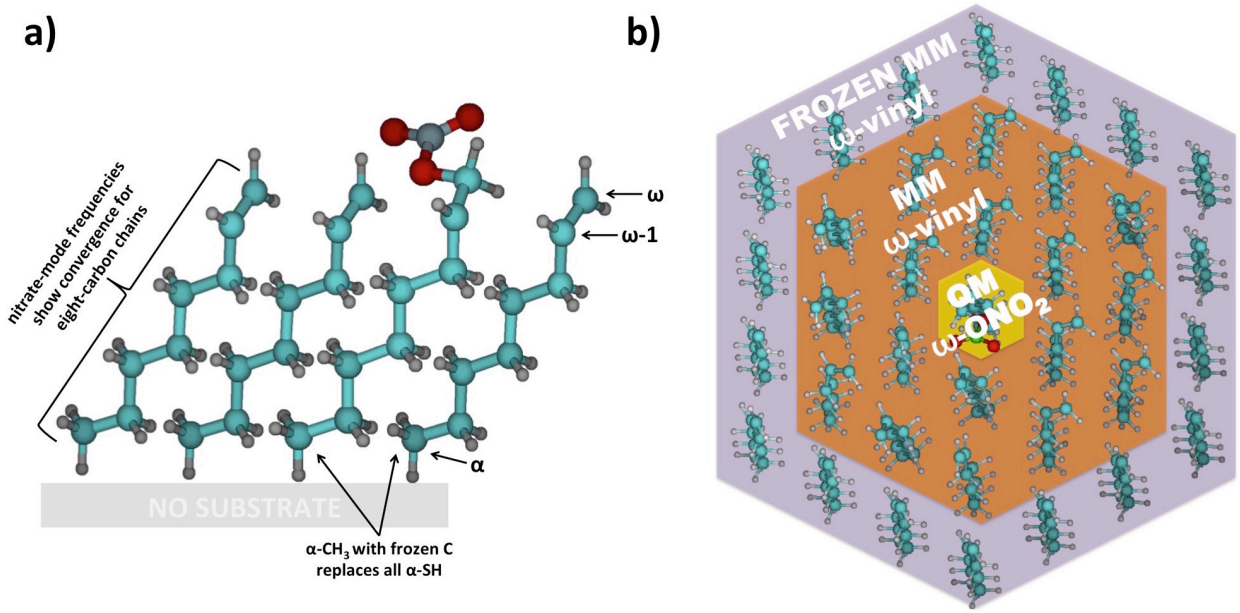

Figure 4.4. a) A visual summary of the approximations made in the computational model of the ω-vinyl SAM and nitrate radical product chains (for comparison with the experimental system shown in Figure 4.2, left pane). b) Schematic of the QM:MM model used for calculation of theoretical spectra of a terminal alkyl nitrate radical chain surrounded by terminal vinyl chains. See description of QM:MM approach in text. For atoms, same color scheme as in Figure 4.2. Zhang, Y.; Chapleski, R. C.; Lu, J. W.; Rockhold, T. H.; Troya, D.; Morris, J. R. Physical Chemistry Chemical Physics 2014, 16, 16659. – Reproduced (adapted) by permission of the PCCP Owner Societies.

4.3 Results

4.3.1 Theoretical Vibrational Spectra

4.3.1.1 ω-ONO_2 SAM

Once the structure of the SAM model shown in Figure 4.4b was optimized, all ω-vinyl chains were subsequently frozen, and a vibrational frequency calculation was performed on just the ω-ONO_2 chain. The resulting theoretical IR spectrum, including modes only for the central ω-ONO_2 chain, is shown in Figure 4.5. In this spectrum, four intense peaks are exhibited: an –ONO_2 scissoring band at 841 cm^{-1}, symmetric and asymmetric –ONO_2 stretching bands at 1283

and 1674 cm^{-1}, respectively, and a region of symmetric and asymmetric $–CH_2$ stretching along the backbone of the chain above 2800 cm^{-1}.

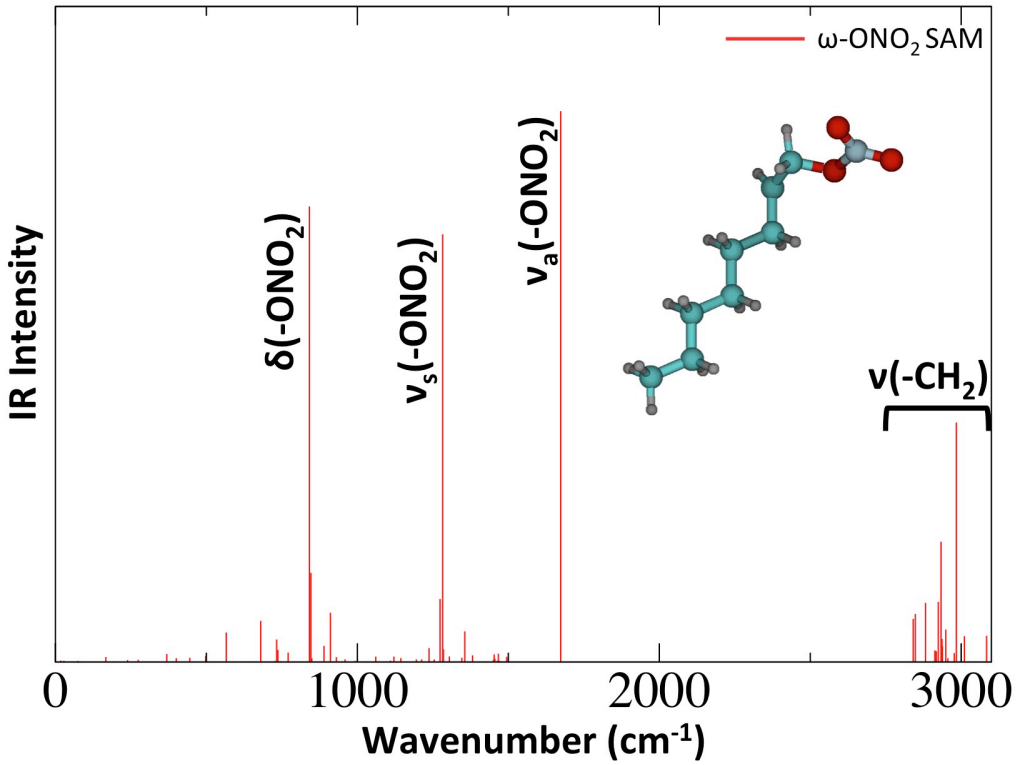

Figure 4.5. Theoretical (B3LYP/6-31G*:UFF) IR spectrum of a ω-ONO_2 alkyl radical chain surrounded by ω-vinyl chains. All frequencies have been scaled by 0.96. The SAM model is described in text. The inset shows the optimized structure of the ω-ONO_2 alkyl radical chain that is embedded within the SAM model. For inset, same color scheme as in Figure 4.2.

To further show the robustness of our model, optimizations were also performed and frequencies calculated using the AMBER force field in the MM region. Not all terms necessary to completely describe this system are included in the Amber force field, and thus, several terms had to be input manually. These harmonic terms are specified in Table 4.2.

Bond Stretch	Stretching Force Constant (K_b, kcal mol^{-1} Å^{-2})	Equilibrium Distance (r_{eq}, Å)
O-N (in C-O-N)	600.0	1.390
O-N (in O-N-O)	1530.0	1.200
Angle Bend	Bending Force Constant (K_θ, kcal mol^{-1} rad^{-2})	Equilibrium Angle (θ_{eq}, °)
C-O-N	111.0	109.6
O-C-H	210.0	106.7
O(C)-N-O	210.0	115.0
C-C-C(=)	63.0	111.0
C=C-H	50.0	119.7
H-C(=)-H	40.0	120.0
O-N-O	210.0	130.0
C-C(=)-H	50.0	120.0

Table 4.2. Manually specified force field terms augmenting AMBER MM calculations. Bond stretching and angle bending energies are calculated using $\boldsymbol{E_{bond} = K_b(r - r_{eq})^2}$ and $\boldsymbol{E_{angle} = K_\theta(\theta - \theta_{eq})^2}$, respectively. Zhang, Y.; Chapleski, R. C.; Lu, J. W.; Rockhold, T. H.; Troya, D.; Morris, J. R. Physical Chemistry Chemical Physics 2014, 16, 16659. - Reproduced by permission of the PCCP Owner Societies.

The frequencies of the vibrational modes characteristic to the nitrate moiety for each level of theory are provided in Table 4.3. It is interesting to note that, at the same level of theory, the frequencies of the nitrate vibrational modes in single-chain gas-phase calculations vary by less than 10 cm^{-1} compared to the same modes in the SAM model. That is, incorporating a nitrate alkyl chain into a SAM has little effect on nitrate vibrational modes. More generally, the effect of incorporating the nitrate radical product chain was investigated through a comparison of the theoretical spectrum of the gas-phase chain to that of the chain included in the SAM model. These spectra are compared in Figure 4.6. Further, the frequencies of sixteen sample vibrational modes were compared for both spectra. Of these, twelve modes were blueshifted due to inclusion in the SAM model, with an average blueshift of 7.2 cm^{-1}. The remaining four modes were redshifted by 12.3 cm^{-1} on average.

Method	$\delta(-ONO_2)$	$\nu_s(-ONO_2)$	$\nu_a(-ONO_2)$
Experiment	857	1280	1649
B3LYP/6-31G* (gas-phase)	831	1275	1673
MP2/6-31G* (gas-phase)	825	1234	1750
Multilevel SAM (B3LYP/6-31G*:UFF)	841	1283	1673
Multilevel SAM (B3LYP/6-31G*:Amber)	834	1277	1673

Table 4.3. Vibrational modes for experimental ω-ONO_2 SAM chain and theoretical vibrational modes for gas-phase ω-ONO_2 octyl radical in both the gas phase and embedded in the SAM model. B3LYP frequencies were scaled by 0.96, and MP2 by 0.94. Zhang, Y.; Chapleski, R. C.; Lu, J. W.; Rockhold, T. H.; Troya, D.; Morris, J. R. Physical Chemistry Chemical Physics 2014, 16, 16659. – Reproduced (adapted) by permission of the PCCP Owner Societies.

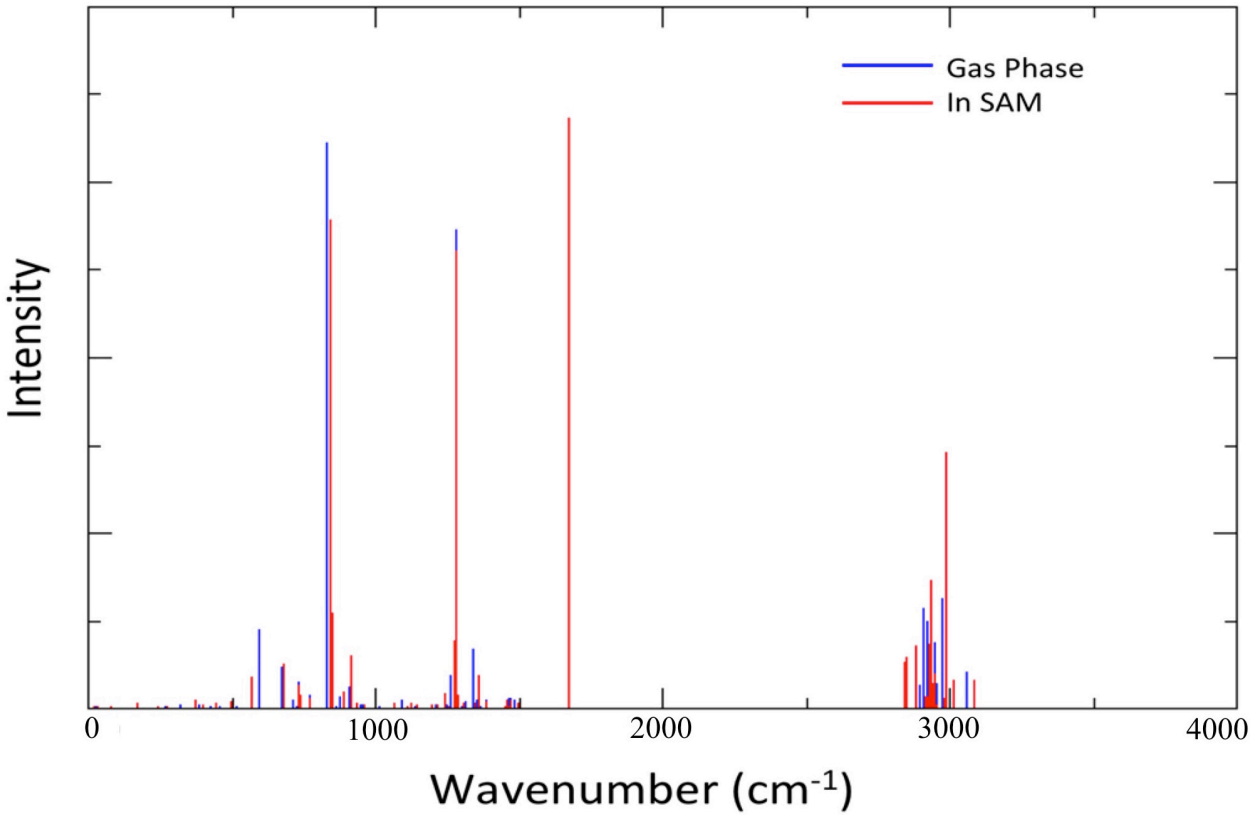

Figure 4.6. Theoretical vibrational spectrum for $CH_3(CH_2)_5CHCH_2ONO_2$ in the gas phase (blue) and surrounded by 1-octene chains in the SAM model (red). Note: the red peak at 1673 cm^{-1} overlaps a blue peak at the same frequency. Zhang, Y.; Chapleski, R. C.; Lu, J. W.; Rockhold, T. H.; Troya, D.; Morris, J. R. Physical Chemistry Chemical Physics 2014, 16, 16659. - Reproduced by permission of the PCCP Owner Societies.

Figure 4.7 shows the agreement between the B3LYP/6-31G*:UFF theoretical spectrum for the nitrate radical product surrounded by ω-vinyl chains and the experimental RAIRS spectrum of the 18-C vinyl-terminated SAM after 5000 Langmuir (L; 1 L = 1 torr•s) exposure to NO_3. In each spectrum, the three most intense bands correspond to those nitrate vibrational modes: NO_2 scissoring (841 cm^{-1} in the QM:MM model), $–ONO_2$ symmetric stretch (1283 cm^{-1}), and $–ONO_2$ asymmetric stretch (1673 cm^{-1}). As the figure shows, there is good agreement between the experimental long-exposure SAM and the theoretical QM:MM product model.

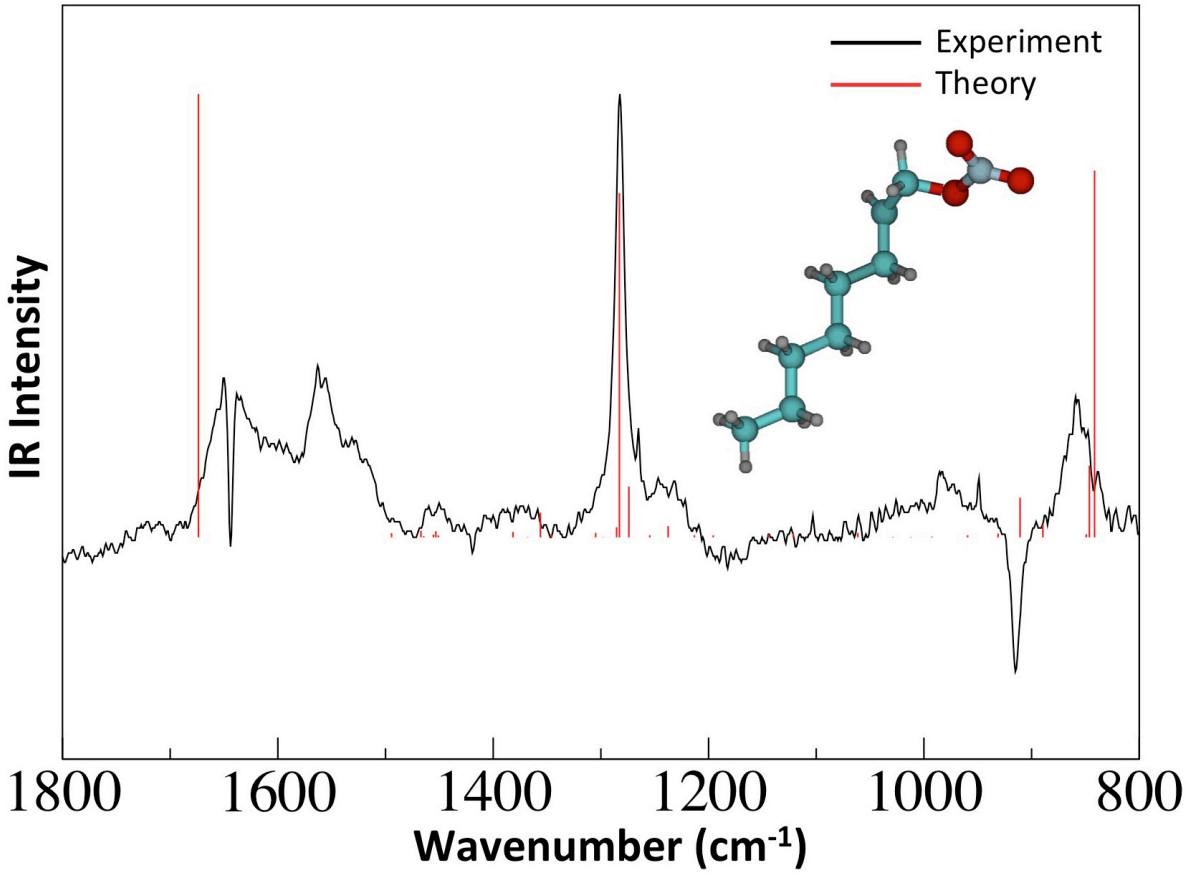

Figure 4.7. Experimental RAIRS spectrum showing changes in the ω-vinyl SAM following 5000 L exposure to NO_3 superposed with the theoretical spectrum of ω-ONO_2 alkyl radical chain (inset) embedded in an environment of ω-vinyl chains. See text for a description of theoretical model. For inset, same color scheme as in Figure 4.2. Zhang, Y.; Chapleski, R. C.; Lu, J. W.; Rockhold, T. H.; Troya, D.; Morris, J. R. Physical Chemistry Chemical Physics 2014, 16, 16659. - Reproduced (adapted) by permission of the PCCP Owner Societies.

4.3.1.2 Addition of a Second Nitrate Radical

Along with experimental data, our theoretical calculations suggest that exposure of a vinyl-terminated SAM to gas-phase nitrate radicals results in the addition of nitrate to the terminal carbon atom (ω, Fig. 4.4a) in a vinyl SAM chain, yielding a subterminal ((ω-1), Fig. 4.4a) radical on the carbon chain. This arrangement is thermodynamically more stable than that resulting from nitrate addition to the subterminal vinyl carbon atom by 3.8 kcal/mol.

Following addition of a single NO_3 radical to the vinyl terminus of a SAM chain, a reactive radical species remains, potentially available to react with a second nitrate radical. Figure 4.8 shows the 800-1800 cm^{-1} region of the B3LYP/6-31G*:UFF spectrum for the addition product for a second NO_3 to the subterminal (ω-1, see Fig. 4.4a) carbon atom of the nitrate alkyl radical chain in the SAM model. In the figure, the theoretical spectrum is presented with the same long-exposure experimental spectrum shown in Figure 4.7. The frequencies of the modes characteristic to the ω-ONO_2 adduct vary inconsistently due to the addition of a second –ONO_2 moiety at the ω-1 position. In the theoretical spectrum for the chain with –NO_3 moieties present at both positions, the ω-ONO_2 scissoring mode is redshifted to 831 cm^{-1}, the symmetric stretching frequency of this moiety is not shifted (1283 cm^{-1}), and the asymmetric stretching frequency is blueshifted to 1707 cm^{-1}. Additionally, vibrational modes characteristic of the (ω-1)-ONO_2 adduct are now present: the scissoring mode at 815 cm^{-1}, the symmetric stretching mode at 1273 cm^{-1}, and the asymmetric stretching mode at 1693 cm^{-1}. Taken together, both ω- and (ω-1)-ONO_2 scissoring, symmetric, and asymmetric stretching modes may account for the experimental features at 857 cm^{-1}, 1280 cm^{-1}, and 1649 cm^{-1}, respectively. Additionally, a the ω(C-O) stretching mode becomes pronounced in this spectrum at 998 cm^{-1}, which may account for the experimental feature around 980 cm^{-1} in the experimental spectrum. Thus, the presence of an –ONO_2 moiety at the ω-1 position in addition to that at the ω position cannot be ruled out by this analysis.

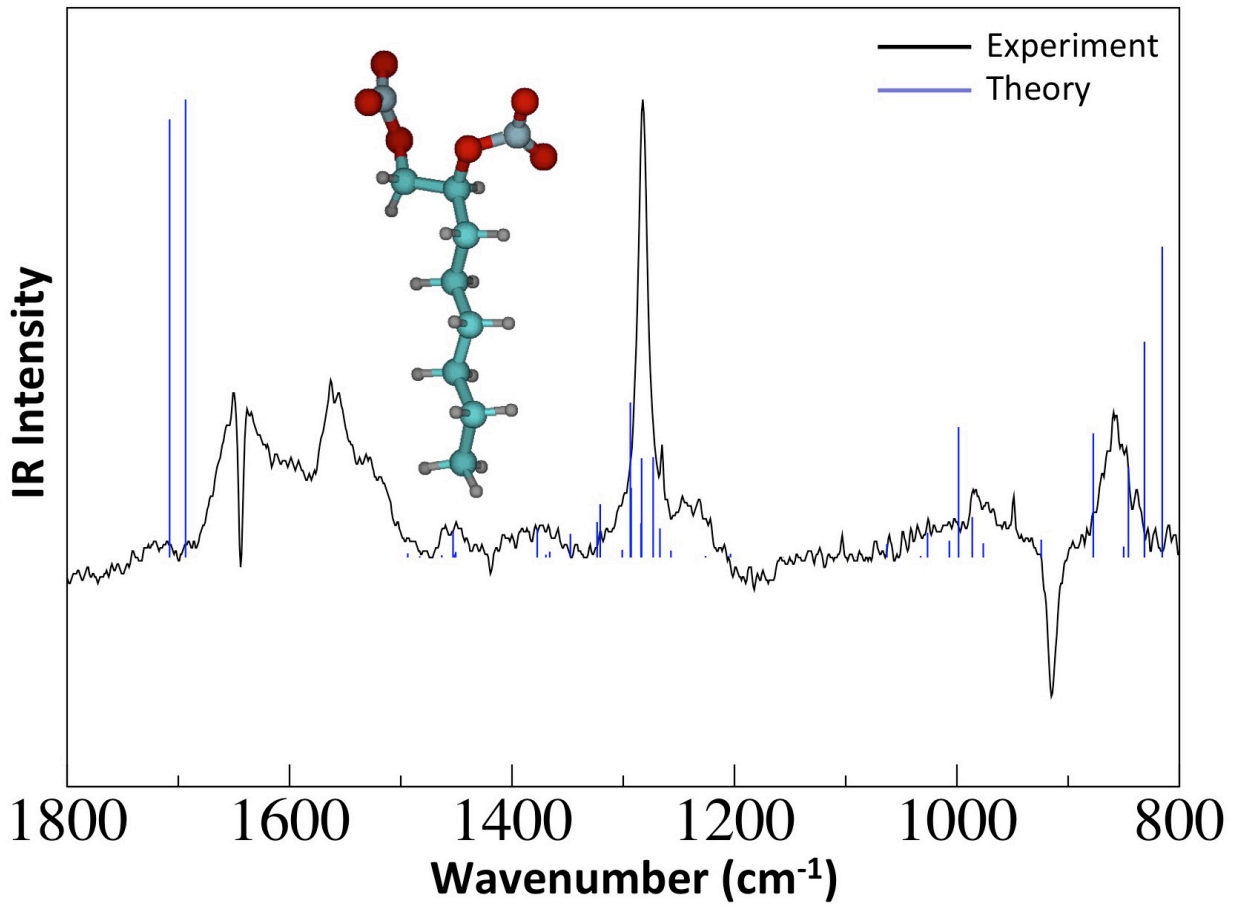

Figure 4.8. Experimental RAIRS spectrum showing changes in the ω-vinyl SAM following 5000 L exposure to NO_3 superposed with theoretical (B3LYP/6-31G*:UFF) IR spectrum of a ω-ONO_2, (ω-1)-ONO_2 alkyl chain surrounded by 1-octene chains. All frequencies scaled by 0.96. SAM model described in text. Inset shows the optimized structure of the ω-ONO_2, (ω-1)-ONO_2 alkyl chain that is embedded in the SAM model. For inset, same color scheme as in Figure 4.2.

Alternatively, an NO_2 radical, present in the experimental environment from the thermal decomposition of N_2O_5 to produce nitrate (Scheme 4.4), may react with this radical chain.

$$N_2O_5 \rightarrow NO_2 + NO_3 \qquad (4.4)$$

Although a control experiment by Zhang et al. in which the ω-vinyl SAM was exposed to a flux of NO_2 showed no sign of reaction in the absence of NO_3, the possibility for NO_2 reaction with an ω–ONO_2 radical chain remains. Figure 4.9 shows a comparison in the 800-1800 cm^{-1} region between the long-exposure experimental spectrum and the theoretical spectrum for the SAM model with a central chain containing ONO_2 bound at the ω position and NO_2 bound at the ω-1 position. Along with the nitrate features present in the ω-ONO_2 theoretical spectrum (here, the

ONO_2 scissoring mode has a frequency of 831 cm^{-1}, the ONO_2 symmetric stretch has a frequency around 1290 cm^{-1}, and the ONO_2 asymmetric stretch has a frequency of 1702 cm^{-1}), additional modes for the (ω-1)-NO_2 moiety are pronounced in the theoretical spectrum as well. Symmetric and asymmetric NO_2 stretching modes have frequencies of 1385 cm^{-1} and 1610 cm^{-1}, respectively. Also, as with the case in which nitrate moieties are present at both the ω and ω-1 positions, the ω(C-O) stretching frequency blueshifts relative to the SAM model without an adduct at the ω-1 position to 1002 cm^{-1}. Similarly, an agreement is evident between the experimental spectrum and this theoretical one for the ω-ONO_2 modes, and additional features between the experimental and theoretical spectra seem to agree. Namely, the ω(C-O) stretch may contribute to the feature around 980 cm^{-1} in the experimental spectrum, and the ω-1(NO_2) stretch may contribute to the experimental feature around 1550 cm^{-1}. Therefore, as with (ω-1)-ONO_2, the possibility for addition of NO_2 at the ω-1 position should not be ruled out along with addition of ω(ONO_2) in the experiment. Regardless of the type (or absence of) a moiety at the ω-1 position, all three spectra agree with an –ONO_2 adduct present at the ω position.

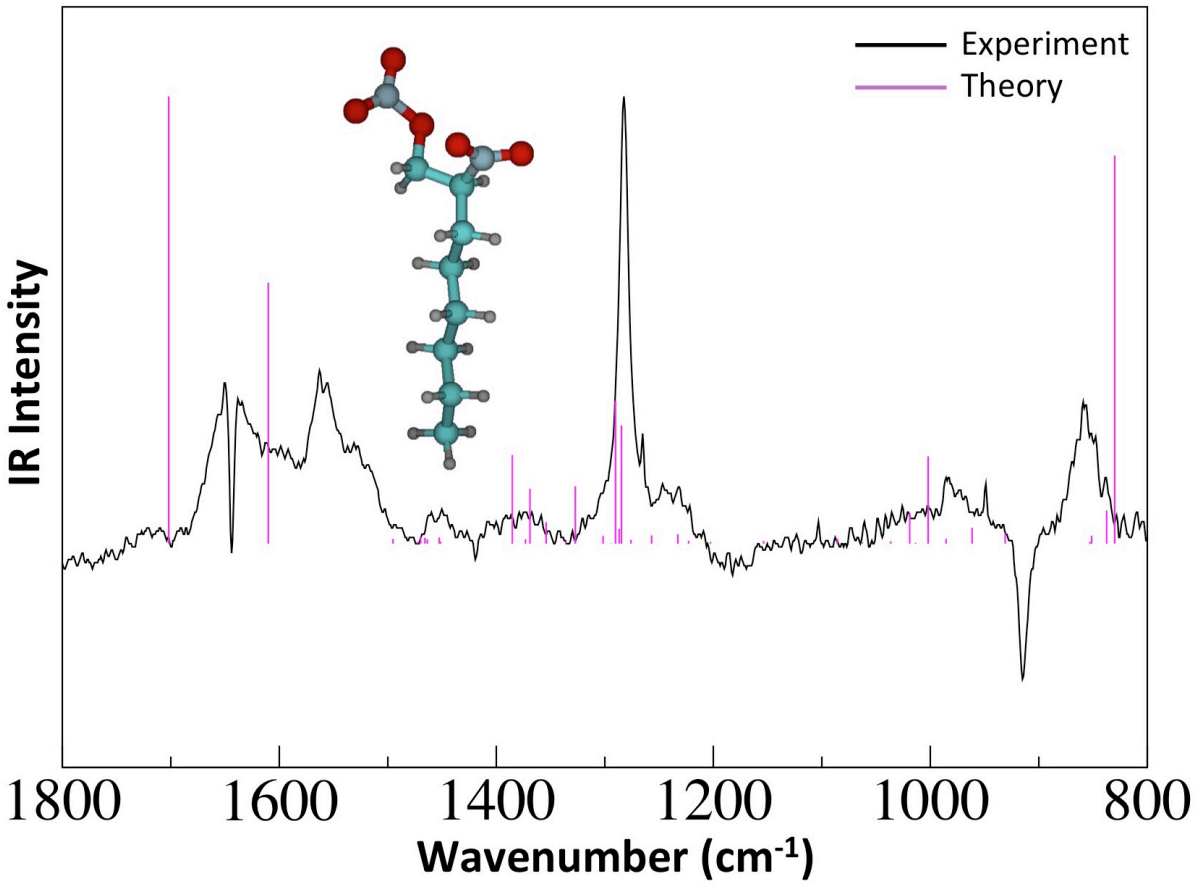

Figure 4.9. Experimental RAIRS spectrum showing changes in the ω-vinyl SAM following 5000 L exposure to NO_3 superposed with theoretical (B3LYP/6-31G*:UFF) IR spectrum of a ω-ONO_2, (ω-1)-NO_2 alkyl chain surrounded by 1-octene chains. All frequencies scaled by 0.96. SAM model described in text. Inset shows the optimized structure of the ω-ONO_2, (ω-1)-NO_2 alkyl chain that is embedded in the SAM model. For inset, same color scheme as in Figure 4.2.

4.3.2 Competing Pathway: Hydrogen Abstraction

The prior section has identified products for NO_3 addition to the vinyl group of a SAM. A competing reaction pathway was also investigated in which the nitrate radical abstracted a hydrogen atom from a SAM chain, yielding a terminal vinyl radical species, •CH=CH-$(CH_2)_{16}$SAu, and HNO_3.. Previous experimental studies have shown evidence for similar products in reactions of nitrate with hydrocarbons,[38] yet such a pathway was not evident in the experiments by Zhang et al. Thus, we performed electronic structure calculations with propene as a model to delve deeper into the possibility of the hydrogen-abstraction pathway. Single-point calculations at the CCSD(T)/aug-cc-pVDZ level of theory calculated using geometries optimized

with B3LYP/6-31G* reveal that the hydrogen abstraction reaction with propene, NO_3• + H_2C=CH-CH_3 → •CH=CH-CH_3 + HNO_3, is endothermic by 8.3 kcal mol^{-1}, with a barrier of 9.9 kcal/mol. At room temperature, very few NO_3 radicals have enough energy to surmount this barrier, and thus, reaction is unlikely. Conversely, at the same level of theory, a transition state could not be found for the nitrate addition reaction to the terminal vinyl carbon atom of propene, though this reaction was found to be exothermic by 19.1 kcal/mol. A potential energy surface (PES) scan was performed in which the distance between the C and O atoms which form a bond during nitrate addition is varied while all other coordinates were allowed to relax during optimization. The results of this scan using B3LYP/6-31G* geometries are shown in Figure 4.10 and predict a continuously downhill energy path leading from separated reagents to addition products. Single-point energies calculated with other density functionals and basis sets using B3LYP/6-31G* geometries are also shown in the figure and corroborate this result. Finally, CCSD(T)/aug-cc-pVDZ single-point energies were calculated for selected points in the scan using B3LYP/6-31G* geometries. This scan, like the rest, predicts that nitrate addition to propene, and extensively to the vinyl-terminated SAM, is barrierless. Thus, without reaction barrier and with greater exothermicity, nitrate radical addition to the terminal carbon atom of the vinyl group likely dominates hydrogen abstraction from the same carbon atom.

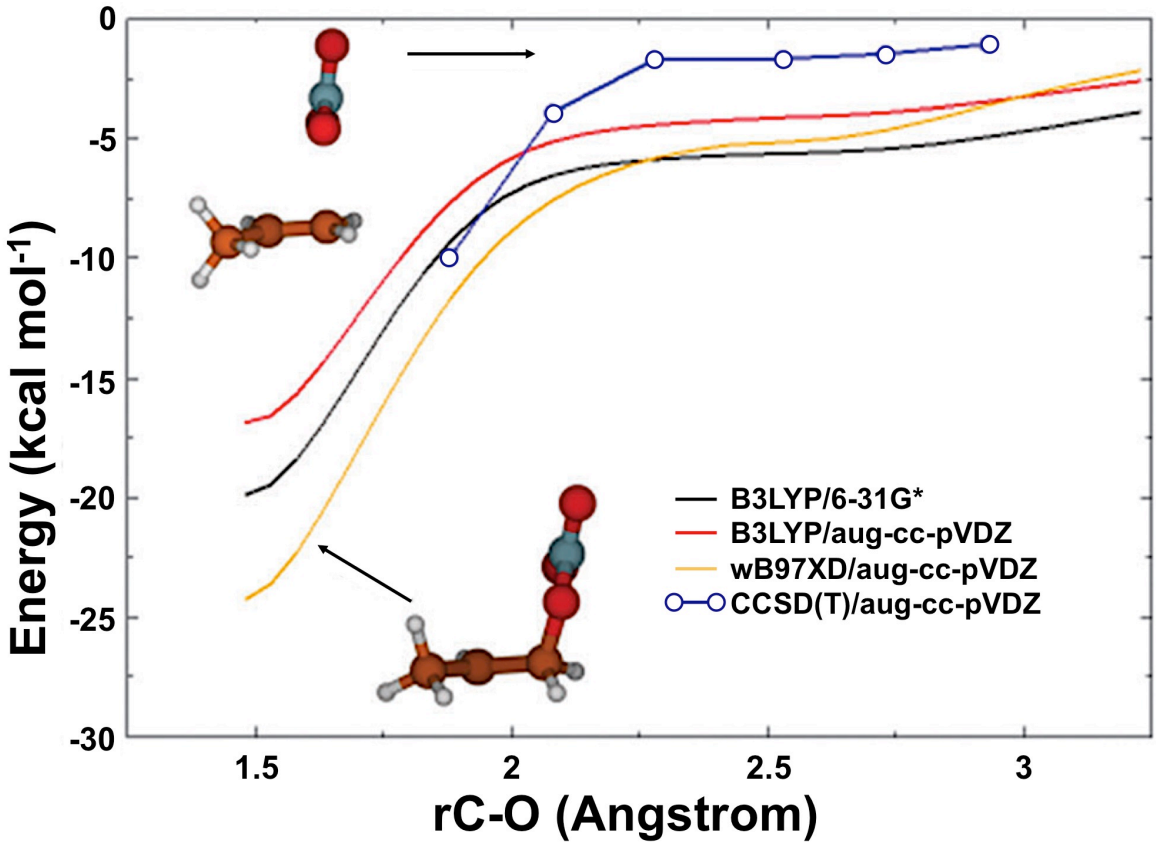

Figure 4.10. Potential energy scan for C-O distance in the addition reaction of nitrate to propene. All scans were performed using B3LYP/6-31G* geometries, and energies have not been zero-point corrected. Zhang, Y.; Chapleski, R. C.; Lu, J. W.; Rockhold, T. H.; Troya, D.; Morris, J. R. Physical Chemistry Chemical Physics 2014, 16, 16659. - Reproduced by permission of the PCCP Owner Societies

4.4 Concluding Remarks

We have performed theoretical vibrational mode calculations on a SAM system built to model the experimental product of nitrate exposure to a ω-vinyl SAM. Following careful and validated approximations to our model, we were able to calculate theoretical spectra that align closely with the ω-ONO_2 alkyl radical product described by Zhang et al. in their experimental study. The same study reveals an initial reaction probability of 2.3 x 10^{-3} for this reaction.[1] This is much greater than that for the reaction of ozone with the same experimental SAM system (1.1 x 10^{-5}).[44] Future work will implement molecular dynamics methods to investigate the geometric conditions required for the two-order-of-magnitude difference in initial reaction probability.

4.5 References

(1) Zhang, Y.; Chapleski, R. C.; Lu, J. W.; Rockhold, T. H.; Troya, D.; Morris, J. R. *Physical Chemistry Chemical Physics* **2014**, *16*, 16659.

(2) Love, J. C.; Estroff, L. A.; Kriebel, J. K.; Nuzzo, R. G.; Whitesides, G. M. *Chemical Reviews* **2005**, *105*, 1103.

(3) Widrig, C. A.; Alves, C. A.; Porter, M. D. *Journal of the American Chemical Society* **1991**, *113*, 2805.

(4) Gates, B. D.; Xu, Q.; Stewart, M.; Ryan, D.; Willson, C. G.; Whitesides, G. M. *Chemical Reviews* **2005**, *105*, 1171.

(5) L H Dubois, a.; Nuzzo, R. G. *Annual Review of Physical Chemistry* **1992**, *43*, 437.

(6) Nuzzo, R. G.; Allara, D. L. *Journal of the American Chemical Society* **1983**, *105*, 4481.

(7) Nuzzo, R. G.; Zegarski, B. R.; Dubois, L. H. *Journal of the American Chemical Society* **1987**, *109*, 733.

(8) Hu, J.; Fox, M. A. *The Journal of Organic Chemistry* **1999**, *64*, 4959.

(9) Ulman, A.; Eilers, J. E.; Tillman, N. *Langmuir* **1989**, *5*, 1147.

(10) Noxon, J. F.; Norton, R. B.; Henderson, W. R. *Geophysical Research Letters* **1978**, *5*, 675.

(11) Finlayson-Pitts, B. J.; Pitts Jr, J. N. *Chemistry of the upper and lower atmosphere: theory, experiments, and applications*; Academic press, 1999.

(12) Wayne, R. P.; Barnes, I.; Biggs, P.; Burrows, J. P.; Canosa-Mas, C. E.; Hjorth, J.; Le Bras, G.; Moortgat, G. K.; Perner, D.; Poulet, G.; Restelli, G.; Sidebottom, H. *Atmospheric Environment. Part A. General Topics* **1991**, *25*, 1.

(13) Chapleski, R. C.; Zhang, Y.; Troya, D.; Morris, J. R. *Chemical Society Reviews* **2016**, *45*, 3731.

(14) Xiao, H.; Maeda, S.; Morokuma, K. *The Journal of Physical Chemistry Letters* **2011**, *2*, 934.

(15) Stewart, D. J.; Almabrok, S. H.; Lockhart, J. P.; Mohamed, O. M.; Nutt, D. R.; Pfrang, C.; Marston, G. *Atmospheric Environment* **2013**, *70*, 227.

(16) Ellison, G. B.; Tuck, A. F.; Vaida, V. *Journal of Geophysical Research: Atmospheres* **1999**, *104*, 11633.

(17) Novakov, T.; Corrigan, C. E.; Penner, J. E.; Chuang, C. C.; Rosario, O.; Bracero, O. L. M. *Journal of Geophysical Research: Atmospheres* **1997**, *102*, 21307.

(18) Kerdouci, J.; Picquet-Varrault, B.; Durand-Jolibois, R.; Gaimoz, C.; Doussin, J.-F. *The Journal of Physical Chemistry A* **2012**, *116*, 10135.

(19) Mellouki, A.; Le Bras, G.; Sidebottom, H. *Chemical Reviews* **2003**, *103*, 5077.

(20) Platt, U.; LeBras, G.; Poulet, G.; Burrows, J. P.; Moortgat, G. *Nature* **1990**, *348*, 147.

(21) Brown, S. S.; Stutz, J. *Chemical Society Reviews* **2012**, *41*, 6405.

(22) Atkinson, R.; Plum, C. N.; Carter, W. P. L.; Winer, A. M.; Pitts, J. N. *The Journal of Physical Chemistry* **1984**, *88*, 1210.

(23) Zhao, Z.; Husainy, S.; Smith, G. D. *The Journal of Physical Chemistry A* **2011**, *115*, 12161.

(24) Aschmann, S. M.; Atkinson, R. *The Journal of Physical Chemistry A* **2011**, *115*, 1358.

(25) Tapia, A.; Villanueva, F.; Salgado, M. S.; Cabañas, B.; Martínez, E.; Martín, P. *Atmos. Chem. Phys.* **2011**, *11*, 3227.

(26) Wang, K.; Ge, M.; Wang, W. *Chemical Physics Letters* **2010**, *490*, 29.

(27) Salgado, M. S.; Gallego-Iniesta, M. P.; Martín, M. P.; Tapia, A.; Cabañas, B. *Environmental Science and Pollution Research* **2011**, *18*, 940.

(28) Gai, Y.; Wang, W.; Ge, M.; Kjaergaard, H. G.; Jørgensen, S.; Du, L. *Atmospheric Environment* **2013**, *77*, 696.

(29) Wille, U.; Goeschen, C. *Australian Journal of Chemistry* **2011**, *64*, 833.

(30) Skov, H.; Benter, T.; Schindler, R. N.; Hjorth, J.; Restelli, G. *Atmospheric Environment* **1994**, *28*, 1583.

(31) Hjorth, J.; Lohse, C.; Nielsen, C. J.; Skov, H.; Restelli, G. *The Journal of Physical Chemistry* **1990**, *94*, 7494.

(32) WINER, A. M.; ATKINSON, R.; PITTS, J. N. *Science* **1984**, *224*, 156.

(33) Barnes, I.; Bastian, V.; Becker, K. H.; Tong, Z. *The Journal of Physical Chemistry* **1990**, *94*, 2413.

(34) Atkinson, R.; Aschmann, S. M.; Winer, A. M.; Pitts, J. N. *Environmental Science & Technology* **1985**, *19*, 159.

(35) D. King, M.; E. Canosa-Mas, C.; P. Wayne, R. *Physical Chemistry Chemical Physics* **1999**, *1*, 2231.

(36) Gross, S.; Iannone, R.; Xiao, S.; Bertram, A. K. *Physical Chemistry Chemical Physics* **2009**, *11*, 7792.

(37) Moise, T.; Talukdar, R. K.; Frost, G. J.; Fox, R. W.; Rudich, Y. *Journal of Geophysical Research: Atmospheres* **2002**, *107*, AAC 6.

(38) Shiraiwa, M.; Pöschl, U.; Knopf, D. A. *Environmental Science & Technology* **2012**, *46*, 6630.

(39) Xiao, S.; Bertram, A. K. *Physical Chemistry Chemical Physics* **2011**, *13*, 6628.

(40) Zhao, Z.; Husainy, S.; Stoudemayer, C. T.; Smith, G. D. *Physical Chemistry Chemical Physics* **2011**, *13*, 17809.

(41) Gross, S.; Bertram, A. K. *Journal of Geophysical Research: Atmospheres* **2009**, *114*, n/a.

(42) Greenler, R. G. *The Journal of Chemical Physics* **1966**, *44*, 310.

(43) Duan, L.; Garrett, S. J. *Langmuir* **2001**, *17*, 2986.

(44) Lu, J. W.; Fiegland, L. R.; Davis, E. D.; Alexander, W. A.; Wagner, A.; Gandour, R. D.; Morris, J. R. *The Journal of Physical Chemistry C* **2011**, *115*, 25343.

(45) Peanasky, J. S.; McCarley, R. L. *Langmuir* **1998**, *14*, 113.

(46) Wandas, M.; Puszko, A. *Chemistry of Heterocyclic Compounds* **2000**, *36*, 796.

(47) Aubuchon, C. M.; Rector, K. D.; Holmes, W.; Fayer, M. D. *Chemical Physics Letters* **1999**, *299*, 84.

(48) Noda, J.; Hallquist, M.; Langer, S.; Ljungstrom, E. *Physical Chemistry Chemical Physics* **2000**, *2*, 2555.

(49) Frisch, M. J.; Trucks, G. W.; Schlegel, H. B.; Scuseria, G. E.; Robb, M. A.; Cheeseman, J. R.; Scalmani, G.; Barone, V.; Mennucci, B.; Petersson, G. A.; Nakatsuji, H.; Caricato, M.; Li, X.; Hratchian, H. P.; Izmaylov, A. F.; Bloino, J.; Zheng, G.; Sonnenberg, J. L.; Hada, M.; Ehara, M.; Toyota, K.; Fukuda, R.; Hasegawa, J.; Ishida, M.; Nakajima, T.; Honda,

Y.; Kitao, O.; Nakai, H.; Vreven, T.; Montgomery Jr., J. A.; Peralta, J. E.; Ogliaro, F. ß.; Bearpark, M. J.; Heyd, J.; Brothers, E. N.; Kudin, K. N.; Staroverov, V. N.; Kobayashi, R.; Normand, J.; Raghavachari, K.; Rendell, A. P.; Burant, J. C.; Iyengar, S. S.; Tomasi, J.; Cossi, M.; Rega, N.; Millam, N. J.; Klene, M.; Knox, J. E.; Cross, J. B.; Bakken, V.; Adamo, C.; Jaramillo, J.; Gomperts, R.; Stratmann, R. E.; Yazyev, O.; Austin, A. J.; Cammi, R.; Pomelli, C.; Ochterski, J. W.; Martin, R. L.; Morokuma, K.; Zakrzewski, V. G.; Voth, G. A.; Salvador, P.; Dannenberg, J. J.; Dapprich, S.; Daniels, A. D.; Farkas, O.; Foresman, J. B.; Ortiz, J. V.; Cioslowski, J.; Fox, D. J.; Gaussian, Inc.: Wallingford, CT, USA, 2009.

(50) **2011**.

(51) Rappe, A. K.; Casewit, C. J.; Colwell, K. S.; Goddard, W. A.; Skiff, W. M. *Journal of the American Chemical Society* **1992**, *114*, 10024.

Chapter 5

The Reaction Mechanism of Nerve-Agent Hydrolysis with the $Cs_8Nb_6O_{19}$ Lindqvist Hexaniobate Catalyst

Robert C. Chapleski Jr.,[1] Djamaladdin G. Musaev,[2] Craig L. Hill,[3] and Diego Troya[1,*]

[1] *Department of Chemistry, Virginia Tech, Blacksburg, VA*

[2] *Cherry L. Emerson Center for Scientific Computation, Emory University, Atlanta, GA*

[3] *Department of Chemistry, Emory University, Atlanta, GA*

Abstract

We present a detailed mechanism for the hydrolysis of Sarin catalyzed by $Cs_8Nb_6O_{19}$ obtained using electronic structure calculations. The initial steps of the reaction involve the adsorption of water and Sarin on the hexaniobate catalyst via non-bonding interactions. Dissociation of the coordinated water molecule generates a hydroxide ion that adds nucleophilically to the co-adsorbed Sarin molecule in a concerted manner, following a general base catalysis mechanism. The addition of OH^- to the nerve agent generates a trigonal bipyramidal pentacoordinated phosphorus intermediate that subsequently undergoes facile dissociation forming either HF or isopropanol and a corresponding phosphonic acid. The rate-determining step of the overall reaction is found to be the dissociation of water on the catalyst in concert with the nucleophilic addition of the nascent OH^- to the nerve agent. The calculated barrier for this step is considerably smaller than that measured for bulk base hydrolysis. This work represents a blueprint for future studies aimed to optimize catalysts for base hydrolysis of nerve agents at the gas–surface interface.

5.1 Introduction

Interest in developing efficient catalytic decontamination strategies for chemical warfare agents remains unabated.[1,2] Early decontamination procedures employed a variety of general-purpose techniques ranging from bleaching to enzymatic biodegradation,[3] but many of these approaches required highly corrosive solution-phase treatments. More recently, the quest for improved decontamination processes has examined a number of solid-phase catalysts including zirconium hydroxide,[4] zeolites,[5] organic polymers,[6] polyoxometalates (POM),[7,8] metal organic frameworks (MOF),[9-13] and MOF/POM architectures.[14,15]

Among the various classes of chemical warfare agents, nerve agents (e.g., Sarin, Soman, VX, Tabun) have arguably received the most attention in decontamination studies. These nerve agents consist of organophosphorus (OP) compounds with a central tetrahedral phosphorus atom. In vivo, these species inhibit acetylcholinesterase (a serine protease) following nucleophilic addition of the –OH group of a serine residue in the active site of the enzyme to the nerve agent.[16] The susceptibility of OP compounds toward nucleophilic addition has been exploited in the development of many of the catalysts mentioned above, which generally aim to decompose the OP species via base hydrolysis.[3]

Even though the experimental efforts to develop synthetic nerve-agent decontamination catalysts have been rather vigorous recently, there remains a lack of fundamental understanding of the fine details of their reaction mechanisms. Indeed, while the basic decontamination catalysts appear to involve general base hydrolysis,[7,11,12] the atomistic details of the formation of hydroxide on the catalyst, the addition of OH^- to the nerve agents, and the subsequent dissociation of the agents have not conclusively been revealed. This is in sharp contrast to the mechanism for nerve agents reacting with OH^- in bulk solution, which has received significant computational scrutiny.[17-19]

There are two main mechanisms for catalytic base hydrolysis of a substrate in solution. In *specific* base catalysis, water is deprotonated to fully form a hydroxide ion in a first step, followed by nucleophilic attack of hydroxide on the substrate in a second step. In *general* base catalysis, the water deprotonation and nucleophilic addition to the substrate take place simultaneously. Recent work with Lindqvist hexaniobate alkali salts ($X_8Nb_6O_{19}$, X=Li, K, Cs) measured fast hydrolysis of Sarin both in aqueous solution and at the gas–surface interface.[7] Small-angle x-ray scattering (SAXS) measurements showed the aggregation of the OP

compounds under study to the polyoxoniobate (PONb), which led to the suggestion that the reaction follows a general base catalysis mechanism. Finally, a study just published on the basic hydrolysis of nerve agents and their analogues, by polymeric polyniobates, $K_{12}Ti_2O_2XNb_{12}O_{40}$, $X = Ge^{IV}$ or Si^{IV}, includes three lines of evidence that these PONbs, which share many molecular attributes in common with $Nb_6O_{19}^{8-}$, clearly hydrolyze these OP compounds by a general base catalyzed mechanism.[8]

In this paper, we probe the general base catalysis reaction mechanism for the degradation of nerve agents on $Cs_8Nb_6O_{19}$ (CsPONb), using density functional theory (DFT) calculations. Computational work on the structure and reactivity of polyoxometalate catalysts has a rich history,[20-26] and has been essential, in combination with synthetic and characterization approaches, to develop a profound understanding of the properties of these catalysts and to accelerate their discovery. Remarkably, most of the theoretical studies on POM reactivity have focused on acid, oxidation, and redox catalysis,[24] but there is a paucity of investigations of reactions in which the POMs act as base hydrolysis catalysts.

Of the wealth of POM catalysts that have been synthesized over decades,[27-36] Group-V POMs with Lindqvist ion structure, particularly $Nb_6O_{19}^{8-}$, are ideal candidates to act as base hydrolysis catalysts due to the high charge density of the exposed oxygen atoms.[37] It is therefore not surprising that alkali salts of the $Nb_6O_{19}^{8-}$ ion have recently been reported to hydrolyze nerve agents.[7,8] Computational work on $Nb_6O_{19}^{8-}$ has included structural studies using DFT methods,[38] the proposal (also with DFT methods) of an open-cage intermediate that leads to oxygen exchange with solvent measured with NMR,[39] and a recent molecular dynamics study of the protonation of $Nb_6O_{19}^{8-}$ in aqueous media.[40] However, no mechanistic studies of the base hydrolysis reactions with $Nb_6O_{19}^{8-}$ have been reported yet.

In this work, we aim to provide the groundwork for a full understanding of the decomposition of nerve agents over PONb and other catalysts by focusing on the reaction of Sarin with the alkali salt of the Lindqvist PONb, $Cs_8Nb_6O_{19}$, at the gas–surface interface. Experimental evidence for this heterogeneous reaction with well-characterized solid salts[41,42] of $Cs_8Nb_6O_{19}$ has been recently provided, as have related OP hydrolysis processes catalyzed by polymeric PONb.[8] While we are primarily interested in characterization of the reaction at the gas–surface interface, this work might also be applicable to the solution phase, as SAXS measurements indicate that in concentrated solutions of CsOH, the Cs ions are in direct contact

with the Lindqvist ion, without intervening solvent molecules (inner-sphere ion pairs).[43,44] This is in contrast to the K salts, where solvent-separated ion pairs are present. The aggregation of Cs ions to the niobates has also been reported in aqueous solution.[7] The presence of a contact ion pair between Cs and the PONb not mediated by solvent water molecules therefore might make the calculations herein more applicable to the solution-phase process with $Cs_8Nb_6O_{19}$ than with any other alkali PONb salt, even if the role of solvent in the homogeneous process is still unknown.

5.2 Computational Details

All presented calculations have been carried out with the M06-L density functional, as implemented in the Gaussian09 code.[45] Our choice of this functional is motivated by its ability to treat transition elements and non-covalent interactions accurately.[46] Geometry optimizations and harmonic normal mode calculations have used the 6-31G(d,p) basis set for the main-group elements and Lanl2dz basis set with associated effective core potentials for Nb and Cs atoms. Using these geometries, we have carried out single-point energy calculations with the [6-31++G(d,p) + Lanl2dz] basis set to further refine the energy. All reported energies in this paper correspond to M06-L/[6-31++G(d,p) + Lanl2dz] electronic energies corrected by the zero point. The stationary points were located using standard procedures and corroborated by harmonic frequency and intrinsic reaction coordinate analysis. We used an ultrafine integration grid to accelerate convergence of both wavefunction and geometry.

Most of our calculations consider dry hexaniobates in which only the water molecule that participates in the hydrolysis is considered. A subset of the calculations incorporates explicitly 14 additional water molecules to make contact with experiment, which shows the presence of crystallization water molecules.

5.3 Results

5.3.1 Reagents

The reagents of the title reaction are the $Cs_8Nb_6O_{19}$ catalyst, H_2O, and Sarin (GB, propan-2-yl methylphosphonofluoridate). As seen in Figure 5.1, $Cs_8Nb_6O_{19}$ has octahedral point-group symmetry, and it possesses only five symmetry-inequivalent atoms: the central oxygen atom ($O_{central}$), six terminal O atoms ($O_{terminal}$), six Nb atoms, twelve bridging oxygen atoms ($O_{bridging}$),

and eight Cs counterions. The distances between Nb and the $O_{central}$, $O_{terminal}$, and $O_{bridging}$ atoms are 2.407, 1.808, and 2.037 Å, respectively, in good agreement with values obtained from x-ray diffraction[41] of the $Cs_8Nb_6O_{19}$ tetradecahydrate salt (2.360, 1.804, and 1.987 Å, respectively). The radius of gyration of the salt calculated in this work as the root-mean-square displacement of all atoms from $O_{central}$ (3.62 Å) is also in good agreement with the experimental value of 3.6 Å.[43] The Cs counterions are interacting with the faces of the hexaniobate superoctahedron, and the distance between the Cs atom and the nearest $O_{bridging}$ atoms in the PONb is 2.948 Å.

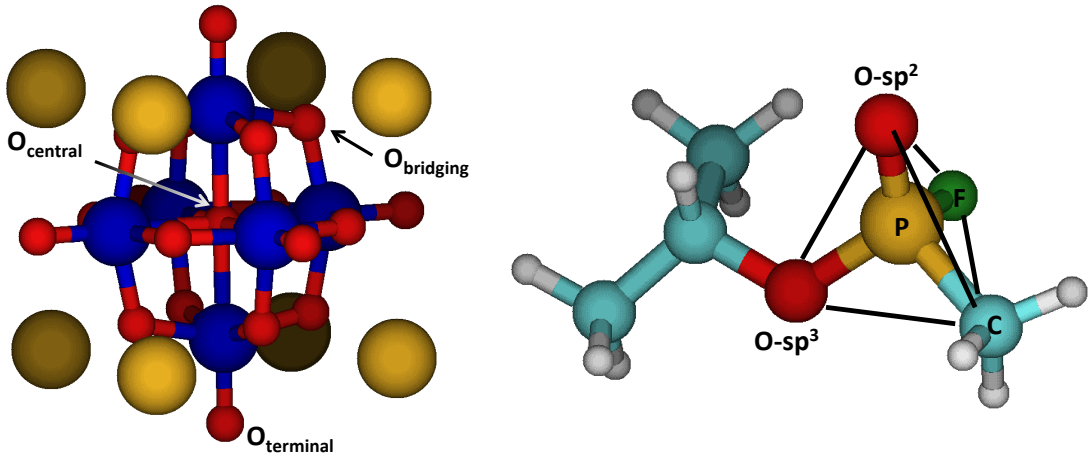

Figure 5.1. Optimum geometries of $Cs_8Nb_6O_{19}$ (left) and *(S)*-Sarin (GB, right). Color scheme: Nb: blue, O: red, Cs: gold, P: gold, C: cyan, F: green, H: gray. Reprinted (adapted) with permission from Chapleski, R. C.; Musaev, D. G.; Hill, C. L.; Troya, D. *The Journal of Physical Chemistry C* **2016**, *120*, 16822. Copyright 2016 American Chemical Society.

Analysis of the standard Mulliken charges reveals the known trend in basicity of the various oxygen sites in the PONb: the calculated atomic charges are -0.943e, -0.994e and -1.137e for the terminal, central, and bridging oxygen atoms, respectively. As shown in earlier experiments[47] and calculations,[40] the bridging oxygen is the most basic of the exposed atoms of the PONb.

Also depicted in Figure 5.1 is the optimum structure of *(S)*-Sarin, the enantiomer of higher toxicity[48] used in all calculations of this work. Highlighted in the figure is the tetrahedral shape around the central phosphorus atom, which undergoes nucleophilic addition of a hydroxide ion during the hydrolysis process. Because this atom is the stereogenic center of the molecule, there are, in principle, four symmetry-inequivalent approaches of hydroxide to the phosphorus

atom. Nucleophilic addition to the tetrahedral OP compound generates a trigonal bipyramidal pentacoordinated species, and early work determined that the approach of lowest barrier is related to the apicophilicity of the substituent that is in an axial position in the forming trigonal bipyramid at the transition state.[49] The tendency of a group to occupy an axial position seems to have various contributions, including electronegativity, but also steric and inductive effects, and this makes it challenging to estimate a priori which one of the approaches might be the one of lowest energy. Below, we present reaction pathways and transition states for all four approaches.

5.3.2 Potential Energy Surface, Structure, and Energetics of the Calculated Intermediates, Transition States, and Products

The calculated potential-energy profile of the catalytic hydrolysis of Sarin by $Cs_8Nb_6O_{19}$ is shown in Figure 5.2. The elementary steps of this catalytic process are: i) binding of water to the CsPONb, ii) binding of GB to the hydrated CsPONb, iii) GB hydrolysis via formation of a pentacoordinated phosphorus intermediate, iv) dissociation of the pentacoordinated intermediate into products bound to the CsPONb, and v) desorption of products. In the following, we analyze each of these steps in turn.

5.3.2.1 Binding of Water to the CsPONb

The first step in the mechanism involves the binding of a water molecule to the catalyst to generate a CsPONb-H_2O complex. Of the two isomers located in this work, the most stable complex corresponds to a structure where H_2O binds in a bidentate manner to the CsPONb via two hydrogen bonds, one with a terminal O atom and the other with a neighboring bridging O atom. The calculated binding energy of this CsPONb complex is 98.3 kJ/mol (see Figure 5.2). Aside from the hydrogen bonds, we note that the oxygen atom of the water molecule is close to two Cs ions of the salt (O_{water}-Cs distances: 3.33 Å), which affords additional stabilization of the complex via electrostatic interactions.

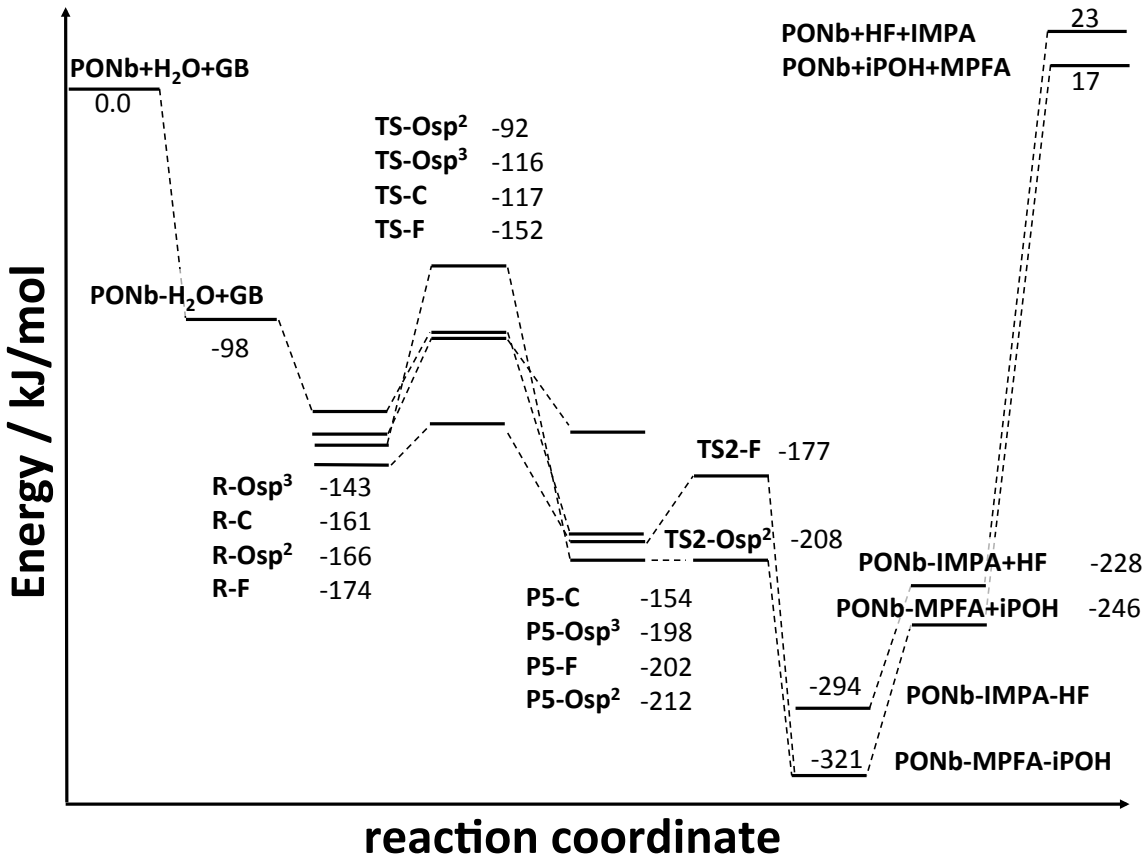

Figure 5.2. Potential-energy profile for the hydrolysis of Sarin by $Cs_8Nb_6O_{19}$. See the text for the nomenclature used to label the various stationary points. Reprinted (adapted) with permission from Chapleski, R. C.; Musaev, D. G.; Hill, C. L.; Troya, D. *The Journal of Physical Chemistry C* **2016**, *120*, 16822. Copyright 2016 American Chemical Society.

5.3.2.2 CsPONb-H_2O-GB complex

Once the CsPONb-H_2O complex is formed, the addition of the nerve agent leads to formation of CsPONb-H_2O-GB complexes (Figure 5.3). The four isomers of these complexes shown in the figure differ in the orientation of GB with respect to the CsPONb. We use the identity of the atom X whose P-X bond is collinear with the forming P-OH bond at the transition state to differentiate these isomers.

The formation of the CsPONb-H_2O-GB complexes is driven by dipole-dipole, dispersion, hydrogen-bonding, and electrostatic interactions between the Cs counterions and electron-rich atoms of the nerve agent. Key hydrogen-bond distances for these complexes are highlighted in Figure 5.3, and interactions between GB atoms and Cs counterions are shown in Figure 5.4. The

binding energies of GB to the CsPONb-H_2O complex are 76.0, 67.7, 63.0, and 45.0 kJ/mol for isomers R-F, R-Osp^2, R-C and R-Osp^3, respectively, and this ranking is related to the number of stabilizing interactions between GB and the hydrated CsPONb. For the most stable complex (R-F), we note the presence of two hydrogen bonds between GB and an $O_{terminal}$ atom of CsPONb, a hydrogen bond between GB and the adsorbed water molecule, and an electrostatic interaction between the O-sp^2 atom of GB and a Cs counterion (Fig. 5.4).

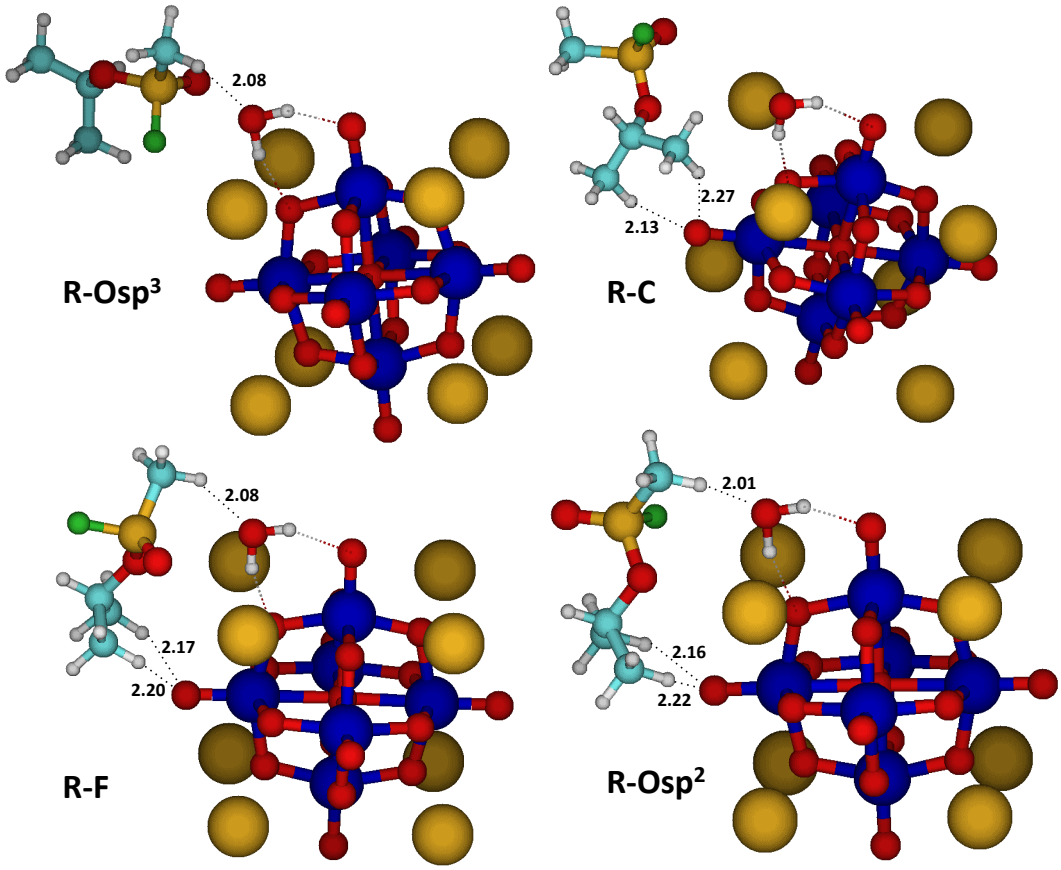

Figure 5.3. CsPONb-H_2O-GB complexes in which each of the faces of the central organophosphorus tetrahedron is interacting with CsPONb-H_2O. Numbers correspond to representative hydrogen-bond distances in Angstroms. Same color code as in Fig. 5.1. Reprinted (adapted) with permission from Chapleski, R. C.; Musaev, D. G.; Hill, C. L.; Troya, D. *The Journal of Physical Chemistry C* **2016**, *120*, 16822. Copyright 2016 American Chemical Society.

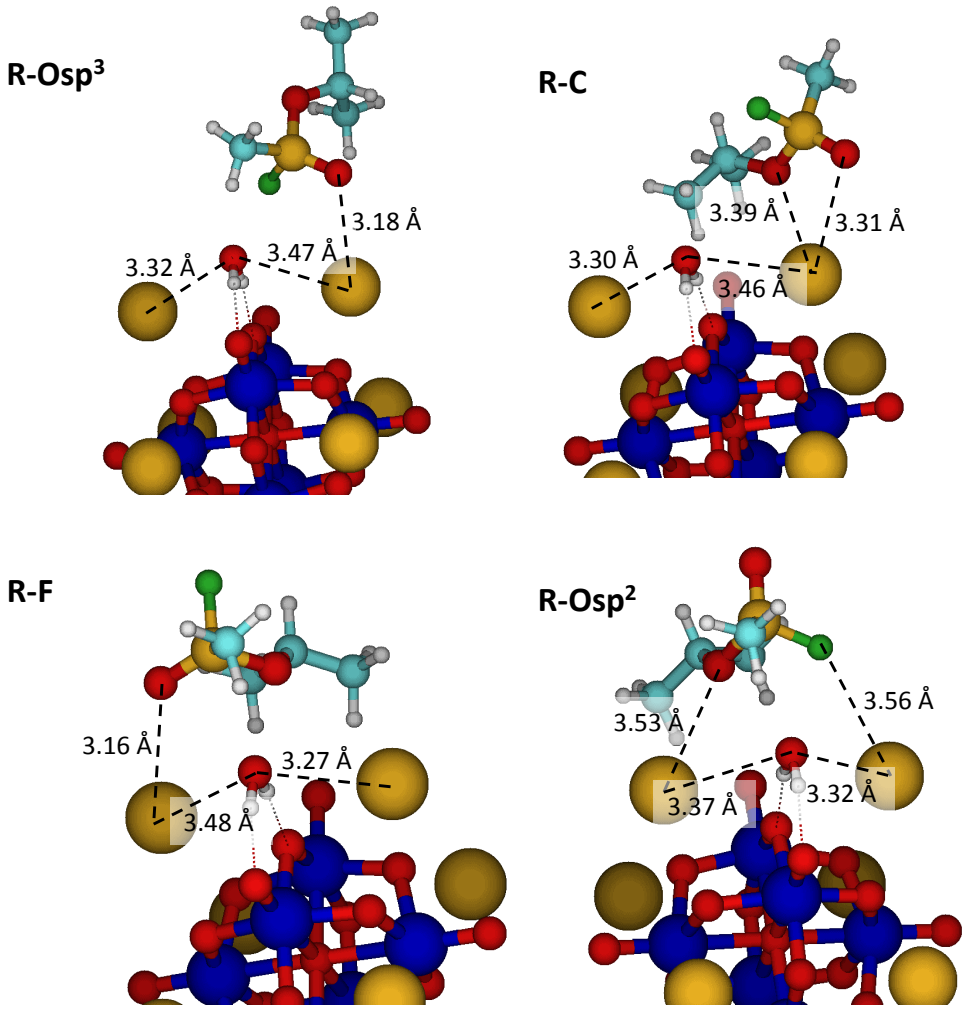

Figure 5.4. CsPONb-H_2O-GB complexes in which each of the faces of the central organophosphorus tetrahedron is interacting with CsPONb-H_2O highlighting electrostatic contacts between Cs counterions and electronegative atoms in the nerve agent. Same color code as in Fig. 5.1. Reprinted (adapted) with permission from Chapleski, R. C.; Musaev, D. G.; Hill, C. L.; Troya, D. *The Journal of Physical Chemistry C* **2016**, *120*, 16822. Copyright 2016 American Chemical Society.

5.3.2.3 Transition State for Water Deprotonation and OH Nucleophilic Addition to the Substrate

Following the potential energy profile of Figure 5.2, the next step of the general base catalysis is the concerted water deprotonation and OH nucleophilic addition to the nerve agent. This is the overall rate-determining step for GB hydrolysis by the CsPONb catalyst. Transition states for the four approaches examined in this work are exhibited in Figures 5.5 and 5.6.

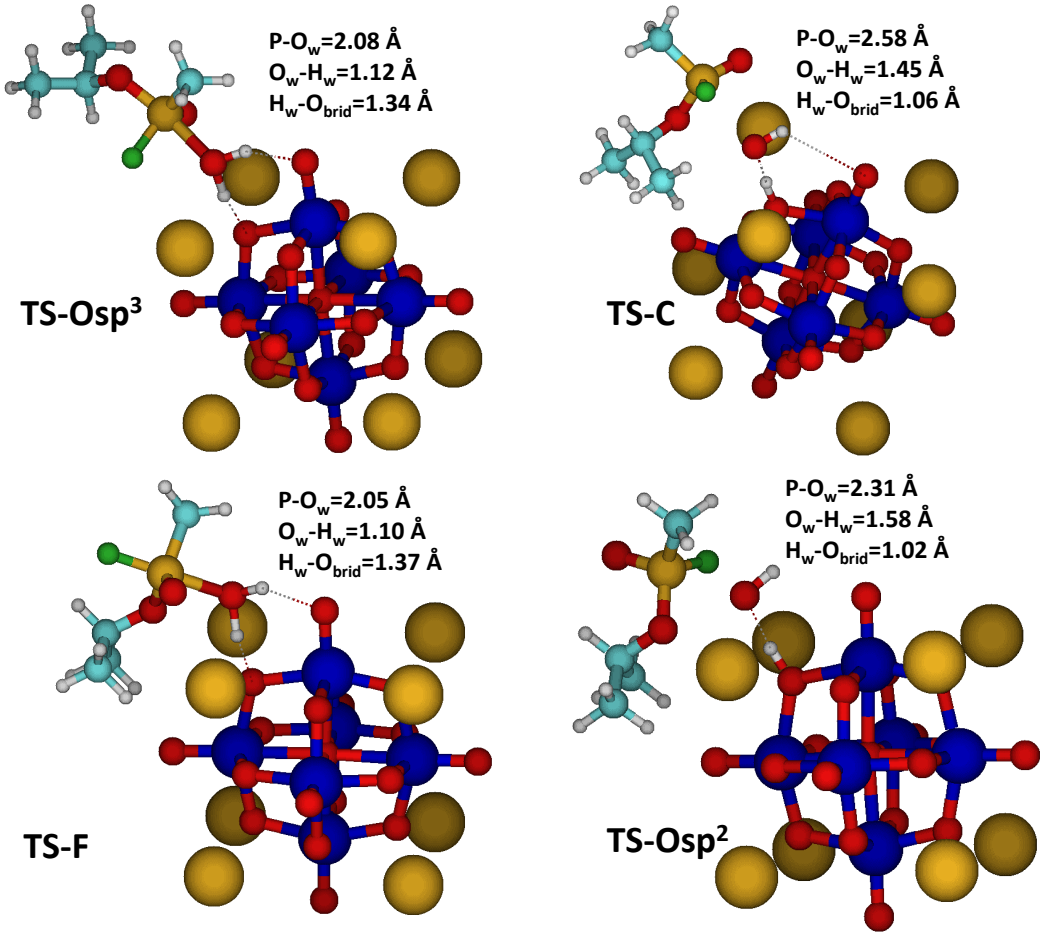

Figure 5.5. Transition state structures for the rate-determining step of the hydrolysis reaction of GB with CsPONb. Same color code as in Fig. 5.1. Additional distances shown in Figure 5.6. Reprinted (adapted) with permission from Chapleski, R. C.; Musaev, D. G.; Hill, C. L.; Troya, D. *The Journal of Physical Chemistry C* **2016**, *120*, 16822. Copyright 2016 American Chemical Society.

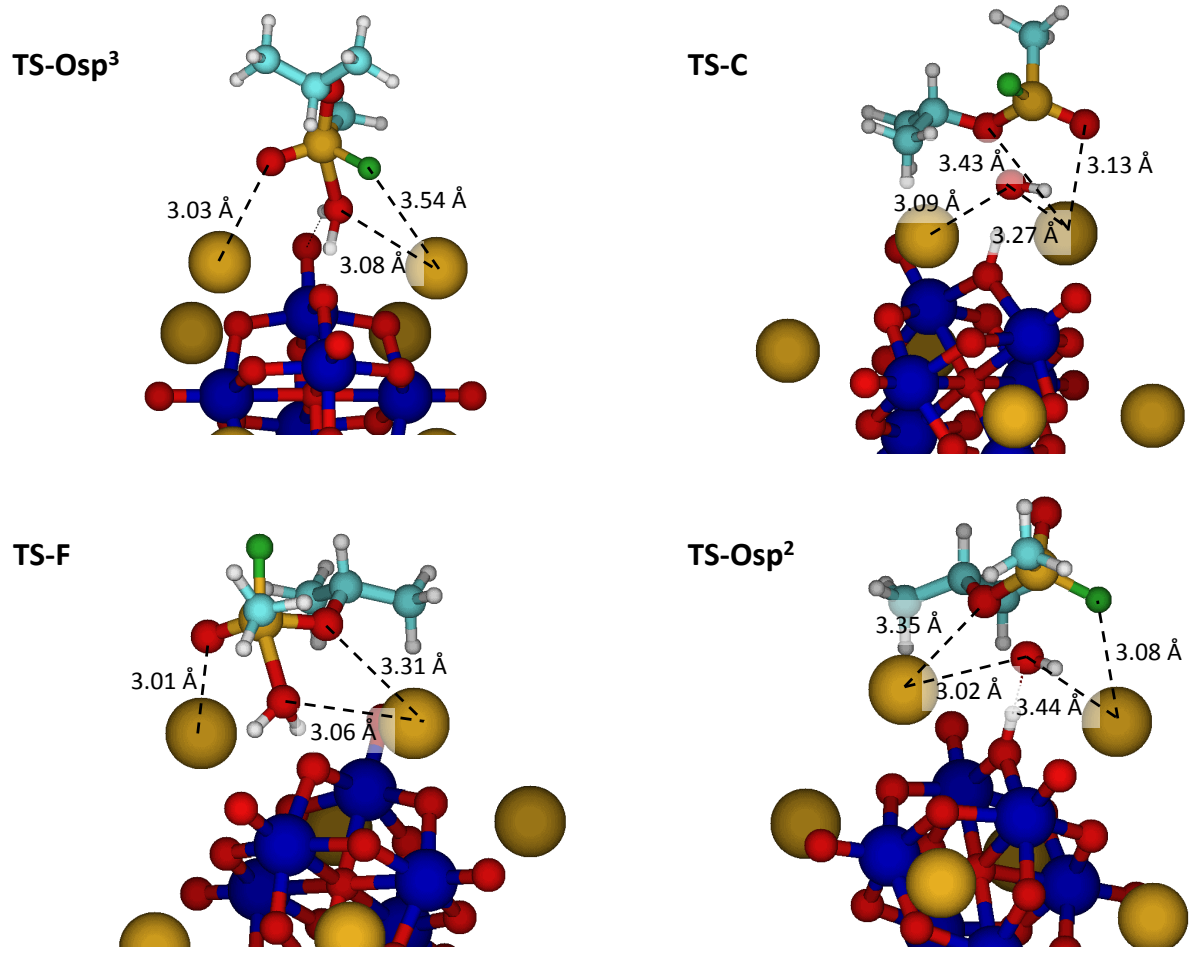

Figure 5.6. Transition states for GB hydrolysis by $Cs_8Nb_6O_{19}$ highlighting electrostatic contacts between Cs counterions and electronegative atoms in the nerve agent. Same color code as in Fig. 5.1. Reprinted (adapted) with permission from Chapleski, R. C.; Musaev, D. G.; Hill, C. L.; Troya, D. *The Journal of Physical Chemistry C* **2016**, *120*, 16822. Copyright 2016 American Chemical Society.

Figure 5.5 reveals that in all transition states, a nascent OH from the protonation of an $O_{bridging}$ atom in the CsPONb elicits nucleophilic addition to the nerve agent in a concerted manner. Interestingly, there are significant differences in the synchronicity of the protonation and addition motions. For instance, in TS-Osp^3 and TS-F, the OH addition is taking place while water is still not quite fully dissociated. On the other hand, in TS-C and TS-Osp^2, it seems that the OH group has been fully formed at the transition state, as the $O_{bridging}$ atom of the catalyst is protonated.

To better characterize these trends, we show in Figure 5.7 the evolution of the three key interatomic distances (the forming P-O_{water} and breaking O_{water}-H_{water} bonds, together with the

$O_{bridging}$-H_{water} distance) along the minimum-energy reaction path for the four approaches considered in this work. The figure indicates that in the TS-Osp^3 and TS-F reaction paths, the water dissociation and CsPONb protonation are taking place at the same time that the P-O bond is forming, and at the transition state, all three bonds are in the process of either forming or breaking. On the other hand, for TS-C and TS-Osp^2, the protonation of the bridging oxygen seems to occur well before the transition state. This is particularly true for the TS-Osp^2 pathway, where the $O_{bridging}$-H_{water} bond is nearly fully formed by the time that the transition state is reached. Interestingly, the separation between the phosphorus atom and the nascent OH is also longer at the transition state for the reaction pathways of the transition states TS-C and TS-Osp^2.

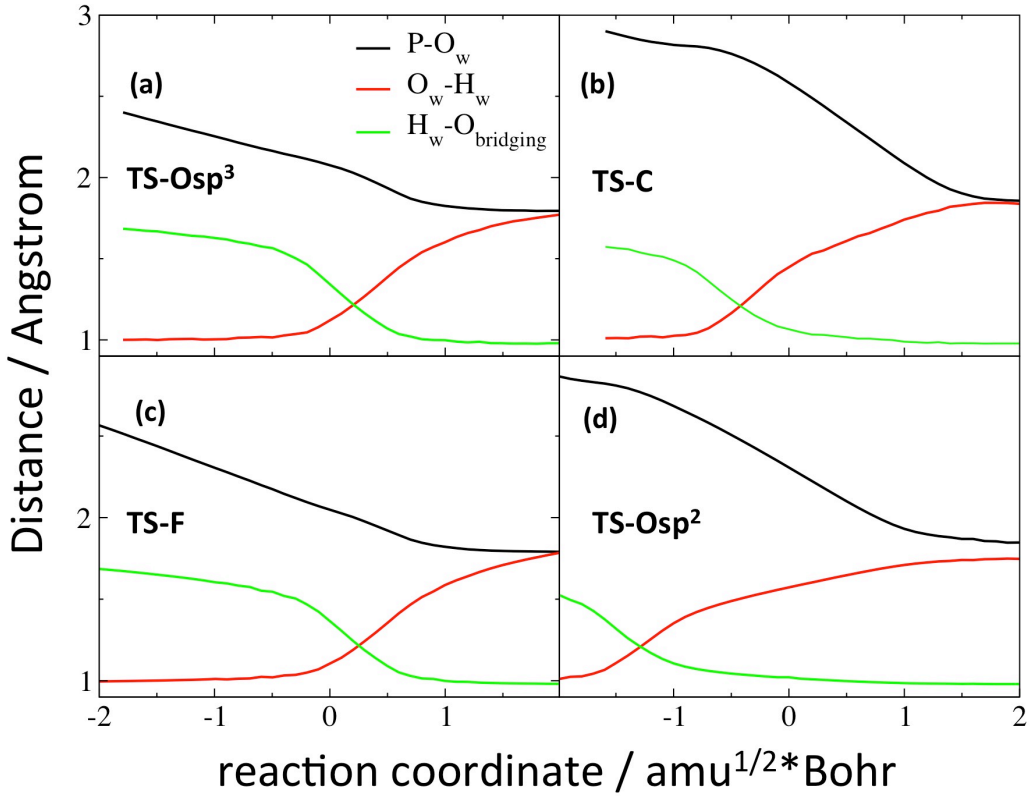

Figure 5.7. Evolution of the three key P-O_{water}, O_{water}-H_{water}, and $O_{bridging}$-H_{water} distances along the minimum energy reaction path for the rate-determining step in the four reaction paths of Sarin hydrolysis at an $O_{bridging}$ site examined in this work. Reprinted (adapted) with permission from Chapleski, R. C.; Musaev, D. G.; Hill, C. L.; Troya, D. *The Journal of Physical Chemistry C* **2016**, *120*, 16822. Copyright 2016 American Chemical Society.

The subtle differences in the atomic motions along the four minimum-energy reaction paths examined in this work appear to be correlated with the transition state energies calculated

from the R complexes in Fig. 5.3. Thus, while the energies for the TS-Osp^3 and TS-F transition states are 27.5 and 22.8 kJ/mol respectively, those for TS-C and TS-Osp^2, which show a larger asynchronicity in the water-dissociation and OH addition motions, are higher: 44.5 and 74.2 kJ/mol, respectively. The transition state energies for the gas–surface TS-Osp^3 and TS-F pathways compare favorably with the room-temperature activation enthalpy determined experimentally from the solution-phase base hydrolysis of GB (41 kJ/mol).[50] They also compare favorably with the calculated values at various levels of theory for the OH^- + GB reaction including implicit solvation (also ~40 kJ/mol).[19]

5.3.2.4 Pentacoordinated Intermediates

Following each of the four the minimum energy reaction pathways towards products, we have located four pentacoordinated intermediates with trigonal bipyramidal shape around the central phosphorus atom, shown in Figure 5.8. All of the intermediates share similarities, but differ in how they are bound to the CsPONb and in the groups that are in axial positions. The pentacoordinated intermediates are bound to the protonated CsPONb through two at least two hydrogen bonds: one between the newly formed phosphonic acid OH group and an $O_{terminal}$ atom in the CsPONb (which is inherited from the transition state), and another one between an electron-rich atom of GB and the H-$O_{bridging}$ group of the CsPONb. In addition to these hydrogen bonds, further interactions contribute to the stability of these P5-CsPONb adducts, including electrostatic contacts between Cs counterions and electron-rich atoms in the intermediate (highlighted in Figure 5.9), two hydrogen bonds between the $–CH_3$ groups in the isopropoxy of moiety and an $O_{terminal}$ atom (present in all complexes except P5-Osp^3), and a hydrogen bond between the P-CH_3 group and an $O_{terminal}$ atom in P5-Osp^3. The rank in terms of overall stability of these complexes is P5-Osp^2 > P5-F > P5-Osp^3 > P5-C.

In all of the structures except for P5-C, the F atom is in an axial position. On the other hand, the former O-sp^2 atom is never axial. These two atoms likely represent the two extrema in the scale of apicophilicity of all the groups bound to the central phosphorus atom examined in this work, which is useful in selecting the lowest-energy path when investigating reaction at the $O_{terminal}$ atom, to which we now turn our attention, and in calculations with explicit crystallization water molecules that we present below.

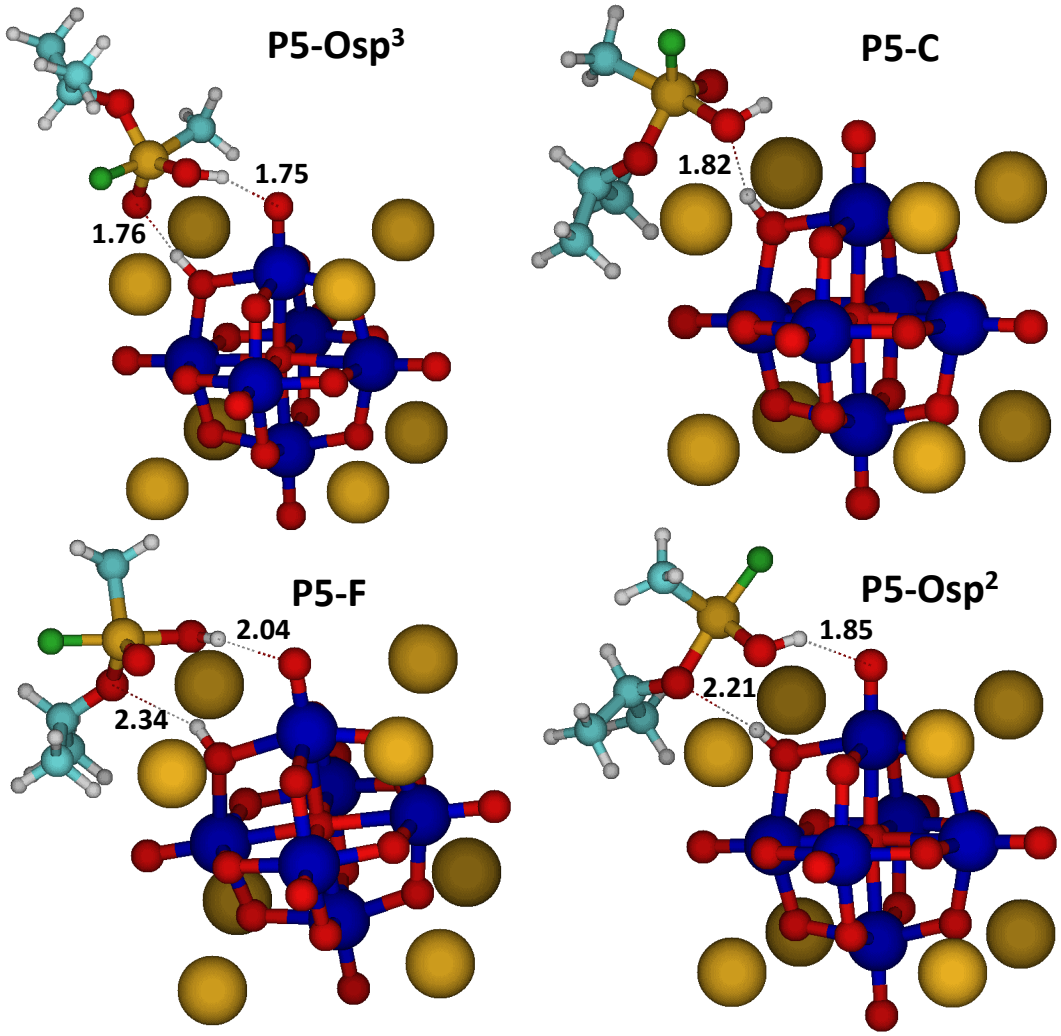

Figure 5.8. Pentacoordinated intermediates generated in the hydrolysis of GB by $Cs_8Nb_6O_{19}$ along the same four pathways as the minima and transition states of Figs. 5.3 and 5.4. Numbers correspond to representative hydrogen bond distances in Angstroms. Same color code as in Fig. 5.1. Reprinted (adapted) with permission from Chapleski, R. C.; Musaev, D. G.; Hill, C. L.; Troya, D. *The Journal of Physical Chemistry C* **2016**, *120*, 16822. Copyright 2016 American Chemical Society.

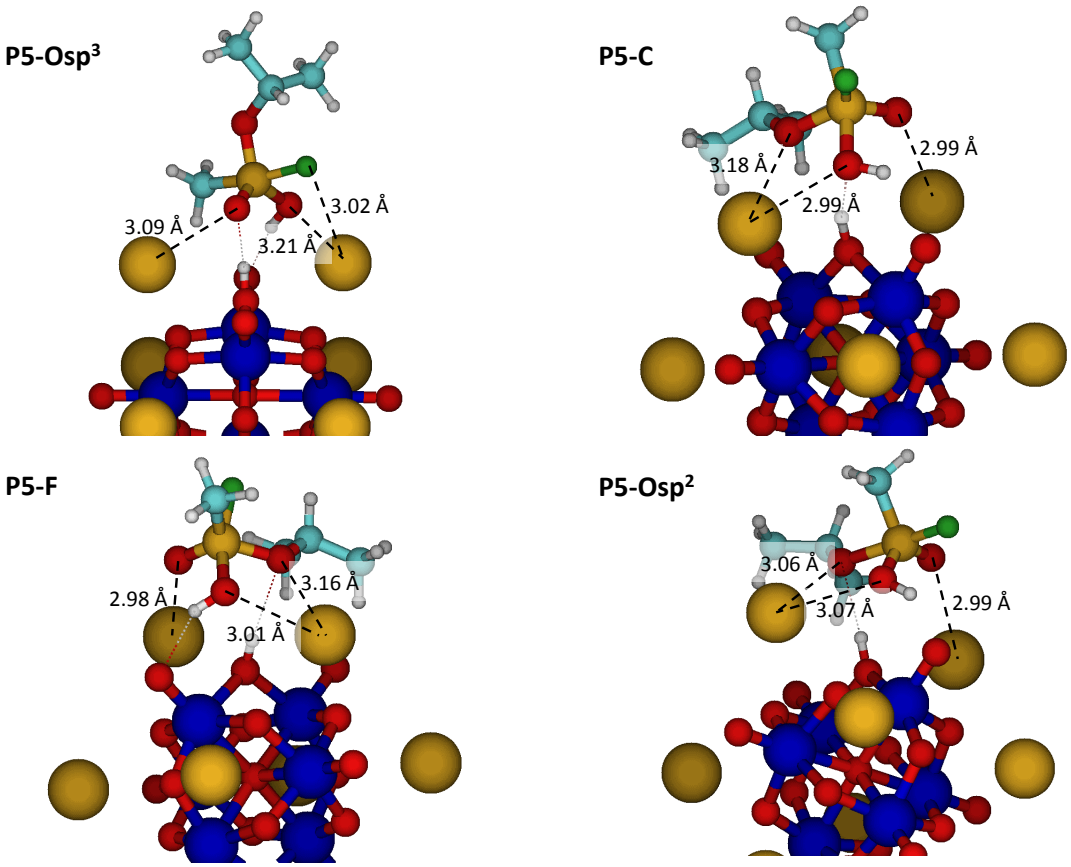

Figure 5.9. Pentacoordinated intermediates in GB hydrolysis by $Cs_8Nb_6O_{19}$ highlighting electrostatic contacts between Cs counterions and electronegative atoms in the nerve agent. Same color code as in Fig. 5.1. Reprinted (adapted) with permission from Chapleski, R. C.; Musaev, D. G.; Hill, C. L.; Troya, D. *The Journal of Physical Chemistry C* **2016**, *120*, 16822. Copyright 2016 American Chemical Society.

5.3.2.5 Reaction at the $O_{terminal}$ Site

The reaction pathways examined until now all involve water dissociation at an $O_{bridging}$ site. This is the most basic site of the CsPONb,[51] and it also participates in the most stable CsPONb-H_2O complex. However, reaction at the $O_{terminal}$ site can also occur. To examine this possibility, we have mapped the likely lowest-energy reaction path departing from the CsPONb-H_2O complex that has a water molecule hydrogen bonding to only the terminal O atom. Using the apicophilicity scale derived from reaction at the bridging site in the prior section, we have assumed that reaction in which the P-F bond of the nerve agent is collinear to the P-OH bond that is forming in the transition state of the rate-determining step is the likely lowest-energy reaction path.

Figure 5.10 presents the potential energy profile of the rate-determining step for reaction at the $O_{terminal}$ site in comparison with the same path at the $O_{bridging}$ site reported above. The energies of the stationary points for reaction at the $O_{terminal}$ site tend to be higher in energy than at the $O_{bridging}$ site. This seems to be a consequence of the more peripheral nature of the $O_{terminal}$ site, which does not allow for as strong interactions between the GB atoms and the CsPONb as the more internal $O_{bridging}$ site. Notwithstanding, the barrier for reaction from the R-F complex is comparable for reaction at both the bridging and terminal sites. The Lindqvist ion has twice as many $O_{bridging}$ sites as $O_{terminal}$ sites, but the similarity of the barriers obtained in this work suggest that hydrolysis of GB with CsPONb might take place at both sites. While we have not studied the energy paths for reactions at the terminal O atom along the other three approaches of GB to the PONb, we expect that the trends for reaction at the $O_{terminal}$ site seen here will likely extend to those other paths.

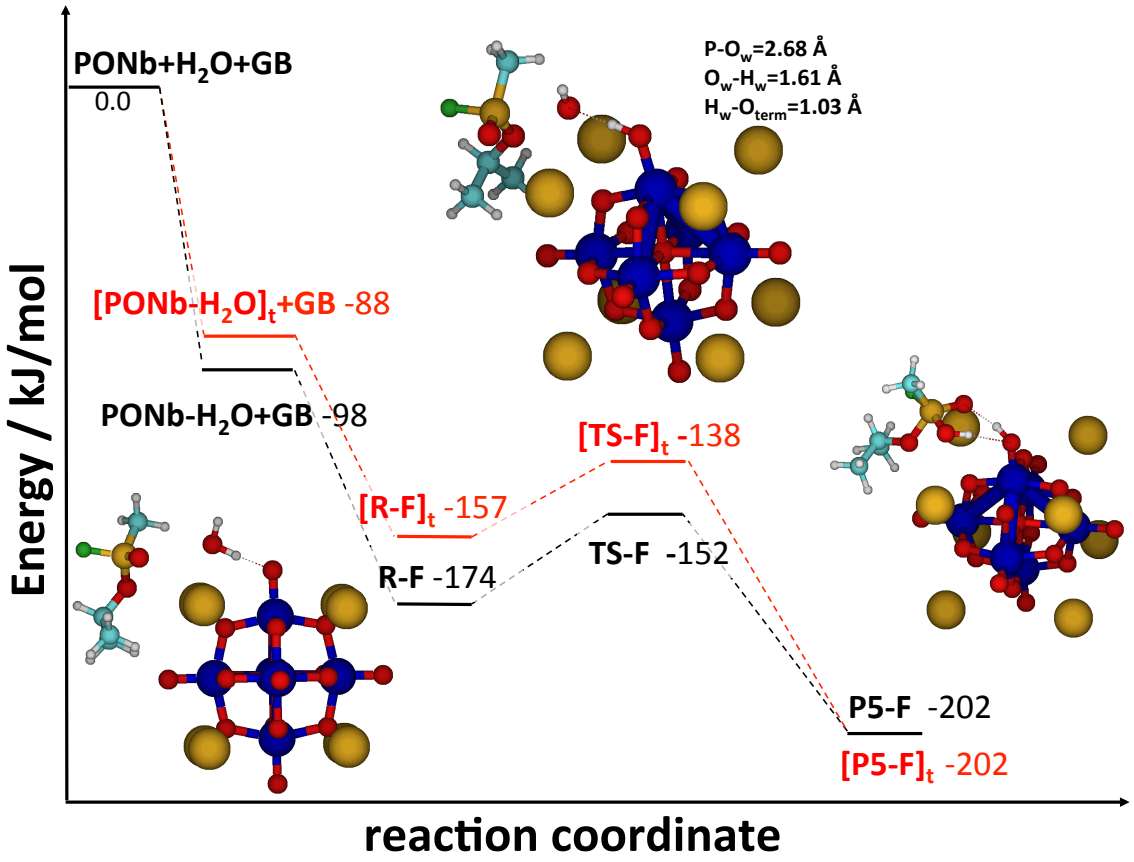

Figure 5.10. Potential-energy profile for the hydrolysis of GB with $Cs_8Nb_6O_{19}$ along the pathways that place the F group of GB in axial position at the transition state. The red trace is for reaction at the $O_{terminal}$ atom of the CsPONb, and the black trace is for reaction at the $O_{bridging}$ atom. See the text for the nomenclature used to label the various stationary points. The insets are for reaction at the $O_{terminal}$ site and use the same color code as Fig. 5.1. Reprinted (adapted) with permission from Chapleski, R. C.; Musaev, D. G.; Hill, C. L.; Troya, D. *The Journal of Physical Chemistry C* **2016**, *120*, 16822. Copyright 2016 American Chemical Society.

5.3.2.6 Pentacoordinated Intermediate Dissociation

Once the pentacoordinated species is formed, reaction will progress along three reaction paths. First, Berry pseudorotation of the trigonal bypiramidal intermediate might occur, as has been reported in bulk hydrolysis calculations of OP compounds using implicit solvent models.[52] In this pseudorotation, groups with the largest apicophilicity are directed to the axial positions. Second, the intermediate might dissociate unimolecularly, without the involvement of the catalyst. Support for this mechanism is also provided by earlier computational studies of the OH^- + GB reaction with implicit solvation, which reported that dissociation of the pentacoordinated

intermediate to generate F atoms occurs over very low barriers and is not rate-limiting.[18,19] This unimolecular dissociation can be competitive with the pseudorotation pathway. While those rapid pseudorotation and autodissociation pathways will likely be present in the pentacoordinated intermediates bound to the CsPONb located in this work, we have examined a third set of pathways that involve the catalyst in order to evaluate the prospect of a fully catalytic process.

There are two major dissociation pathways for the pentacoordinated intermediate: F elimination and isopropoxy elimination. The accompanying products are isopropyl methyl phosphonic acid (IMPA) and methyl phosphonofluoridic acid (MPFA), respectively. In order to obtain full regeneration of the catalyst, the nascent F or isopropoxy groups need to abstract the proton that remains bound to the $O_{bridging}$ site as a consequence of the hydrolysis reaction (see Fig. 5.8). We have therefore attempted to locate transition states that lead either to HF and IMPA or isopropanol (iPOH) and MPFA from the most stable pentacoordinated intermediates.

Transition states have been obtained for the reaction that decomposes P5-F and P5-Osp^2 to iPOH and MPFA. The structures are shown in Figures 5.11 and 5.12, and the energies of these transition states referred to their corresponding pentacoordinated intermediates are 24.9 kJ/mol for TS2-F and 3.1 kJ/mol for TS2-Osp^2. The difference in the barrier seems associated with the fact that the isopropoxy leaving group in TS2-F is initially in an equatorial position in P5-F, and a pseudorotation that places the group in an axial position needs to occur,[52] which carries an energetic penalty.

All attempts to locate a pentacoordinated intermediate in which the F atom is in an axial position and hydrogen bonded to the H-$O_{bridging}$ group directly led to HF + IMPA products adsorbed on the PONb. The potential energy during these failed geometry optimization attempts was steeply downhill, suggesting that P-F dissociation likely occurs through a small barrier or is entirely barrierless. This is consistent with the very small barrier for this dissociation channel found in prior implicit solvation calculations (1.3 kJ/mol).[19]

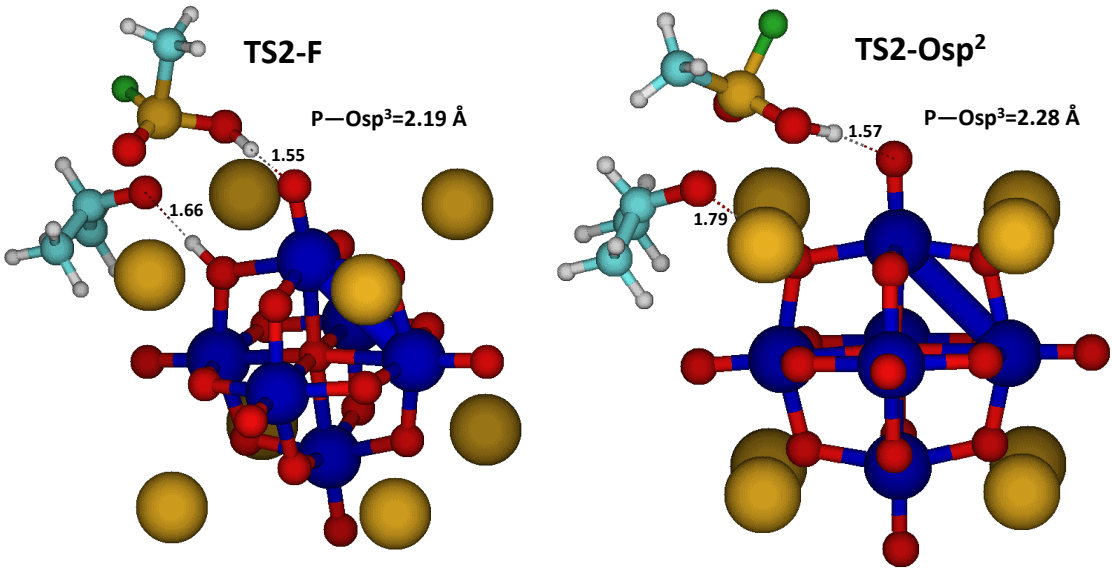

Figure 5.11. Transition states for the decomposition of the P5-F and P5-Osp^2 intermediates generated in the hydrolysis reaction of GB by $Cs_8Nb_6O_{19}$. Values correspond to representative hydrogen-bond distances in Angstroms. Additional distances are available in Figure 5.12. Same color code as in Fig. 5.1. Reprinted (adapted) with permission from Chapleski, R. C.; Musaev, D. G.; Hill, C. L.; Troya, D. *The Journal of Physical Chemistry C* **2016**, *120*, 16822. Copyright 2016 American Chemical Society.

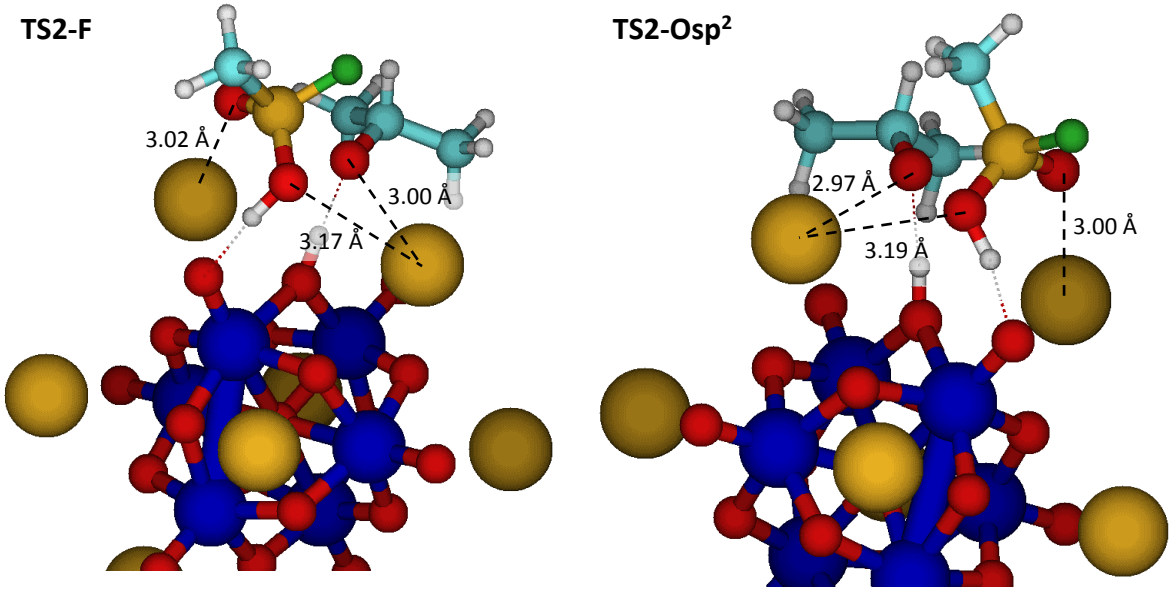

Figure 5.12. Transition states for the decomposition of pentacoordinated intermediates highlighting electrostatic contacts between Cs counterions and electronegative atoms in the hydroxylated nerve agent. Same color code as in Fig. 5.1. Reprinted (adapted) with permission from Chapleski, R. C.; Musaev, D. G.; Hill, C. L.; Troya, D. *The Journal of Physical Chemistry C* **2016**, *120*, 16822. Copyright 2016 American Chemical Society.

The main conclusion of the results presented in this section is that the pentacoordinated species generated in the rate-limiting step of the hydrolysis reaction of GB by CsPONb undergo fast dissociation to HF + IMPA and iPOH + MPFA. This process can take place without the involvement of the catalyst, as shown in prior work, or it can involve the proton transferred from water to an $O_{bridging}$ site of the PONb in the rate-determining step, as revealed in this work. These processes might occur concurrently with the interconversion between pentacoordinated isomers through Berry pseudorotation.

5.3.2.7 Products

The facile dissociation of the P5 species involving the catalyst yields HF and IMPA, or iPOH and MPFA products. All these species are initially bound to the CsPONb, as shown in Figure 5.13. The CsPONb-IMPA-HF complex exhibits an HF molecule forming a hydrogen bond with the $O_{bridging}$ atom that has played a central role in the hydrolysis reaction, and an IMPA molecule hydrogen bonded to an $O_{terminal}$ atom. Additional interactions exist, including close contacts between the Cs ions of the PONb and the electronegative atoms of IMPA (Figure 5.14), and a hydrogen bond between C-H bonds in the isopropoxy group of IMPA and the F atom of the adsorbed HF. The bound products that stem from the P-O dissociation of P5 complexes (CsPONb-MPFA-iPOH) consist of an isopropanol molecule hydrogen bonded to an $O_{terminal}$ atom, and MPFA bound to a neighboring $O_{terminal}$ atom. Following the minimum energy reaction path of the dissociation through TS2-Osp^2 initially leads to isopropanol forming a hydrogen bond with the $O_{bridging}$ atom, much as shown for HF in the CsPONb-IMPA-HF complex. However, repulsion between the adsorbed MPFA and iPOH causes the migration of isopropanol from the $O_{bridging}$ atom to a vicinal $O_{terminal}$ atom, as shown in Figure 5.13. A similar migration was seen in reactions with organosilyl reagents and the Lindqvist complex, $Nb_2W_4O_{19}H^{3-}$.[53]

CsPONb-MPFA-iPOH is the overall lowest-energy structure of all 22 stationary points of the reaction mechanism in Figure 5.2. The high stability of this complex is due in part to the strong hydrogen bonds between the adsorbates and the CsPONb, but also to the additional stabilizing interactions between the Cs counterions and electronegative atoms of the nerve-agent fragments (Fig. 5.14). These interactions are also present in CsPONb-IMPA-HF.

Desorption of HF (66.3 kJ/mol binding energy) and isopropanol (75.5 kJ/mol) generates CsPONb-IMPA and CsPONb-MPFA adducts, respectively. The phosphonic acids are

extraordinarily strongly bound to the PONb, by 251.2 kJ/mol in the case of IMPA, and 262.9 kJ/mol for MPFA. The structure of these tightly bound complexes is also shown in Figure 5.13. Noticeably, even though the protonated phosphonic acids and deprotonated CsPONb separated products are more stable than the corresponding phosphonate + protonated CsPONb products, Fig. 5.13 shows that there is a proton transfer from the phosphonic acids to an $O_{terminal}$ atom of the CsPONb while they are interacting. This proton transfer is already present when HF and isopropanol are still bound to the CsPONb. The reason for the proton transfer seems to be rooted in the ability of the phosphonates to establish stronger interactions with neighboring Cs counterions than if the IMPA and MPFA species are protonated. For deprotonated MPFA bound to the protonated CsPONb, aside from the hydrogen bond between the $O_{terminal}$-H group of the CsPONb and one of the oxygen atoms of MPFA, we see various electrostatic contacts between the two oxygen atoms and the fluorine atom in MPFA and neighboring Cs ions (Fig. 5.14). In the case of deprotonated IMPA bound to the protonated CsPONb, the hydrogen bond is also assisted by contacts between the three oxygen atoms and Cs ions and by a hydrogen bond between a $-CH_3$ group in the isopropoxy moiety and an $O_{terminal}$ atom. The large binding energies between the phosphonate products obtained in this work and the catalyst imply that full regeneration of the catalyst as modeled in this work will likely require the supply of thermal energy.

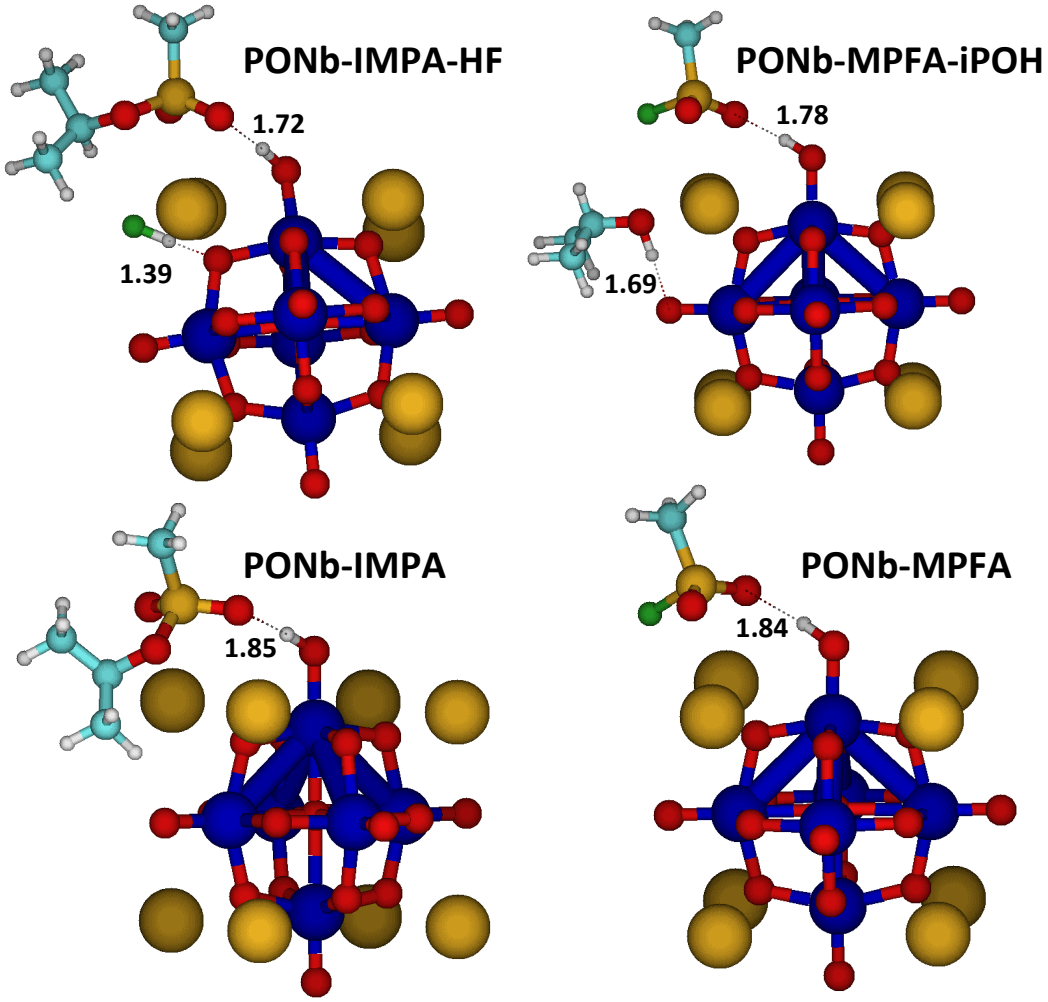

Figure 5.13. Bound products in the hydrolysis reaction of GB with $Cs_8Nb_6O_{19}$. Numbers correspond to representative hydrogen-bond distances in Angstroms. Same color code as in Fig. 5.1. Reprinted (adapted) with permission from Chapleski, R. C.; Musaev, D. G.; Hill, C. L.; Troya, D. *The Journal of Physical Chemistry C* **2016**, *120*, 16822. Copyright 2016 American Chemical Society.

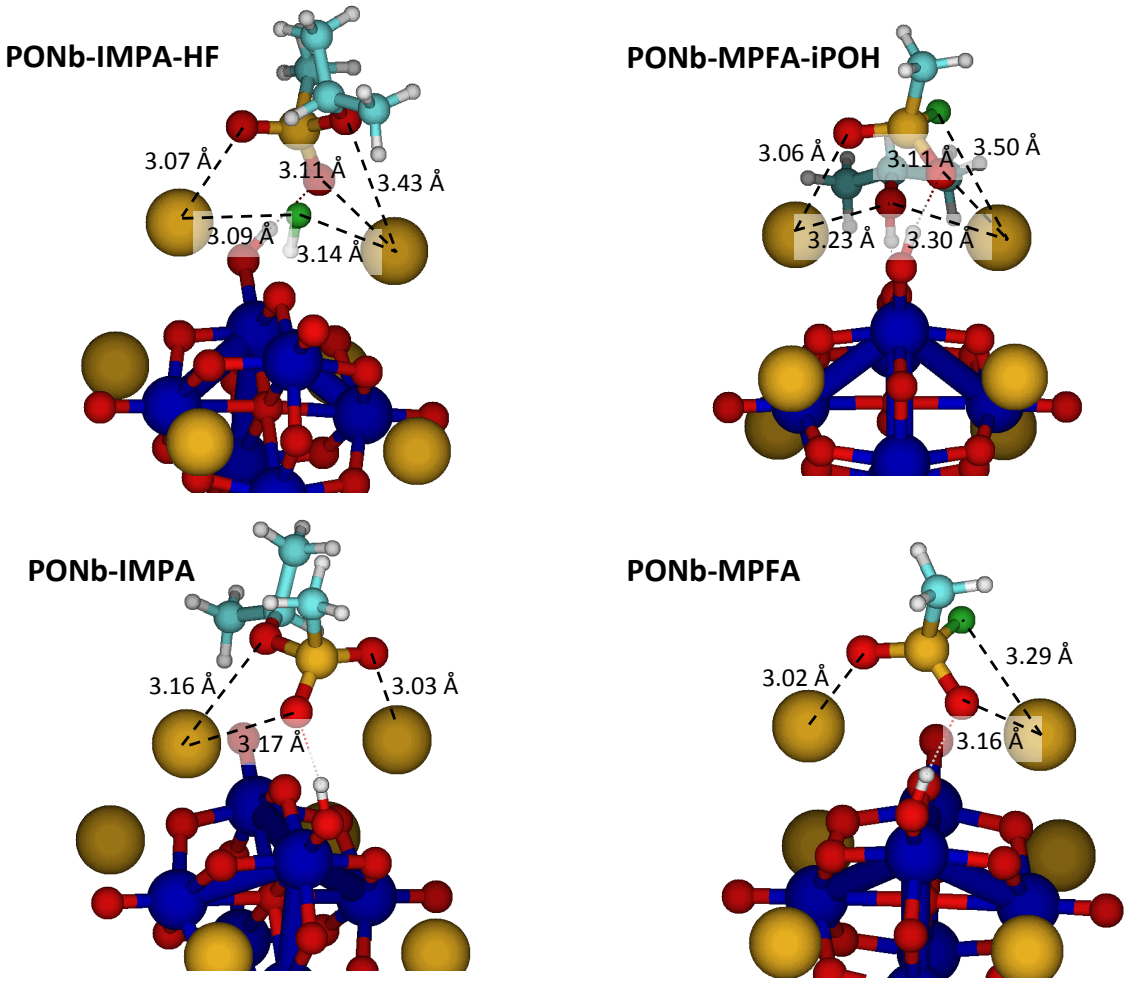

Figure 5.14. Products of GB hydrolysis by $Cs_8Nb_6O_{19}$ bound to the catalyst highlighting electrostatic contacts between Cs counterions and electronegative atoms in the nerve agent hydrolysis product. Same color code as in Fig. 5.1. Reprinted (adapted) with permission from Chapleski, R. C.; Musaev, D. G.; Hill, C. L.; Troya, D. *The Journal of Physical Chemistry C* **2016**, *120*, 16822. Copyright 2016 American Chemical Society.

5.3.3 The Effect of Explicit Solvation

All calculations presented so far consider that the catalyst is a dry hexaniobate. However, even in solid form, CsPONb contains crystallization water molecules.[42] To investigate the effect of hydration on the mechanism of nerve-agent hydrolysis, we have conducted calculations for the minimum-energy reaction path with a CsPONb hydrated with 14 water molecules, which are treated explicitly at the same level of theory as the calculations reported above.

The starting catalyst structure in the calculations was taken from the x-ray diffraction data of the $Cs_8Nb_6O_{19}$•$14H_2O$ salt described in the experiment.[42] After full geometry

optimization, we note that all 14 water molecules are forming hydrogen bonds with O atoms in the niobate, and also solvating the Cs ions. Hydration has a slight effect on the structure of the hexaniobate core, which no longer possesses octahedral point-group symmetry. The average Nb-$O_{central}$ and Nb-$O_{bridging}$ atoms are 0.015 and 0.020 Å shorter than in the dry CsPONb, and the average Nb-$O_{terminal}$ distance is 0.026 Å longer. The most notable difference between the hydrated and dry CsPONb structure is in the average Cs-$O_{bridging}$ nearest-neighbor distance, which increases by 0.232 Å in the hydrated catalyst. It therefore seems that the main effect of crystallization water in the catalyst is to screen the interactions between the Cs counterions and the hexaniobate core.

Figure 5.15 shows the potential energy surface for the "F" pathway with the hydrated CsPONb in comparison with the results for the same pathway presented in Figure 5.2 for the dry catalyst. The potential profile in Fig. 5.15 shows that explicit inclusion of crystallization waters does not affect the reaction mechanism of nerve agent hydrolysis, and suggests that the water molecules that are not undergoing dissociation seem to have an attending or spectator role in the mechanism. The attending water molecules do, however, noticeably affect the energetics of the reaction, and intermediates and transition states are all shifted up in energy compared to those in the dry catalyst. This energy offset appears to be a consequence of the screening effect of the interactions between the CsPONb and the H_2O and GB reagents by the non-reactive water molecules. For instance, the binding of the H_2O molecule that dissociates during reaction is 20 kJ/mol less exothermic in the hydrated CsPONb than in the dry one. Likewise, GB binds 21 kJ/mol less tightly on the hydrated CsPONb than to the dry one. After both H_2O and GB are bound, the rate-limiting step has a barrier of 31 kJ/mol, which is slightly higher than with the dry CsPONb (23 kJ/mol), but still lower than the activation energy measured experimentally for bulk hydrolysis with hydroxide ions (41 kJ/mol).

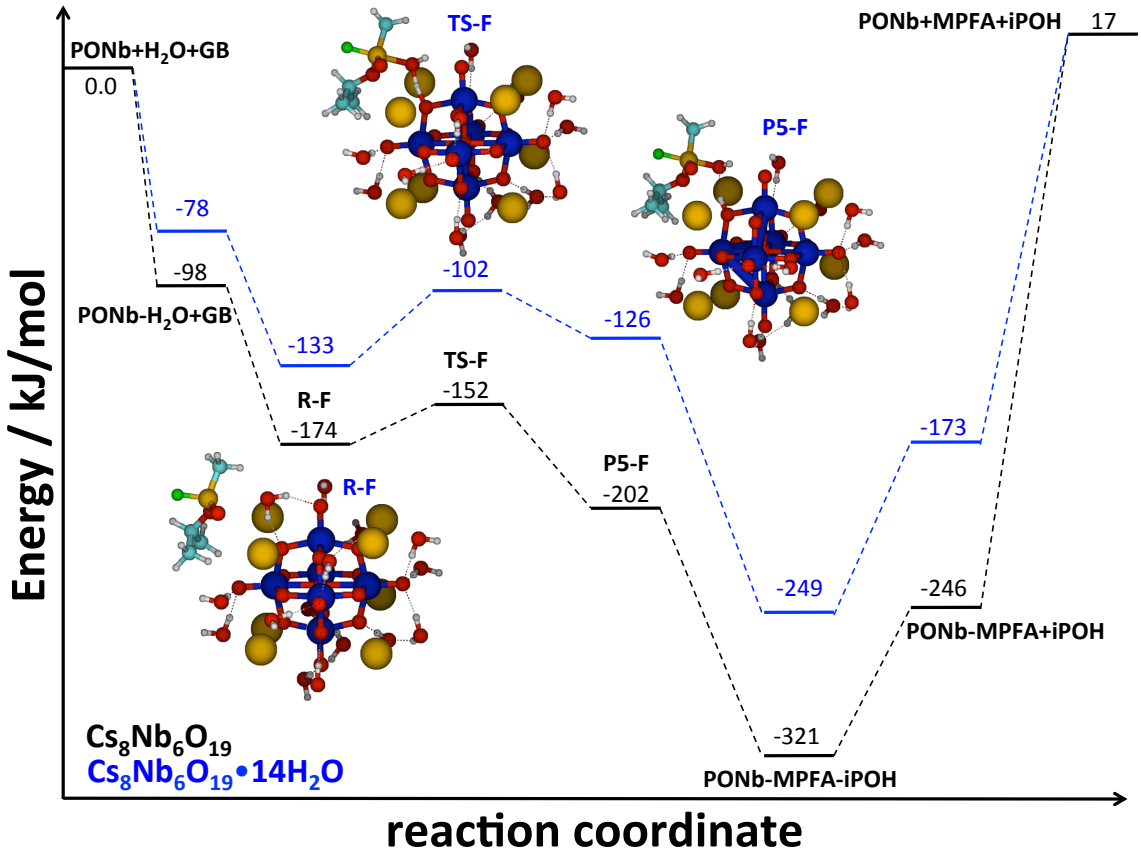

Figure 5.15. Potential-energy profile for the hydrolysis of GB with $Cs_8Nb_6O_{19}$ (black trace) and $Cs_8Nb_6O_{19}$•$14H_2O$ (blue trace) along the minimum-energy reaction path. See the text for the nomenclature used to label the various stationary points. The insets are for reaction $Cs_8Nb_6O_{19}$•$14H_2O$ and use the same color code as Fig. 5.1. Reprinted (adapted) with permission from Chapleski, R. C.; Musaev, D. G.; Hill, C. L.; Troya, D. *The Journal of Physical Chemistry C* **2016**, *120*, 16822. Copyright 2016 American Chemical Society.

Beyond the transition state, we note that the rest of stationary points in the hydrated system are about 75 kJ/mol less stable than in the dry catalysts. Notwithstanding, the desorption of the phosphonic acid generated during reaction (MPFA in Fig. 5.15) from the catalyst still requires a significant amount of energy (190 kJ/mol), suggesting the likely need for thermal treatment to regenerate the catalyst.

5.4 Concluding Remarks

This work presents the potential energy profile for the decomposition of GB by a hexaniobate catalyst whose reactivity has been recently proven experimentally. The early steps of the reaction mechanism involve the adsorption of water and the nerve agent on the $Cs_8Nb_6O_{19}$

catalyst. Both molecules bind to the catalyst through a variety of intermolecular interactions that include hydrogen bonds and electrostatic interactions involving the Cs counterions. Once the reagents are bound, the ensuing rate-determining step is a concerted dissociation of the adsorbed water molecule on a basic oxygen atom of the catalyst and nucleophilic addition of the nascent OH group to the nerve agent. The location of transition states for this concerted process in this work confirms a recent proposal from SAXS measurements and provides fundamental insight into the general base hydrolysis mechanism of nerve agents on solid-state catalysts. The calculated transition-state energies for reaction with the $Cs_8Nb_6O_{19}$ catalyst are well below the fully separated reagents' asymptote. Even if none of the energy released in the formation of the CsPONb-H_2O-GB complexes can be utilized to surmount the barrier, some of the barriers for reaction from these complexes are sufficiently small that thermal reaction can occur rapidly at room temperature. Remarkably, some of the calculated reaction barriers are notably smaller than the activation energy determined experimentally in bulk hydrolysis of GB, which encourages further study of hexaniobate catalysts for base hydrolysis of nerve agents.

The rate-determining step results in pentacoordinated intermediates that undergo rapid subsequent dissociation. This dissociation might occur without participation of the catalyst, as has been reported in earlier studies, or with involvement of the catalyst as calculated here; both processes possess very low barriers. The products of the pentacoordinated intermediate decomposition assisted by the catalyst are either HF+IMPA or iPOH+MPFA. These products are strongly bound to the catalyst through hydrogen bonds and electrostatic interactions with the Cs counterions, suggesting that full catalyst regeneration might entail thermal treatment.

Inclusion of crystallization water molecules in the calculations does not alter the steps of the reaction mechanism, but does influence the energy of the stationary points. The attending water molecules act to screen the interactions amongst the Cs counterions, the hexaniobate core, and all species bound to the catalyst, which results in an upward shift of the stationary point energies with respect to the dry catalyst.

While the results presented in this manuscript support recent experimental findings, a more quantitative connection between the calculations and the experiment is not possible at this time. From the experimental perspective, neither the activation energy nor the characterization of intermediates is available. From the calculations point of view, the energies have been obtained with a moderate basis set due to the system size, and will necessarily show some deviation from

experiment. In addition, the energies seem highly dependent on the level of hydration of the catalyst, which might challenge a quantitative comparison between theory and experiment.

Finally, the discovery in this work of the prominent role played by the Cs ions in stabilizing many of the adsorbed species on the catalyst will warrant additional studies that target the effect of other monovalent counterions of the PONb on the potential energy surface. In conjunction to the seminal mechanistic work presented here, that work will aim to design optimum solid-state catalysts for decontamination of nerve agents.

5.5 Acknowledgments

This material is based upon work supported by the U. S. Army Research Laboratory and the U. S. Army Research Office under grant number W911NF-15-2-0107. The authors are grateful for support of the Defense Threat Reduction Agency. The authors wish to thank May Nyman for providing cif files with the crystal structure of the CsPONb used in this work. The authors acknowledge Advanced Research Computing at Virginia Tech for providing computational resources and technical support that have contributed to the results reported within this paper.

5.6 References

(1) Kim, K.; Tsay, O. G.; Atwood, D. A.; Churchill, D. G. *Chemical Reviews* **2011**, *111*, 5345.

(2) Jang, Y. J.; Kim, K.; Tsay, O. G.; Atwood, D. A.; Churchill, D. G. *Chemical Reviews* **2015**, *115*, PR1.

(3) Yang, Y. C.; Baker, J. A.; Ward, J. R. *Chemical Reviews* **1992**, *92*, 1729.

(4) Bandosz, T. J.; Laskoski, M.; Mahle, J.; Mogilevsky, G.; Peterson, G. W.; Rossin, J. A.; Wagner, G. W. *The Journal of Physical Chemistry C* **2012**, *116*, 11606.

(5) Yang, S.-W.; Doetschman, D. C.; Schulte, J. T.; Sambur, J. B.; Kanyi, C. W.; Fox, J. D.; Kowenje, C. O.; Jones, B. R.; Sherma, N. D. *Microporous and Mesoporous Materials* **2006**, *92*, 56.

(6) Bromberg, L.; Schreuder-Gibson, H.; Creasy, W. R.; McGarvey, D. J.; Fry, R. A.; Hatton, T. A. *Industrial & Engineering Chemistry Research* **2009**, *48*, 1650.

(7) Kinnan, M. K.; Creasy, W. R.; Fullmer, L. B.; Schreuder-Gibson, H. L.; Nyman, M. *European Journal of Inorganic Chemistry* **2014**, *2014*, 2361.

(8) Guo, W.; Lv, H.; Sullivan, K. P.; Gordon, W. O.; Balboa, A.; Wagner, G. W.; Musaev, D. G.; Bacsa, J.; Hill, C. L. *Angewandte Chemie International Edition* **2016**, *55*, 7403.

(9) DeCoste, J. B.; Peterson, G. W. *Chemical Reviews* **2014**, *114*, 5695.

(10) Moon, S.-Y.; Wagner, G. W.; Mondloch, J. E.; Peterson, G. W.; DeCoste, J. B.; Hupp, J. T.; Farha, O. K. *Inorganic Chemistry* **2015**, *54*, 10829.

(11) Liu, Y.; Moon, S.-Y.; Hupp, J. T.; Farha, O. K. *ACS Nano* **2015**, *9*, 12358.

(12) Mondloch, J. E.; Katz, M. J.; Isley Iii, W. C.; Ghosh, P.; Liao, P.; Bury, W.; Wagner, G. W.; Hall, M. G.; DeCoste, J. B.; Peterson, G. W.; Snurr, R. Q.; Cramer, C. J.; Hupp, J. T.; Farha, O. K. *Nat Mater* **2015**, *14*, 512.

(13) Katz, M. J.; Mondloch, J. E.; Totten, R. K.; Park, J. K.; Nguyen, S. T.; Farha, O. K.; Hupp, J. T. *Angewandte Chemie International Edition* **2014**, *53*, 497.

(14) Song, J.; Luo, Z.; Britt, D. K.; Furukawa, H.; Yaghi, O. M.; Hardcastle, K. I.; Hill, C. L. *Journal of the American Chemical Society* **2011**, *133*, 16839.

(15) Ma, F.-J.; Liu, S.-X.; Sun, C.-Y.; Liang, D.-D.; Ren, G.-J.; Wei, F.; Chen, Y.-G.; Su, Z.-M. *Journal of the American Chemical Society* **2011**, *133*, 4178.

(16) Rando, R. R. *Accounts of Chemical Research* **1975**, *8*, 281.

(17) Zheng, F.; Zhan, C.-G.; Ornstein, R. L. *Journal of the Chemical Society, Perkin Transactions 2* **2001**, 2355.

(18) Dyguda-Kazimierowicz, E.; Sokalski, W. A.; Leszczynski, J. *The Journal of Physical Chemistry B* **2008**, *112*, 9982.

(19) Šečkutė, J.; Menke, J. L.; Emnett, R. J.; Patterson, E. V.; Cramer, C. J. *The Journal of Organic Chemistry* **2005**, *70*, 8649.

(20) Poblet, J. M.; Lopez, X.; Bo, C. *Chemical Society Reviews* **2003**, *32*, 297.

(21) Miró, P.; Poblet, J. M.; Ávalos, J. B.; Bo, C. *Canadian Journal of Chemistry* **2009**, *87*, 1296.

(22) Bo, C.; Poblet, J. M. *Israel Journal of Chemistry* **2011**, *51*, 228.

(23) López, X.; Miró, P.; Carbó, J. J.; Rodríguez-Fortea, A.; Bo, C.; Poblet, J. M. *Theoretical Chemistry Accounts* **2011**, *128*, 393.

(24) Lopez, X.; Carbo, J. J.; Bo, C.; Poblet, J. M. *Chemical Society Reviews* **2012**, *41*, 7537.

(25) Matt, B.; Xiang, X.; Kaledin, A. L.; Han, N. N.; Moussa, J.; Amouri, H.; Alves, S.; Hill, C. L.; Lian, T. Q.; Musaev, D. G.; Izzet, G.; Proust, A. *Chem. Sci.* **2013**, *4*, 1737.

(26) Kuznetsov, A. E.; Geletii, Y. V.; Hill, C. L.; Morokuma, K.; Musaev, D. G. *J. Am. Chem. Soc.* **2009**, *131*, 6844.

(27) Hill, C. L.; Prosser-McCartha, C. M. *Coordination Chemistry Reviews* **1995**, *143*, 407.

(28) Cronin, L.; Muller, A. *Chem. Soc. Rev.* **2012**, *41*, 7333.

(29) Long, D.-L.; Tsunashima, R.; Cronin, L. *Angewandte Chemie International Edition* **2010**, *49*, 1736.

(30) Long, D.-L.; Tsunashima, R.; Cronin, L. *Angew. Chem.* **2010**, *122*, 1780.

(31) Borrás-Almenar, J. J.; Coronado, E.; Müller, A.; Pope, M. *Polyoxometalate Molecular Science. Proceedings of the NATO Advanced Study Institute, Tenerife, Spain from 25 August to 4 September 2001*; Kluwer Academic Publishers: Dordrecht, 2003; Vol. 98.

(32) Hill, C. L. *Chem. Rev.* **1998**, *98*, 1.

(33) Pope, M. T.; Müller, A. *Angew. Chem.* **1991**, *103*, 56.

(34) Pope, M. T.; Müller, A. *Angew. Chem., Int. Ed. Engl.* **1991**, *30*, 34.

(35) Hill, C. L. *J. Mol. Catal. A: Chem.* **2007**, *262*, 2.

(36) Neumann, R. In *Progress in Inorganic Chemistry*; John Wiley & Sons, Inc.: 2007, p 317.

(37) Nyman, M. *Dalton Trans.* **2011**, *40*, 8049.
(38) Bridgeman, A. J.; Cavigliasso, G. *Inorg. Chem.* **2002**, *41*, 1761.
(39) Black, J. R.; Nyman, M.; Casey, W. H. *J. Am. Chem. Soc.* **2006**, *128*, 14712.
(40) Kaledin, A. L.; van Duin, A. C. T.; Hill, C. L.; Musaev, D. G. *J. Phys. Chem. A* **2013**, *117*, 6967.
(41) Anderson, T. M.; Rodriguez, M. A.; Bonhomme, F.; Bixler, J. N.; Alama, T. M.; Nyman, M. *Dalton Trans.* **2007**, 4517.
(42) Nyman, M.; Alam, T. M.; Bonhomme, F.; Rodriguez, M. A.; Frazer, C. S.; Welk, M. E. *J. Cluster Sci.* **2006**, *17*, 197.
(43) Antonio, M. R.; Nyman, M.; Anderson, T. M. *Angew. Chem., Int. Ed.* **2009**, *48*, 6136.
(44) Fullmer, L. B.; Molina, P. I.; Antonio, M. R.; Nyman, M. *Dalton Trans.* **2014**, *43*, 15295.
(45) Frisch, M. J.; Trucks, G. W.; Schlegel, H. B.; Scuseria, G. E.; Robb, M. A.; Cheeseman, J. R.; Scalmani, G.; Barone, V.; Mennucci, B.; Petersson, G. A.; Nakatsuji, H.; Caricato, M.; Li, X.; Hratchian, H. P.; Izmaylov, A. F.; Bloino, J.; Zheng, G.; Sonnenberg, J. L.; Hada, M.; Ehara, M.; Toyota, K.; Fukuda, R.; Hasegawa, J.; Ishida, M.; Nakajima, T.; Honda, Y.; Kitao, O.; Nakai, H.; Vreven, T.; Montgomery Jr., J. A.; Peralta, J. E.; Ogliaro, F. ß.; Bearpark, M. J.; Heyd, J.; Brothers, E. N.; Kudin, K. N.; Staroverov, V. N.; Kobayashi, R.; Normand, J.; Raghavachari, K.; Rendell, A. P.; Burant, J. C.; Iyengar, S. S.; Tomasi, J.; Cossi, M.; Rega, N.; Millam, N. J.; Klene, M.; Knox, J. E.; Cross, J. B.; Bakken, V.; Adamo, C.; Jaramillo, J.; Gomperts, R.; Stratmann, R. E.; Yazyev, O.; Austin, A. J.; Cammi, R.; Pomelli, C.; Ochterski, J. W.; Martin, R. L.; Morokuma, K.; Zakrzewski, V. G.; Voth, G. A.; Salvador, P.; Dannenberg, J. J.; Dapprich, S.; Daniels, A. D.; Farkas, O.; Foresman, J. B.; Ortiz, J. V.; Cioslowski, J.; Fox, D. J.; Gaussian, Inc.: Wallingford, CT, USA, 2009.
(46) Zhao, Y.; Truhlar, D. G. *J. Chem. Phys.* **2006**, *125*, 194101.
(47) Alam, T. M.; Nyman, M.; Cherry, B. R.; Segall, J. M.; Lybarger, L. E. *J. Am. Chem. Soc.* **2004**, *126*, 5610.
(48) Benschop, H. P.; De Jong, L. P. A. *Acc. Chem. Res.* **1988**, *21*, 368.
(49) Buono, G.; Llinas, J. R. *Journal of the American Chemical Society* **1981**, *103*, 4532.
(50) Gustafson, R. L.; Martell, A. E. *J. Am. Chem. Soc.* **1962**, *84*, 2309.
(51) Balogh, E.; Anderson, T. M.; Rustad, J. R.; Nyman, M.; Casey, W. H. *Inorganic Chemistry* **2007**, *46*, 7032.
(52) Daniel, K. A.; Kopff, L. A.; Patterson, E. V. *Journal of Physical Organic Chemistry* **2008**, *21*, 321.
(53) Day, V. W.; Klemperer, W. G.; Schwartz, C. *J. Am. Chem. Soc.* **1987**, *109*, 6030.

Chapter 6

Hydrolysis of the Nerve-agent Simulant Dimethyl methylphosphonate as Catalyzed by $Cs_8Nb_6O_{19}$

Abstract

By working with compounds similar in structure and properties but lower toxicity, experimentalists are able to learn about the fundamental aspects of nerve-agent reactions without risking their health and safety. One such compound is dimethyl methylphosphonate, a simulant for the organophosphorus nerve agent Sarin. Here, we follow the reaction pathway for the decomposition of the simulant dimethyl methylphosphonate (DMMP) by the Lindqvist polyoxoniobate, $Cs_8Nb_6O_{19}$. Though DMMP follows a similar reaction pathway as Sarin, we find that the rate-limiting barrier is about twice as high. Following a discussion of the reaction pathway, we examine the changes that occur in the structure and atomic charges within the polyoxoniobate during reaction with DMMP, and relate these changes to experimental x-ray spectroscopy results. Finally, we compare theoretical Raman spectra with experiment, revealing that the polyoxoniobate becomes protonated in DMMP exposure experiments.

6.1 Introduction

In this chapter, we examine the base-catalyzed hydrolysis of dimethyl methylphosphonate (DMMP) by $Cs_8Nb_6O_{19}$. DMMP serves as a common precursor in the production of chemical weapons[1] as well as a flame retardant.[2] Due to its low toxicity (oral LD_{50} > 6810 mg/kg in mice) and similar structure, DMMP is an army-approved mimic of the highly toxic nerve agent Sarin (oral LD_{50} = 0.67 mg/kg in rats[3]) and other organophosphorus nerve agents.[4] Thus, for the sake of safety, several experimental groups have used DMMP to gain insight into the behavior of nerve agents such as Sarin.

Figure 6.1 shows the optimized structure of the lowest-energy rotamer of DMMP along with that of the more toxic *(S)* enantiomer of Sarin. Notably, both compounds exhibit a tetrahedral phosphorus atom bound to an sp^2-hybridized oxygen atom (Osp^2) as well as a methyl group. At least one sp^3 oxygen atom (Osp^3) is also bound in both compounds; however, in Sarin,

this atom is part of an isopropoxy moiety, and in DMMP, there are two bound methoxy groups. Also, instead of a second sp^3 oxygen atom, Sarin showcases a bound fluorine atom.

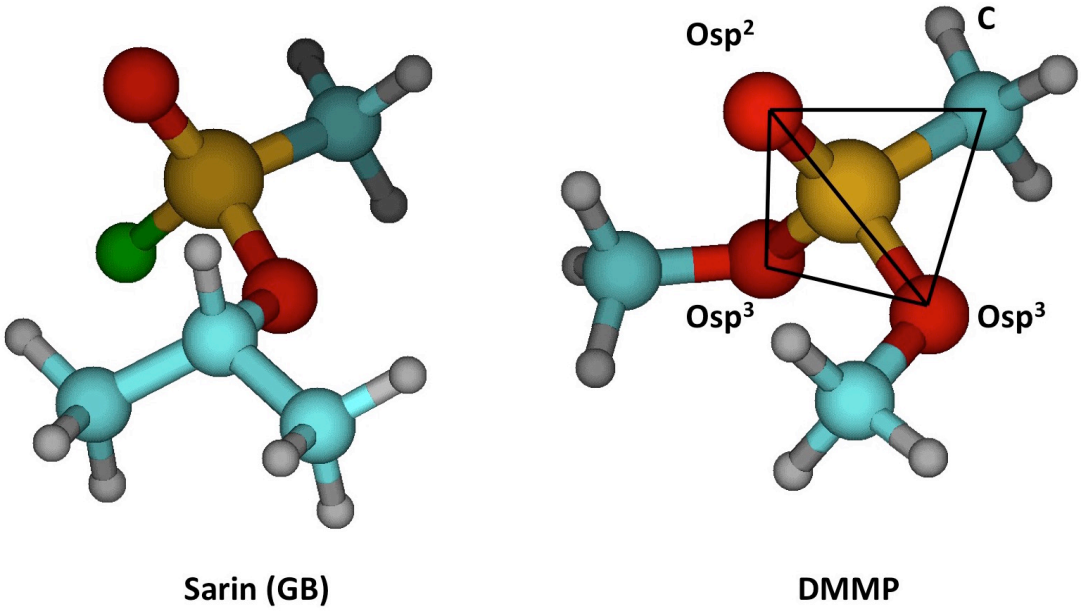

Figure 6.1. Lowest-energy structures of *(S)*-Sarin (left) and dimethyl methylphosphonate (DMMP, right). For DMMP, black lines indicate the edges of a tetrahedron with phosphorus at its center. Color scheme: P: gold, O: red, F: green, C: cyan, H: gray.

Due to similarities in their chemical structures, the base catalyzed hydrolysis of DMMP by $Cs_8Nb_6O_{19}$ (PONb) is very similar to that of Sarin, described previously.[5] For both the agent and the mimic, the reaction mechanism begins with the adsorption of water to a basic site on the polyoxoniobate core. Subsequent adsorption of DMMP yields a bound-reagent complex, which follows through a rate-limiting transition state to a pentacoordinated phosphorus intermediate. This intermediate then readily dissociates into phosphonic acid and methanol products, which are strongly bound to the PONb. The large binding energies suggest a stoichiometric reaction with PONb instead of a catalytic one. The potential energy diagram of this reaction for DMMP hydrolysis is shown in Figure 6.2. Following a brief description of methods, each of these steps along the reaction pathway will be discussed in detail.

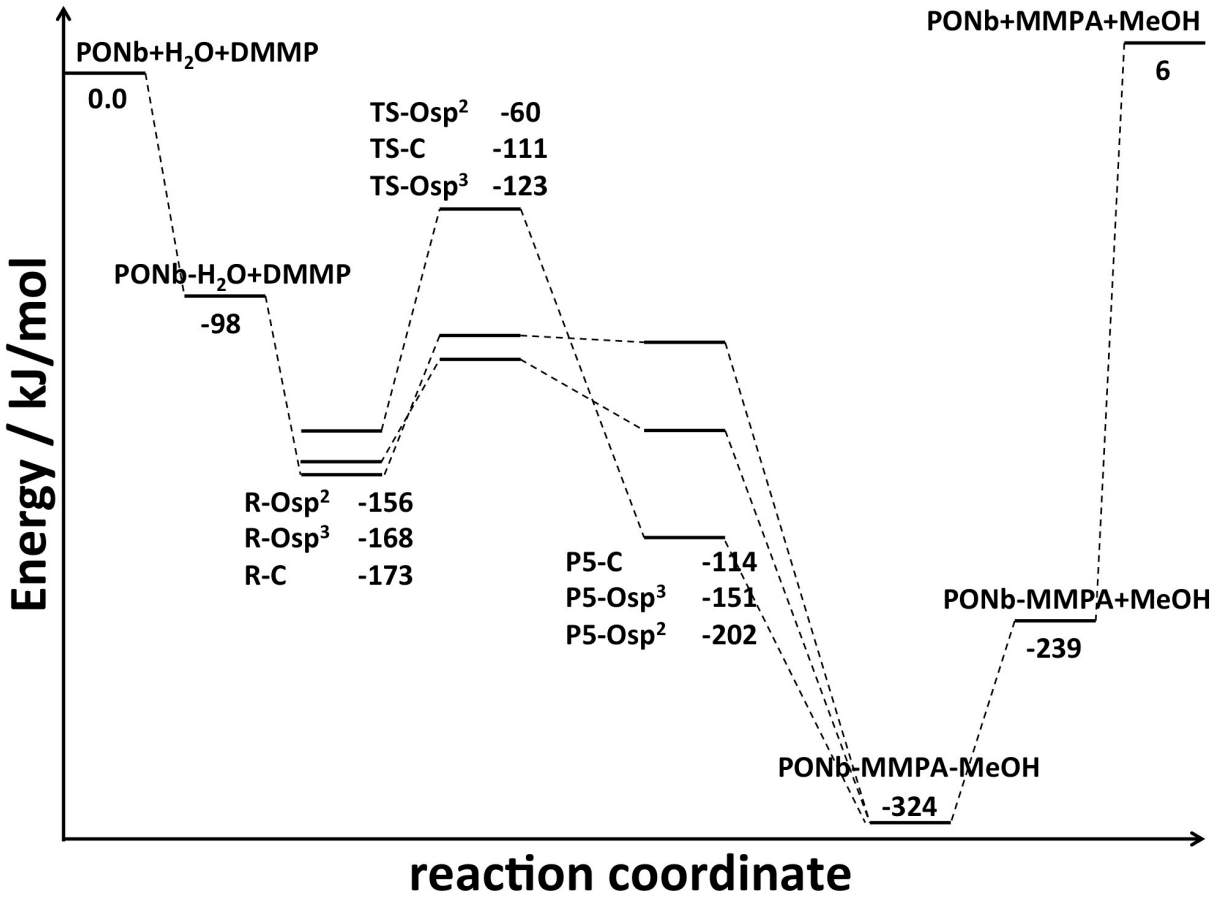

Figure 6.2. Potential-energy profile for the hydrolysis of DMMP with a $Cs_8Nb_6O_{19}$ catalyst. See the text for the nomenclature used to label the various stationary points.

6.2 Computational Details

Calculations were carried out using the Gaussian 09 suite of software.[6] All stationary point structures along the pathway of DMMP hydrolysis by PONb were optimized with the M06-L density functional as well as the 6-31G(d,p) basis set for nonmetal atoms and the Lanl2dz basis set and pseudopotentials for metal atoms. Frequency calculations were performed at this level as well, following optimization, and were used to verify stationary points and obtain zero-point energies. To improve accuracy, energies of all optimized structures were refined by M06-L/6-31++G(d,p)–Lanl2dz stationary-point calculations. To facilitate convergence of both wavefunction and geometry, an ultrafine integration grid was applied to all calculations.

6.3 Results

6.3.1 Reaction Pathways

6.3.1.1 Adsorption of Water to the PONb

In an identical first step along the catalytic hydrolysis pathway to that of Sarin, the reaction of DMMP with PONb begins with the adsorption of water to the catalyst. We examined two possible water-adsorption motifs, subsequently allowing for hydrolysis at two different basic oxygen sites on the PONb core: the most basic bridging oxygen atom (O_b) and the terminal oxygen (O_{te}). Adsorption leading to reaction at an O_b site exhibits bidentate binding of water through the donation of two hydrogen bonds from water, one each to accepting O_b and O_{te} atoms on the niobate core. The left panel of Figure 6.3 shows the optimized geometry of this PONb-H_2O complex, along with intermolecular hydrogen bonding H_{water}-O distances, given in Angstroms. Aside from the interactions shown in the figure, the adsorbed water molecule is stabilized by two nearby Cs counterions, with Cs-O_{water} distances of 3.33 Å for both interactions. Water binds to PONb in this orientation with an adsorption energy of 98.3 kJ/mol.

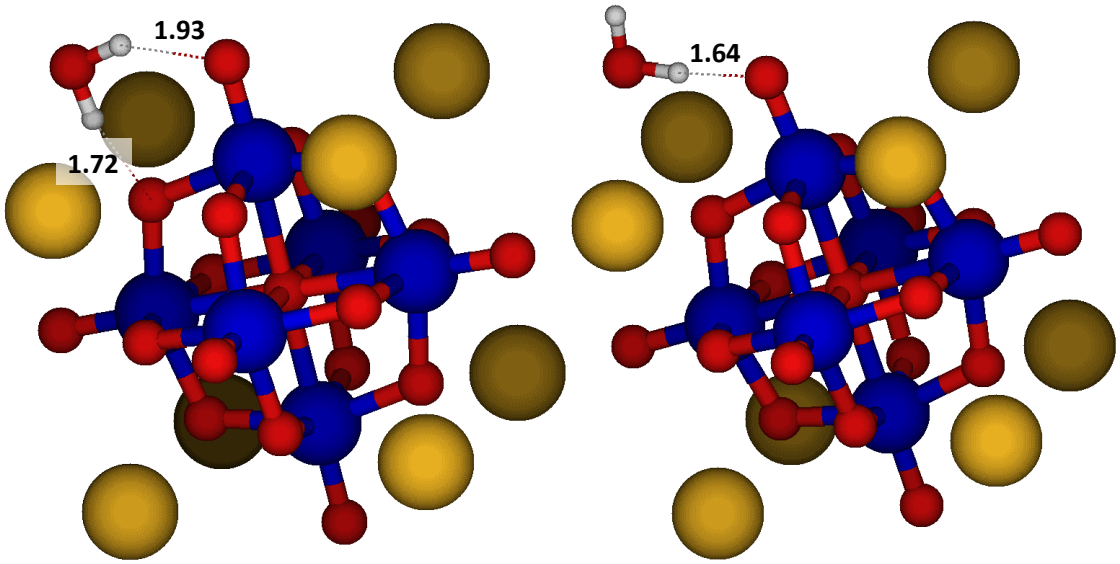

Figure 6.3. Two possible modes of water binding to the PONb. Key hydrogen bonding distances are given in Angstroms. Same color scheme as in Figure 6.1, along with Nb: blue, Cs: gold. Reprinted with permission from Chapleski, R. C.; Musaev, D. G.; Hill, C. L.; Troya, D. *The Journal of Physical Chemistry C* **2016**, *120*, 16822. Copyright 2016 American Chemical Society.

Alternatively, water may bind in a monodentate fashion leading to hydrolysis at an O_{te} site. The structure of this binding orientation is shown in the right panel of Figure 6.3, exhibiting

donation of a single hydrogen bond from water to an O_{te} atom on PONb. Aside from this H_{water}-O_{te} interaction, water adsorption is stabilized by interaction of the water molecule with two neighboring Cs counterions (the Cs-O_{water} distance for the interaction with both neighboring counterions is 3.42 Å), as in the bidentate case. As a consequence of fewer hydrogen bonding interactions, this complex has a water adsorption energy of 88.4 kJ/mol. Thus, our focus for following the DMMP hydrolysis pathway will continue with that for the reaction at an O_b site on PONb, and the reaction pathway shown in Figure 6.2 includes only this pathway, beginning with the bidentate adsorption of water. Our discussion will return to reaction at an O_{te} site, only after a full treatment of the reaction beginning with the stronger water-adsorption motif.

6.3.1.2 Formation of the PONb-H_2O-DMMP Complex

Reaction at an O_b atom in PONb continues with the adsorption of DMMP to the PONb-H_2O complex via intermolecular interactions between DMMP and H_2O, the $[Nb_6O_{19}]$ core of PONb, as well as the Cs counterions. As we will discuss further, during the rate-limiting step of catalytic hydrolysis, the adsorbed water molecule donates a proton to the basic O_b site on PONb, and the remaining OH from the water molecule adds nucleophilically to the phosphorus atom on DMMP, forming a P-OH bond. Considering DMMP as a tetrahedron with phosphorus at its center and the Osp^2, both Osp^3, and the methyl C atoms as its vertices (Figure 6.1), three unique faces are available for approach and attack by the nascent OH. For the remainder of this discussion, these approaches will be demarcated by the atom bound to the central phosphorus whose bond is collinear with the forming P-OH bond. For example, along the $–Osp^2$ pathway, OH approach is perpendicular to the face of the tetrahedron with one C and two Osp^3 vertices, and leads to a P-OH bond that is collinear with the existing P-Osp^2 bond.

As there are three unique approaches of the nascent hydroxyl moiety, there are three orientations with which DMMP can adsorb onto the PONb-H_2O complex, leading to three unique PONb-H_2O-DMMP reagent (R) complexes. All three of these isomers are shown in Figure 6.4. Due to differences in intermolecular interactions with the PONb core and Cs counterions, these three R complexes vary in their stability. R-C, with the highest DMMP binding energy (74.8 kJ/mol), exhibits an interaction between a hydrogen atom in a methoxy moiety and the oxygen atom in the bound water molecule, and another between a hydrogen atom in the other methoxy moiety and a nearby O_{te} atom. These interactions and their characteristic distances, in Angstroms, are shown in the figure. Additionally, interactions between DMMP and

Cs counterions stabilize adsorption. For instance, the Osp^2 atom and an Osp^3 atom interact with the same Cs counterion with Cs-O distances of 3.32 and 3.18 Å, respectively.

R-Osp^3, with a weaker DMMP binding energy of 69.7 kJ/mol, also exhibits interactions between a methoxy hydrogen atom and an O_{te} neighboring the adsorption site of water, and between DMMP and the oxygen atom in water. Here, the latter interaction is formed with a hydrogen atom in the methyl group, as opposed to one in a methoxy group for R-C. Most likely contributing to weaker DMMP binding, however, is the decreased contribution of DMMP-Cs counterion interactions. For R-Osp^3, there is only one said interaction, involving the Osp^2 atom (Cs-Osp^2 distance: 3.18 Å).

R-Osp^2, like R-C, shows two electrostatic interactions between DMMP and the Cs counterions. These involve the two Osp^3 atoms interacting with the same counterion (Cs-Osp^3 distances: 3.12 and 3.25 Å). Further, hydrogen atoms in the methoxy groups to which the Osp^3 atoms belong donate hydrogen bonds to the O_{te} to which water is bound as well as a neighboring O_{te}, as shown in Figure 6.4. Finally, as with R-Osp^3, a hydrogen atom in the methyl group interacts with the oxygen atom in the bound water molecule. Although the greatest number of interactions are present between DMMP and PONb-H_2O for R-Osp^2, this complex shows the weakest adsorption of DMMP (57.4 kJ/mol). This may be attributed to the fact that the water molecule becomes displaced from the O_b-Nb-O_{te} plane in order to accommodate these interactions. Here, the Nb-O_{te}-O_{water}-O_b dihedral angle involving the relevant atoms nearest the water molecule is -12°, whereas the same angle is 3° in R-C and -2° in R-Osp^2. This same angle in the absence of DMMP is 0°.

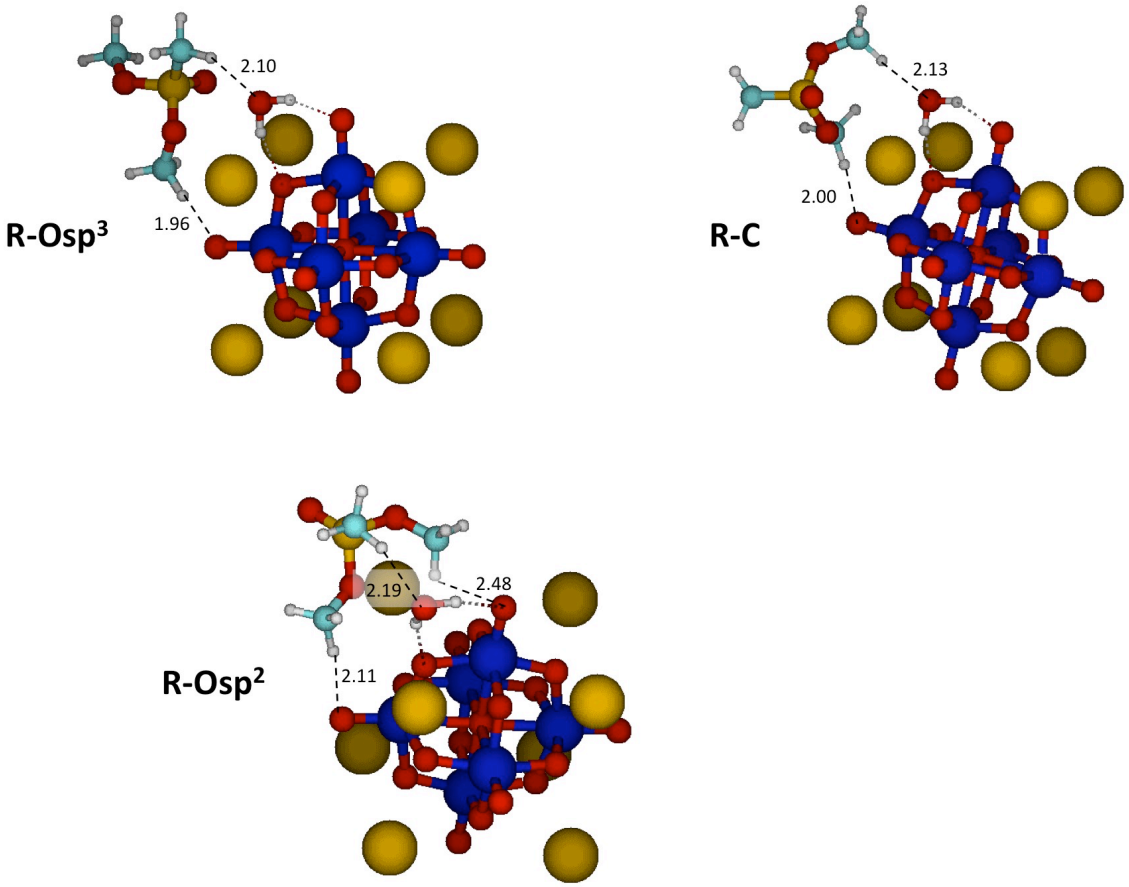

Figure 6.4. PONb-H_2O-DMMP complexes in which each face of the tetrahedron at which hydrolysis will occur in DMMP is interacting with PONb. Hydrogen bonding interactions are shown between DMMP and the PONb-H_2O complexes, with distances given in Angstroms. Same color scheme as in Figure 6.3.

6.3.1.3 DMMP Adsorption in the Absence of Water

In the catalytic hydrolysis of DMMP by PONb, reaction is initiated by the activation of a bound PONb-H_2O-DMMP complex. However, with a binding energy of 108.0 kJ/mol, or twice that found for the experimental adsorption of DMMP to amorphous silica (54.5 kJ/mol),[7] DMMP adsorbs much more strongly to PONb in the absence of a bound water molecule. Figure 6.5 shows the lowest energy configuration resulting from the adsorption of DMMP onto PONb. The interactions leading to this complex are very similar to those for R-C, with one methoxy hydrogen interacting with an O_{te} and two Cs-O interactions (Cs-Osp^2 distance: 3.21 Å, Cs-Osp^3 distance: 3.34 Å). However, instead of hydrogen bond donation from the other methoxy group to the oxygen atom in water, this interaction is donated to an O_b. This difference in acceptor

contributes to the high binding energy of DMMP to the water-absent PONb relative to that to the PONb-H_2O complex. Mulliken population analysis reveals that the oxygen atom in the water molecule of the PONb-H_2O complex has a charge of -0.79 e—much less basic than an O_b atom in the octahedral PONb (Mulliken charge: -1.14 e).

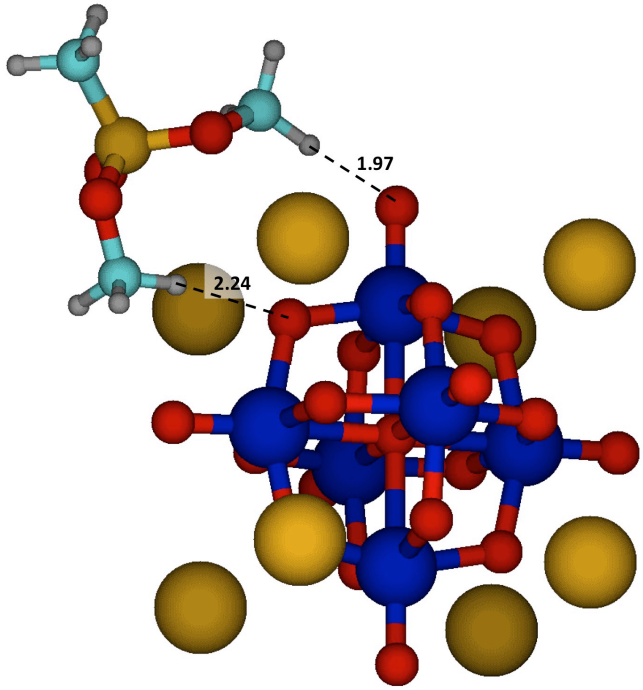

Figure 6.5. Lowest-energy conformation of DMMP binding to $Cs_8Nb_6O_{19}$. Hydrogen-bond distances are given in Angstroms. Same color scheme as in Figure 6.3.

Although DMMP adsorption is much stronger to PONb than to the PONb-H_2O complex, we importantly note that a water molecule is integral to catalytic hydrolysis of DMMP. This water moiety is the source of the nucleophilic OH which adds to the phosphorus atom in, and eventually leads to the degradation of, DMMP. Additionally, X-ray crystallography data show that, even in dry powder form, PONb has 14 H_2O molecules associated with each PONb core.[8] Thus, the likelihood of a PONb site for DMMP adsorption not mediated by water is low. Considering this, we return our discussion to the catalytic hydrolysis pathway, which includes an adsorbed water molecule.

6.3.1.4 Hydrolysis Transition State

Following adsorption of DMMP to the PONb-H_2O complex, reaction proceeds through a transition state in which the water molecule protonates the O_b atom to which it formerly donated

a hydrogen bond. In the same step, the hydroxide moiety that remains of the water molecule adds nucleophilically to the phosphorus atom in DMMP. Figure 6.6 shows the structures of the transition states resulting from the three R complexes, along with key interatomic distances.

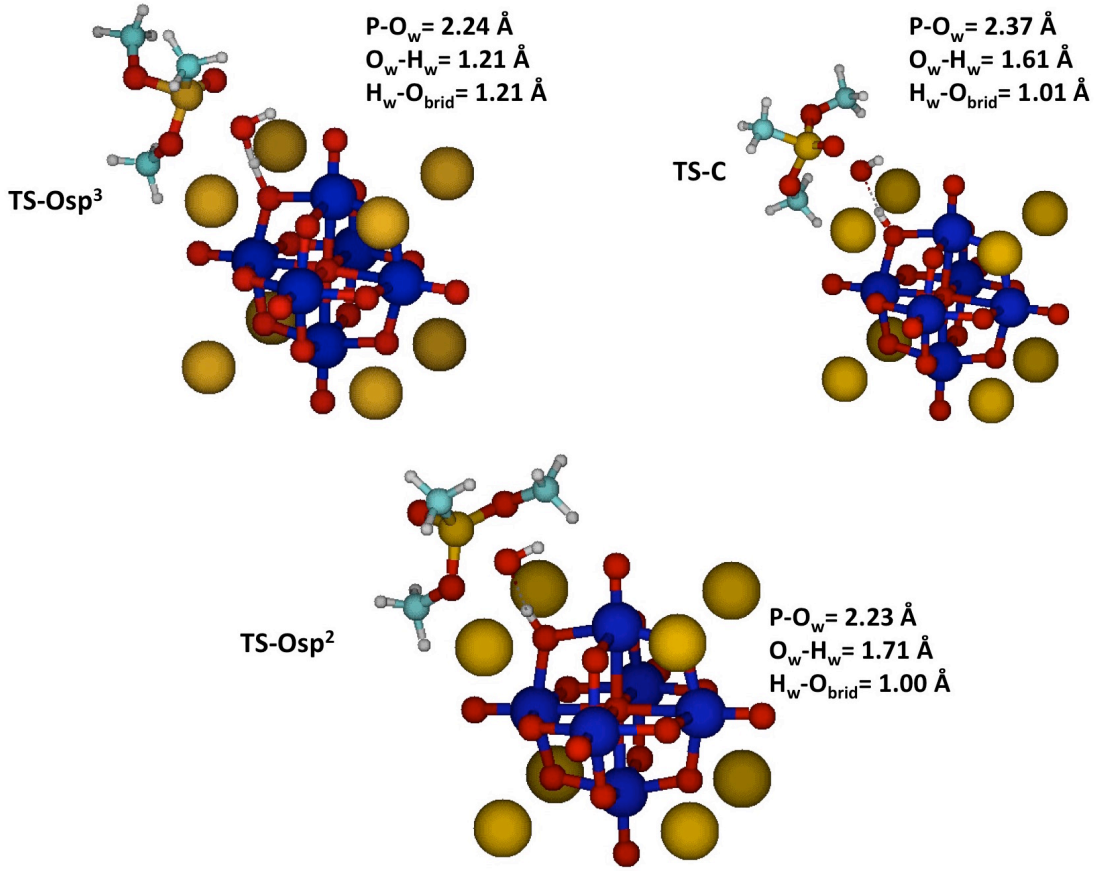

Figure 6.6. Transition state structures for the rate-limiting step of the hydrolysis of DMMP by $Cs_8Nb_6O_{19}$. Same color scheme as in Fig. 6.3.

In an effort to further examine the geometric changes that are taking place around the transition state, we have plotted in Figure 6.7 the three interatomic distances given in Figure 6.6 as a function of reaction coordinate along the minimum energy path around the transition state. In each panel in Figure 6.7, a reaction coordinate of zero reflects the transition state, negative values reflect geometries towards reagent complexes, and positive values reflect geometries towards pentacoordinated intermediate complexes. In Figure 6.7 (red), we can track protonation as the distance increases between the proton (H_w) donated from the water molecule and the oxygen atom in water (O_w). Protonation is also evidenced by a decrease in distance between H_w and O_b (Figure 6.7, green). Within each of the three reaction pathways, the greatest changes in

both these distances occur at the same point along the reaction coordinate. The other process characteristic to our transition state—nucleophilic addition of OH—can be examined in Figure 6.7 (black) as a decrease in distance between the phosphorus atom in DMMP and O_w.

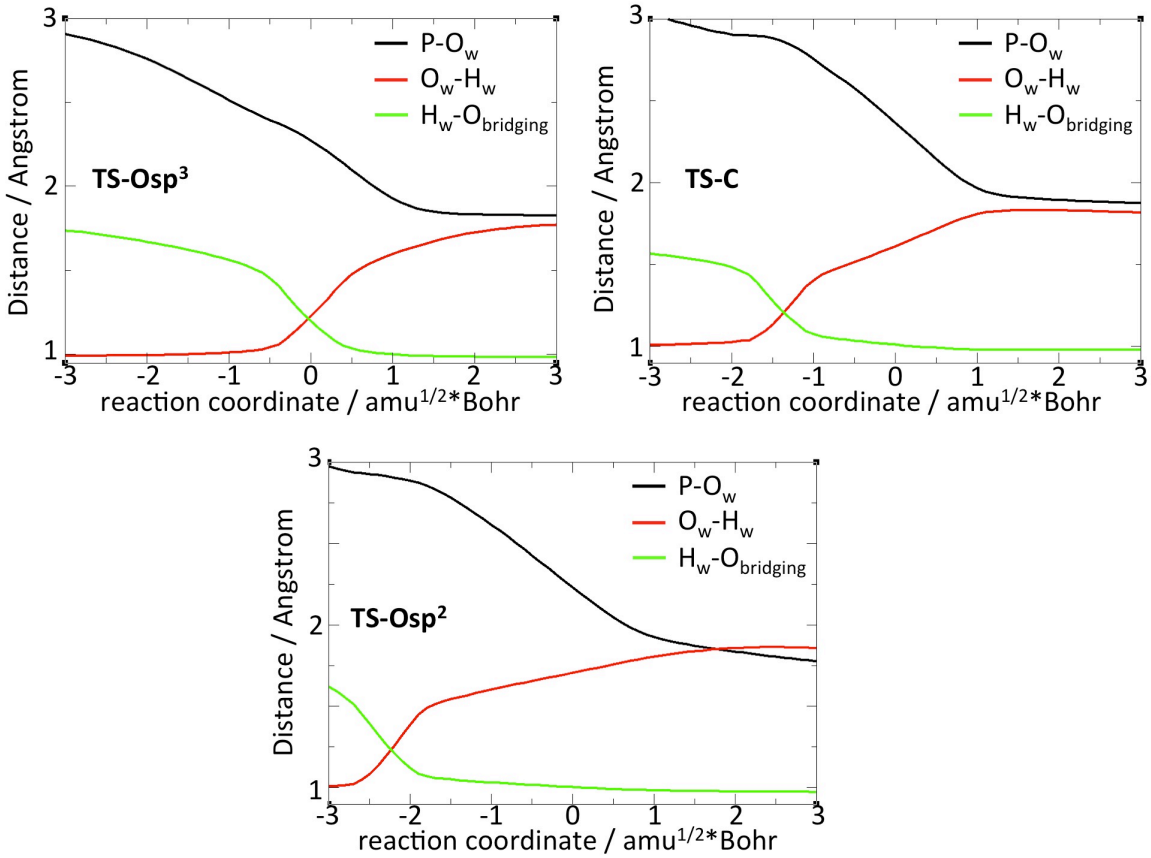

Figure 6.7. Evolution of three key distances around the rate-limiting transition state for the base-catalyzed hydrolysis of DMMP using $Cs_8Nb_6O_{19}$. The transition state occurs at reaction coordinate 0.

Interestingly, as with Sarin hydrolysis, there appears to be a correlation between the barrier energy for each pathway leading from reagents to pentacoordinated intermediates and the synchronicity of protonation with nucleophilic OH addition. For TS-Osp^3, with the lowest energy relative to its respective R-complex (44.6 kJ/mol), protonation occurs near a reaction coordinate of zero, and nucleophilic addition fully occurs before a reaction coordinate of one amu$^{1/2}$*Bohr. The nearness of these two processes along the reaction coordinate suggests that they are well synchronized. On the other hand, TS-C shows less synchronization, with protonation occurring around -1.3 amu$^{1/2}$*Bohr and OH full addition occurring before 1 amu$^{1/2}$*Bohr on the reaction

coordinate scale. This transition state has a higher barrier—62.4 kJ/mol relative to R-C. The trend continues with TS-Osp^2, which has the greatest activation energy (96.1 kJ/mol) and the least synchronicity of protonation and nucleophilic addition. Interestingly, the lowest rate-limiting barrier, that for the –Osp^3 pathway, is about twice as large as the lowest barrier for Sarin hydrolysis by $Cs_8Nb_6O_{19}$ (22.8 kJ/mol).[9] Taking this into consideration, DMMP does not appear to be a great simulant for studies of Sarin hydrolysis.

6.3.1.5 Pentacoordinated Intermediates

Activation of reagent complexes through transition states leads to trigonal bipyramidal pentacoordinated phosphorus intermediates bound to protonated PONb. These three resulting P5 complexes are shown in Figure 6.8. A comparison of the three stationary points reveals some commonalities, such as a protonated bridging oxygen atom, hydrogen bonding between the acidic P-OH hydrogen and O_{te}, and interactions between oxygen atoms in methoxy and hydroxyl groups, as well as Osp^2 atoms, and Cs counterions. An analysis of the differences in interactions between adsorbed pentacoordinated intermediates and the protonated PONb amongst the three P5 species partially accounts for differences in energies of these isomers.

P5-Osp^2 has the lowest energy relative to separated PONb, H_2O, and DMMP reagents (Figure 6.2). This is a result of stabilization by five interactions between Cs counterions and oxygens in the pentacoordinated intermediate: the oxygen atoms in the acidic OH group (Cs-O distance: 3.22 Å), both Osp^3 atoms (3.03 Å and 3.14 Å), and the Osp^2 atom (this atom interacts with two Cs counterions; distances: 3.15 Å and 3.49 Å). The Osp^2 atom, which now carries a full negative charge, also accepts a hydrogen bond from the proton on PONb.

P5-Osp^3 is of second-lowest energy, and exhibits three Cs-O interactions, involving the following oxygen atoms: the acidic OH oxygen (distance: 2.21 Å), an Osp^3 atom (3.15 Å), and the Osp^2 atom (3.00 Å). Further contributing to weaker adsorption in this isomer is the lack of an interaction between the negative Osp^2 and the niobate core of the protonated PONb. Aside from the interaction between the hydrogen in the P-OH group and an O_{te} mentioned above, interactions between the bound intermediate and the protonated niobate core include those between the oxygen in the P-OH group and the transferred proton (O-H distance: 2.23 Å), between an Osp^3 and the same proton, and between a methoxy hydrogen atom and another O_{te}.

Finally, with the highest energy of the bound pentacoordinated intermediate complexes, P5-C also reveals three Cs-O interactions in its structure, between counterions and oxygen atoms

in the acidic P-OH group (Cs-O distance: 3.17 Å), the Osp^2 (3.03 Å), and an Osp^3 (3.48 Å). Also similarly to P5-Osp^3, there is no interaction between the Osp^2 atom and the niobate core. A further decrease in stabilization of this species lies in the fact that there are only a total of two hydrogen bonding interactions between the bound intermediate and the core: the aforementioned acid OH-O_{te} interaction, and one between the acid OH and the proton on the core.

In addition to intermolecular interactions, the orientation of specific functional groups in axial and equatorial positions may contribute to the relative stability of each complex. In both P5-Osp^3 and P5-C, those atoms which form bonds with phosphorus that are collinear to the forming P-OH bond at the transition state (i.e, Osp^3 and C, respectively) remain collinear, in axial positions. Conversely, leading to P5-Osp^2 from the rate-limiting transition state, a Berry pseudorotation occurs such that the Osp^2 atom is no longer in an axial position in P5-Osp^2. In this intermediate, both methoxy groups occupy axial positions. Thus, none of the three pentacoordinated intermediate complexes show the Osp^2 atom in an axial position. This was similarly found for the pentacoordinated intermediates in the hydrolysis of GB by PONb, in which the Osp^2 moiety was identified as least apicophilic of all groups in GB. One or more methoxy groups, on the other hand, occupy axial positions in all P5 structures for DMMP hydrolysis except for P5-C. Thus, it is likely the most apicophilic moiety in DMMP. Further, P5-Osp^2, with the lowest energy of all three pentacoordinated intermediates, has both Osp^3 groups in an axial position, and P5-C, with no axial Osp^3 groups, has the highest energy. Thus, some stability can be attributed to the axial positioning of functional groups in these intermediates.

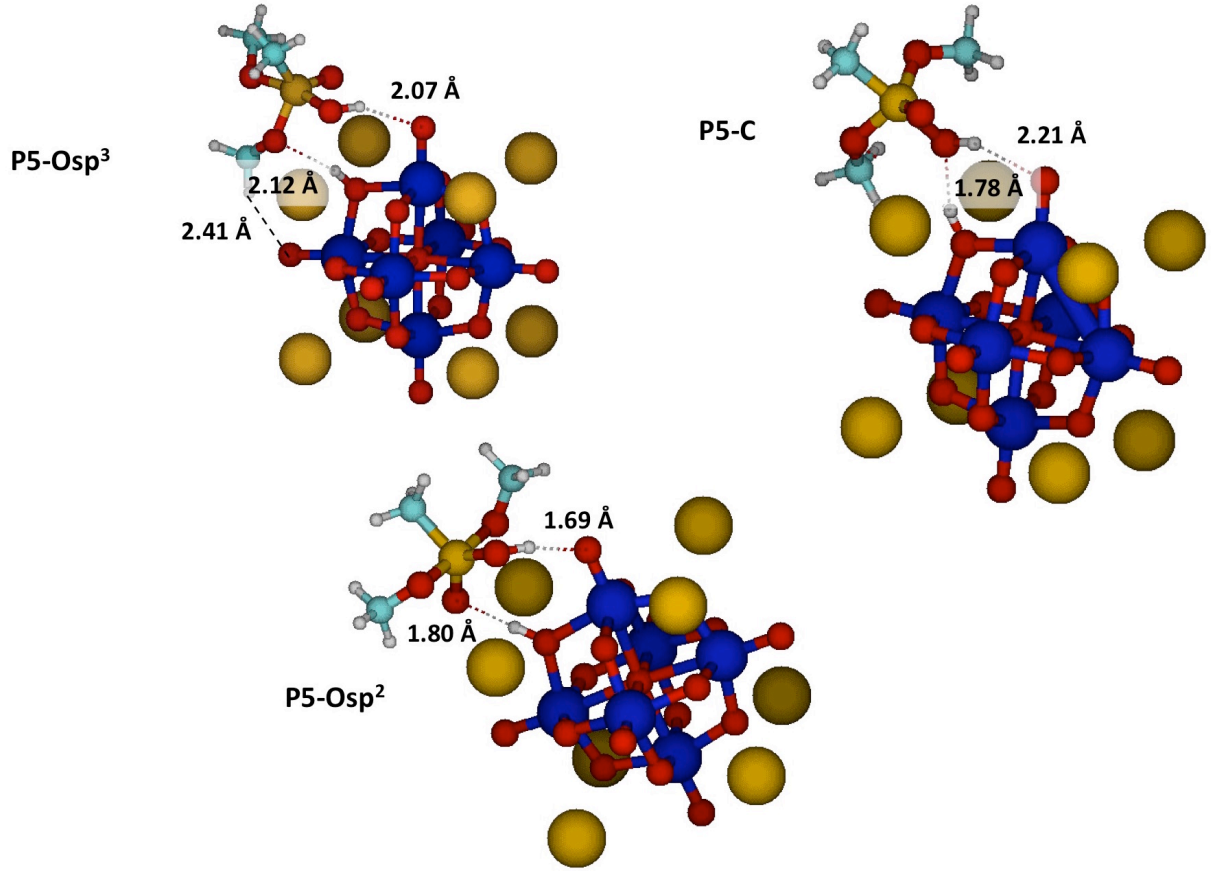

Figure 6.8. Structures of trigonal bipyramidal pentacoordinate intermediates for the hydrolysis of DMMP catalyzed by $Cs_8Nb_6O_{19}$. Values correspond to hydrogen bonding distances. Same color scheme as in Fig. 6.3.

6.3.1.6 Decomposition of the Pentacoordinated Intermediate

Once formed, the pentacoordinated intermediate can undergo one of two changes. An additional Berry pseudorotation can occur, as seen in previous studies,[10,11] or a bond between an Osp^3 atom and the phosphorus atom can break, yielding methanol (MeOH) and methyl methylphosphonic acid (MMPA) products. Bond breakage is more favorable when the $–OCH_3$ group is in an axial position, so this step may be subsequent to Berry pseudorotation that places this group in an axial site.[10] Once in axial position, P-Osp^3 bond dissociation is facilitated by proton transfer to the oxygen atom in the methoxy group, yielding adsorbed methanol instead of an ionic or radical methoxy species. This proton can come from either the acidic P-OH group or the protonated PONb. In the interest of investigating the full catalytic nature of PONb, we have chosen to focus our work on pathways that include proton transfer from the PONb at this step.

Thus, we have tried to locate a transition state that exhibits P-Osp^3 bond breakage in concert proton transfer from the PONb. A converged transition state for methanol formation in this manner was not found, but the estimates from a relaxed scan of the P-Osp^3 bond distance along the reaction pathway with the lowest-energy rate-limiting step indicate a barrier of less than 6 kJ/mol, affirming that this step non-rate-limiting.

6.3.1.7 Adsorbed Products

The dissociation of the pentacoordinated intermediate yields MeOH and MMPA products bound to PONb, as shown in Figure 6.9. This product complex marks the point of lowest energy along the entire reaction pathway. Hydrogen-bonding interactions between bound products and PONb are indicated with interatomic O-H distances in Figure 6.9. Though significant hydrogen bonding does contribute to the strong adsorption of products, electrostatic interactions between Cs counterions and product oxygen atoms continue to play a key role in adsorption. The oxygen atom in methanol interacts with a nearby Cs ion (Cs-O distance: 3.27 Å), and four Cs-O interactions take place with MMPA: one with that oxygen atom participating in hydrogen bonding at a protonated O_{te} (3.24 Å), one with the Osp^3 atom (3.20 Å), and two with the Osp^2 atom (3.21 Å and 3.34 Å).

With fewer intermolecular interactions to PONb, methanol is not as strongly adsorbed to PONb as MMPA. The adsorption energy of methanol to PONb is 85.0 kJ/mol. Desorption of methanol yields a strongly bound MMPA product (Figure 6.9), with a binding energy of 250.5 kJ/mol. The strong binding of this phosphonic acid product to PONb suggests that there is product inhibition of the catalyst. As such, the hydrolysis of DMMP by PONb is stoichiometric in nature, as opposed to catalytic. As shown in Figure 6.9, the binding of MMPA to PONb is accompanied by a proton transfer from the P-OH group to an O_{te} in PONb. This may occur to facilitate Cs-O interactions between MMPA and PONb. We would like to note, however, that transfer of this proton back to MMPA yields lower energy separated products than if the proton remained on the PONb. Thus, we hypothesize that desorption of the MMPA phosphonate, when possible, is accompanied by proton transfer from the PONb.

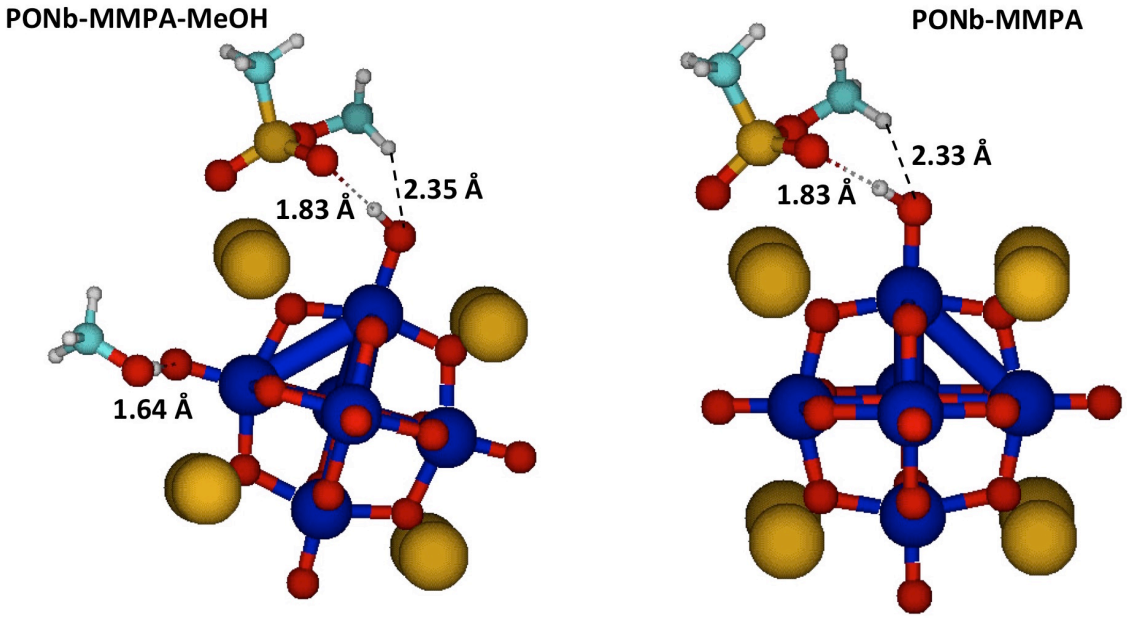

Figure 6.9. Structures of bound products in the hydrolysis of DMMP as catalyzed by $Cs_8Nb_6O_{19}$. Values shown indicate hydrogen bonding distances. Same color scheme as in Fig. 6.3.

6.3.1.8 Reaction at a Terminal Oxygen Site

Having thoroughly discussed catalytic hydrolysis involving reaction at a O_b site in PONb, we would like to briefly return our attention to the possibility for reaction at a O_{te} site. This pathway begins with the monodentate adsorption of water, shown in the right panel of Figure 6.3. From this point, we followed a pathway analogous to that with the lowest rate-limiting barrier in the reaction at O_b. Figure 6.10 shows the energy profile and structures of stationary points for DMMP binding and reacting with a terminal water molecule (red) in comparison to the pathway for reaction at a bidentate-bound water molecule (black). We find that, aside from the decrease in binding energy due to single-hydrogen-bond formation in monodentate water adsorption, the energetics of the reaction at a O_{te} site are very similar to that at a O_b site.

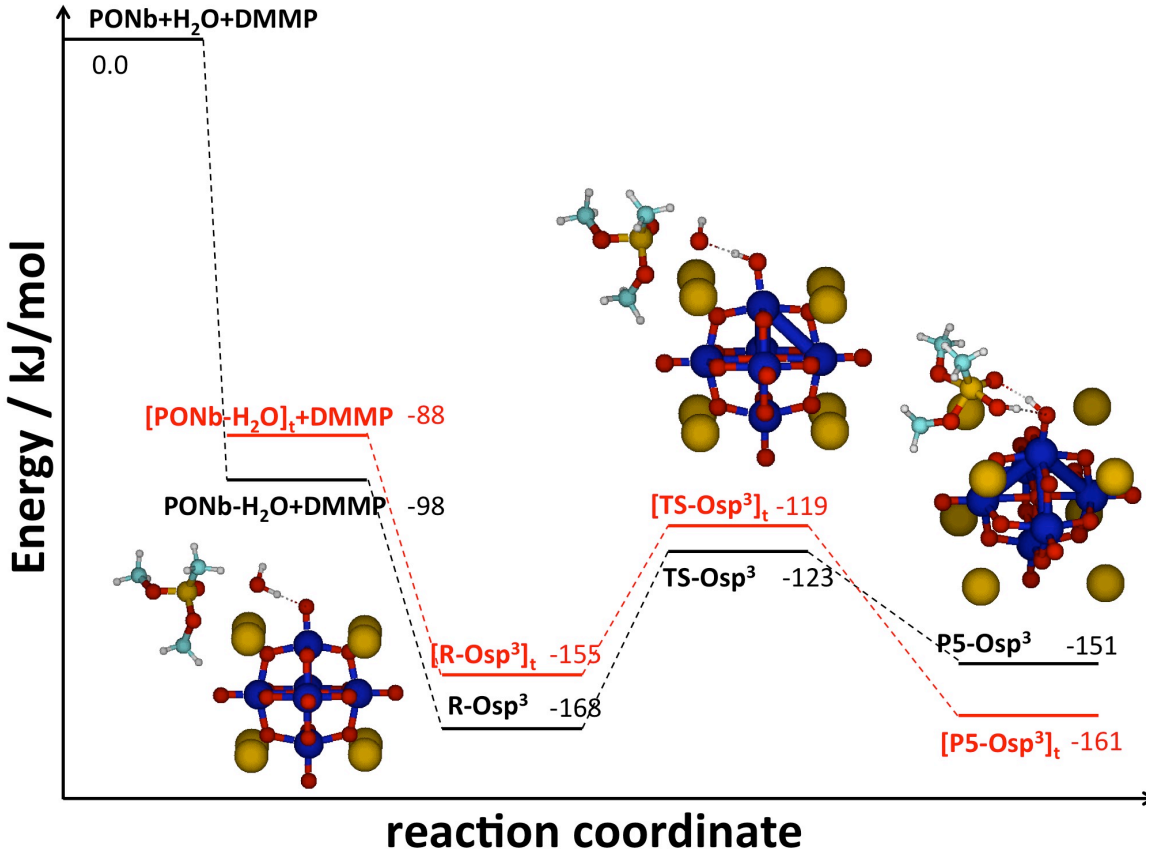

Figure 6.10. Potential-energy profile for reaction of DMMP with a water molecule which is monodenate-bound to $Cs_8Nb_6O_{19}$ and results in protonation of an $O_{terminal}$ site (red) as compared to the same reaction with a water molecule that is bidentate-bound and protonates an $O_{bridging}$ site (black). Insets show stationary-point geometries corresponding to the $O_{terminal}$ reaction. For insets, same color scheme as in Fig. 6.3.

6.3.2 Changes to the Catalyst During Reaction

So far, we have examined the changes occurring within the DMMP and water molecules during catalytic hydrolysis with PONb, paying attention to the role of the catalyst in the reaction. Now, in order to gain a more complete understanding of both this catalytic process and of experimental data obtained during exposure of $Cs_8Nb_6O_{19}$ to DMMP, we focus on changes that occur within the PONb catalyst during reaction. As the reaction in which an O-sp^3 atom and the OH nucleophile are in axial positions of the forming trigonal bipyramid has the lowest barrier, the following analysis will focus on changes that occur along that pathway.

The pristine $Cs_8Nb_6O_{19}$ catalyst has octahedral symmetry. Within this molecule, Nb atoms are 1.8076 Å from neighboring terminal oxygen atoms, 2.4071 Å from the central oxygen,

and 2.0372 Å from neighboring bridging oxygen atoms. Further, Nb atoms are 3.4042 Å from nearest-neighbor Nb atoms, and 4.8143 Å from next-nearest neighbor Nb atoms. Cs counterions are directly associated with the $[Nb_6O_{19}]^{8-}$ Lindqvist ion with a distance of 4.7613 Å from the central oxygen atom. During DMMP hydrolysis, this highly symmetric system is disordered, and individual bond lengths in the catalyst begin to vary. Figure 6.11 shows variances in key distances during reaction. Reported variances have been calculated as the square of the standard deviation from the mean for each distance examined. In octahedral PONb, each distance of a given type is identical, yielding variances of zero for all distance types.

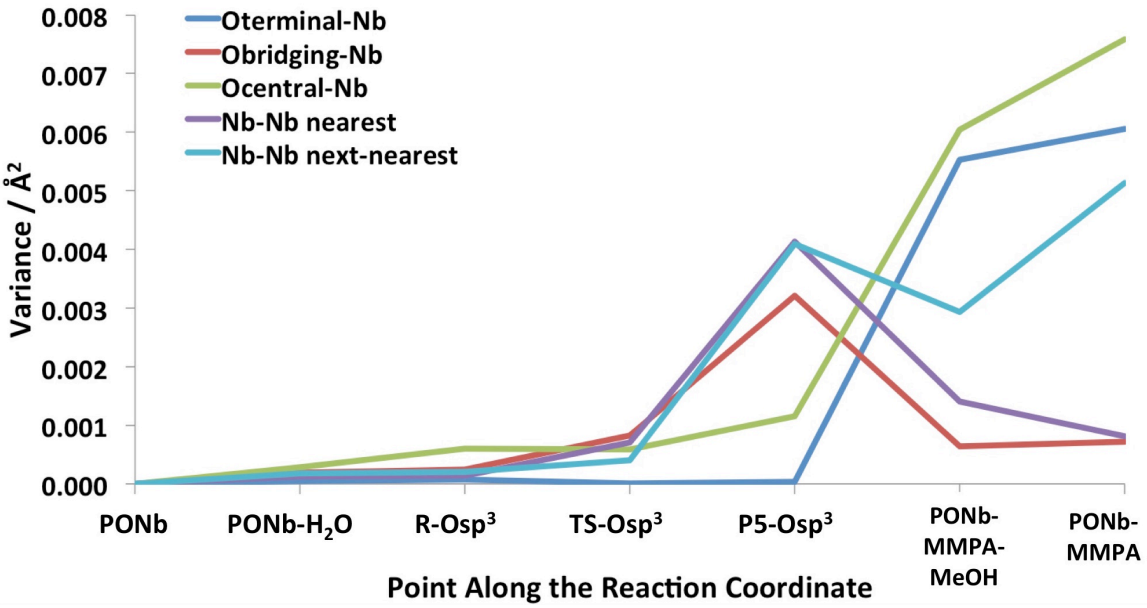

Figure 6.11. Variances in key PONb distances at several points during DMMP hydrolysis with $Cs_8Nb_6O_{19}$ along the lowest-energy pathway.

The catalyst remains mostly ordered in the initial steps involving water and DMMP adsorption. Most of the distance variance is introduced in the hydrolysis transition state leading to the pentacoordinated intermediate and following through to bound products. To further understand these changes, we now examine changes in interatomic distances and Mulliken charges on each atom in the catalyst.

6.3.2.1 PONb-H_2O Complex

The left panel of Figure 6.12 shows changes in interatomic distances upon water adsorption relative to octahedral $Cs_8Nb_6O_{19}$. Spheres located in between Nb and O atoms indicate changes those in Nb-O bond distances, and spheres located on Cs atoms indicate

changes in Cs-$O_{central}$ distance. In the figure, the color of the sphere indicates the direction of the change; red indicates a longer distance than in octahedral PONb, and blue indicates a shorter distance. The size of the sphere is related to the magnitude of the difference. The right panel of Figure 6.12 shows spheres on individual atoms as differences in Mulliken charges relative to charges on corresponding atoms in octahedral PONb (for octahedral $Cs_8Nb_6O_{19}$, Cs: 0.8182e, Nb: 2.2921e, $O_{central}$: -0.9938e, $O_{bridging:}$ -1.1373e, $O_{terminal}$: -0.9429e). Similarly to the left panel, the color of the sphere indicates the direction of the change, with green spheres indicating a more positively charged atom than in the octahedral PONb, and magenta spheres indicating a more negative atom. The size of the sphere is related to the magnitude of the difference.

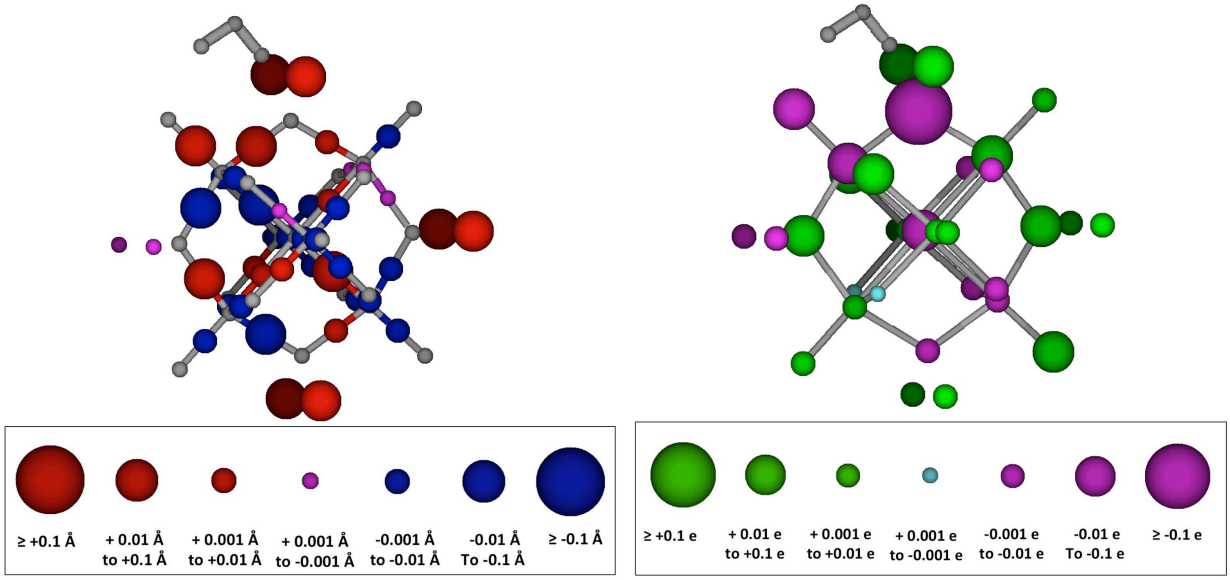

Figure 6.12. Structural and electronic analysis of water adsorbed on $Cs_8Nb_6O_{19}$. Left: Spheres showing changes in Nb-O bond lengths and Cs-$O_{central}$ distances relative to octahedral $Cs_8Nb_6O_{19}$. Right: Spheres showing changes in Mulliken charges of each atom relative to octahedral $Cs_8Nb_6O_{19}$. An explanation of the color/size convention is given in the text.

From Figure 6.12, we can see minor changes in the structure and charge of the PONb upon water adsorption in the region nearest the water molecule. As water hydrogen bonds with both a bridging and a terminal oxygen, the bond length between those oxygens and the nearest Nb atom in the PONb increases. Hydrogen bonding also increases the negative charge on both these oxygen atoms and the intervening Nb atom.

6.3.2.2 PONb-H_2O-DMMP Complex

Figure 6.13 shows differences in distances and charges for DMMP adsorbed onto the PONb-H_2O complex, again relative to octahedral $Cs_8Nb_6O_{19}$. Similar changes are shown here as for the adsorbed-water complex near the site of adsorption. A key difference occurs around the terminal oxygen atom that forms a hydrogen bond with DMMP. As this oxygen atom is now also a hydrogen-bond acceptor, a lengthening of the Nb-O bond is shown, where this bond is shortened slightly in the absence of DMMP adsorption. This is accompanied by an increase in negative charge on the O_{te} atom. Also due to DMMP adsorption, the Nb atom nearest bidentate water adsorption is now slightly more positive than in the octahedral case, and the hydrogen-bond-accepting bridging oxygen is not as negative as in the case of water adsorption alone. Thus, it appears that co-adsorption of DMMP mitigates the rearrangement of charge in PONb caused by water adsorption alone. Finally, a Cs atom now carries a larger positive charge due to an electrostatic interaction with the O-sp^2 atom in DMMP.

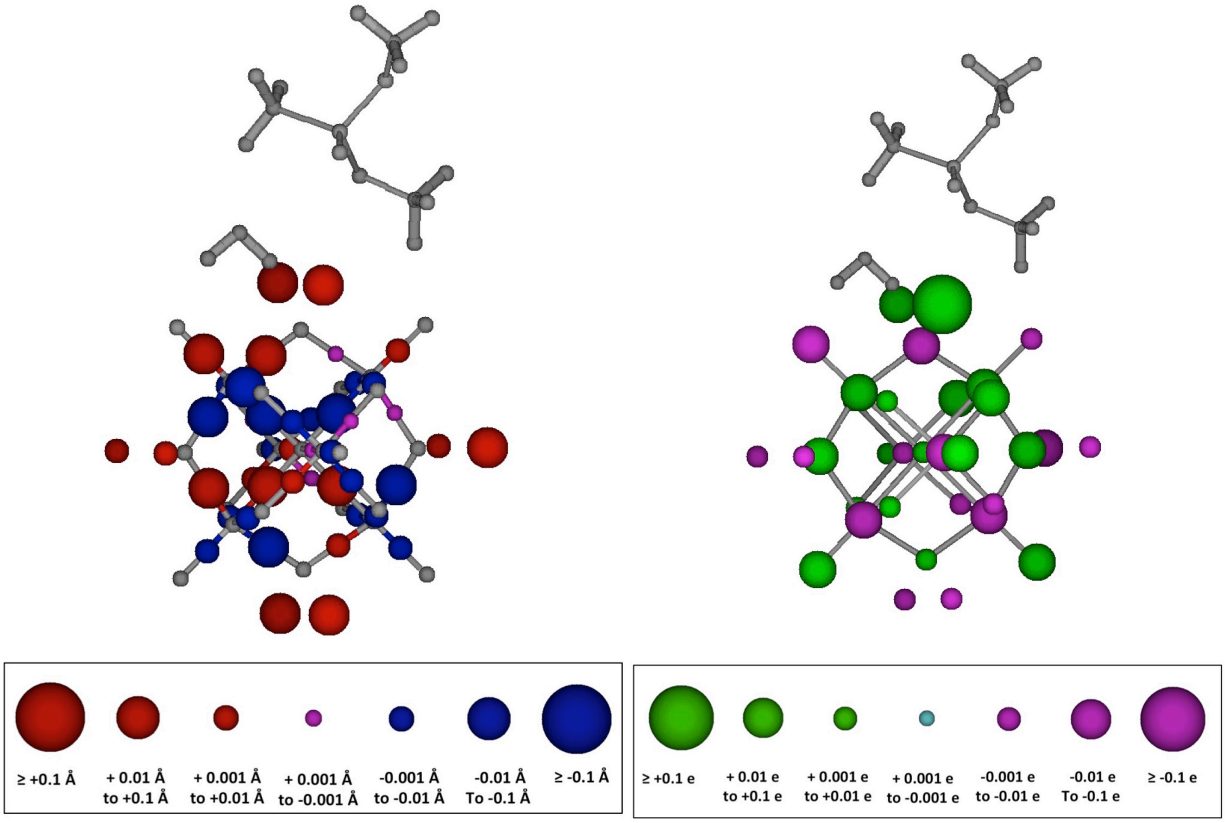

Figure 6.13. Structural and electronic analysis of the PONb-H_2O-DMMP complex. Left: Spheres showing changes in Nb-O bond lengths and Cs-$O_{central}$ distances relative to octahedral $Cs_8Nb_6O_{19}$. Right: Spheres showing changes in Mulliken charges of each atom relative to octahedral $Cs_8Nb_6O_{19}$. An explanation of the color/size convention is given in the text.

6.3.2.3 Hydrolysis Transition State

Notable changes in the structure and atomic charges in the PONb can be seen when water dissociation protonates an $O_{bridging}$ atom in the rate-limiting step, as shown in Figure 6.14. Both Nb-$O_{bridging}$ bonds are lengthened relative to the octahedral case when the at the site being protonated at the transition state. On the other hand, the rest of Nb-O bonds in the vicinity of the $O_{bridging}$ site undergoing protonation become shorter. The protonation makes the $O_{bridging}$ site more negative than in reagents, with the neighboring Cs ions becoming significantly more positive.

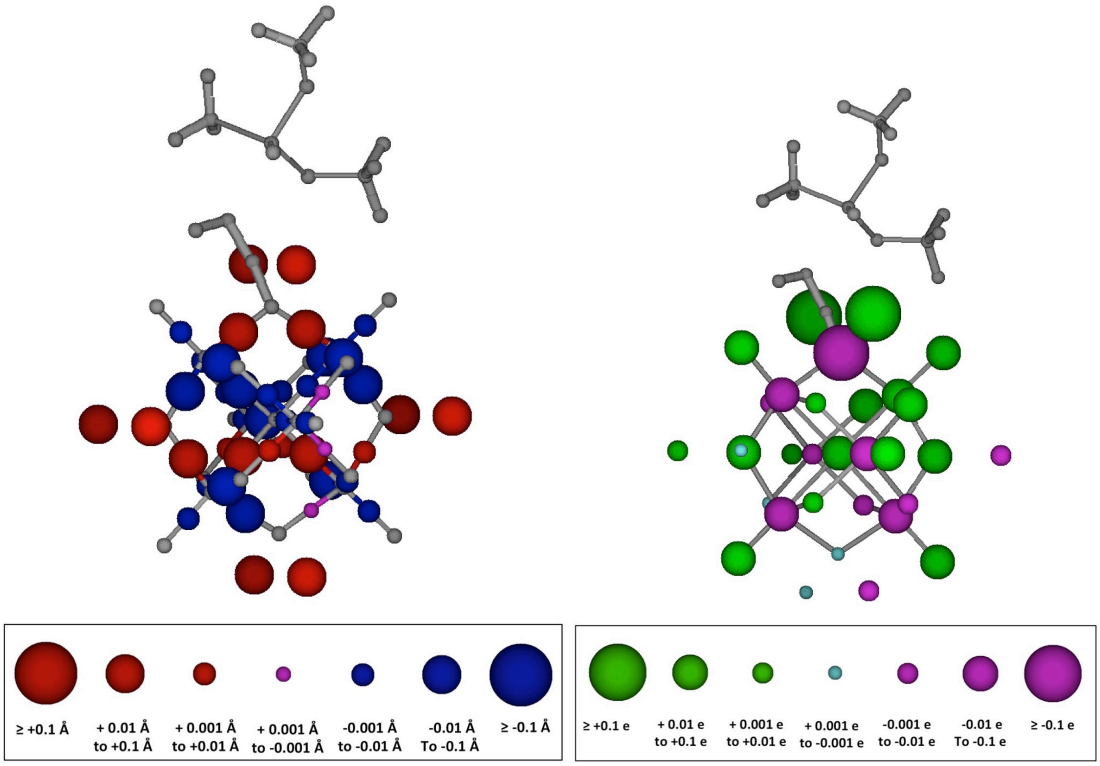

Figure 6.14. Structural and electronic analysis of the transition state structure for the rate-limiting step of catalytic DMMP hydrolysis by $Cs_8Nb_6O_{19}$. Left: Spheres showing changes in Nb-O bond lengths and Cs-$O_{central}$ distances relative to octahedral $Cs_8Nb_6O_{19}$. Right: Spheres showing changes in Mulliken charges of each atom relative to octahedral $Cs_8Nb_6O_{19}$. An explanation of the color/size convention is given in the text.

6.3.2.4 Pentacoordinated Intermediate

Up to this point in the reaction, we have seen changes in the structure of the catalyst relative to the structure of octahedral $Cs_8Nb_6O_{19}$ due to interactions with adsorbing molecules. However, these structures have shown little disorder (Fig. 6.11). This is confirmed by the lack of any distance changes of 0.1 Angstroms or greater as compared to octahedral PONb. We also have only begun to look at the formation of a new covalent bond with the catalyst. In the pentacoordinated intermediate, we see much more appreciable disorder in the catalyst. At this point in the reaction pathway, there is full protonation at the bridging oxygen site, which causes a large increase in bond length between this oxygen and its neighboring Nb atoms, as shown in Figure 6.15. Consequently, the Nb-Nb distance between the two Nb atoms bonded to the protonated $O_{bridging}$ site is significantly longer than any other Nb-Nb pairs. Such a lengthening does not occur at other points on the catalyst, and a disorder in both the $O_{bridging}$-Nb and nearest Nb-Nb distances is thereby introduced. Further, the Cs counterions appear to recede from the PONb, especially near the site of protonation.

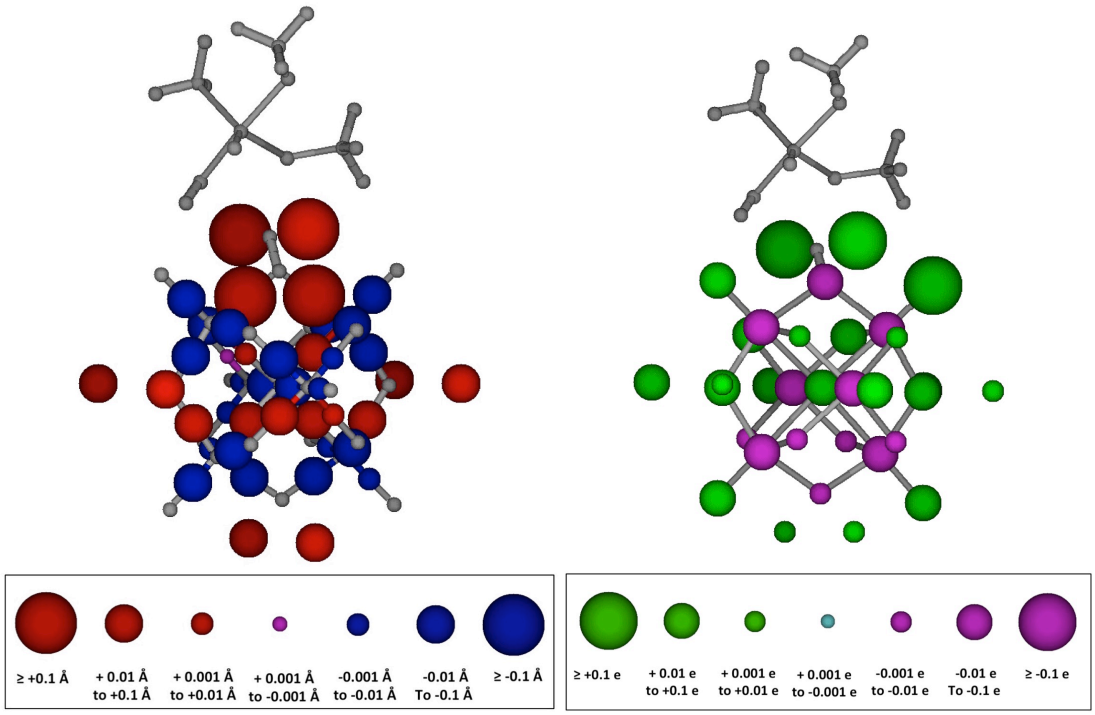

Figure 6.15. Structural and electronic analysis of the pentacoordinated intermediate in catalytic DMMP hydrolysis by $Cs_8Nb_6O_{19}$. Left: Spheres showing changes in Nb-O bond lengths and Cs-$O_{central}$ distances relative to octahedral $Cs_8Nb_6O_{19}$. Right: Spheres showing changes in Mulliken charges of each atom relative to octahedral $Cs_8Nb_6O_{19}$. An explanation of the color/size convention is given in the text.

Also resulting from this new bond, there is an apparent rippling effect in bond distances beginning at the bridging-oxygen reaction site and moving through the other hemisphere of the catalyst to the bridging site on the opposite side of the catalyst. The lengthening of the Nb-$O_{bridging}$ bonds around the reactive site is accompanied by a shortening of the other Nb-$O_{bridging}$ bonds involving these nearby Nb atoms. In turn, the next-nearest Nb-$O_{bridging}$ bonds are lengthened, but not to the magnitude of those near the reaction site, and the Nb-$O_{bridging}$ bonds furthest from the reaction site are shortened. This results in an increase in disorder in Nb-$O_{bridging}$ bond lengths. This effect is also manifested in the Mulliken charges of bridging atoms throughout the PONb. While the protonated $O_{bridging}$ atom becomes more negative, bridging oxygen atoms nearest to the reaction site become slightly more positive, and those further away become slightly more negative than in the octahedral catalyst. All Cs atoms become more positive, especially those that are interacting with the negatively charged pentacoordinated intermediate.

Just as the rippling effect leads to disorder by affecting next-nearest Nb-Nb distances differently, hydrogen bonding at the bridging site leads to disorder in $O_{central}$-Nb bonds. Those $O_{central}$-Nb bonds in the plane containing the reactive Nb-$O_{bridging}$-Nb were lengthened relative to the octahedral PONb, while those $O_{central}$-Nb orthogonal to the reactive plane were shortened.

In order to fully separate the role of protonation on the structure of PONb from the role of binding of the pentacoordinated phosphorus species, we now compare the structure of the pentacoordinated complex with that of a PONb protonated at the bridging site in the absence of an adsorbed species. Figure 6.16 shows the changes in structure and charge of the protonated molecule relative to octahedral $Cs_8Nb_6O_{19}$.

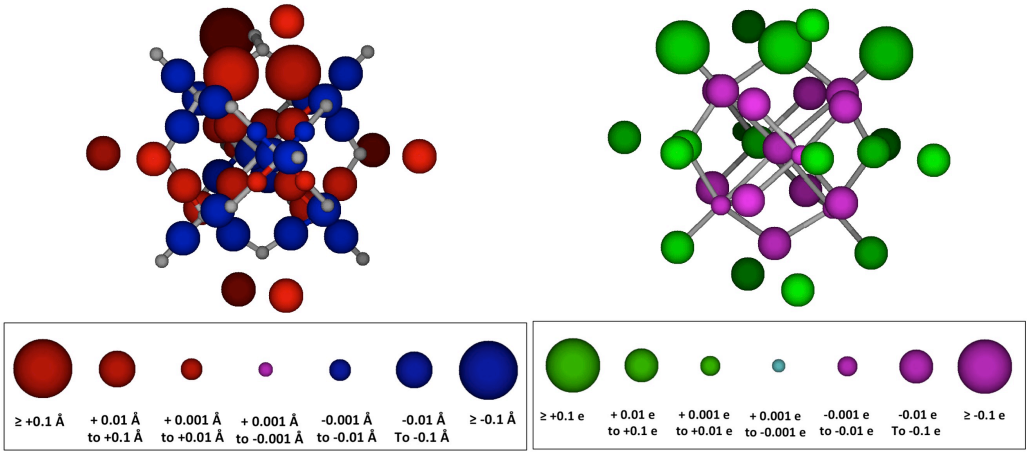

Figure 6.16. Structural and electronic analysis of $[HCs_8Nb_6O_{19}]^+$ with a proton at a bridging oxygen site. Left: Spheres showing changes in Nb-O bond lengths and Cs-$O_{central}$ distances relative to octahedral $Cs_8Nb_6O_{19}$. Right: Spheres showing changes in Mulliken charges of each atom relative to octahedral $Cs_8Nb_6O_{19}$. An explanation of the color/size convention is given in the text.

The changes in structure, relative to octahedral, for the PONb protonated at the $O_{bridging}$ site with and without a bound pentacoordinated species are very similar. Both show an increase in Nb-$O_{bridging}$ near the protonation site, and both show a rippling of other Nb-$O_{bridging}$ distances throughout the rest of the catalyst. An increase in $O_{central}$-Nb distance in the reaction plane is shown, along with a decrease of this distance in the orthogonal plane. Overall, the magnitude of Nb-O distances may vary slightly upon organophosphorus adsorption, but the changes relative to octahedral PONb seem to be dominated by protonation.

Although interatomic distances in the catalyst are not greatly affected by an adsorbate, atomic charges do differ in the presence of an interacting molecule. For instance, due to hydrogen bonding with the O-sp^3 atom of the organophosphorus adsorbate, the protonated bridging oxygen atom is much more negative when bound to the pentacoordinate molecule than in the absence of an adsorbate. Similarly, the terminal oxygen that forms a hydrogen bond with the acid OH group is less positive than in the protonated non-adsorbed catalyst. The terminal oxygen atom that accepts a hydrogen bond from the $–OCH_3$ group does not exhibit such a significant change, as there is a large increase in charge on that atom relative to the octahedral PONb in both the pentacoordinated intermediate and the bridging-protonated PONb. This suggests that the acid OH group is a better hydrogen-bond donor than the $–OCH_3$ group. In both protonated PONb structures (with and without the pentacoordinated intermediate), the Cs counterions are more positive than in the original octahedral PONb.

For the protonated catalyst at the $O_{bridging}$ site in the absence of an adsorbing species, the average charge differences related to the octahedral PONb for each type of atom are +0.0318e for Cs atoms, -0.0451e for Nb atoms, +0.0083e for $O_{bridging}$ atoms, +0.0799e for $O_{terminal}$ atoms, and +0.0478e for the $O_{central}$ atom.

6.3.2.5 Adsorbed Products

Following the dissociation of the pentacoordinated intermediate into bound MMPA and methanol, disorder in the PONb catalyst changes (Fig 6.11). From a chemical perspective, the major change from the pentacoordinated intermediate to bound products is that the protonation site changes from the $O_{bridging}$ site to an $O_{terminal}$ site. This change originates because the nascent methoxy product from the dissociation of the intermediate abstracts the proton at the bridging site, while the MMPA fragment transfers its proton to an $O_{terminal}$ atom. This process might compete, in reality, with other dissociation pathways that will leave the proton on the $O_{bridging}$ site. Figure 6.17 shows the changes in Nb-O distances and Mulliken charges relative to octahedral $Cs_8Nb_6O_{19}$ for products bound to a PONb in which an $O_{terminal}$ atom becomes protonated.

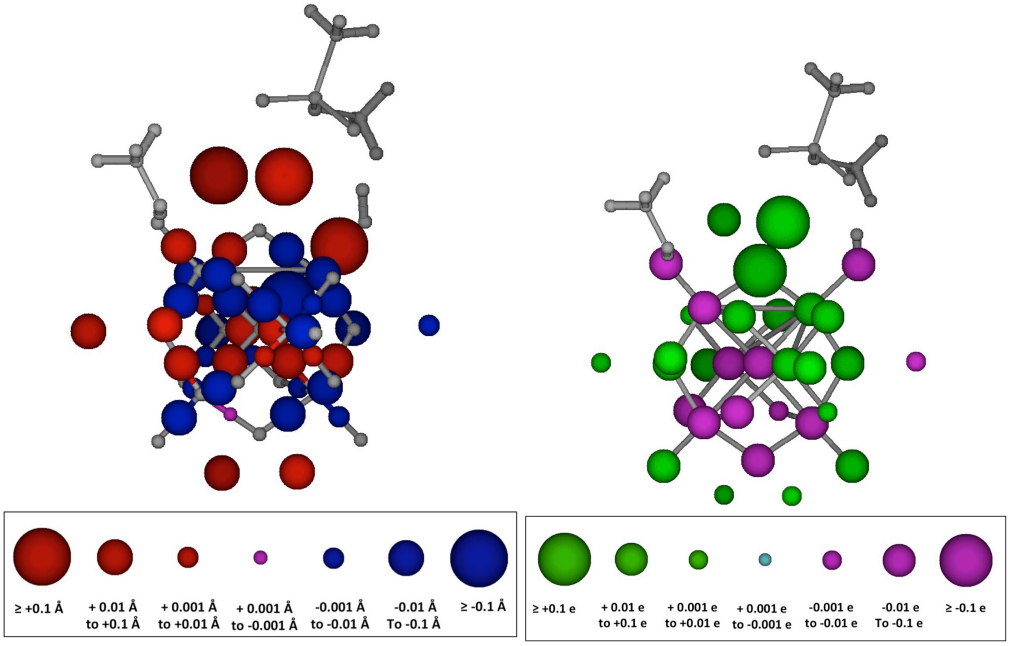

Figure 6.17. Structural and electronic analysis of products of DMMP hydrolysis on $Cs_8Nb_6O_{19}$. Left: Spheres showing changes in Nb-O bond lengths and Cs-$O_{central}$ distances relative to octahedral $Cs_8Nb_6O_{19}$. Right: Spheres showing changes in Mulliken charges of each atom relative to octahedral $Cs_8Nb_6O_{19}$. An explanation of the color/size convention is given in the text.

In this bound-product structure, a large increase in $O_{terminal}$-Nb bond length where protonation takes place is shown relative to octahedral PONb. A similar increase, yet smaller in magnitude, is also shown at the $O_{terminal}$ site participating in hydrogen bonding with the adsorbed methanol, even though this site is not protonated. Conversely, decreases relative to the octahedral structure are shown for the four $O_{terminal}$-Nb distances not participating in bonding. This variation in distances, including the large increase at the protonation site, accounts for the heightened disorder in $O_{terminal}$-Nb lengths at this point in the reaction pathway.

Along with these changes in distance in the bound products, we note also changes in atomic charges. Most notably, the charge on the bridging oxygen atom between both terminal oxygen atoms involved in hydrogen bonding with hydrolysis products is much more positive than in the pentacoordinated intermediate. This is likely due to the redistribution of charge from this atom to the neighboring terminal oxygen atoms, which are either involved in a hydrogen bond, or protonated. The increase in negative charge in these terminal oxygens is also evidence for this inductive effect. Most of the Cs ions are still more positive than in reagents.

As in the pentacoordinate intermediate, a thorough understanding of the roles of protonation and nonbonding interactions requires a comparison of the changes in bound products

with changes merely due to protonation in the absence of an adsorbate. Figure 6.18 shows changes in the catalyst protonated at a terminal site without adsorbed fragments relative to the octahedral PONb.

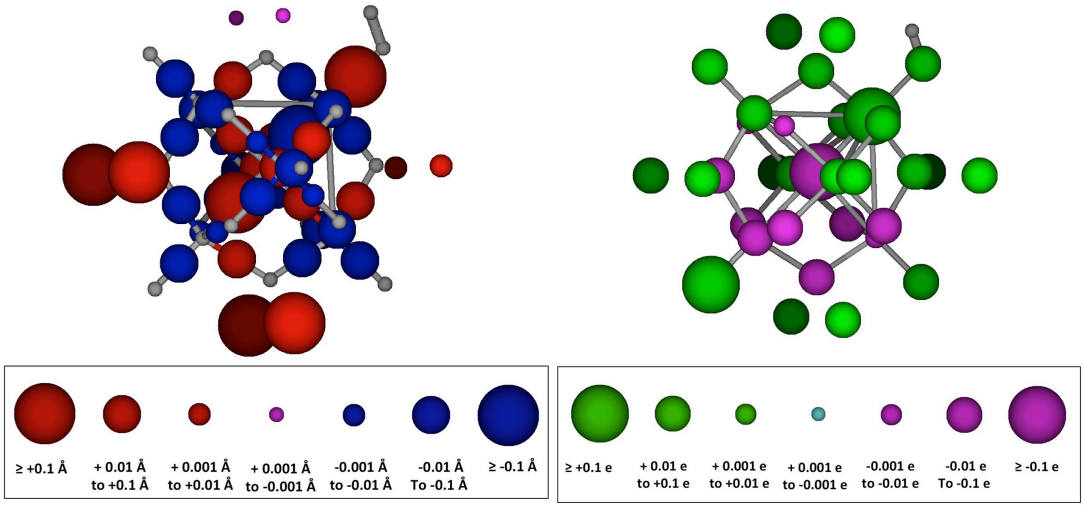

Figure 6.18. Structural and electronic analysis of protonated $[HCs_8Nb_6O_{19}]^+$ with the proton at a terminal site. Left: Spheres showing changes in Nb-O bond lengths and Cs-$O_{central}$ distances relative to octahedral $Cs_8Nb_6O_{19}$. Right: Spheres showing changes in Mulliken charges of each atom relative to octahedral $Cs_8Nb_6O_{19}$. An explanation of the color/size convention is given in the text.

Relative to the octahedral catalyst, a significant elongation in the $O_{terminal}$-Nb bond length at the protonation site is seen in the protonated PONb. This lengthening is coupled with a large decrease in the adjacent $O_{central}$-Nb bond length. These interrelated changes are seen also seen in the PONb with adsorbed products. Regarding charges, we see that, much as with protonation at the $O_{bridging}$ site in Figure 6.16, all Cs ions become more positive when the $O_{terminal}$ site becomes protonated.

For the protonated catalyst in the absence of an adsorbing species, the average charge differences related to the octahedral PONb for each type of atom are +0.0260e for Cs atoms, +0.0252e for Nb atoms, -0.0019e for $O_{bridging}$ atoms, +0.0843e for $O_{terminal}$ atoms, and -0.1430e for the $O_{central}$ atom.

Following the desorption of methanol, MMPA remains bound to the catalyst. For the most part, the structure of the catalyst remains unchanged, except for a small contraction of the $O_{terminal}$-Nb bond and a small elongation of the $O_{central}$-Nb bond near the former binding site of

methanol, as shown in Figure 6.19. Notable increases in disorder (Fig. 6.11) are shown for $O_{central}$-Nb and nearest Nb-Nb distances due to the desorption of methanol. These changes in bond distances may account for these increases in disorder.

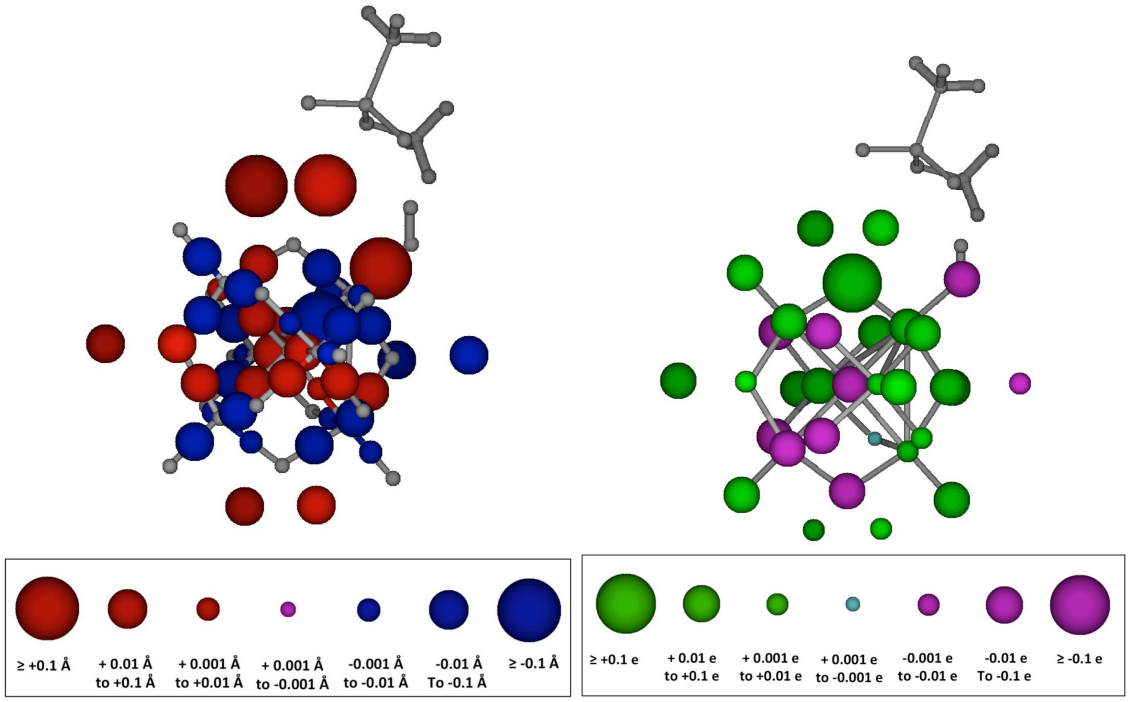

Figure 6.19. Structural and electronic analysis of products of catalytic hydrolysis of DMMP by $Cs_8Nb_6O_{19}$ following the desorption of methanol. Left: Spheres showing changes in Nb-O bond lengths and Cs-$O_{central}$ distances relative to octahedral $Cs_8Nb_6O_{19}$. Right: Spheres showing changes in Mulliken charges of each atom relative to octahedral $Cs_8Nb_6O_{19}$. An explanation of the color/size convention is given in the text.

These structural changes are accompanied by a redistribution of charge near the MMPA adsorption site, as the $O_{terminal}$ and Nb atoms which were more negative than in the octahedral case when accepting a hydrogen bond from methanol are now more positive. For the catalyst with MMPA adsorbed, the average charge differentials related to the octahedral PONb for each type of atom are +0.0226e for Cs atoms, +0.0131e for Nb atoms, +0.0172e for $O_{bridging}$ atoms, +0.0377e for $O_{terminal}$ atoms, and -0.0827e for the $O_{central}$ atom. Except for $O_{bridging}$ atoms, we note that the binding of MMPA to the protonated PONb diminishes the variation in the charges compared to the protonated PONb catalyst without MMPA.

6.3.3 Comparison with Experimental Results

A main purpose of these calculations is the support experimental results. In work yet to be published, members of the Frenkel group at Brookhaven National Lab performed in situ experiments in which a powdered sample of $Cs_8Nb_6O_{19}$ was exposed to DMMP, and products were characterized using Raman spectroscopy. Changes to the PONb sample were also tracked using x-ray spectroscopy.

6.3.3.1 Raman Spectroscopy

The top panel of Figure 6.20 shows experimental Raman spectra for the PONb sample before (black trace) and over the course of exposure to DMMP (pink, green, blue), as well as following exposure and a subsequent purge of the experimental environment with helium (red). In an attempt to elucidate these spectra, we show in the bottom panel theoretical Raman spectra of the octahedral PONb (gray trace, structure shown in Figure 5.1), as well as the bound-MMPA product discussed in this chapter (PONb-(t)MMPA, orange trace, structure shown in Figure 6.9, right panel) in the same spectral region. An alternate structure for this product is also considered, in which MMPA is bound to PONb at a protonated bridging site (PONb-(b)MMPA, blue trace, structure shown in the inset of Figure 6.20). Theoretical spectra were calculated at the M06-L/6-31G(d,p)—Lanl2dz level of theory, and Raman intensities have been corrected with M06-L/6-31++G(d,p)—Lanl2dz.

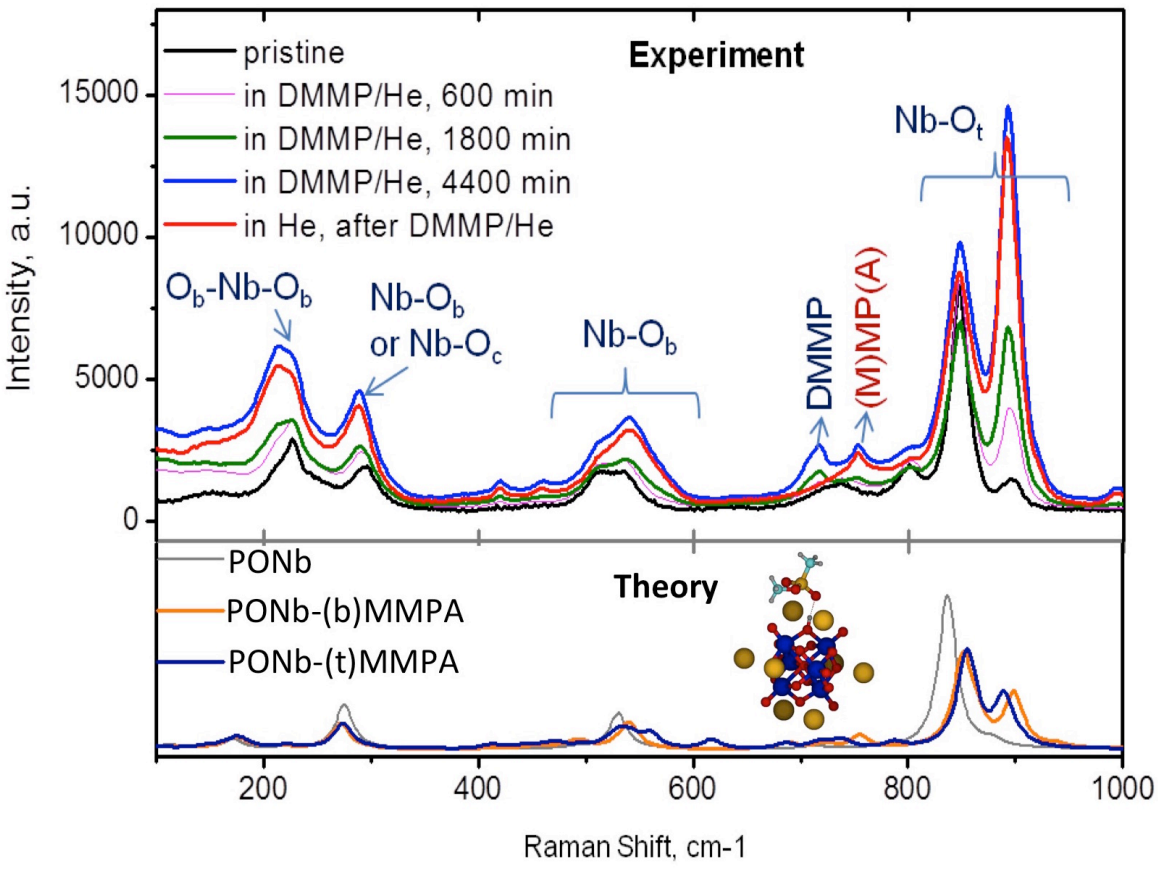

Figure 6.20. Top: Time-resolved experimental Raman spectra for a $Cs_8Nb_6O_{19}$ sample prior to, during, and following exposure to DMMP. Bottom: Theoretical Raman spectra; gray: $Cs_8Nb_6O_{19}$; orange: PONb-(b)MMPA complex; blue: PONb-(t)MMPA complex. The inset shows the structure of PONb-(b)MMPA, using the same color code as in Figure 6.3.

The theoretical Raman spectra are in agreement with several features in the experimental spectra. For instance, the band at 530 cm^{-1} broadens and becomes blueshifted following PONb protonation and product adsorption. This band corresponds to an out-of-sync Nb-O_b motion in the octahedral PONb. Most prominently, however, is the increase in intensity of the band at 879 cm^{-1}, which corresponds to an in-sync Nb-O_{te} stretching motion. The adjacent peak at 837 cm^{-1} also corresponds to an Nb-O_{te} stretching mode, only out-of-sync. Theoretical Raman spectra of protonated PONb in the absence of an adsorbate also show a greater increase in intensity of the in-sync Nb-O_{te} mode relative to the out-of-sync mode, suggesting that this effect is due more to protonation than to product adsorption. Thus, we propose that the in-sync stretching mode becomes more Raman active than the out-of-sync as the PONb becomes protonated. Therefore, in the experimental spectra, the progressive increase in intensity reveals that the PONb sample is

becoming more protonated with increased DMMP exposure. This is in agreement with the hydrolysis mechanism discussed in the first part of this chapter.

6.3.3.2 X-Ray Spectroscopy

Finally, experimental extended x-ray absorption fine structure (EXAFS) spectra were obtained on the PONb sample prior to and following exposure to DMMP. As discussed in Chapter 1, EXAFS data informs of the local environment of atoms and provides interatomic distances for atoms in the PONb. In this experiment, this data is provided in the form of bond disorder, or variance (σ^2), for several key distances in order to account for the macroscale nature of the experimental sample. In Figure 6.11, we performed a similar theoretical analysis for a single PONb. As EXAFS data were taken prior to and following DMMP exposure, a comparison between experimental and theoretical data can be made when the difference in variance between the octahedral PONb and the PONb-MMPA product is considered. Table 6.1 compares this difference in variance for theoretical PONb-(t)MMPA and PONb-(b)MMPA formation with the difference in variance before and after experimental DMMP exposure.

Distance Type	Theoretical PONb-(t)MMPA	Theoretical PONb-(b)MMPA	Experimental
Nb-O_{te}	0.00605	0.00004	0.00106(18)
Nb-O_b	0.00071	0.00274	0.00054(13)
Nb-Nb	0.00082	0.00401	0.00011(5)

Table 6.1. Bond Disorder (σ^2, in $Å^2$): Theory vs. Experiment

Table 6.1 shows that theoretical variances are typically greater than experimental values. This may be related to the stoichiometry of reaction; theoretical calculations assume that DMMP reacts with PONb in a 1:1 ratio, whereas not every PONb cluster may be available to DMMP adsorption and reaction in the experimental system. Nonetheless, a comparison of ratios of Nb-O_{te} to Nb-O_b variances provides insight to experimental phenomena. In the experiment, the Nb-O_{te} variance increases more than the Nb-O_b during reaction with DMMP, commensurate with theoretical variances for protonation and MMPA binding at a terminal site. However, the magnitude of σ^2(Nb-O_{te})/σ^2(Nb-O_b) is significantly smaller in the experiment than for theoretical PONb-(t)MMPA. The theoretical variances for protonation and MMPA binding at a bridging site show an opposing trend; σ^2(Nb-O_b) is greater than σ^2(Nb-O_{te}) in this system. Combined, these

results suggest that protonation is likely at both terminal and bridging oxygen atoms on PONb. Regardless of protonation site, theoretical Raman and distance variance data provide insight into experimental data, showing that protonation of PONb is a fundamental result of DMMP exposure.

6.4 Concluding Remarks

In this chapter, we have described the mechanism and energetics of the hydrolysis of DMMP by $Cs_8Nb_6O_{19}$. Though the mechanism of reaction does not vary greatly from the analogous hydrolysis of GB by PONb, we do find that the rate-limiting transition-state energies are much greater for DMMP hydrolysis. Thus, DMMP may not be the most appropriate simulant for GB in hydrolysis studies on PONb surfaces.

Further, we described changes in the structure and atomic charges in the $Cs_8Nb_6O_{19}$ polyoxoniobate catalyst during the reaction. In comparing changes in each Nb-O bond length and charge on each atom relative to a pristine octahedral PONb, we were able to pinpoint specific changes to the catalyst at each step in the reaction pathway. This allowed us to specify sources of disorder in the catalyst. By comparing protonated PONbs with stationary points along the reaction pathway, we have elucidated the roles of protonation and hydrogen bonding on changes in structure and atomic charge during reaction. As such, we conclude that protonation of the PONb plays a dominant role in the structure and charge distribution during this reaction, and the effects of protonation are notably modulated by adsorption.

Also, by comparing theoretical Raman spectra and distance variances to experimental spectra, we were able to show protonation of PONb during DMMP exposure—a fundamental aspect of the reaction mechanism proposed in this chapter.

Regarding the effects of reaction on the counterions, we have examined changes in $O_{central}$-Cs distances. However, these distances do not provide an adequate picture of ion association to the rest of the catalyst, as changes in these distances may be affected by changes in Nb-O and Nb-Nb distances in the niobate. Future work will attempt to describe counterion association during DMMP hydrolysis by examining changes in the distance between Cs atoms and the face of the niobate ion, perhaps using $O_{bridging}$-Cs distances. Nevertheless, the Cs ions become more positive during reaction.

6.5 References

(1) Hoggard, J. C.; Wahl, J. H.; Synovec, R. E.; Mong, G. M.; Fraga, C. G. *Analytical Chemistry* **2010**, *82*, 689.

(2) Xiang, H. F.; Xu, H. Y.; Wang, Z. Z.; Chen, C. H. *Journal of Power Sources* **2007**, *173*, 562.

(3) Misik, J.; Pavlikova, R.; Cabal, J.; Kuca, K. *Drug and chemical toxicology (New York, N.Y. 1978)* **2015**, *38*, 32.

(4) *Toxicology and Carcinogenesis Studies of Dimethyl Methylphosphonate in F344/N Rats and BC6C3F1 Mice*, U.S. Department of Health and Human Services, 1987.

(5) Chapleski, R. C.; Musaev, D. G.; Hill, C. L.; Troya, D. *The Journal of Physical Chemistry C* **2016**, *120*, 16822.

(6) Frisch, M. J.; Trucks, G. W.; Schlegel, H. B.; Scuseria, G. E.; Robb, M. A.; Cheeseman, J. R.; Scalmani, G.; Barone, V.; Mennucci, B.; Petersson, G. A.; Nakatsuji, H.; Caricato, M.; Li, X.; Hratchian, H. P.; Izmaylov, A. F.; Bloino, J.; Zheng, G.; Sonnenberg, J. L.; Hada, M.; Ehara, M.; Toyota, K.; Fukuda, R.; Hasegawa, J.; Ishida, M.; Nakajima, T.; Honda, Y.; Kitao, O.; Nakai, H.; Vreven, T.; Montgomery Jr., J. A.; Peralta, J. E.; Ogliaro, F. ß.; Bearpark, M. J.; Heyd, J.; Brothers, E. N.; Kudin, K. N.; Staroverov, V. N.; Kobayashi, R.; Normand, J.; Raghavachari, K.; Rendell, A. P.; Burant, J. C.; Iyengar, S. S.; Tomasi, J.; Cossi, M.; Rega, N.; Millam, N. J.; Klene, M.; Knox, J. E.; Cross, J. B.; Bakken, V.; Adamo, C.; Jaramillo, J.; Gomperts, R.; Stratmann, R. E.; Yazyev, O.; Austin, A. J.; Cammi, R.; Pomelli, C.; Ochterski, J. W.; Martin, R. L.; Morokuma, K.; Zakrzewski, V. G.; Voth, G. A.; Salvador, P.; Dannenberg, J. J.; Dapprich, S.; Daniels, A. D.; Farkas, O.; Foresman, J. B.; Ortiz, J. V.; Cioslowski, J.; Fox, D. J.; Gaussian, Inc.: Wallingford, CT, USA, 2009.

(7) Wilmsmeyer, A. R.; Uzarski, J.; Barrie, P. J.; Morris, J. R. *Langmuir* **2012**, *28*, 10962.

(8) Nyman, M.; Alam, T. M.; Bonhomme, F.; Rodriguez, M. A.; Frazer, C. S.; Welk, M. E. *Journal of Cluster Science* **2006**, *17*, 197.

(9) Chapleski, R. C.; Zhang, Y.; Troya, D.; Morris, J. R. *Chemical Society Reviews* **2016**, *45*, 3731.

(10) Buono, G.; Llinas, J. R. *Journal of the American Chemical Society* **1981**, *103*, 4532.

(11) Daniel, K. A.; Kopff, L. A.; Patterson, E. V. *Journal of Physical Organic Chemistry* **2008**, *21*, 321.

Chapter 7

Hydrolysis of the Nerve-agent Simulant Dimethyl chlorophosphate as Catalyzed by $Cs_8Nb_6O_{19}$

Abstract

In this chapter, we describe the hydrolysis mechanism for the organophosphorus nerve-agent simulant dimethyl chlorophosphate (DMCP) by the Lindqvist polyoxoniobate $Cs_8Nb_6O_{19}$ (PONb). We find that the mechanism differs slightly from that for the nerve agent Sarin in that the rate-limiting transition state leads directly to the formation of products adsorbed to the polyoxoniobate, in the absence of a pentacoordinated phosphorus intermediate. After a discussion of the mechanism, we describe changes that occur in the structure and atomic charges within the polyoxoniobate, showing that the largest structural changes are related to protonation that occurs during DMCP hydrolysis. We conclude by comparing the DMCP hydrolysis mechanism on PONb with those for Sarin and dimethyl methylphosphonate (DMMP), revealing that DMCP, with a similar rate-limiting barrier, better simulates Sarin hydrolysis than DMMP in investigations with PONb.

7.1 Introduction

Dialkyl chlorophosphates are commonly used as nerve agent simulants.[1-4] Dimethyl chlorophosphate (DMCP) has a structure similar to those of the G-series of nerve agents (e.g., Sarin, Soman, VX). Shown in the right panel of Figure 7.1, both DMCP and Sarin (GB) exhibit a central tetrahedral phosphorus atom bound to an sp^2-hybridized oxygen atom. Beyond that, these two molecules have similar moieties bound to phosphorus. Both compounds showcase a halogen; in DMCP, a chlorine atom is found in the place of fluorine in GB. Also, DMCP has two bound sp^3-hybridized oxygen atoms, both parts of methoxy groups, where GB has one bound sp^3 oxygen in an isopropyl group as well as a methyl group. In this paper, we describe different pathways for the gas-phase catalytic hydrolysis of dimethyl chlorophosphate (DMCP) using $Cs_8Nb_6O_{19}$ polyoxoniobate (PONb). Then, we describe changes that occur in the catalyst during this reaction.

7.2 Computational Details

All calculations were performed with the Gaussian 09 suite of software.[5] Geometries of all points were optimized with the M06-L density functional, the 6-31G(d,p) basis set for nonmetal atoms, and the Lanl2dz basis set and pseudopotentials for metal atoms. Optimized extrema were verified using vibrational frequency calculations performed at this level of theory. Energies of optimized points were refined through single-point calculations at the same level as geometry optimizations, only with the application of the 6-31++G(d,p) basis set for nonmetal atoms. Thus, reported energies are a result of dual-level M06-L/6-31++G(d,p)—Lanl2dz//6-31G(d,p)—Lanl2dz calculations, corrected by zero-point energies obtained from vibrational frequency calculations at the lower level. Unless otherwise noted, an ultrafine integration grid was applied to all calculations.

7.3 Results

7.3.1 Reaction Pathways

As shown in the left panel of Figure 7.1, $Cs_8Nb_6O_{19}$ is a highly ordered molecule with octahedral symmetry. There are three types of oxygen atoms in PONb: one central oxygen bound to six niobium atoms, twelve bridging oxygen atoms each bound to two niobium atoms, and six terminal oxygen atoms each bound to one niobium atom. Eight Cs^+ counterions are directly associated with the $[Nb_6O_{19}]^{8-}$ core. DMCP, as shown in the bottom-right panel of Figure 7.1, is comprised of a tetrahedral phosphorus center bound to an sp^2 oxygen atom, two methoxy groups, and a chlorine atom.

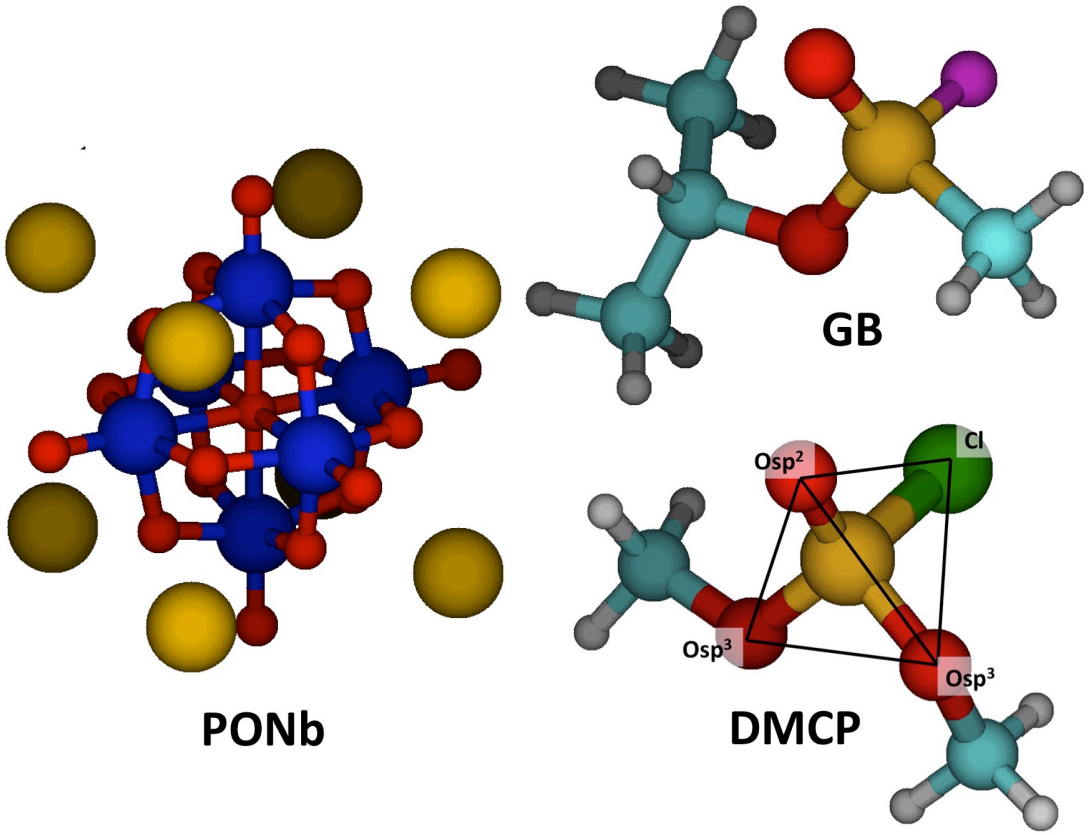

Figure 7.1. Left: Octahedral $Cs_8Nb_6O_{19}$ polyoxoniobate. Right: Top: *(S)*-Sarin. Bottom: dimethyl chlorophosphate showing tetrahedral arrangement around a central phosphorus atom, with atoms immediately bound to phosphorus identified. Color scheme: Cs: gold, Nb: blue, O: red, P: gold, Cl: green, F: magenta, C: cyan, H: gray.

During hydrolysis of DMCP, hydroxide formed on $Cs_8Nb_6O_{19}$ adds nucleophilically to the tetrahedral phosphorus atom. This hydroxide can approach from any of three unique faces of the tetrahedron surrounding the phosphorus atom. This tetrahedron is shown in Figure 7.1, with atoms at the corners of the tetrahedron identified in the figure. This paper will differentiate reaction pathways by identifying the atom which shares a bond with phosphorus that is collinear with the P-OH bond being formed at the hydrolysis transition state.

The hydrolysis of DMCP as catalyzed by PONb occurs in several steps: adsorption of H_2O onto PONb to form a PONb-H_2O complex, adsorption of DMCP onto PONb-H_2O to form reagent (R) complexes, dissociation of H_2O in concert with nucleophilic addition of OH to DMCP to form product (P) complexes, and desorption of products. Figure 7.2 shows the energies for each unique reaction pathway. Now, we will describe each step in the pathway, examining important interactions and comparing individual mechanisms.

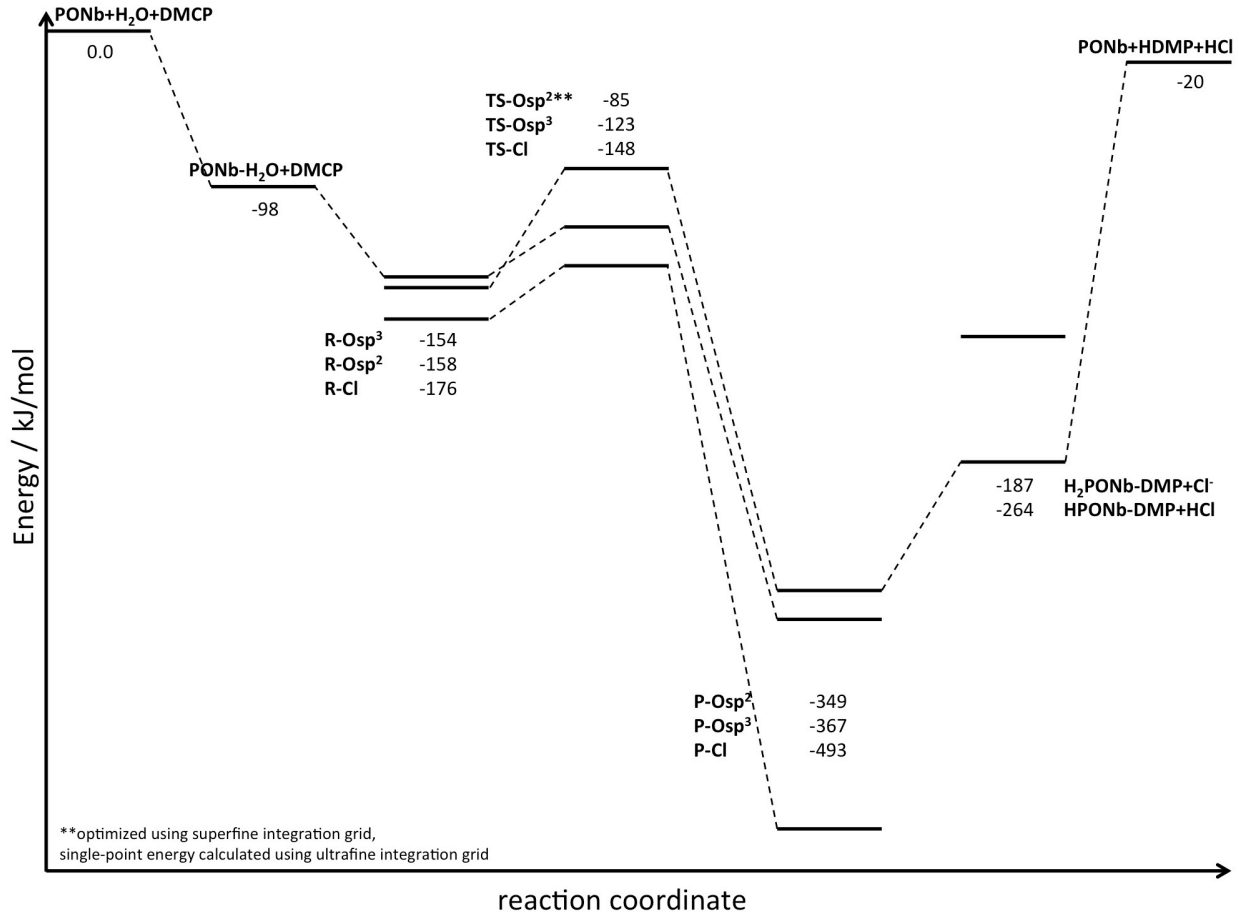

Figure 7.2. Reaction pathways for hydrolysis of DMCP by $Cs_8Nb_6O_{19}$ at a bidentate-bound water molecule site. See text for nomenclature.

7.3.1.1 Adsorption of Water to the PONb

This first step in catalytic hydrolysis was described in detail in our works with catalytic hydrolysis of the nerve agent Sarin[6] and the simulant dimethyl methylphosphonate (previous chapter) and will only be summarized here. Most importantly, there are two binding modes of water to PONb: monodentate binding through hydrogen-bond donation to a terminal oxygen atom, and bidentate binding through hydrogen-bond donation to both a bridging oxygen atom and a terminal oxygen atom. In each binding mode, the bidentate water molecule is more strongly bound to the PONb, and therefore, our efforts focus on reaction at this site.

7.3.1.2 Formation of the PONb-H_2O-DMCP Complex

Following the adsorption of water, DMCP adsorbs onto the PONb-H_2O complex. The resulting PONb-H_2O-DMCP reagent complexes are shown in Figure 7.3. R-Osp^3, with the

lowest binding energy (55.3 kJ/mol) of the three complexes, shows a hydrogen bond between a methoxy hydrogen in DMCP and a terminal oxygen atom in PONb, as well as an electrostatic interaction between the O-sp^2 atom and a Cs atom (distance: 3.30 Å). R-Osp^2, with a slightly higher binding energy (59.6 kJ/mol), also shows a hydrogen bond between a methoxy group and a terminal oxygen. In addition, the other methoxy group donates a hydrogen bond to the water molecule. An electrostatic interaction between one of the O-sp^3 oxygen atoms and a Cs atom (distance: 3.40 Å) also stabilizes this complex.

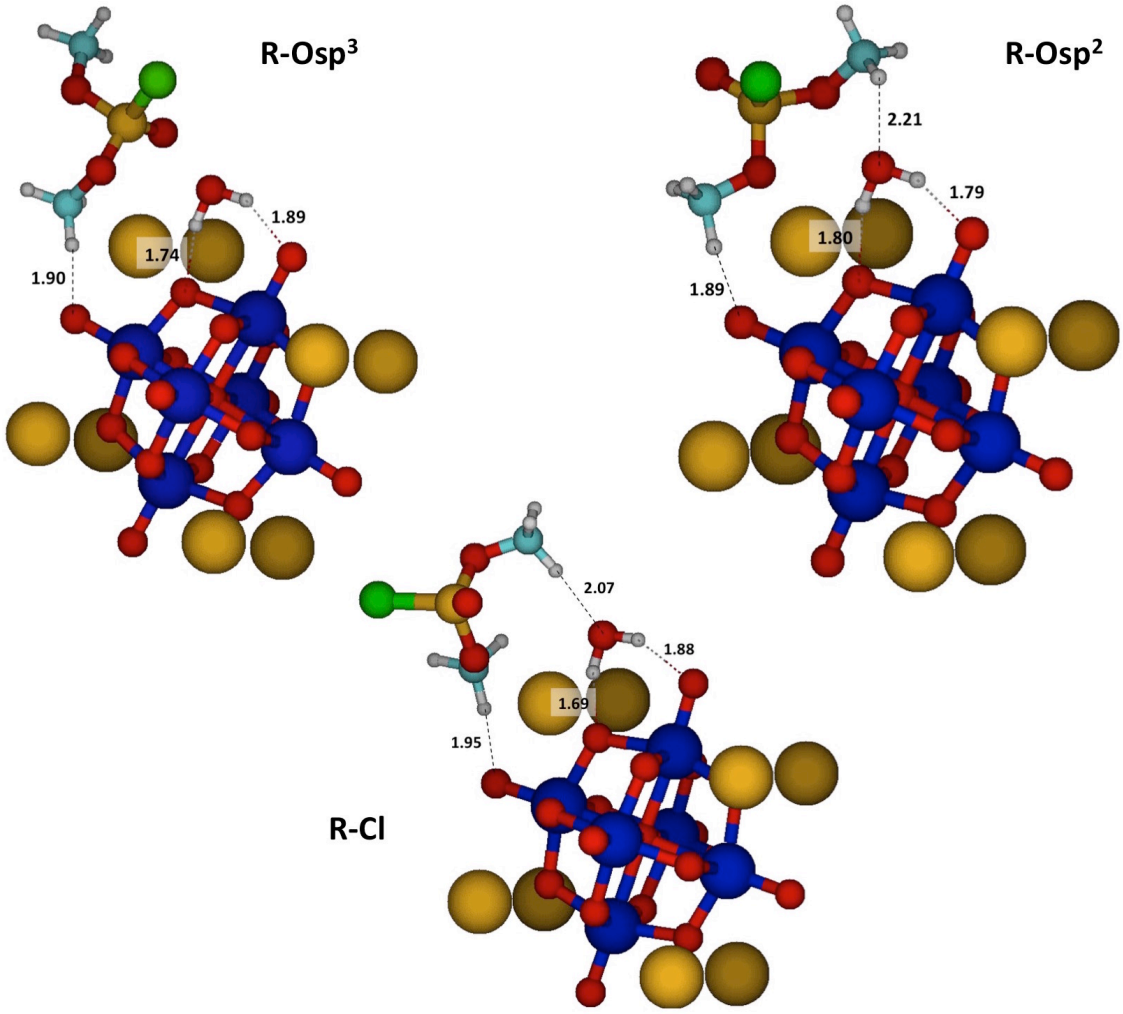

Figure 7.3. PONb-H_2O-DMCP reagent complexes with key hydrogen bonds shown, with interatomic distances given in Angstroms. Same color scheme as in Figure 7.1.

The R-Cl complex is the most stable of the three, with a DMCP binding energy of 77.8 kJ/mol. In this complex, as in R-Osp^2, two methoxy groups donate hydrogen bonds to a terminal oxygen

atom and to the oxygen atom in water. Two close electrostatic interactions (instead of one) between oxygen atoms in DMCP and Cs atoms account for the higher binding energy in R-Cl; the distance between the O-sp^2 atom and a Cs atom is 3.35 Å, and the distance between an O-sp^3 atom and a Cs atom is 3.22 Å.

7.3.1.3 Transition State

Following the formation of the PONb-H_2O-DMCP complex, cleavage of an O-H bond in water occurs, and the nascent hydroxide adds nucleophilically to the phosphorus atom. Simultaneously, the proton from the water molecule adds to the bridging oxygen atom to which the water molecule was hydrogen bonded. Figure 7.4 shows the transition state structures for DMCP hydrolysis by PONb. Relative to reagent PONb-H_2O-DMCP complexes, TS-Cl has the lowest energy barrier (28.1 kJ/mol), similar to that for Sarin hydrolysis (22.8 kJ/mol),[7] and smaller than that for DMMP (44.6 kJ/mol). The energy of TS-Cl is followed closely by TS-Osp^3 (30.3 kJ/mol). Ts-Osp^2 has a much larger hydrolysis barrier (72.6 kJ/mol).

We note here that the geometry of the TS-Osp^2 transition state did not converge in calculations using an ultrafine integration grid; thus, a superfine grid was used for the optimization of this point. The single-point energy calculation of the optimized state did, however, use an ultrafine integration grid. Since the optimized geometry is not expected to differ greatly based on integration grid, the reported single-point energy for TS-Osp^2 should be similar to that which would result from an ultrafine-optimized geometry.

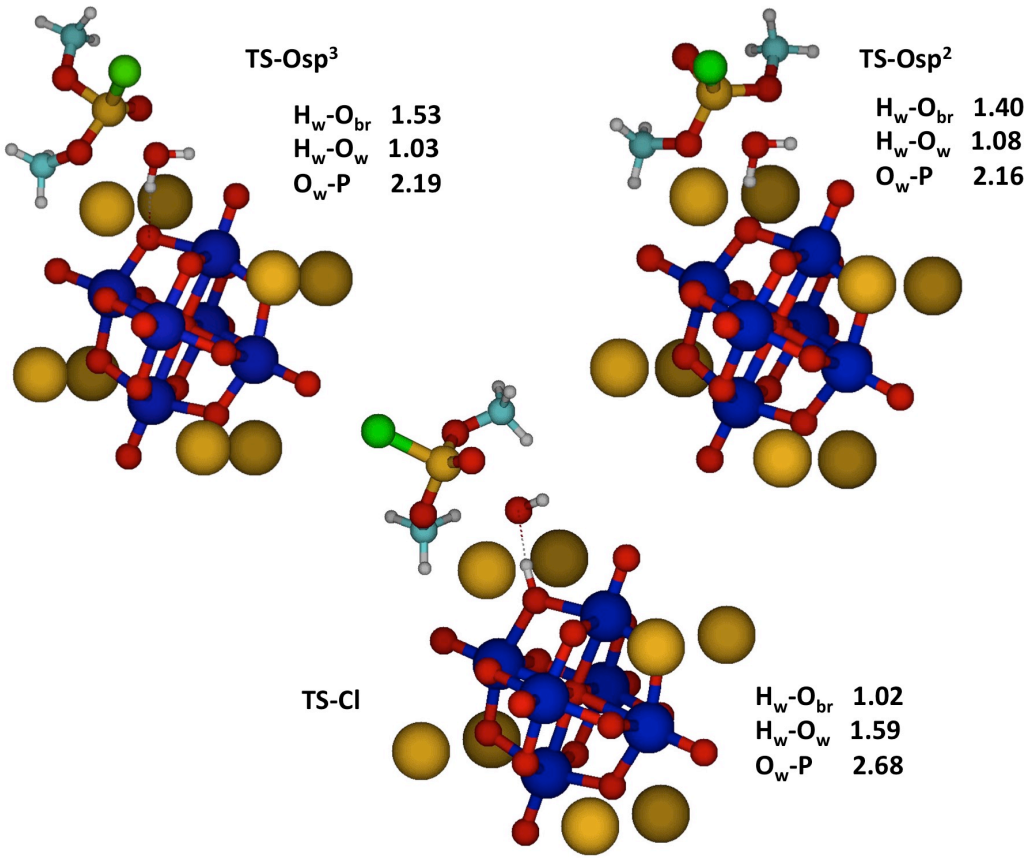

Figure 7.4. Transition state structures for DMCP hydrolysis catalyzed by $Cs_8Nb_6O_{19}$. Interatomic distances are given in Angstroms. Same color scheme as in Figure 7.1.

7.3.1.4 Adsorbed Products

Following the hydrolysis transition state, the P—Cl bond in DMCP is broken, yielding adsorbed Cl and dimethylphosphate (DMP). P—Cl bond scission occurs leading from transition state to products without a stable intermediate. This is in contrast to analogous reaction pathways for Sarin and DMMP, which include a stable pentacoordinated intermediate complex. In the stable product structures, shown in Figure 7.5, the chlorine atom remains electrostatically bound to the rest of the complex. In P-Osp^2 and P-Osp^3 species, this adsorption is through interactions between the Cl atom and the hydrogen atom in the acid P-OH group (P-OH distances: 3.42 Å for P-Osp^2, 3.12 Å for P-Osp^3) as well as between the Cl atom and a single Cs atom (3.39 Å and 3.43 Å, respectively). Conversely, in P-Cl, the Cl atom interacts electrostatically with two nearby Cs atoms (3.38 Å and 3.44 Å). As a result of this increased prevalence of counterion interactions, P-Cl is by far the most stable species in the entire reaction pathway (Figure 7.2).

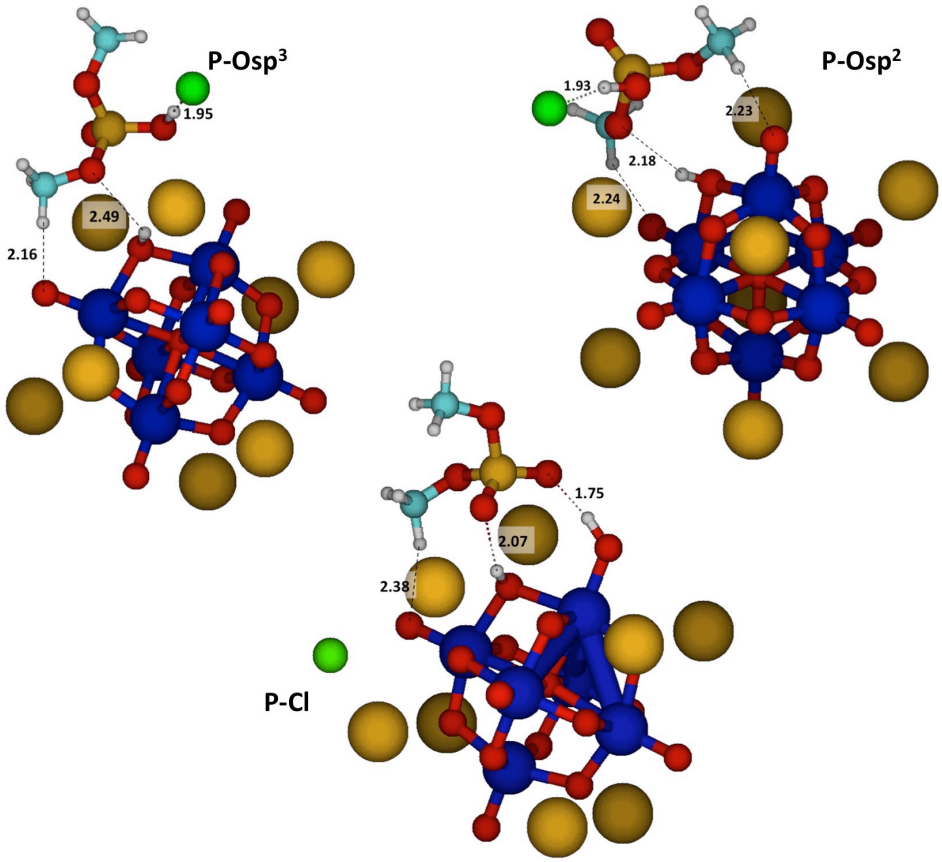

Figure 7.5. Structures of bound-product complexes in the catalytic hydrolysis of DMCP by $Cs_8Nb_6O_{19}$. Key interatomic distances are given in Angstroms. Same color scheme as in Figure 7.1.

Other notable interactions emerge in these product complexes. Interestingly, in P-Cl, DMP donates an additional proton to a nearby terminal site, yielding a diprotonated PONb. Also, in all three complexes, the hydrogen bond donated by a methoxy group to a terminal oxygen remains intact from reagents. In P-Osp^3 and P-Osp^2, this same methoxy group now accepts a hydrogen bond from the proton at the bridging oxygen site, while in P-Cl, two phosphate oxygens accept hydrogen bonds from the protons in PONb.

7.3.1.5 Reaction at a Terminal Oxygen Site

Up to this point, we have only considered catalytic hydrolysis pathways that initially involve a water molecule that is hydrogen bonded to both a bridging oxygen and a terminal oxygen in PONb, leading to protonation of a bridging oxygen on PONb at the hydrolysis transition state. In order to provide a more thorough treatment of this reaction, we now show the energetics of reaction involving a water molecule that is monodentate-bound to a terminal

oxygen atom in PONb. We consider only the pathway that involves P-OH bond formation collinear to Cl at the transition state, as that pathway has the lowest barrier leading from bound reagents to products. Figure 7.6 shows the energetics of this pathway (in red) as compared to the reaction at the bridging site, beginning with the bidentate binding of water (in black). Insets in Figure 7.6 show the structures of reagent (R), transition state (TS), and adsorbed-product (P) complexes.

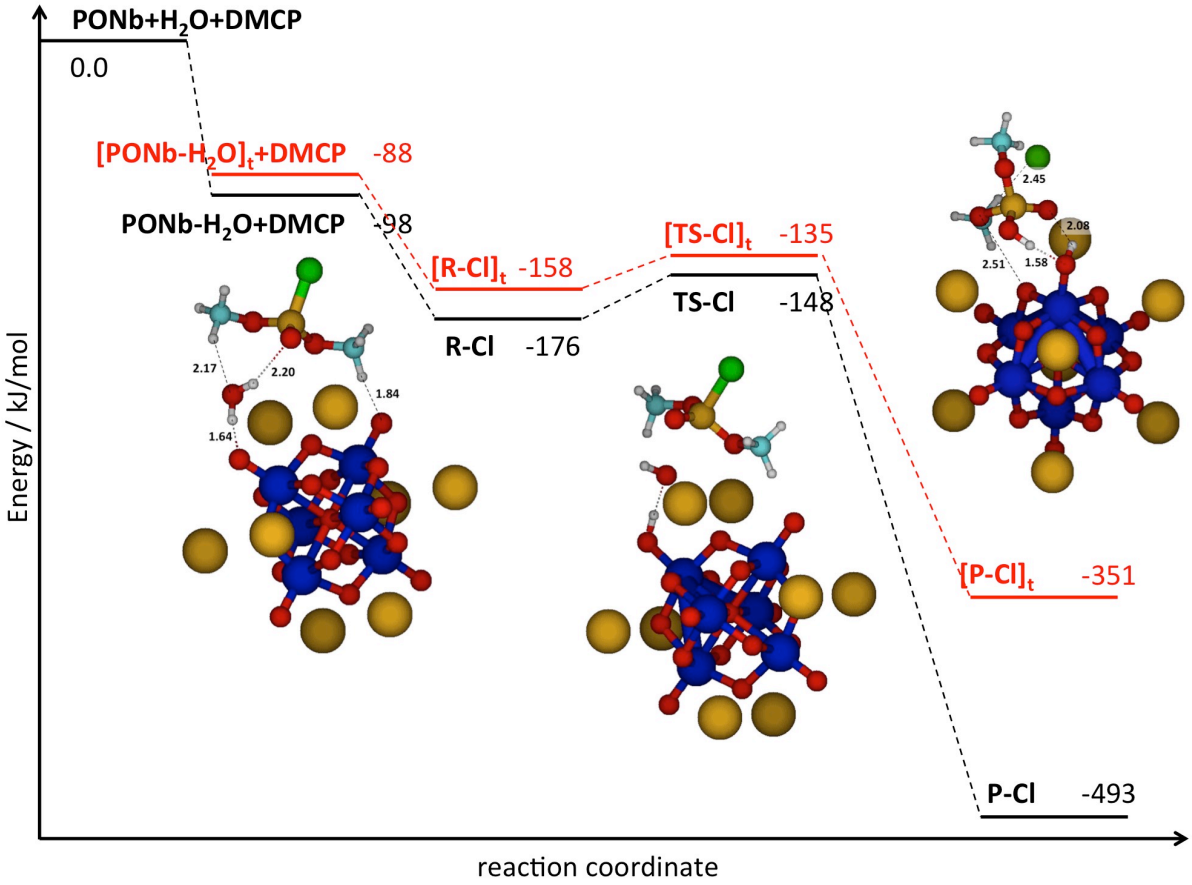

Figure 7.6. Two reaction pathways for catalytic DMCP hydrolysis by $Cs_8Nb_6O_{19}$, beginning with the adsorption of a monodentate-bound water molecule (red) and a bidentate-bound water molecule (black) to PONb. Insets show structures of reagent, transition state, and product complexes along the red pathway, with key interactions labeled with distances in Angstroms. For insets, same color scheme as in Figure 7.1. See text for nomenclature.

The energetics of the terminal reaction pathway beginning with the monodentate binding of water are similar to those of the bridging pathway, with a similar gap in energy between the pathways at all points leading from the adsorption of water through the transition state.

Conversely, the energy of the bound product structure is much lower in the terminal pathway, and this may be due to the interactions of the dissociated chlorine atom. In the terminal pathway, the chlorine atom interacts with a hydrogen atom in a methoxy group as well as a Cs atom (Cl—Cs distance: 3.41 Å). Conversely, as previously mentioned, in the bridging P-Cl pathway, the Cl atom interacts with two Cs atoms. This difference in counterion interaction and stationary-point energy is also noted when comparing P-Cl in the bridging pathway with analogous P-Osp^2 or P-Osp^3, which involve Cl-DMP interactions in place of an additional Cl-Cs interaction.

7.3.1.6 Product Desorption

Following the formation of DMP and Cl on protonated PONb, the desorption of products is required to regenerate the PONb catalyst. In the cases of P-Osp^2 and P-Osp^3, chlorine may desorb from DMP, extracting a proton from the acid P-OH group, to yield HCl and a monoprotonated PONb-DMP complex. For P-Cl, in which the PONb is diprotonated, the chlorine atom may desorb in anionic form, leaving a diprotonated PONb-DMP complex, or it may abstract a hydrogen atom from the PONb, yielding the same monoprotonated PONb-DMP complex as for P-Osp^2 and P-Osp^3. The structures for both the monoprotonated and diprotonated PONb-DMP complexes are shown in Figure 7.7. Though the diprotonated complex has an additional hydrogen bond between an O-sp^2 atom and a terminal proton as compared to the monoprotonated complex, the ionic nature of this species resulting from Cl^- desorption creates such an energy penalty as to render this complex 77 kJ/mol less favorable (Figure 7.2) than the monoprotonated complex accompanied by HCl desorption.

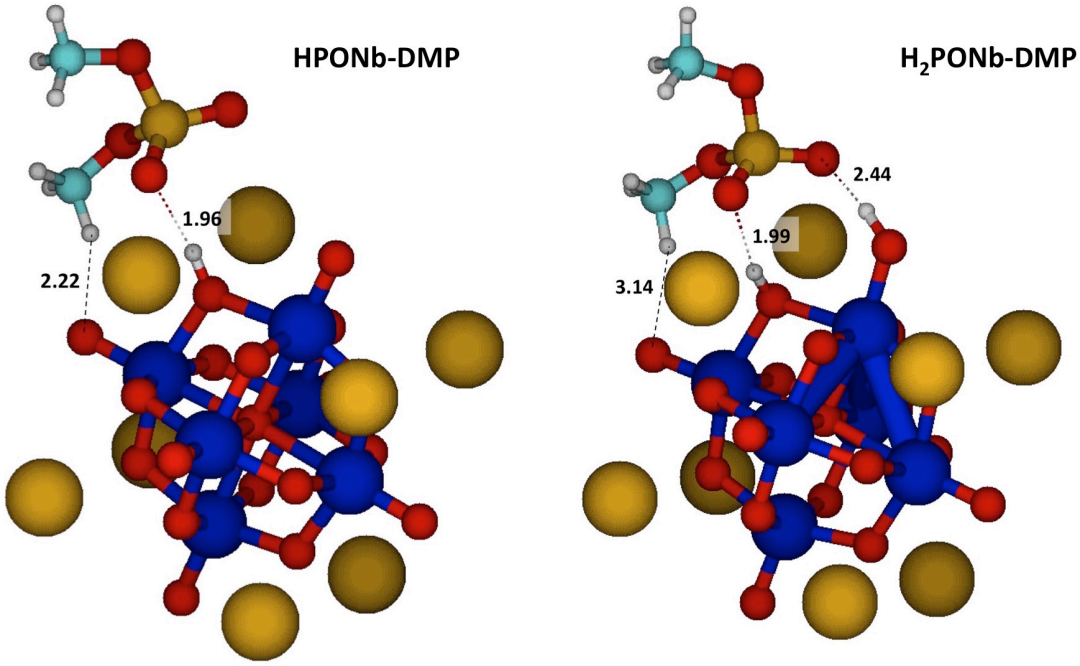

Figure 7.7. Adsorbed products of DMCP hydrolysis catalyzed by $Cs_8Nb_6O_{19}$. Key distances given in Angstroms. Same color scheme as in Figure 7.1.

Following Cl or HCl desorption, DMP desorption must occur. Hydrogen abstraction from the protonated PONb will likely accompany desorption. In HPONb-DMP, the abstraction of the proton at the bridging site to DMP results in separated products with energy 52.4 kJ/mol lower than if the proton remained on the PONb. In H_2PONb-DMP, the abstraction of the proton from the terminal (less basic) oxygen to DMP during desorption results in products 321.4 kJ/mol lower in energy than in the absence of abstraction. Overall, only one of the possible combinations of separated products yielded an energy lower than that of separated reagents—that in which both HCl and monoprotonated DMP desorb, leaving behind deprotonated PONb—a fully regenerated catalyst. It is important to note, however, that with a very high binding energy (243.2 kJ/mol), DMP likely will not desorb from the catalyst under ambient conditions, rendering the catalyst poisoned, regardless of protonation state.

7.3.2 Changes to the Catalyst During Reaction

So far, we have examined changes that occur at the site of DMCP hydrolysis. Now, we turn our view to changes in the catalyst during reaction. The highly ordered $Cs_8Nb_6O_{19}$ reagent, which has octahedral symmetry, serves as our starting point as well as our basis for comparison. In this molecule, every Nb-$O_{terminal}$ bond is identical (bond length: 1.81 Å), as is every Nb-

$O_{bridging}$ bond (2.04 Å) and every Nb-$O_{central}$ bond (2.41 Å). Furthermore, the distance between each Nb atom and its nearest Nb atom is identical (3.40 Å), as is the distance between each Nb atom and its next-nearest Nb atom (4.81 Å). Additionally, the distance between every Cs counterion and $O_{central}$ is the same (4.76 Å). As we proceed through the hydrolysis reaction pathway, however, disorder becomes introduced, and bond lengths begin to vary, as shown in Figure 7.8. In the figure, variances are reported as the square of the standard deviation from the norm for each interatomic distance. In octahedral PONb, all of the bond lengths of the same type (e.g., O_{te}-Nb, $O_{bridging}$-Nb, etc.) are identical, and thus the variances are all equal to zero. Initial adsorption of water, for example, slightly affects some interatomic distances more than others, resulting in small, nonzero variances. Conversely, in the bound-products species, one $O_{terminal}$ atom is protonated, resulting in a large decrease in Nb-$O_{central}$ distance proximal to the protonation site while the length of the other Nb-$O_{central}$ bond along the axis containing the protonated Nb-$O_{terminal}$ bond increases. This inconsistency, along with others amongst Nb-$O_{central}$ distances due to protonation and product adsorption, contributes to the large $O_{central}$-Nb variance seen in the P-Cl point in the figure. For this study, we have chosen to examine the X-Cl pathway, as it has the lowest reaction barrier at a bridging oxygen site. Further, as the variances of the first three points along the reaction pathway are insignificant for all distances considered, our discussion will begin with changes that occur at the transition state.

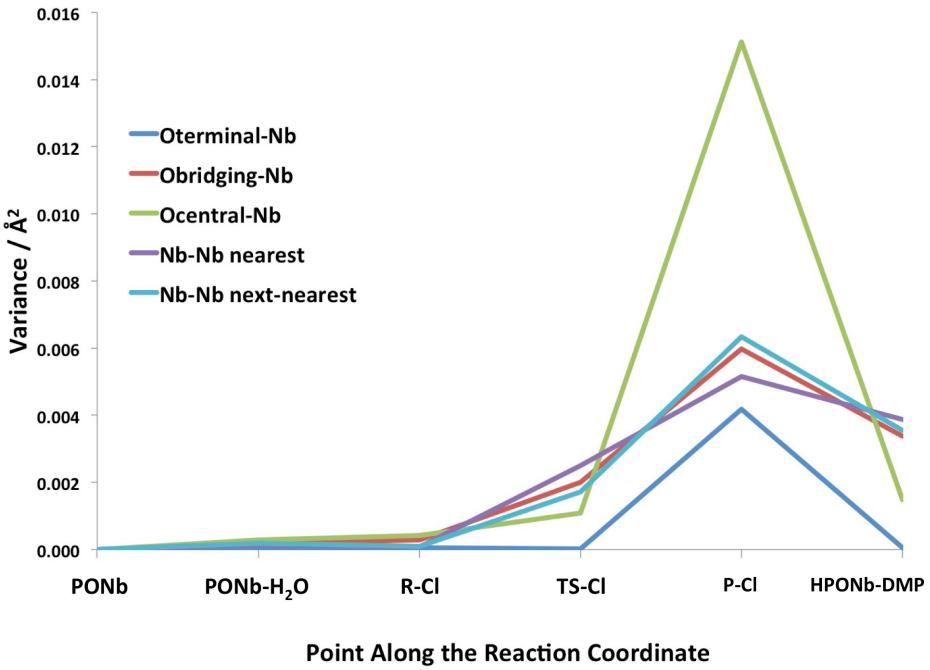

Figure 7.8. Variances in key distances in $Cs_8Nb_6O_{19}$ during catalytic DMCP hydrolysis.

7.3.2.1 Transition State

The first large-scale changes in distance are noted in the transition state, as shown in Figure 7.9. Those Nb-$O_{bridging}$ distances nearest the protonation site are significantly elongated, and those next-nearest decrease. Consequently, bonds connected to these next-nearest bonds increase, and so on. Thus, a small rippling effect is noted in the structure of the molecule, as seen in the PONb during DMMP hydrolysis (Chapter 6). At this point in the reaction, a large increase in positive charge is seen in the terminal oxygen atom which formerly accepted a hydrogen bond from the water molecule. Additionally, the increase in charge on the Cs atom interacting with the O-sp^2 atom in DMCP persists from bound reagents.

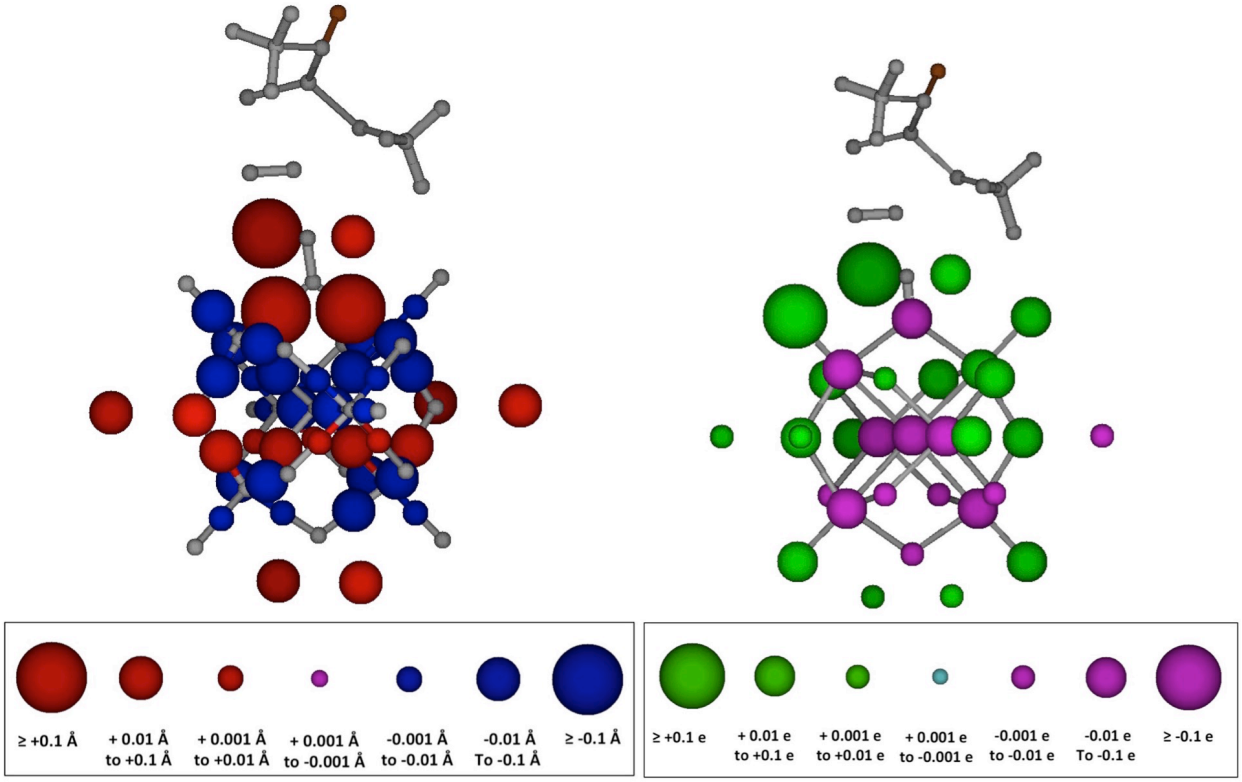

Figure 7.9. Changes in interatomic distances (left) and atomic charges (right) shown in the transition state structure of DMCP hydrolysis catalyzed by $Cs_8Nb_6O_{19}$. Changes are relative to octahedral PONb. Color/size scheme described in text.

7.3.2.2 Bound Products

After the transition state, the chlorine atom is eliminated from DMCP leading to bound products, as described earlier in this text. For the X-Cl pathway, a second protonation also occurs at a terminal oxygen atom. Further, a great amount of disorder is introduced into the catalyst, as seen in Figure 7.8. Consequently, we note many significant changes in the structure and charges of the catalyst at the bound-products point in the reaction, as shown in Figure 7.10. All the Nb-O bonds nearest protonation sites are greatly elongated relative to octahedral. The rippling effect is even more pronounced than before, with great decreases in Nb-O distances next-nearest the protonation sites as well as great increases in Nb-O distances adjacent to these next-nearest bonds.

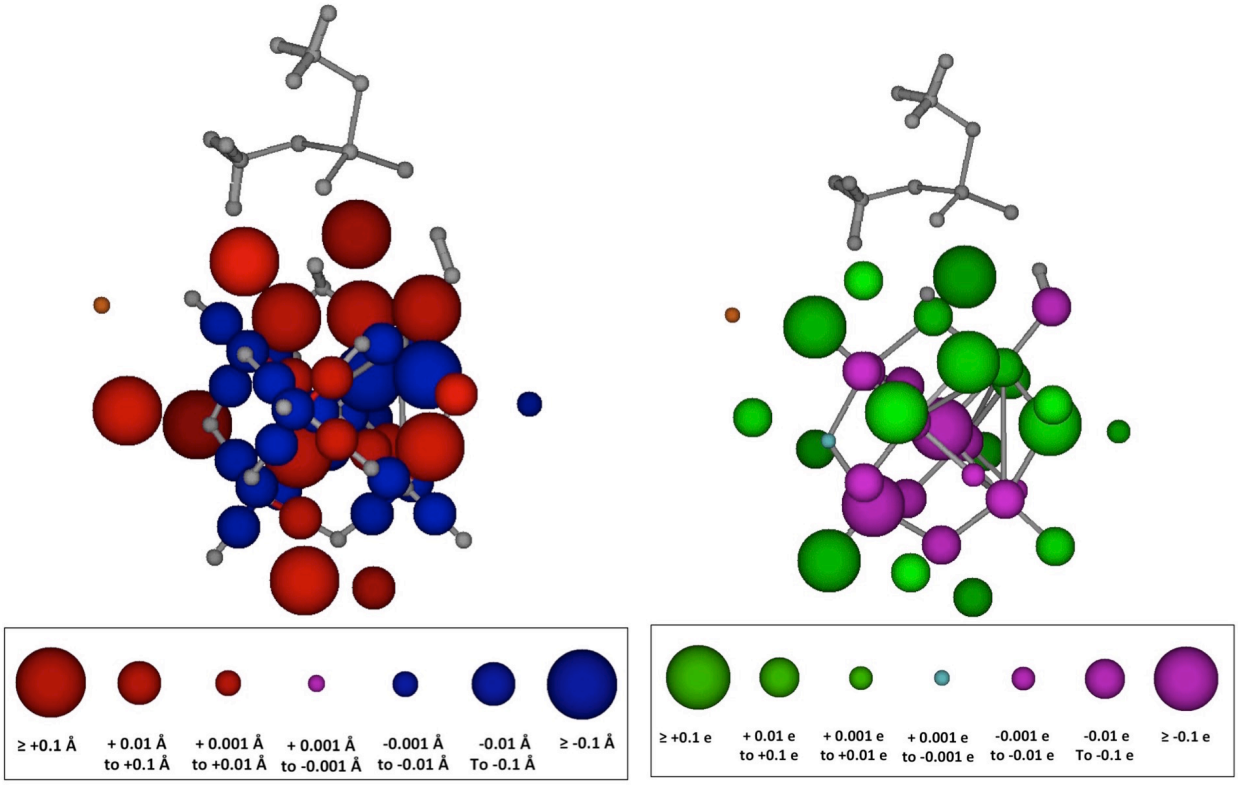

Figure 7.10. Changes in interatomic distances (left) and atomic charges (right) in $Cs_8Nb_6O_{19}$ due to adsorbed products of DMCP hydrolysis. Color/size scheme described in the text.

An entire region of Nb-O bond shortening can be seen near the site of Cl (shown in brown) adsorption. This calls to question the relative influences of protonation and adsorption on the structure of the catalyst. Figure 7.11 shows changes in the catalyst due to protonation at the same sites as in the adsorbed product structure, only this time in the absence of adsorbed products. The structural changes seen in P-Cl, including significant rippling as well as the entire region of bond shortening are also shown in the non-adsorbing diprotonated catalyst, affirming the predominant role of protonation in changes to the catalyst structure.

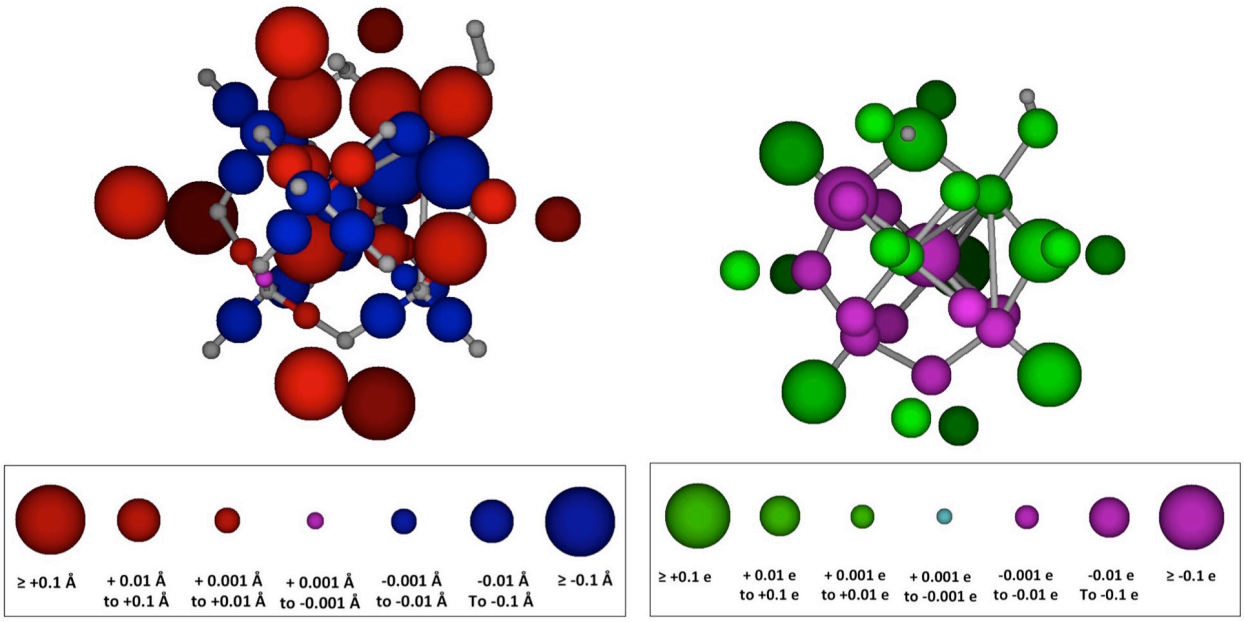

Figure 7.11. Changes in interatomic distances (left) and atomic charges (right) in $Cs_8Nb_6O_{19}$ due to protonation at a bridging oxygen atom and an adjacent terminal oxygen atom. Color/size scheme described in the text.

Differences in atomic charges are evident, however, between the bound-product catalyst and the non-bound diprotonated catalyst. While both species show an increase in positive charges in the region nearest the protonation sites and an increase in negative charges away from protonation sites, some effects of adsorption are seen. For example, in the diprotonated catalyst, a significant increase in positive charge is seen at the protonated $O_{bridging}$ atom, where a less significant increase is seen in this atom on the product-adsorbed catalyst. Also, the non-protonated $O_{terminal}$ atom nearest the protonated $O_{bridging}$ atom is bound to a Nb atom which shows a significant increase in negative charge relative to the octahedral PONb, whereas this increase is minor in the adsorbed catalyst. Thus, as is the case in DMMP hydrolysis by PONb, protonation appears to dominate structural and charge differences, while adsorption plays a secondary moderating role. For the adsorbed-product catalyst, average charge differences relative to octahedral PONb are as follows: Cs: +0.0432 e, Nb: -0.0294 e, $O_{bridging}$: +0.0140 e, $O_{terminal}$: +0.0905 e, $O_{central}$: -0.1074 e. Similarly, in the diprotonated, non-adsorbing catalyst differences are: Cs: +0.0550 e, Nb: -0.0066 e, $O_{bridging}$: +0.0125 e, $O_{terminal}$: +0.1433 e, $O_{central}$: -0.1301 e. We note that in both cases, all Cs atoms increase in positive charge relative to the octahedral case.

Following desorption of chlorine, DMP remains bound to the monoprotonated catalyst as shown in Figure 7.12, and we see from Figure 7.8 a restoration of order near to that seen in the transition state. Structural and atomic charge changes for this bound state, shown in Figure 7.12, are similar to those seen in the transition state (Figure 7.9). A notable exception, however, shows all negative changes in Nb atom charges and all positive changes in Cs atom charges in the DMP-bound PONb. This level of similarity suggests that, at the transition state, protonation of the PONb is nearly complete. For DMP bound to the monoprotonated PONb, charge differences relative to the octahedral PONb are: Cs: +0.0313 e, Nb: -0.0484 e, $O_{bridging}$: +0.0029 e, $O_{terminal}$: +0.0722 e, $O_{central}$: -0.0146 e. In Chapter 6, we examined the changes in distances and charges in a non-adsorbed, $O_{bridging}$-protonated PONb (Figure 6.16). Noting similar changes in both the DMP-monoprotonated PONb and the same PONb in the absence of adsorbed DMP, we again attribute the greatest effects on PONb structure and charge during this stage of DMCP hydrolysis to protonation.

Importantly, we note in this complex that bridging oxygen atoms in the hemisphere of PONb opposite that of DMP binding are more basic than those in the octahedral PONb, while terminal oxygen atoms in this region are more positive. This carries with it implications of the PONb as a host for a second hydrolysis reaction with DMCP. Although adsorption energies for the second set of water and DMCP molecules in this region may be lower than those for the first due to the increased charge on $O_{terminal}$, activation of the bound-reagents complex may see a lower barrier as a result of the increased negative charge on $O_{bridging}$. Thus, while product binding energies suggest the poisoning of the site on the PONb to which DMP is adsorbed, hydrolysis of a second DMCP molecule by the poisoned PONb is likely, and might perhaps entail a lower barrier.

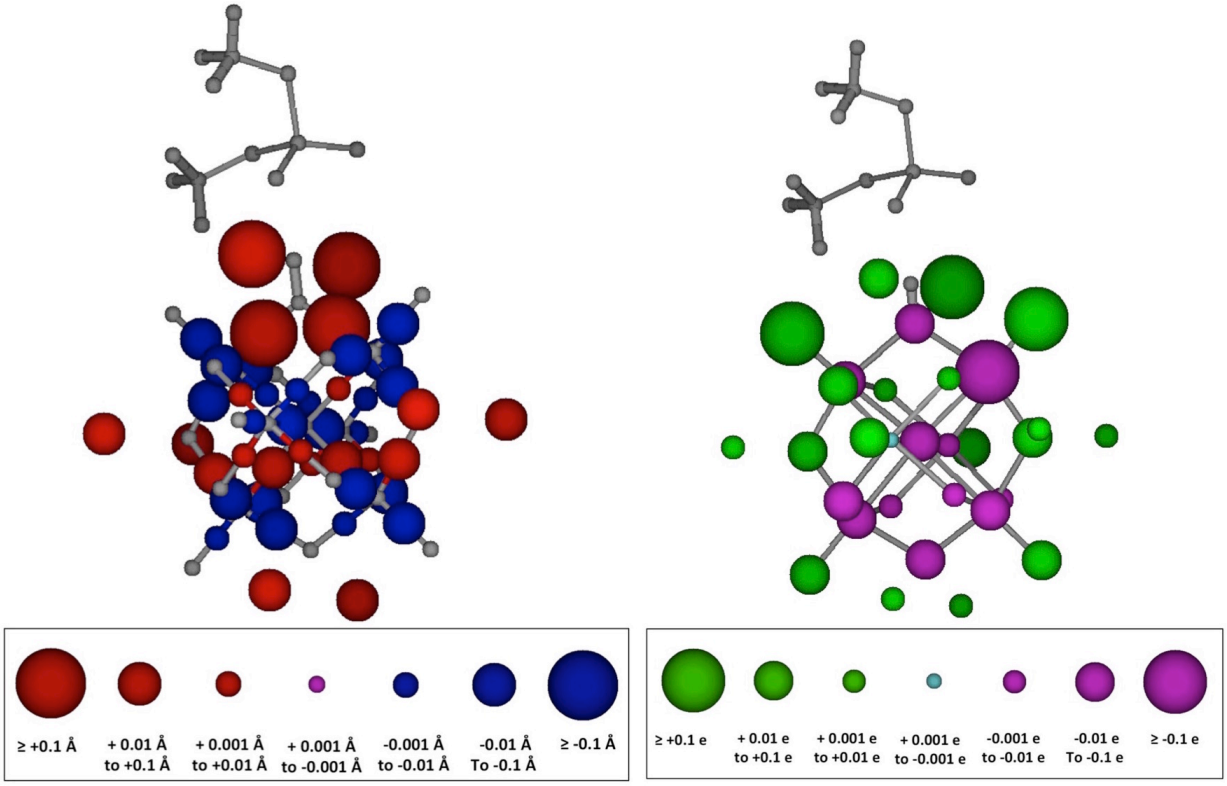

Figure 7.12. Dimethyl phosphate bound to monoprotonated $Cs_8Nb_6O_{19}$. Left: Changes in interatomic distances shown as colored spheres. Right: Changes in atomic charges shown as colored spheres. Full description of color/size scheme in text.

7.4 Comparison of Minimum-Energy Reaction Pathways for GB and Simulants

In chapters 5 and 6, we described the reaction pathways for the hydrolysis of GB and the simulant DMMP, respectively, on the surface of $Cs_8Nb_6O_{19}$. We continued with an analogous discussion for DMCP in this chapter. Our discussion of heterogeneous gas—solid reactions with these compounds now concludes with a comparison of their minimum-energy reaction pathways. Figure 7.13 shows the energetics of pathways with the lowest rate-limiting barrier for GB, DMMP, and DMCP on the surface of $Cs_8Nb_6O_{19}$.

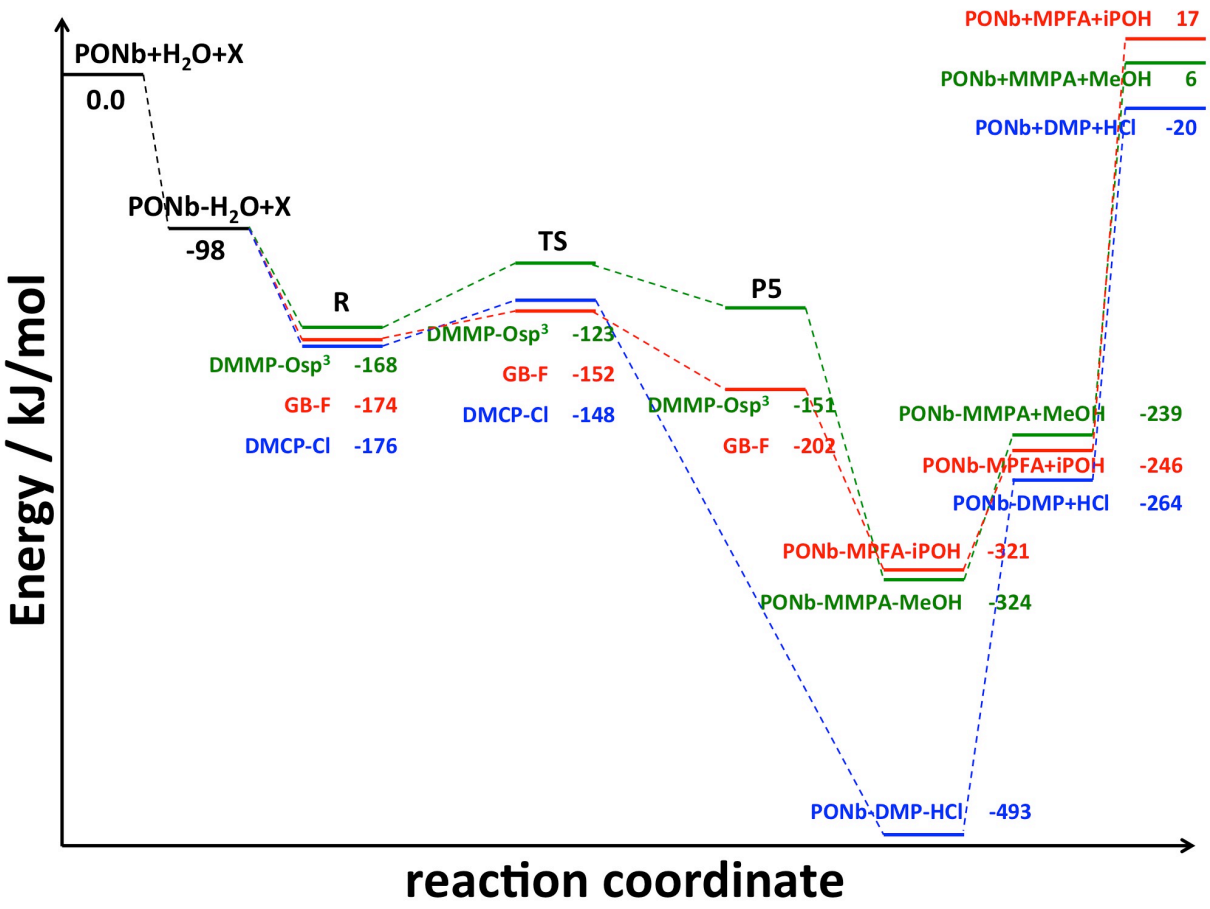

Figure 7.13. Minimum-energy reaction pathways for hydrolysis of GB (red), DMMP (green), and DMCP (blue), by $Cs_8Nb_6O_{19}$.

For the three pathways, the mechanisms of hydrolysis are very similar: initial water adsorption is followed by agent or simulant adsorption and a subsequent rate-limiting transition state leading to the formation of strongly bound products. The binding energies of the agent or simulant molecules to the PONb-H_2O complex is similar in all three pathways, but the energetics begin to diverge at the transition state. While the barriers for GB and DMCP hydrolysis are very similar, at 22.8 kJ/mol and 28.1 kJ/mol, respectively, that for DMMP is much greater—44.6 kJ/mol. Considering that the rate-limiting step determines the overall rate of reaction, the similarity to GB in this barrier makes DMCP a much better simulant than DMMP.

Following the transition state, a mechanistic difference emerges, as both DMMP and GB pathways reveal stable pentacoordinated intermediates before product formation, while DMCP does not. Instead, product formation results directly from the activation of the bound-reagents complex in DMCP hydrolysis.

Next, bound-product complexes remain the most stable stationary points along each of the three reaction pathways, although the energy of the PONb-DMP-HCl complex in DMCP hydrolysis is much lower than for the analogous complexes in GB and DMMP hydrolysis. As such, in order to desorb HCl, an energetic cost of 228.7 kJ/mol must be incurred. Conversely, desorption of gaseous alcohol products require energies of 75.5 kJ/mol and 85.0 kJ in the GB and DMMP pathways, respectively. Thus, desorption of HCl is much less likely than iPOH or MeOH without thermal treatment of the reaction system. Following desorption of these small molecules, all three pathways show similar large desorption energies of organophosphorus products.

7.5 Concluding Remarks

In this work, we described the energetics and structures of several reaction pathways for the gas-phase hydrolysis of DMCP, as catalyzed by $Cs_8Nb_6O_{19}$. In a similar mechanism to GB and DMMP hydrolysis by the same catalyst, initial adsorption of water is followed by adsorption of the simulant. Likewise, a rate-limiting transition state shows concerted protonation of the PONb and nucleophilic addition of a nascent OH to the tetrahedral phosphorous atom as the bound water molecule reacts. In the pathway discussed in this chapter, however, this rate-limiting step is accompanied by dissociation of the P-Cl bond in DMCP, whereas the transition state in GB and DMMP hydrolysis leads to a pentacoordinated-phosphorous intermediate. Once formed, products remain strongly bound to the PONb.

After a discussion of the reaction pathway for DMCP hydrolysis by PONb, we explained changes in the catalyst during the course of reaction for the lowest-barrier pathway. As in the catalytic hydrolysis of DMMP by PONb, we find that changes in the catalyst are dominated by protonation that occurs during reaction, yet these changes are moderated by interactions with adsorbed species. As these results are for the gas-phase, future work is needed to describe similar reactions in solution. In the next chapter, we return our focus to GB hydrolysis by $Cs_8Nb_6O_{19}$, only this time in both heterogeneous gas—solution and homogeneous solution-phase environments. The inclusion of explicit-solvent water molecules will allow us to describe the role of not only solvent molecules but also Cs counterions on reaction energetics.

7.6 References

(1) Jang, Y. J.; Mulay, S. V.; Kim, Y.; Jorayev, P.; Churchill, D. G. *New Journal of Chemistry* **2017**.

(2) Zhou, X.; Zeng, Y.; Liyan, C.; Wu, X.; Yoon, J. *Angewandte Chemie International Edition* **2016**, *55*, 4729.

(3) Arcibar-Orozco, J. A.; Giannakoudakis, D. A.; Bandosz, T. J. *Advanced Materials Interfaces* **2015**, *2*, n/a.

(4) Wilmsmeyer, A. R.; Uzarski, J.; Barrie, P. J.; Morris, J. R. *Langmuir* **2012**, *28*, 10962.

(5) Frisch, M. J.; Trucks, G. W.; Schlegel, H. B.; Scuseria, G. E.; Robb, M. A.; Cheeseman, J. R.; Scalmani, G.; Barone, V.; Mennucci, B.; Petersson, G. A.; Nakatsuji, H.; Caricato, M.; Li, X.; Hratchian, H. P.; Izmaylov, A. F.; Bloino, J.; Zheng, G.; Sonnenberg, J. L.; Hada, M.; Ehara, M.; Toyota, K.; Fukuda, R.; Hasegawa, J.; Ishida, M.; Nakajima, T.; Honda, Y.; Kitao, O.; Nakai, H.; Vreven, T.; Montgomery Jr., J. A.; Peralta, J. E.; Ogliaro, F. ß.; Bearpark, M. J.; Heyd, J.; Brothers, E. N.; Kudin, K. N.; Staroverov, V. N.; Kobayashi, R.; Normand, J.; Raghavachari, K.; Rendell, A. P.; Burant, J. C.; Iyengar, S. S.; Tomasi, J.; Cossi, M.; Rega, N.; Millam, N. J.; Klene, M.; Knox, J. E.; Cross, J. B.; Bakken, V.; Adamo, C.; Jaramillo, J.; Gomperts, R.; Stratmann, R. E.; Yazyev, O.; Austin, A. J.; Cammi, R.; Pomelli, C.; Ochterski, J. W.; Martin, R. L.; Morokuma, K.; Zakrzewski, V. G.; Voth, G. A.; Salvador, P.; Dannenberg, J. J.; Dapprich, S.; Daniels, A. D.; Farkas, O.; Foresman, J. B.; Ortiz, J. V.; Cioslowski, J.; Fox, D. J.; Gaussian, Inc.: Wallingford, CT, USA, 2009.

(6) Chapleski, R. C.; Musaev, D. G.; Hill, C. L.; Troya, D. *The Journal of Physical Chemistry C* **2016**, *120*, 16822.

(7) Chapleski, R. C.; Zhang, Y.; Troya, D.; Morris, J. R. *Chemical Society Reviews* **2016**, *45*, 3731.

Chapter 8

Mechanistic Insight for Hydrolysis of Sarin by $Cs_8Nb_6O_{19}$ in Heterogeneous Gas—Solution and Homogeneous Solution-Phase Environments

Abstract

We present reaction pathways for the hydrolysis of Sarin (GB) by $Cs_8Nb_6O_{19}$ (PONb) in the presence of solvent water molecules. Beginning with a heterogeneous gas—solution pathway, we adsorb gas-phase GB onto explicitly solvated PONb at a site that limits interaction with Cs counterions. We find that, while the overall hydrolysis mechanism does not change, all energies along the reaction pathway are shifted upwards, towards the reagents' asymptote, as a consequence of PONb solvation. Then, we extend our solvation model to include GB as well, in an effort to describe the homogeneous solution-phase reaction. We find a different mechanism, one in which a water molecule adds to GB prior to protonation of PONb in a subsequent step. Finally, we discuss the possible role of a specific base mechanism for GB hydrolysis by PONb.

8.1 Introduction

Previous theoretical work has examined the base-catalyzed hydrolysis of Sarin (GB) by $Cs_8Nb_6O_{19}$ in the gas phase (Figure 5.2).[1] Therein, a mechanism was revealed in which a water molecule adsorbs onto a $Cs_8Nb_6O_{19}$ molecule (PONb), forming a bound-water complex (PONb-H_2O) via hydrogen bond donation to a basic oxygen site on PONb. GB can adsorb to this complex via interactions with both the niobate core and Cs counterions, as well as the bound water molecule, to form a bound-reagents complex (R). From this R complex, reaction proceeds through a transition state in which the bound water molecule reacts to donate a proton to a basic oxygen site on $Cs_8Nb_6O_{19}$ while the nascent hydroxide adds nucleophilically to the phosphorus atom in GB. This transition state leads to a pentacoordinated trigonal bipyramidal phosphorus intermediate (P5), which can readily decompose into either isopropanol (iPOH) or HF and a phosphonic acid (methyl phosphonofluoridic acid (MPFA) or isopropyl methyl phosphonic acid (IMPA), released with iPOH and HF, respectively). These phosphonic acid products remain

bound to $Cs_8Nb_6O_{19}$ with binding energies in excess of 220 kJ/mol. This irreversible product adsorption suggests that the catalyst is poisoned as a result, preventing catalytic turnover.

Solid $Cs_8Nb_6O_{19}$ has water molecules incorporated into its crystal structure— 14 H_2O for each PONb.[2] The effect of these crystallization water molecules on the reaction mechanism was also investigated in the above study, using density functional theory methods along with insight from experimental crystal structures.[1,2] While attending water molecules did not affect the overall hydrolysis mechanism of Sarin, the energies of all stationary points were shifted upward towards the reagents' asymptote relative to the dehydrated system, leading to lower binding energies of all adsorbed intermediates and products (Figure 5.15). Further, an increase of 8 kJ/mol in the rate-limiting barrier was noted as a result of the presence of crystalline water molecules. These effects were attributed to the screening of electrostatic interactions, including those between the adsorbates and the Cs counterions.

In an effort to further understand the nature of changes in reaction energy due to the presence of attending water molecules, we have expanded the crystallization model implemented previously. By increasing the number of explicit water molecules surrounding $Cs_8Nb_6O_{19}$ prior to the introduction of GB, we are able to model a solvated polyoxoniobate salt species. Examining the hydrolysis reaction between this solvated species and a gas-phase GB molecule thus provides a picture of the heterogeneous reaction at the gas—solution interface. For the sake of comparison with hydrolysis in the dehydrated catalyst, we have examined this reaction at a bridging oxygen (O_b) site on the solvated polyoxoniobate along the pathway described in the previous study in which the P-OH bond that forms at the transition state is collinear with the existing P-F bond. This pathway was the one with the lowest rate-limiting barrier in the gas phase. The energetics of this reaction pathway for the dehydrated and solvated-PONb systems are summarized as the black and blue traces, respectively, in Figure 8.1.

8.2 Computational Details

All electronic structure calculations were performed with the Gaussian 09 suite of software[3] using the M06-L density functional and a superfine integration grid. Geometries of all structures were optimized with the application of the 6-31G(d,p) basis set for nonmetal atoms and the Lanl2dz basis set and pseudopotentials for metal atoms. Stationary points along the potential energy surface were confirmed through the examination of vibrational frequencies calculated at this level subsequent to geometry optimization. To further account for the effects of

interatomic interactions along the solvated-PONb pathway, single-point energies were corrected through calculations implementing diffuse functions on the nonmetal atoms. Thus, single point energies are reported at the M06-L/6-31++G(d,p)—Lanl2dz level of theory for the gas—solution reaction, using optimized geometries and zero-point energies from M06-L/6-31G(d,p)—Lanl2dz calculations. A similar correction with the larger basis set was not possible for all stationary points in the homogeneous solution-phase reaction reported herein. Thus, M06-L/6-31G(d,p)—Lanl2dz energies are reported for this system, unless otherwise noted.

8.2.1 Solvation model

Although contact-ion paring has been shown between $[Nb_6O_{19}]^{8-}$ and Cs counterions in solution,[4-6] the Cs counterions are likely to dissociate somewhat, potentially leaving reactive sites on the niobate core exposed for reaction with GB without involvement of nearby Cs counterions. In order to obtain an initial guess for density functional theory optimization calculations on the structure of the solvated PONb, a molecular dynamics (MD) simulation was performed in which octahedral $Cs_8Nb_6O_{19}$ was placed in a 3.0 nm x 3.0 nm x 3.0 nm periodic box and solvated with water molecules. In this simulation, forcefield parameters for solvent water molecules were assigned according to the SPC/E water model.[7] Equilibrium covalent bond lengths and angles in $[Nb_6O_{19}]^{8-}$ were assigned according to geometries optimized using electronic structure calculations for the geometry of octahedral PONb (Figure 5.1), as were atomic charges. During the simulation, bond lengths and atoms in the niobate anion were frozen at their equilibrium values of Lennard-Jones terms. Oxygen atoms in the SPC/E water model were used for all atoms in $[Nb_6O_{19}]^{8-}$. For Cs^+ counterions, charges resulting from the optimized geometry of electronic structure calculations were assigned, and Lennard-Jones parameters from the AMBER forcefield[8] were used.

A classical NVT simulation was then initiated using GROMACS molecular dynamics software[9,10] at a temperature of 300 K with 1-fs timesteps. Shortly after the beginning of the simulation, a snapshot was taken which showed Cs counterions beginning to dissociate from the core, leaving a bridging oxygen site out of the vicinity of any counterions. From this snapshot, the coordinates of the niobate core, the Cs counterions, and a shell of 34 water molecules at a distance less than 8.5 Å from the central oxygen in the niobate core were taken as the initial guess for a density functional theory optimization.

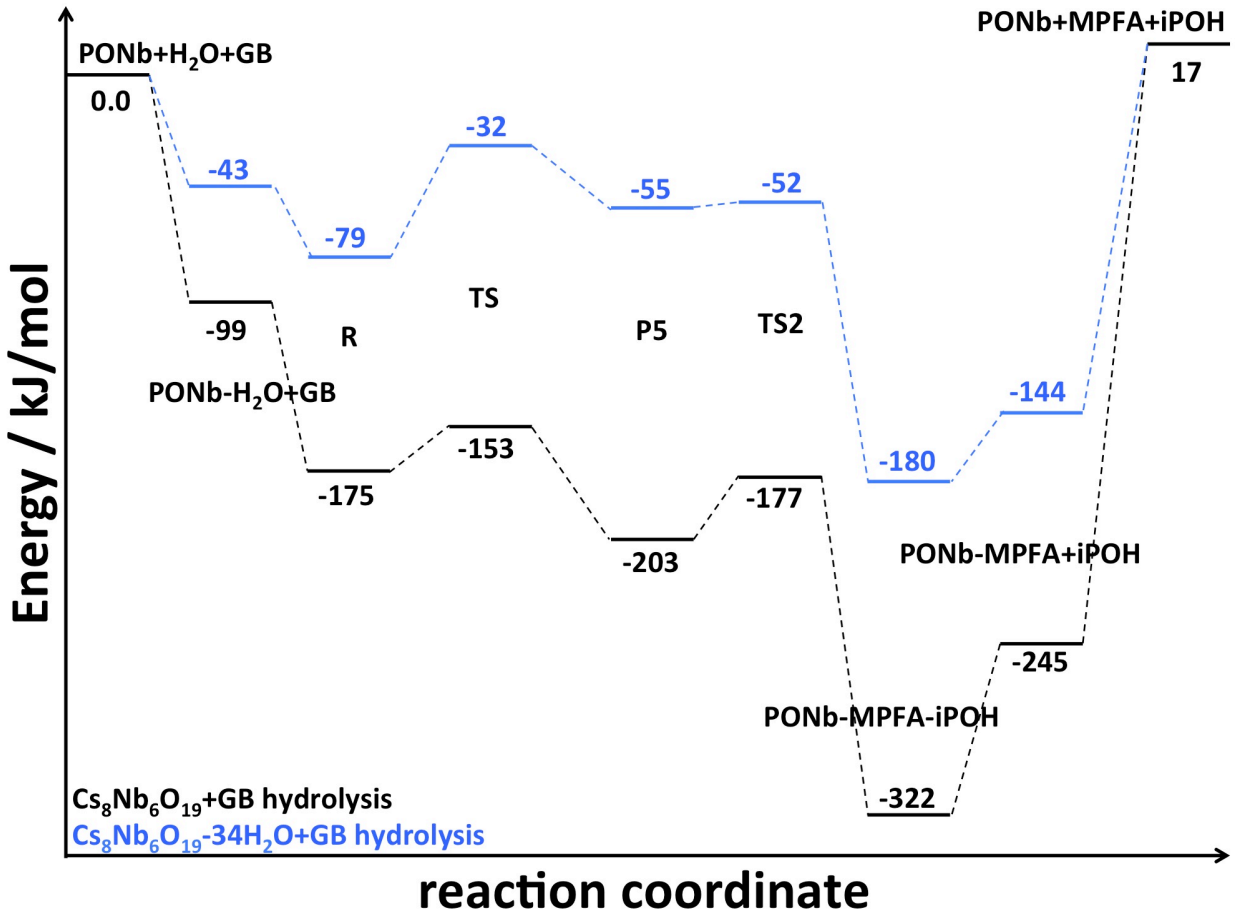

Figure 8.1. M06-L/6-31++G(d,p)—Lanl2dz//6-31G(d,p)—Lanl2dz reaction pathway for the base hydrolysis of *(S)*-Sarin (GB) by $Cs_8Nb_6O_{19}$. Black pathway: In the absence of attending water molecules. Blue: With explicit water solvent molecules surrounding $Cs_8Nb_6O_{19}$ prior to GB adsorption. See text for description of solvation model.

8.3 Results

8.3.1 Heterogeneous Gas—Surface Hydrolysis

8.3.1.1 Bound-water Complex

The results of the DFT optimization subsequent to the MD simulation give the structure of the bound-water complex (PONb-H_2O), shown in Figure 8.2. The previous theoretical work notes that, in gas—solid systems, both in the presence and absence of crystalline water molecules, Cs-O_{water} interactions stabilize the binding of water to form this complex.[1] We have designed our solution model, however, so that there are no nearby Cs counterions to provide such stabilization. Instead, solvent water molecules interact with the water molecule that will react in the hydrolysis step of the reaction. It should be noted that the previous theoretical study

of GB hydrolysis by PONb at an O_b site showed bidentate water adsorption to the PONb core. Conversely, our PONb-H_2O complex did not reveal any such water molecules which were hydrogen-bonded to both an O_b and a terminal oxygen (O_{te}) on PONb. As such, the water molecule we selected for reaction with GB in the solvated-PONb system is bound to an O_b as well as three solvating water molecules through hydrogen bonds. This reacting water molecule is identified with a white asterisk in Figure 8.2. The reacting water molecule donates two hydrogen bonds—one to O_b and the other to the oxygen atom of a solvent water molecule—and accepts two hydrogen bonds from two solvent water molecules. With the nearest Cs counterion over 5.2 Å away, this water molecule has a binding energy of 43 kJ/mol, about 56 kJ/mol weaker than in the PONb-H_2O complex without attending water molecules. The optimization of the solvated catalyst in the absence of the reacting water molecule yielded the structure of the catalyst before the adsorption of this water molecule, i.e., PONb, in the pathway shown in Figure 8.1.

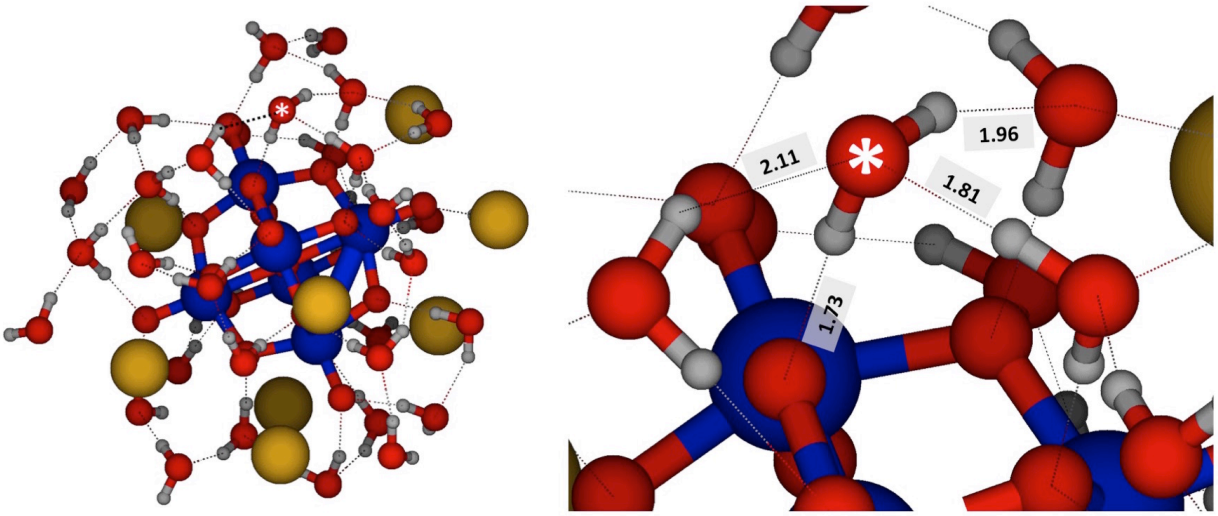

Figure 8.2. $Cs_8Nb_6O_{19}$ solvated by 34 explicit water molecules. The water molecule which reacts during GB hydrolysis is marked with a white asterisk. The right panel shows a zoomed-in region of the left panel and identifies key hydrogen-bonding interactions with interatomic O-H distances, given in Angstroms. Color scheme: Nb: blue, O: red, Cs: yellow, H: gray.

8.3.1.2 Bound-reagents Complex

GB was added to the PONb-H_2O complex at the site of the reacting water molecule, forming the bound-reagents complex, R, from which reaction proceeded. Previous work that

explored the hydrolysis of GB with $Cs_8Nb_6O_{19}$ (Chapter 5) investigated the reaction involving four different bound-reagents complexes, resulting from the binding of GB in four different orientations. Therein, the orientation in which the P-F bond in GB is collinear with the forming P-OH bond in the rate-limiting transition state was found to yield the lowest energy reaction barrier. Thus, this work will continue only with reactions along an analogous pathway, with a GB binding orientation such that the P-F bond and the forming P-OH bond are collinear at the transition state.

The bound-reagents complex in the solvated-PONb reaction pathway is shown in Figure 8.3. Whereas this complex exhibited direct interactions between GB and the niobate core, Cs counterions, and the water molecule for dry system, only direct interactions between GB and water molecules are present in the system with solvated $Cs_8Nb_6O_{19}$. In this complex, one of the water molecules that had donated a hydrogen bond to the rearranging water molecule in PONb-H_2O now interacts with the sp^2-hybridyzed oxygen atom on GB. A hydrogen bond between another solvent water molecule and the sp^3-hybridized oxygen in the isopropoxy group in GB is also present, as is one between the methyl group and the oxygen atom in the water molecule which reacts in the rate-limiting step. Along with the absence of interactions between GB and Cs counterions comes, as in the PONb-H_2O complex, a decrease in binding energy. GB binds with an energy of 36 kJ/mol, which is 40 kJ/mol less than the analogous binding energy in the dry catalyst.

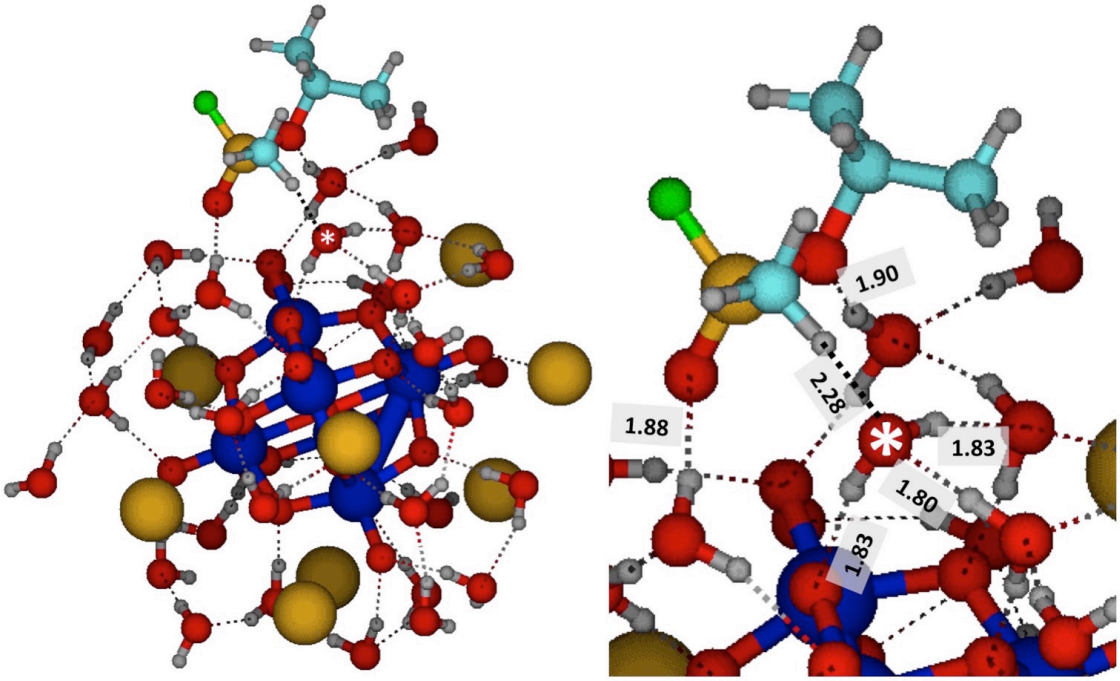

Figure 8.3. Optimized structure resulting from the binding of GB to solvated $Cs_8Nb_6O_{19}$ (R-complex). A white asterisk labels the oxygen atom of the water molecule which will react during the hydrolysis step. The right panel shows a zoomed-in region of the left panel and identifies key hydrogen bonding interactions with interatomic O-H distances, given in Angstroms. Same color scheme as in Figure 8.2, with C: cyan, P: gold, F: green.

8.3.1.3 Hydrolysis Transition State

Activation of the R complex involves the protonation of a basic O_b atom on the PONb core concurrent with the nucleophilic addition of the nascent hydroxide to the phosphorus atom on GB. The structure of this transition state is shown for the solvated-PONb system in Figure 8.4. During this step, the sp^2-hybridized oxygen atom acquires a full negative charge. In the dehydrated system, this increase in negative charge facilitates a stronger interaction with a nearby Cs counterion than in the preceding R complex, resulting in stronger adsorption of the GB moiety at the transition state and, consequently, differential transition-state stabilization. Conversely, the solvated-PONb system, by design, has no counterions vicinal to the reaction site. Instead, a solvent water molecule donates a hydrogen bond to the sp^2-hybridized oxygen atom on the GB moiety. Thus, in the absence of PONb-O_{sp2} interactions, GB adsorption to PONb is likely not greatly increased at the transition state. As such, the rate-limiting barrier in the solvated-PONb case is 25 kJ/mol greater than in the dehydrated system.

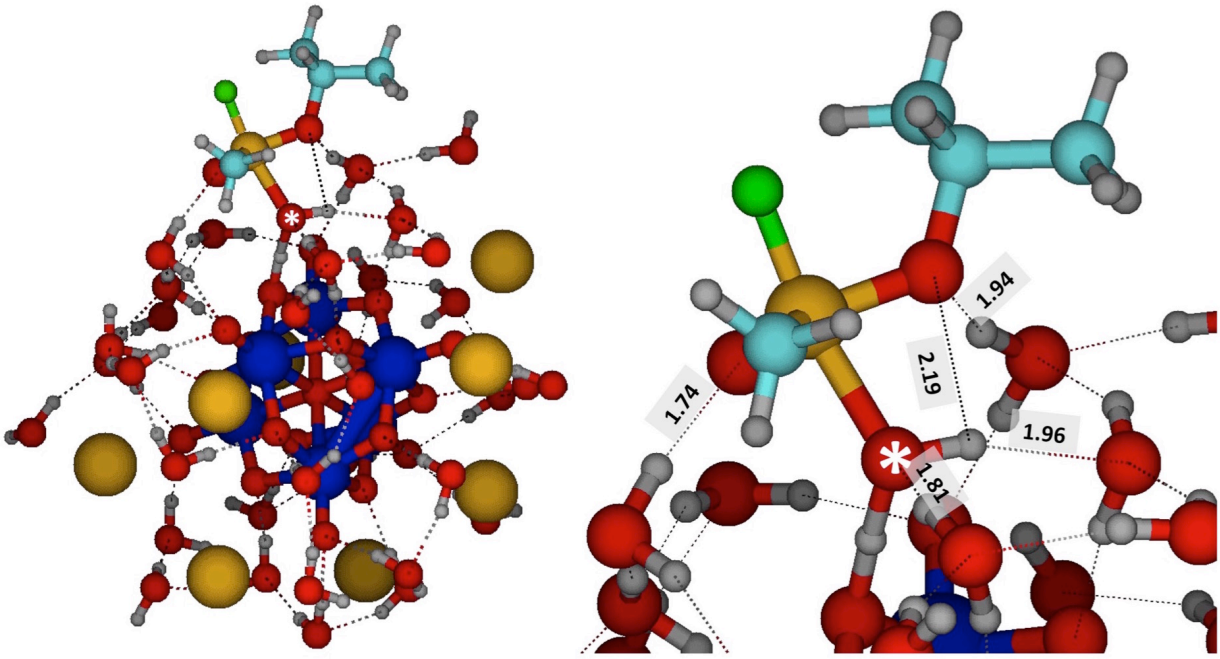

Figure 8.4. Transition state for the hydrolysis of GB by solvated $Cs_8Nb_6O_{19}$. A white asterisk labels the oxygen atom of the water molecule which is reacting at this step. In the right panel, key hydrogen bonding interactions are identified by O-H distances in Angstroms. Same color scheme as in Figure 8.3.

8.3.1.4 Pentacoordinated Intermediate

The rate-limiting transition state leads to a pentacoordinated phosphorus intermediate, which remains bound to the now-protonated PONb through an interaction between the proton on the PONb and the acidic-OH oxygen atom in the pentacoordinated adsorbate. Further, as shown in Figure 8.5, the sp^2-hybridized oxygen atom in the adsorbate accepts two hydrogen bonds from solvent water molecules, and the acidic OH group is hydrogen bonded to two solvent water molecules as well. Aside from the hydrogen bond that remains from the transition state between the proton on the PONb and the oxygen atom on the OH group, no direct interactions exist between the adsorbed intermediate and the PONb.

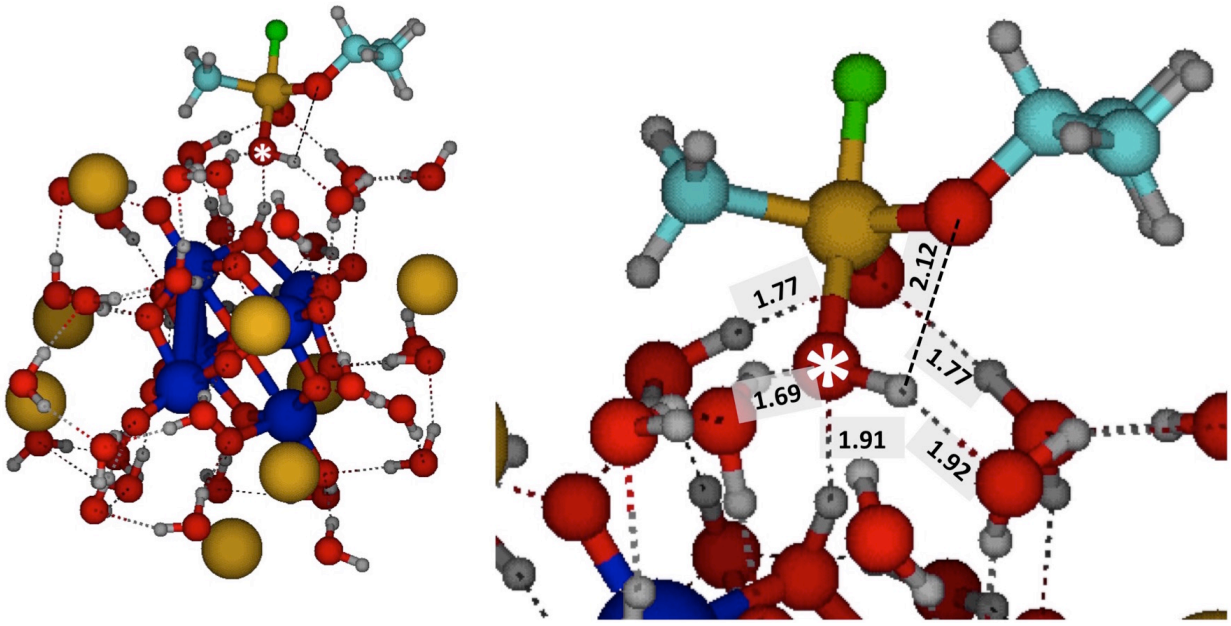

Figure 8.5. Optimized structure of the pentacoordinated intermediate resulting from the hydrolysis of GB by solvated $Cs_8Nb_6O_{19}$. A white asterisk labels the oxygen atom from the water molecule which reacted during the hydrolysis step. The right panel shows a zoomed-in region of the cluster, highlighting key hydrogen bonding interactions with O-H distances given in Angstroms. Same color scheme as in Figure 8.3.

8.3.1.5 Pentacoordinated Intermediate Dissociation

Once formed, the pentacoordinated intermediate can readily dissociate into products. Along some reaction pathways in the absence of attending water molecules, this can occur through the dissociation of the P-F bond with concomitant proton transfer from the PONb, yielding bound HF and IMPA. This step essentially occurs without an energy barrier in the gas-phase reaction. In the solvated-PONb system, along the pathway we have chosen to investigate, the orientation of the pentacoordinated intermediate and solvent water molecules prevents proton transfer. Thus, dissociation of the P-F bond is not possible.

Along our solvated-PONb reaction pathway, the pentacoordinated intermediate can, however, dissociate into isopropanol and MPFA products, with a barrier of 3 kJ/mol relative to the previous P5 minimum. This decrease in barrier relative to that for the analogous dehydrated pathway (26 kJ/mol) is due to both the orientation of the adsorbed pentacoordinated intermediate as well as the influence of solvent molecules. In the solvated-PONb system, the acid-OH hydrogen atom is oriented in such a way that it donates a hydrogen bond to the isopropyl sp^3

oxygen at the pentacoordinated intermediate step. In the solvent-free intermediate, a hydrogen bond between the acidic OH group and an O_{te} atom restricts such an interaction.

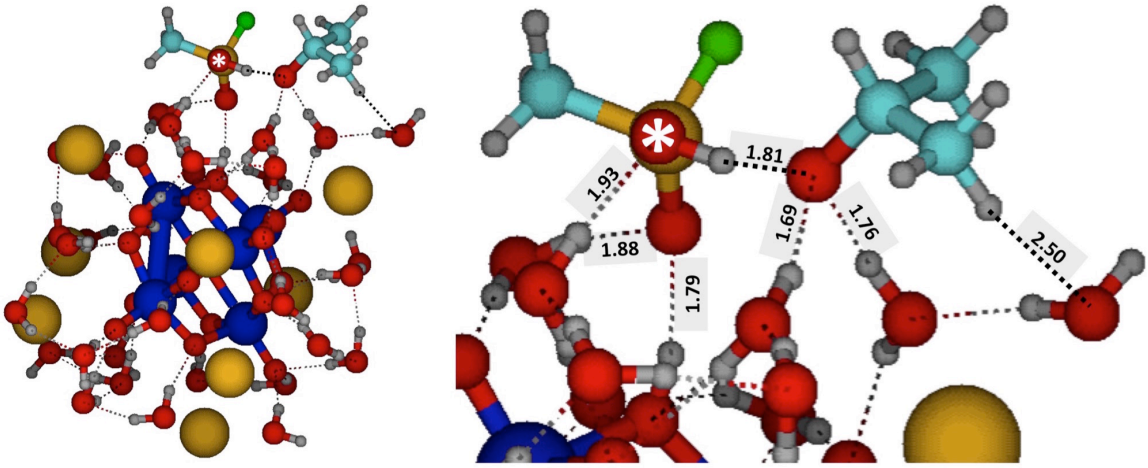

Figure 8.6. Transition state structure for the decomposition of the pentacoordinated intermediate adsorbed to solvated $Cs_8Nb_6O_{19}$. A white asterisk labels the oxygen atom from the water molecule which reacted during the hydrolysis step. The right panel shows a zoomed-in region, highlighting key hydrogen bonding interactions with O-H distances given in Angstroms. Same color scheme as in Figure 8.3.

8.3.1.6 Adsorbed Products

The decomposition of the pentacoordinated intermediate leads to MPFA and iPOH products strongly bound to PONb. The structure of this state along the solvated-PONb pathway is shown in Figure 8.7a. This is the most stable point in the hydrolysis of GB. However, in the absence of nearby countercations, these products are not adsorbed nearly as strongly as in the dehydrated case. Desorption of isopropanol, which interacts with an oxygen atom on MPFA as well as two solvent water molecules, requires 36 kJ/mol; less than half as much than in the solvent-free system (77 kJ/mol).

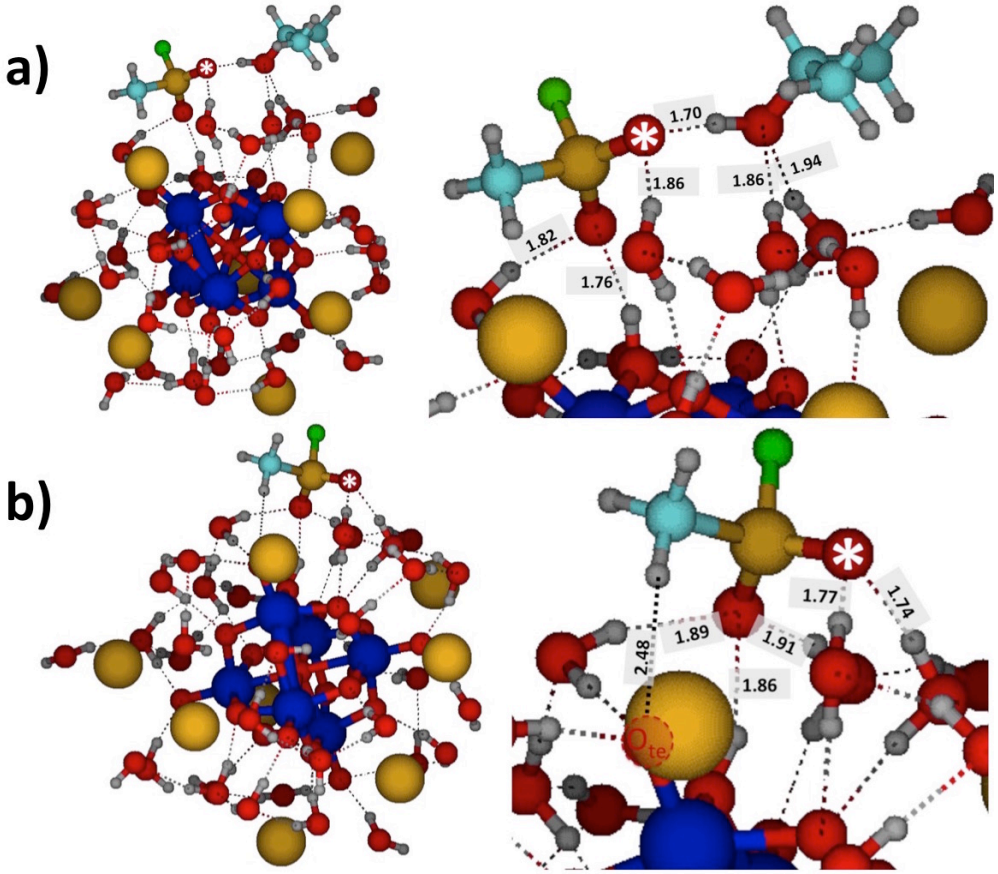

Figure 8.7. Optimized structure of GB hydrolysis products bound to solvated $Cs_8Nb_6O_{19}$. A white asterisk labels the oxygen atom from the water molecule which reacted during the hydrolysis step. Right panels show key interatomic interactions, with O-H distances given in Angstroms. a) Bound MPFA and iPOH, b) Bound MPFA, following iPOH desorption. The dashed O_{te} identifies an atom on PONb obstructed by a Cs counterion. Same color scheme as in Figure 8.3.

The desorption of iPOH leaves behind MPFA adsorbed to the protonated PONb complex (Figure 8.7b). The remaining MPFA interacts with PONb through a hydrogen bond between an MPFA oxygen atom and the PONb proton. Another hydrogen bond emerges between a hydrogen on the methyl group of MPFA and an O_{te}. This marks the first direct interaction between a GB moiety and PONb at a site other than the protonated O_b or its proton. This additional interaction contributes to the high binding energy of MPFA (161 kJ/mol) to PONb. However, in the absence of counterion interactions, this energy remains much lower than in the dehydrated case (262 kJ/mol).

8.3.2 Homogeneous Solution-Phase Hydrolysis

Our discussion of the base catalysis of gas-phase GB by explicit-water solvated $Cs_8Nb_6O_{19}$ has shown that the energetics of reaction are greatly influenced by interactions of adsorbed organophosphonate species with counterions and solvent. Specifically, interactions between electronegative atoms and Cs counterions serve to strengthen the adsorption of species to the PONb. Stationary points can also be stabilized by interactions with solvent water molecules, as seen for the decomposition transition state of the pentacoordinated intermediate along the solvated-PONb pathway.

With a basic understanding of the role of solvent molecules in the hydrolysis of GB by PONb, we now turn to extend our solvation model even further to initiate an investigation of the reaction in a homogeneous solvated system. To do this, we begin with our heterogeneous gas—solution bound-reagents system, in which a gas-phase GB molecule was added to a solvated $Cs_8Nb_6O_{19}$ cluster. To that, we manually add explicit water molecules in order to fully surround the adsorbed GB species and then proceed to follow the reaction pathway through the concerted protonation/nucleophilic addition transition state to pentacoordinated intermediate. In contrast to the pathways we have seen for GB hydrolysis by dry PONb (Chapter 5) and solvated PONb systems (this chapter), in which protonation of the PONb and hydroxide addition to GB occur in a single step, these processes take place in separate steps in the fully solvated system. The solution-phase pathway begins with the nucleophilic addition of the water molecule to the phosphorus atom of GB followed by the transfer of a proton from the added-water to the PONb. The black trace in Figure 8.8 shows the energetics of this reaction pathway, calculated at the M06-L/6-31G(d,p)—Lanl2dz level of theory. Orange values correspond to energies of the same stationary points, without zero-point corrections.

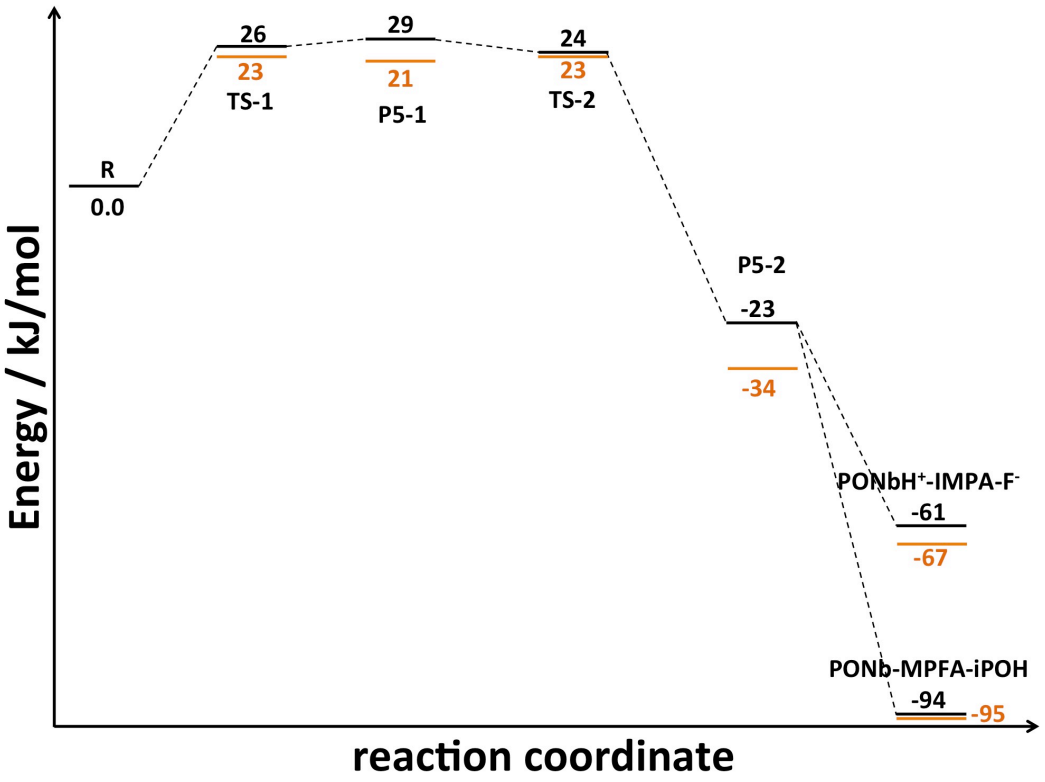

Figure 8.8. M06-L/6-31G(d,p)—Lanl2dz reaction pathway for the base hydrolysis of *(S)*-Sarin (GB) by $Cs_8Nb_6O_{19}$ in the solution phase. See text for description of solvation model. Black pathway: zero-point corrected energies. Orange: without zero-point corrections.

8.3.2.1 Bound-reagents Complex

The optimized structure of the adsorbed PONb-H_2O-GB complex (R), explicitly solvated by 53 water molecules, is shown in Figure 8.9. Due to increased solvation, GB and the reacting water molecule are involved in many more interactions with water molecules than in the heterogeneous reaction. Here, we designate these interactions as those with O/F—H distances less than 2.5 Å. In this complex, GB interacts directly with seven water molecules. Further, GB interacts with a terminal oxygen atom on PONb through two hydrogen atoms of the methyl group. A contrast is thus introduced with the bound-reagents complex along the heterogeneous gas—solution pathway, which showed no direct GB—PONb interactions. Also, the water molecule which will be added to the phosphorus atom in GB, marked with an asterisk in Figure 8.9, hydrogen bonds with two nearby solvent molecules, as well as with the $–CH_3$ group of GB, and an O_b site adjacent to that which will become protonated in a future step of the reaction. In the figure, the O_b site which will become protonated is marked with a lowercase r. This is the

first case along all the pathways we have investigated for the hydrolysis of GB or a simulant by $Cs_8Nb_6O_{19}$ in which the reacting water molecule did not directly interact with the O_b site of protonation prior to reaction.

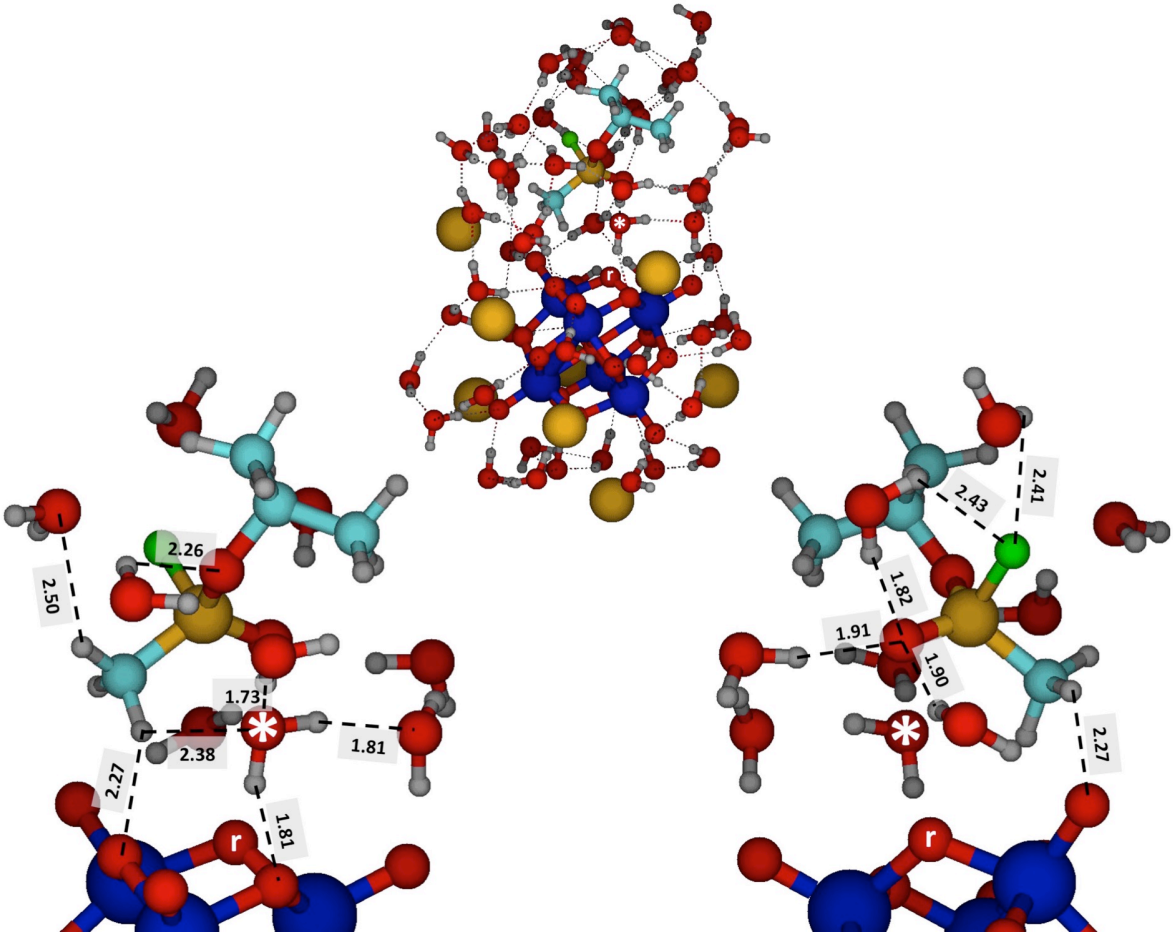

Figure 8.9. Bound-reagents complex for the hydrolysis of GB by $Cs_8Nb_6O_{19}$ surrounded by 53 solvent water molecules. A white asterisk labels the oxygen atom from the water molecule which will react during hydrolysis, and the O_b atom which will become protonated is marked with a lowercase r. The top panel shows the entire system, and the bottom panels show zoomed-in regions of the same structure highlighting intermolecular interactions with O/F—H distances less than 2.5 Angstroms. In the bottom panels, only those water molecules which participate in hydrogen bonding with atoms from GB or the rearranging water molecule are shown, and the Cs atoms have been removed for ease of interpretation. Key hydrogen bonds are indicated with interatomic distances, in Angstroms. Same color scheme as in Figure 8.3.

8.3.2.2 Transition State for the Addition of Water to GB

From the bound-reagents complex, the first step in the solution-phase hydrolysis of GB on PONb is the nucleophilic addition of a water molecule to the phosphorus atom in GB. The structure of the transition state for this step (TS-1 in Fig. 8.8), is shown in Figure 8.10. All of the

interactions involving GB remain from the bound-reagents complex, except for one between a methyl hydrogen atom and an O_{te} on the PONb (bottom right panel, Figure 8.9). In addition to these, three new hydrogen bonds between GB and solvent molecules emerge involving the fluorine and isopropoxy oxygen atoms.

Interestingly, at this transition state, the water molecule which is adding to GB moves away from the O_b atom with which it shared a hydrogen bond in the previous state. Animation of the normal mode characteristic of this transition state shows a decrease in P-O_w distance as a bond is formed between these two atoms, along with motion of the plane containing the water molecule as it moves from one O_b to that which will become protonates in the next step. The energy of this transition state relative to the bound-reagents complex is 25.6 kJ/mol.

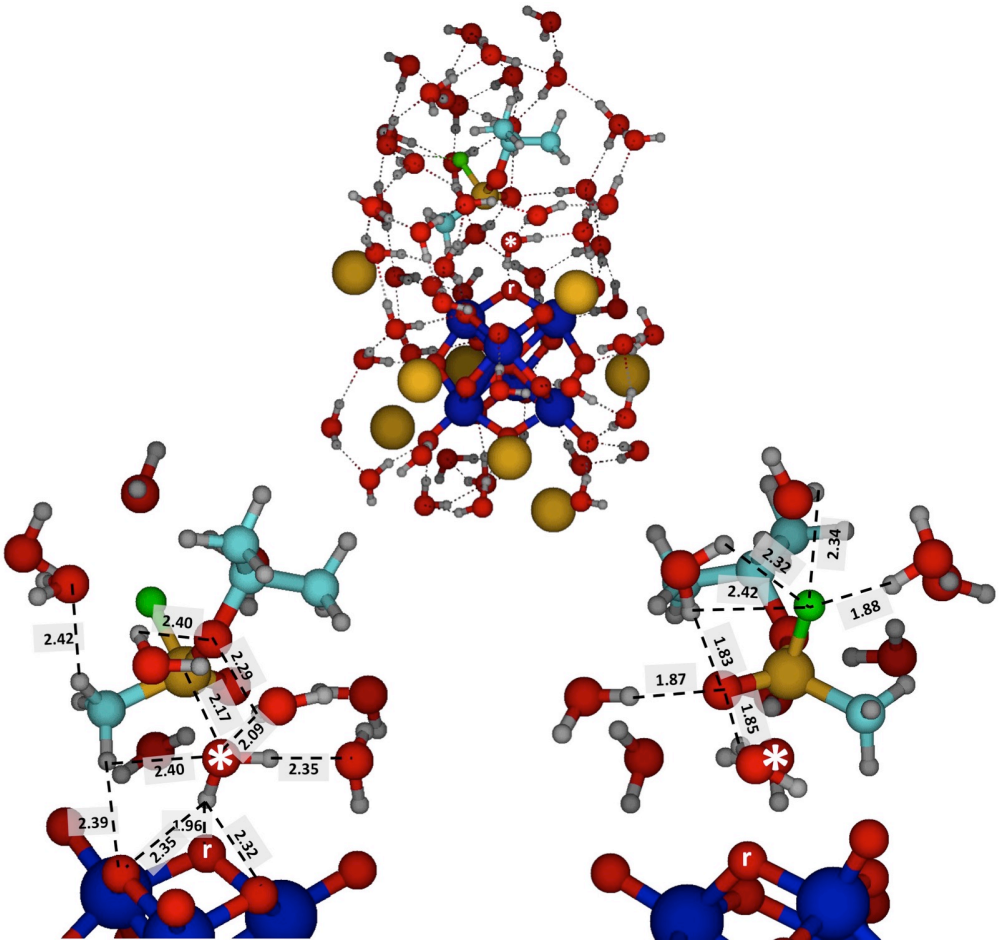

Figure 8.10. Transition state for the addition of water to GB (TS-1) during hydrolysis by $Cs_8Nb_6O_{19}$, surrounded by 53 solvent water molecules. A white asterisk labels the oxygen atom from the water molecule being added at this step, and the O_b atom which will become protonated is marked with a lowercase r. The top panel shows the entire system, and the bottom panels show zoomed-in regions of the same structure highlighting intermolecular interactions with O/F—H distances less than 2.5 Angstroms. In the bottom panels, only those water molecules which participate in hydrogen bonding with atoms from GB or the reacting water molecule are shown, and the Cs atoms have been removed for ease of interpretation. Key interactions are indicated with interatomic distances, in Angstroms. Same color scheme as in Figure 8.3.

8.3.2.3 First Pentacoordinated Intermediate

The structure of the activated pentacoordinated complex (P5-1) resulting from the nucleophilic addition of water to GB is shown in Figure 8.11. At this point, the added water molecule is much closer to the adsorbed GB molecule (P-O_{water} distance: 1.99 Å). Further, as a consequence of this close association, the structure of GB in the solvated reagents system exhibits a trigonal bipyramidal arrangement, with F-P-CH_3, F-P-Osp^2, and F-P-Osp^3 angles of

88.3°, 96.9°, and 93.1°, respectively. The solvation of those functional groups from GB remains largely the same, with two additional hydrogen bonds with the isopropoxy group. Further, the methyl group now interacts with an O_{te} atom on PONb instead of an O_b. Importantly, resulting from addition to GB, the water moiety now interacts with PONb solely at the O_b site which will become protonated in the next step.

The energy of this activated complex is 29.0 kJ/mol greater than that of the bound-reagents complex, and 3.4 kJ/mol greater than that of the preceding transition state. The fact that the energy of this minimum is greater than the barrier leading to its formation is a consequence of vibrational energy. Without correction by the zero-point, the energy of this complex is 1.2 kJ/mol below that of the transition state.

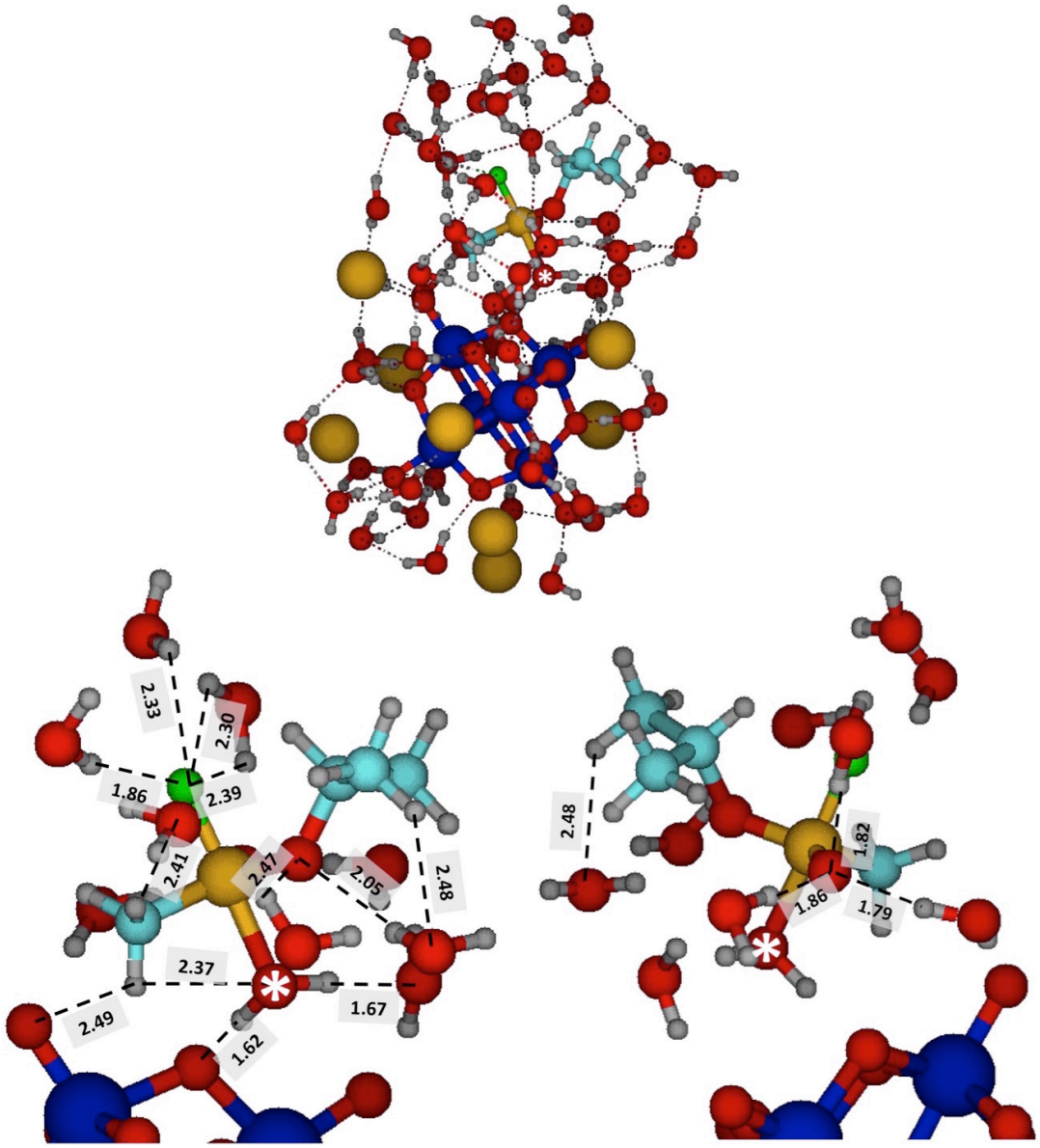

Figure 8.11. First pentacoordinated complex (P5-1) for the hydrolysis of GB by $Cs_8Nb_6O_{19}$ surrounded by 53 solvent water molecules. A white asterisk labels the oxygen atom from the original water molecule that reacts during hydrolysis. The top panel shows the entire system, and the bottom panels show zoomed-in regions of the same structure highlighting intermolecular interactions with O/F—H distances less than 2.5 Angstroms. In the bottom panels, only those water molecules which participate in hydrogen bonding with atoms from GB or the reacting water molecule are shown, and the Cs atoms have been removed for ease of interpretation. Key interactions are indicated with interatomic distances, in Angstroms. Same color scheme as in Figure 8.3.

8.3.2.4 Proton-transfer Transition State

Moving along the hydrolysis pathway, a transition state which closely resembles the first pentacoordinated intermediate complex is exhibited next. Animation of the imaginary vibrational mode characteristic of this transition state (TS-2) shows the transfer of a proton from the added water moiety to O_b on PONb. The optimized structure of this state is shown in Figure 8.12. Here, the P-O_{water} distance decreases slightly to 1.88 Å, which is similar to that seen in the rate-limiting transition state in the solvated-PONb reaction (2.03 Å). The hydrogen-bonding arrangement seen in this solvated state is nearly identical to that for the first pentacoordinated intermediate, with additional interactions between the water molecule and the sp^3-hybridized isopropoxy oxygen (H-O distance in the P5-1 complex: 2.56 Å) as well as between an isopropyoxy hydrogen atom and a solvent molecule (in P5-1: 2.51 Å). The mean absolute difference in hydrogen-bonding distances as shown in Figure 8.12 (excluding the O_b-H_{water} interaction integral to the rearrangement which takes place at the transition state) between the P5-1 state and this transition state is 0.03 Å, illustrating the similarity in intermolecular interactions between both states. Further, the trigonal bipyramidal geometry seen in the activated complex is maintained at the transition state, with F-P-CH_3, F-P-Osp^2, and F-P-Osp^3 angles of 86.3°, 94.9°, and 91.9°, respectively.

Due to similarities in both GB structure and hydrogen bonding motifs for both the P5-1 and solvated water-addition transition-state complexes, the energies of both systems are very similar. The non-zero-point-corrected electronic energy of the optimized transition state before application of diffuse functions (M06-L/6-31G(d,p)—Lanl2dz) is only 2.0 kJ/mol greater than that of the P5-1 complex. In fact, the addition of zero-point energies brings this energy to 5.0 kJ/mol below that of the preceding complex.

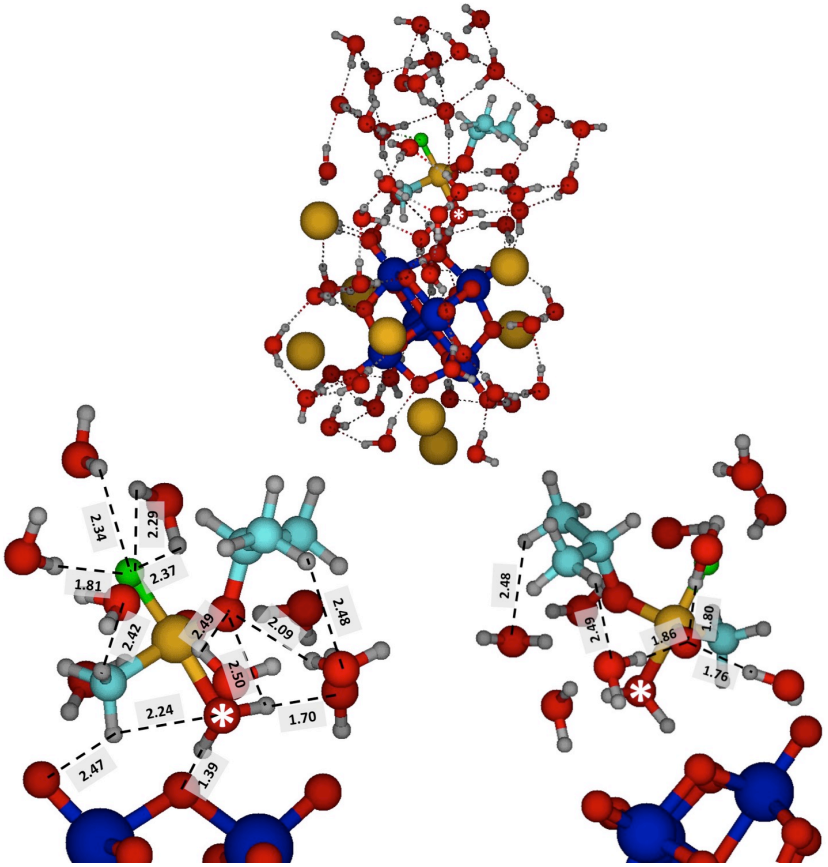

Figure 8.12. Transition state for the transfer of a proton (TS-2) to a bridging oxygen from a water moiety which has been added to GB during hydrolysis by $Cs_8Nb_6O_{19}$ surrounded by 53 solvent water molecules. A white asterisk labels the oxygen atom from the original water molecule that reacts during hydrolysis. The top panel shows the entire system, and the bottom panels show zoomed-in regions of the same structure highlighting intermolecular interactions with O/F—H distances less than 2.5 Angstroms. In the bottom panels, only those water molecules which participate in hydrogen bonding with atoms from GB or the reacting water molecule are shown, and the Cs atoms have been removed for ease of interpretation. Key interactions are indicated with interatomic distances, in Angstroms. Same color scheme as in Figure 8.3.

Protonation results in a second pentacoordinated intermediate with a net –OH substituent on GB, similar to that seen in solvent-free and heterogeneous gas—surface reactions. Thus, we have once again reached a familiar point along the reaction pathway, allowing for a comparison of hydrolysis energy barriers. The gas-phase and heterogeneous gas—surface hydrolysis mechanisms of GB on the surface of $Cs_8Nb_6O_{19}$ exhibited pentacoordinated intermediate formation in one reaction step following adsorption of reagents. In both cases, this was shown to be the rate-limiting step, with barriers of 18.9 kJ/mol and 44.2 kJ/mol, respectively, at the M06-

L/6-31G(d,p)—Lanl2dz level of theory with zero-point corrections. In the solvated-PONb reaction, the large increase in barrier relative to the gas-phase was attributed to a lack of counterion interaction with reacting adsorbates. In the homogeneous solution-phase reaction, pentacoordinated intermediate formation requires two steps: water addition and subsequent proton transfer. The first step is the rate-limiting one, with a barrier of 25.6 kJ/mol. Thus, full solvation appears to not only change the hydrolysis mechanism leading to pentacoordinated-intermediate formation, but it also lowers the rate-limiting barrier to a value similar to that seen in the gas phase reaction.

8.3.2.5 Second Pentacoordinated Intermediate

The optimized structure of the pentacoordinated intermediate (P5-2) resulting from proton transfer to O_b is shown in Figure 8.13. Compared to the proton-transfer transition state, there are fewer interactions between the bound intermediate and solvent. The fluorine atom still accepts four hydrogen bonds from three water molecules, and the sp^2-hybridized oxygen still interacts with three solvent molecules. However, the isopropoxy group only interacts with one solvent molecule, and the methyl group does not form hydrogen-bonding interactions with solvent at all. Further, there is no longer an interaction between the methyl group and an O_{te} atom, and the interaction between the hydrogen of the acid P-OH group and the isopropyl sp^3-hybridized oxygen atom has also been broken. The latter interaction, present only at the preceding transition state, thus seems to have facilitated proton transfer. The energy of this point is 23.5 kJ/mol below that of the bound-reagents complex.

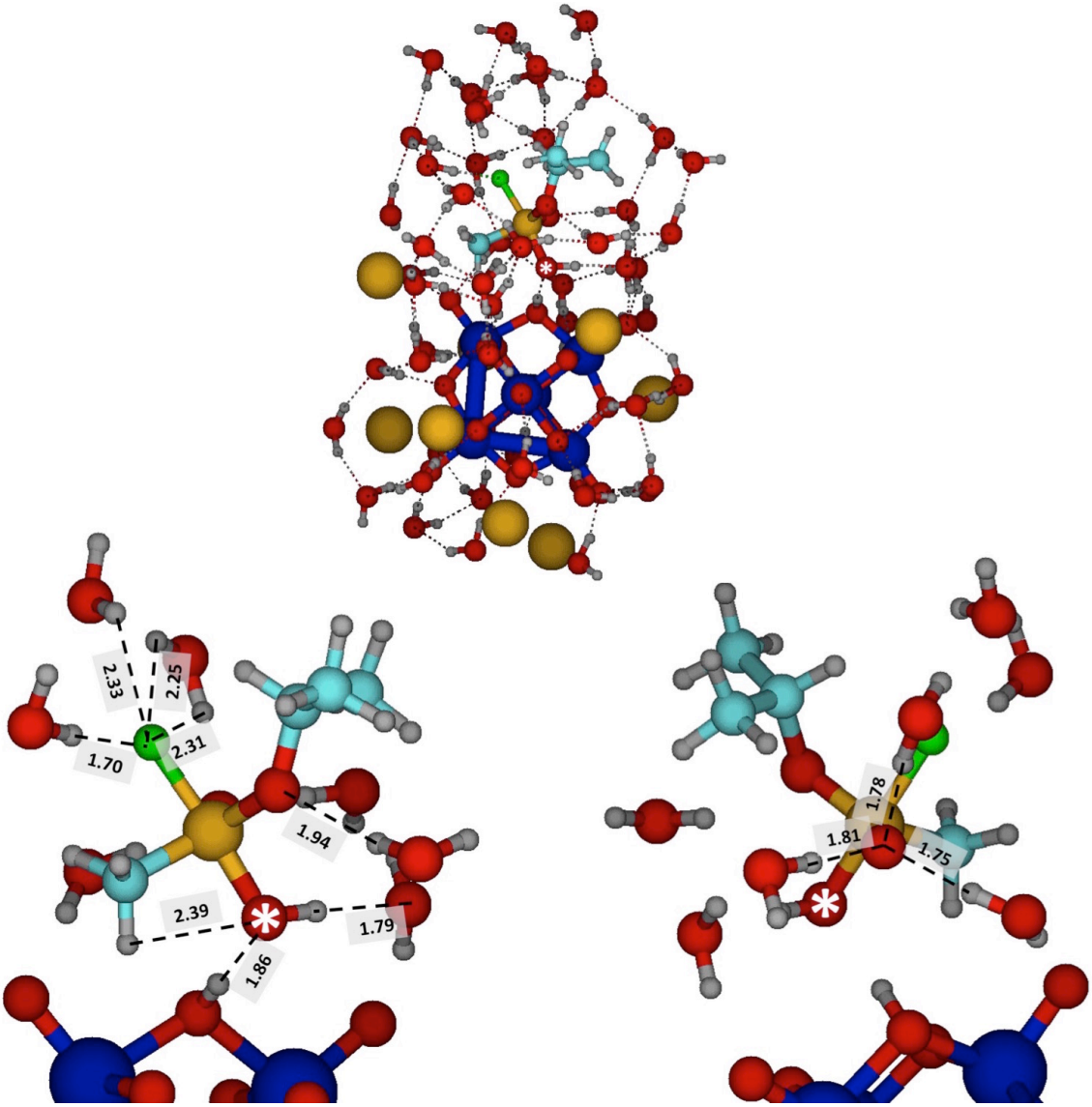

Figure 8.13. Second pentacoordinated intermediate complex (P5-2) for the hydrolysis of GB by $Cs_8Nb_6O_{19}$ surrounded by 53 solvent water molecules. A white asterisk labels the oxygen atom from the original water molecule that reacts during hydrolysis. The top panel shows the entire system, and the bottom panels show zoomed-in regions of the same structure highlighting intermolecular interactions with O/F—H distances less than 2.5 Angstroms. In the bottom panels, only those water molecules which participate in hydrogen bonding with atoms from GB or the reacting water molecule are shown, and the Cs atoms have been removed for ease of interpretation. Key interactions are indicated with interatomic distances, in Angstroms. Same color scheme as in Figure 8.3.

8.3.2.6 Adsorbed Products

As discussed for the dehydrated system,[1] the preceding pentacoordinated intermediate can readily eliminate HF, yielding HF + IMPA products which remain bound to PONb. In the solvated-PONb reaction, solvent molecules obstruct the proton transfer from the PONb required for elimination, preventing fluoride dissociation. However, when the entire system is surrounded by explicit water molecules, the fluoride ion resulting from P-F bond dissociation is solvated by water molecules and can persist without hydrogen abstraction. The resulting complex is shown in Figure 8.14. Here, the fluoride ion interacts with the methyl group on IMPA and a hydrogen atom on iPOH, as well as four water molecules. Additionally, even though the P-F bond has dissociated to yield fluoride, this ion still interacts with the now tetrahedral phosphorus atom in IMPA, with a P-F distance of 2.67 Å. IMPA is adsorbed to the PONb through interactions between the methyl group and O_{te}, as well as between the acid P-OH group and the proton bound to O_b. Further, IMPA is subject to increased solvation at this step as well, showing an additional interaction between the methyl group and a solvent water molecule that was not evidenced in the pentacoordinated intermediate. Other interactions between IMPA and explicit solvent persist from the bound intermediate.

The energy of this $PONbH^+$-IMPA-F^- complex is 61.4 kJ/mol less than that of the homogeneous bound-reagents complex. A comparison with the analogous energy in the dehydrated complex (-114.4 kJ/mol relative to bound reagents) reveals the combined influence of counterion association, explicit solvation, and proton transfer on the overall energy of this bound-products complex.

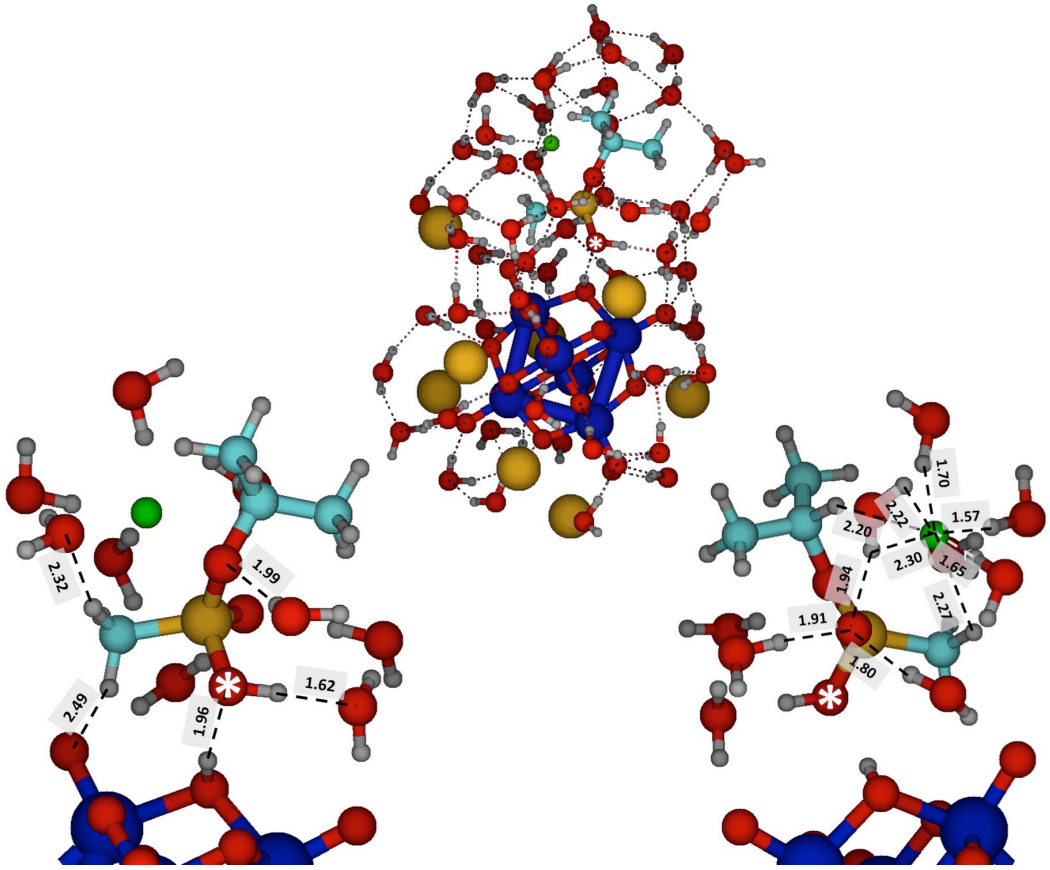

Figure 8.14. $PONbH^{+}$-IMPA-F^{-} complex for the hydrolysis of GB by $Cs_8Nb_6O_{19}$ surrounded by 53 solvent water molecules. A white asterisk labels the oxygen atom from the original water molecule that reacts during hydrolysis. The top panel shows the entire system, and the bottom panels show zoomed-in regions of the same structure highlighting intermolecular interactions with O/F—H distances less than 2.5 Angstroms. In the bottom panels, only those water molecules which participate in hydrogen bonding with atoms from GB or the reacting water molecule are shown, and the Cs atoms have been removed for ease of interpretation. Key interactions are indicated with interatomic distances, in Angstroms. Same color scheme as in Figure 8.3.

iPOH + MPFA production is also likely in the homogeneous solution system. While we were unable to optimize transition states leading from the second pentacoordinated intermediate to either set of products, we suspect that the barrier for iPOH + MPFA formation will fall as low as that for the solvated-PONb system (3 kJ/mol) due to the increased influence of solvent water molecules. Figure 8.15 shows the optimized structure of the solvated PONb-MPFA-iPOH complex in explicit water solvent as well as key intermolecular interactions within this complex and between this complex and explicit solvent molecules. In this state, we note that MPFA

interacts with both the protonated site and a terminal oxygen atom on PONb, contributing to the adsorption of MPFA to PONb. Further, the following of the solvated reaction pathway to this state incidentally resulted in the approach of a Cs counterion proximal to an oxygen atom in bound MPFA. This counterion, which is a distance of 3.14 Å from the oxygen atom in the rearranged water molecule, likely results in increased adsorption of MPFA to PONb relative to the pentacoordinated intermediate complex (Cs-O_{water} distance: 3.63 Å).

Isopropanol, on the other hand, exhibits no direct interactions with the niobate core or with Cs counterions. Instead, two hydrogen atoms on iPOH—one from the hydroxide moiety and the other from a methyl group—interact with the fluoride atom on MPFA. These two interactions restrict solvation of the MPFA fluorine atom, which now interacts with only one water molecule. Finally, solvation of the isopropanol moiety is increased in this state relative to the preceding pentacoordinated intermediate; interactions with three additional solvent molecules are exhibited in this bound-products structure.

We have seen in both the dehydrated and solvated-PONb reactions that adsorption of MPFA and iPOH products is very strong. This remains the case in solution. The energy of this bound-products complex is -93.6 kJ/mol relative to the bound-reagents complex. This energy is less than those for the solvent-free (-150.5 kJ/mol), and gas—solution systems (-98.7 kJ/mol). The difference in energy continues to highlight the role of counterions and explicit solvent molecules. In the solvated-PONb system, a lack of interactions with counterions resulted in a decrease in product binding energy compared to the dry system. Leading from the heterogeneous gas—solution system to the homogeneous solution-phase, a further increase in explicit solvation in a system which already mostly lacks Cs counterions proximal to reacting species results in a further decrease in product binding energy.

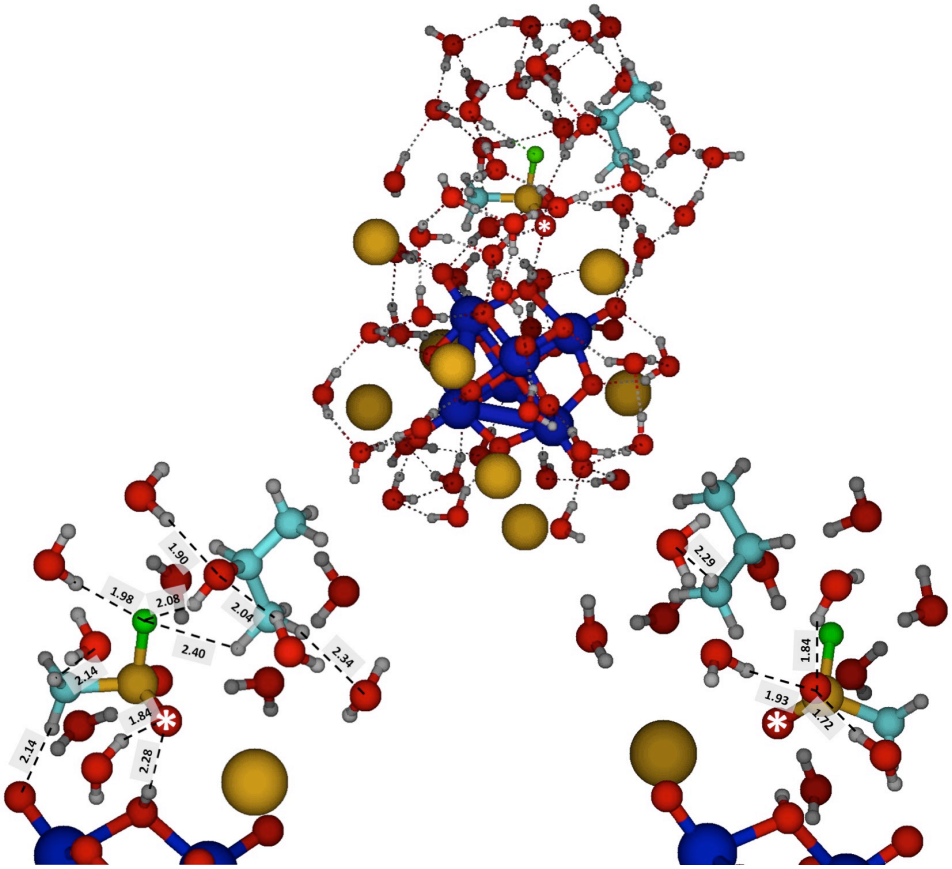

Figure 8.15. PONb-MPFA-iPOH complex for the hydrolysis of GB by $Cs_8Nb_6O_{19}$ surrounded by 53 solvent water molecules. A white asterisk labels the oxygen atom from the original water molecule that reacts during hydrolysis. The top panel shows the entire system, and the bottom panels show zoomed-in regions of the same structure highlighting intermolecular interactions with O/F—H distances less than 2.5 Angstroms. In the bottom panels, only those water molecules which participate in hydrogen bonding with atoms from GB or the reacting water molecule are shown, and the Cs atoms have been removed for ease of interpretation. Key interactions are indicated with interatomic distances, in Angstroms. Same color scheme as in Figure 8.3.

8.4 General vs. Specific Base Catalysis

Having examined both the heterogeneous gas—solution and homogeneous solution-phase hydrolysis reactions of GB on $Cs_8Nb_6O_{19}$, we now turn to a discussion on the roles of general and base hydrolysis in these reactions.[11] To this point, we have investigated a mechanism, originally proposed by Kinnan et al.,[6] in which a water molecule protonates a basic oxygen site on PONb in the same step in which the OH remaining from that water molecule adds nucleophilically to the phosphorus atom in GB (Figure 8.16a). This mechanism, in which

protonation and nucleophilic addition occur in a single step, describes general base catalysis. Conversely, in specific base catalysis, protonation and nucleophilic addition occur in two separate steps. In a specific base mechanism, shown in Figure 8.16b for GB hydrolysis by PONb, protonation occurs in one step, yielding a free hydroxide, which adds to the phosphorus atom in GB in a subsequent step. To investigate the possible role of a specific base catalysis mechanism in GB hydrolysis by PONb, we consider the likelihood of free hydroxide generation by PONb in the absence of GB. This OH^-, once generated, can perhaps diffuse through a system and add to GB in a future step.

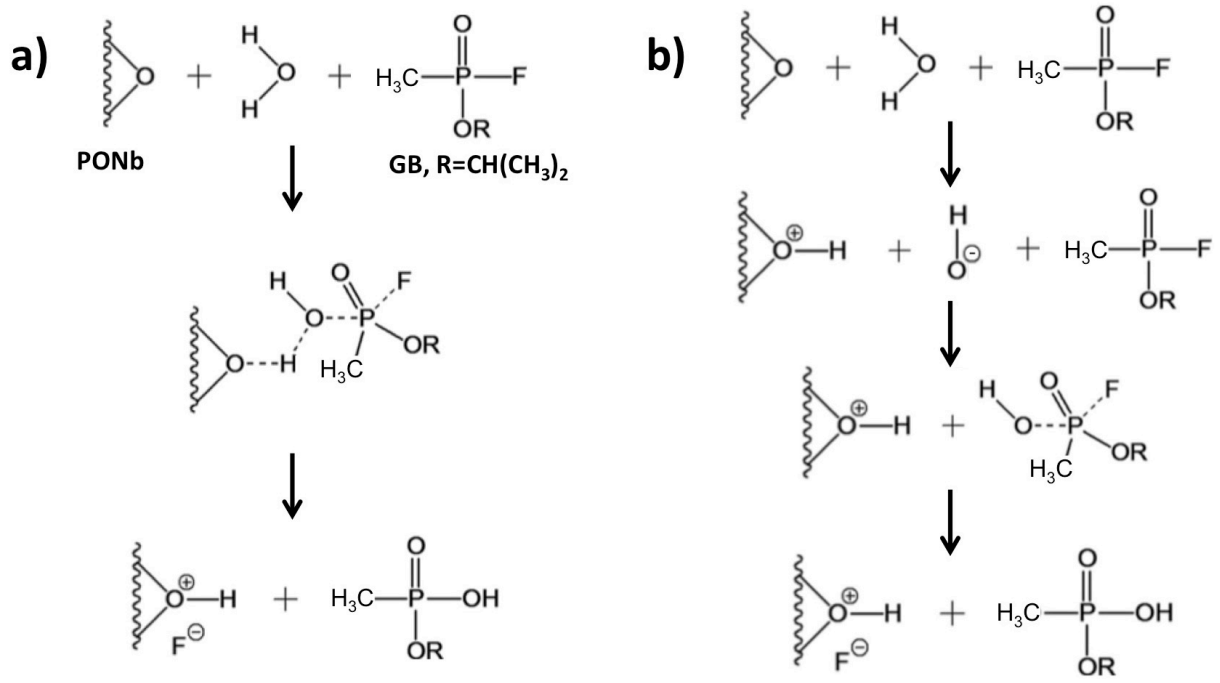

Figure 8.16. Reaction pathways for a) general and b) specific base catalysis of Sarin (GB) by a Lindqvist polyoxoniobate (PONb). Reprinted (adapted) from Kinnan, M. K.; Creasy, W. R.; Fullmer, L. B.; Schreuder-Gibson, H. L.; Nyman, M. *European Journal of Inorganic Chemistry* **2014**, *2014*, 2361. © 2014 Wiley-VCH Verlag GmbH & Co. KCaA, Weinheim.

For GB hydrolysis by PONb in the dehydrated system, we note a general base hydrolysis barrier of 22 kJ/mol in the presence of GB (Figure 8.1, black trace). Because the OH^- generated in the dissociation of water by PONb cannot be stabilized in the absence of GB in the gas phase, a specific base catalysis mechanism is impossible. Only general base catalysis can be present in a dry system.

Conversely, OH^- can be stabilized by the solvent in a solution-phase system. Indeed, in the presence of 53 explicit water molecules, a transition state for water deprotonation by PONb was located. The optimized structures for stationary points for the PONb-H_2O → $PONbH^+ + OH^-$ reaction are shown in Figure 8.17. The transition state for deprotonation/hydroxide generation in the absence of GB has an energy 22.0 kJ/mol greater than of the PONb-H_2O state. The rate-limiting transition state for the general base mechanism in solution (Figures 8.8 and 8.10) has an energy 25.6 kJ/mol relative to the bound-reagents complex. (We note that, in the homogeneous solution-phase reaction described in section 8.3.2, the addition of water occurs in the rate-limiting step, and protonation occurs in a subsequent step. However, protonation is barrierless, and thus limited by the rate of addition. Further, free hydroxide—a hallmark of specific base hydrolysis—is never released. Thus, we classify this reaction as general base hydrolysis.)

Given the similarity of these rate-limiting barriers, it is entirely possible that both general and specific base catalysis mechanisms are likely for GB hydrolysis by PONb in solution.

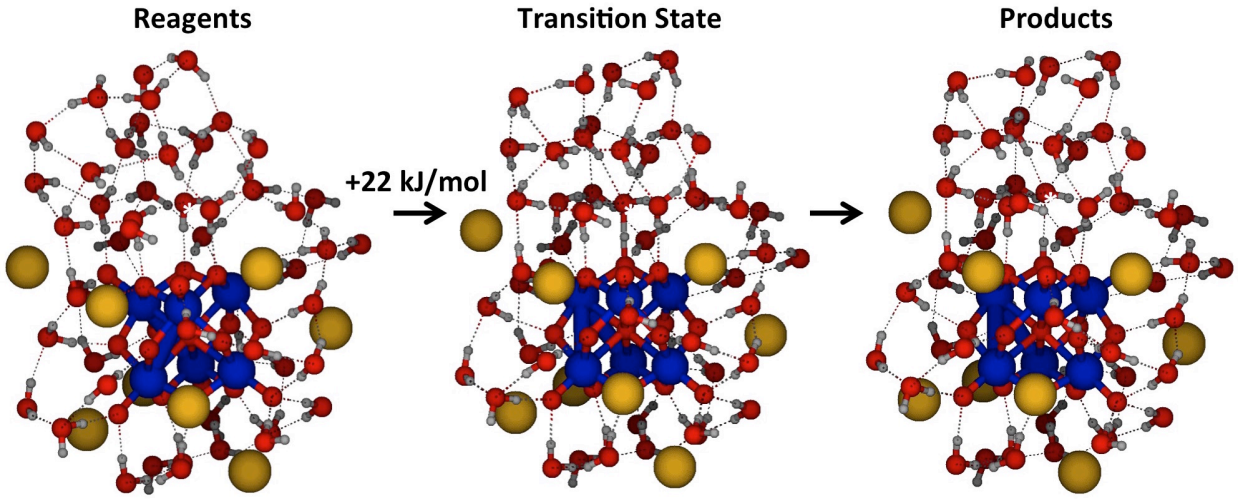

Figure 8.17. Reaction pathway for water deprotonation by $Cs_8Nb_6O_{19}$ in the presence of 53 explicit solvent water molecules. A white asterisk labels the oxygen atom from the water molecule which will be rearranged during the deprotonation step. Same color scheme as in Figure 8.3.

8.5 Concluding Remarks

In this chapter, we investigated the catalysis of GB by PONb in the presence of solvent water molecules. To model reaction in at the gas—liquid interface, we adsorbed gas-phase GB onto a solvated PONb. Comparison of this reaction to the dehydrated one reported previously shows an increase in hydrolysis reaction barrier and decrease of product adsorption energy due to screened intermolecular interactions by the solvent. We then furthered our solvation model to a homogeneous solution-phase system through the addition of explicit water molecules around GB. This increased influence of solvent resulted in a mechanism which exhibited the rate-limiting nucleophilic addition of water to GB, prior to low-barrier proton transfer to the PONb in a separate step. Further, increased solvation resulted in a decrease in the rate-limiting barrier relative to the heterogeneous reaction. Finally, by examining the rate-limiting barrier for water deprotonation in both the presence and absence of GB, we suggested that a specific base hydrolysis mechanism might complete with general base hydrolysis.

A previous theoretical study used density-functional-theory calculations to examine solvation of a polyoxometalate cluster, finding convergence of molecular orbital and solvation energies after adsorption of 49 water molecules in the first solvation shell.[12] Our heterogeneous calculations implemented 34 explicit water molecules. In order to fully capture the effects of the first solvation shell on GB hydrolysis by PONb, future work will incorporate more explicit water molecules in both the heterogeneous and homogeneous systems.

Moreover, our primary means of solvation was through the addition of explicit water molecules. Thus, reaction geometries and energies may be heavily dependent upon the specific orientation of solvent molecules in our calculations. Varying the binding motif of explicit solvent molecules may therefore influence the energies of each stationary point, considering that each hydrogen bond has an energy of about 5.0 kJ/mol in this system (i.e., the binding energy of the water dimer). Future work will examine the heterogeneous and homogeneous pathways with multiple orientations of explicit water molecules, towards an increased confidence of binding energies. Further, our attempts to apply a continuum solvation model (i.e., PCM) to the stationary points along the heterogeneous reaction pathway resulted in inconsistent convergence. Future work will consider other means of implicit solvation towards results that converge for each stationary point. Alternatively, studies may implement reactive molecular dynamics

calculations in order to more fully describe all interactions and chemical changes that occur during catalytic hydrolysis.

Finally, when considering the specific base hydrolysis mechanism in solution, we found a barrier for hydroxide generation of 22 kJ/mol. Nucleophilic addition of this hydroxide to GB in solution has been previously shown to exhibit a larger barrier (~40 kJ/mol).[13,14] Future work will consider this step in the specific base mechanism using the methods described herein, as well as implications of this barrier on the role of PONb in the degradation of GB in solution.

8.6 References

(1) Chapleski, R. C.; Musaev, D. G.; Hill, C. L.; Troya, D. *The Journal of Physical Chemistry C* **2016**, *120*, 16822.

(2) Nyman, M.; Alam, T. M.; Bonhomme, F.; Rodriguez, M. A.; Frazer, C. S.; Welk, M. E. *Journal of Cluster Science* **2006**, *17*, 197.

(3) Frisch, M. J.; Trucks, G. W.; Schlegel, H. B.; Scuseria, G. E.; Robb, M. A.; Cheeseman, J. R.; Scalmani, G.; Barone, V.; Mennucci, B.; Petersson, G. A.; Nakatsuji, H.; Caricato, M.; Li, X.; Hratchian, H. P.; Izmaylov, A. F.; Bloino, J.; Zheng, G.; Sonnenberg, J. L.; Hada, M.; Ehara, M.; Toyota, K.; Fukuda, R.; Hasegawa, J.; Ishida, M.; Nakajima, T.; Honda, Y.; Kitao, O.; Nakai, H.; Vreven, T.; Montgomery Jr., J. A.; Peralta, J. E.; Ogliaro, F. ß.; Bearpark, M. J.; Heyd, J.; Brothers, E. N.; Kudin, K. N.; Staroverov, V. N.; Kobayashi, R.; Normand, J.; Raghavachari, K.; Rendell, A. P.; Burant, J. C.; Iyengar, S. S.; Tomasi, J.; Cossi, M.; Rega, N.; Millam, N. J.; Klene, M.; Knox, J. E.; Cross, J. B.; Bakken, V.; Adamo, C.; Jaramillo, J.; Gomperts, R.; Stratmann, R. E.; Yazyev, O.; Austin, A. J.; Cammi, R.; Pomelli, C.; Ochterski, J. W.; Martin, R. L.; Morokuma, K.; Zakrzewski, V. G.; Voth, G. A.; Salvador, P.; Dannenberg, J. J.; Dapprich, S.; Daniels, A. D.; Farkas, O.; Foresman, J. B.; Ortiz, J. V.; Cioslowski, J.; Fox, D. J.; Gaussian, Inc.: Wallingford, CT, USA, 2009.

(4) Antonio, M. R.; Nyman, M.; Anderson, T. M. *Angewandte Chemie International Edition* **2009**, *48*, 6136.

(5) Fullmer, L. B.; Molina, P. I.; Antonio, M. R.; Nyman, M. *Dalton Transactions* **2014**, *43*, 15295.

(6) Kinnan, M. K.; Creasy, W. R.; Fullmer, L. B.; Schreuder-Gibson, H. L.; Nyman, M. *European Journal of Inorganic Chemistry* **2014**, *2014*, 2361.

(7) Berendsen, H. J. C.; Grigera, J. R.; Straatsma, T. P. *The Journal of Physical Chemistry* **1987**, *91*, 6269.

(8) Cornell, W. D.; Cieplak, P.; Bayly, C. I.; Gould, I. R.; Merz, K. M.; Ferguson, D. M.; Spellmeyer, D. C.; Fox, T.; Caldwell, J. W.; Kollman, P. A. *Journal of the American Chemical Society* **1995**, *117*, 5179.

(9) Van Der Spoel, D.; Lindahl, E.; Hess, B.; Groenhof, G.; Mark, A. E.; Berendsen, H. J. C. *Journal of Computational Chemistry* **2005**, *26*, 1701.

(10) Abraham, M. J.; Murtola, T.; Schulz, R.; Páll, S.; Smith, J. C.; Hess, B.; Lindahl, E. *SoftwareX* **2015**, *1–2*, 19.

(11) Anslyn, E. V.; Dougherty, D. A. *Modern Physical Organic Chemistry*; University Science, 2006.

(12) Miró, P.; Poblet, J. M.; Ávalos, J. B.; Bo, C. *Canadian Journal of Chemistry* **2009**, *87*, 1296.

(13) Gustafson, R. L.; Martell, A. E. *Journal of the American Chemical Society* **1962**, *84*, 2309.

(14) Šečkutė, J.; Menke, J. L.; Emnett, R. J.; Patterson, E. V.; Cramer, C. J. *The Journal of Organic Chemistry* **2005**, *70*, 8649.

Chapter 9
Summary and Future Work

9.1 Summary

The general aim of the research presented in this dissertation was to elucidate fundamental aspects of specific reactions that occur at the interface of gas molecules and solid surfaces with computational methods. More specifically, we set out to fulfill three research objectives:

1. Refine the mechanisms of surface-bound alkene oxidation by ozone and nitrate.
2. Delineate the hydrolysis mechanism of nerve agents and simulants on the surface of a Lindqvist polyoxoniobate.
3. Elucidate the results of experimental spectra for the gas—surface reactions described herein.

Motivated by concerns stemming from atmospheric phenomena such as smog and the balance of incoming and outgoing solar radiation, we were interested in reactions between oxidative gases and model surfaces that position a relevant functional group—the carbon-carbon double bond—at the interface. The opportunity to support and elucidate experimental results refined our specific choice of surface.

For ozone, we chose the surface of C_{60} fullerene for reaction. The selection of this surface was in response to research published by Davis et al.,[1] who implemented RAIRS spectroscopy in an ultra-high vacuum environment to probe changes that occur on the fullerene surface during exposure to ozone. While this work was able to detect the short-lived primary ozonide at short exposure times, an infrared band with a frequency around 2200 cm^{-1} remained unassigned. Through the use of electronic structure calculations, we were able to trace a reaction pathway that lead to the formation of a ketene moiety after several intermediate steps. Significantly, a vibrational mode characteristic to the ketene moiety was the only one for any species along the reaction pathway with a vibrational frequency greater than 2000 cm^{-1}. Moreover, previous computational work had described an ozonolysis pathway leading to epoxide formation,[2] but the spectra taken by Davis et al. was unable to corroborate this. Our electronic structure calculations revealed a pathway with a lower reaction barrier than that for epoxide formation, thus supporting the absence of features characteristic of an epoxide in the work by Davis et al.

In our work with the reaction between nitrate and an unsaturated organic surface, we selected the vinyl-terminated self-assembled monolayer as our model surface. Once again, this choice was motivated by experimental work which used RAIRS in an ultra-high vacuum environment. In this case, Zhang et al. were attempting to assign the bands of infrared spectra following long nitrate exposure times to the ω-vinyl SAM surface.[3] Though the literature was tentatively helpful in this analysis, the available vibrational mode data for nitrates was confined to small molecules; thus, this information was not necessarily generalizable to surface-bound products.

To investigate a possible discrepancy between vibrational modes for individual organic molecules containing nitrate functional groups and products of nitrate addition to an organic surface-bound chain, we constructed a model of a self-assembled monolayer. Through the implementation of QM/MM methods, we were able to identify species whose vibrational spectrum correlated well with the RAIRS spectrum of Zhang et al., further allowing us to aid in the assignment of vibrational modes to spectral features. Moreover, we traced the reaction coordinate for a potential competing hydrogen abstraction reaction and subsequently concluded that the competing reaction was unlikely through a comparison of reaction kinetics and dynamics.

Following the two gas—surface studies relevant to atmospheric chemistry, the scope of our work changed towards an understanding of nerve-agent degradation. As the threat of chemical warfare looms in our global society, we developed an interest in understanding the fundamental aspects of decomposition of these nefarious compounds so that we may contribute to the development of filtration materials capable of deactivating chemical warfare agents. In a recent experiment, through the interpretation of small-angle x-ray scattering data, Kinnan et al. proposed a base-hydrolysis mechanism for the decomposition of an organophosphorus nerve agent simulant by a Lindqvist polyoxoniobate.[4] However, the dynamics and kinetics of this reaction were left largely undescribed. Thus, we undertook the task of exploring this reaction with computational methods. By probing the energetics of adsorption, reaction, and desorption, we were able to describe key aspects of the hydrolysis of the nerve agent Sarin on the surface of the Lindqvist polyoxoniobate $Cs_8Nb_6O_{19}$. Further, spurred by our interest in supporting experimental results, we also examined the gas—surface reaction of the nerve-agent simulants DMMP and DMCP with the same niobate. Not only did this allow for elucidation of Raman and

EXAFS spectra obtained by experimental groups that were not equipped to work with a deadly nerve agent, it also provided the opportunity for a comparison of mechanisms amongst adsorbed compounds.

For each compound, we traced several pathways for reaction of gas-phase molecules with the surface of the niobate. In the hydrolysis of each, the rate-limiting step showed protonation of an oxygen atom in the catalyst in concert with nucleophilic addition of the nascent hydroxide as a bound water molecule dissociated. Further, a general base catalysis mechanism was implicated, in agreement with experimental results reported previously.[4,5] Along with having this step in common for all three compounds, strong adsorption of products was prevalent in the hydrolysis of GB, DMMP, and DMCP by $Cs_8Nb_6O_{19}$, suggesting irreversible binding to the surface of the niobate following reaction; thus, hydrolysis with $Cs_8Nb_6O_{19}$ was likely to be stoichiometric as opposed to catalytic.

Despite the similarities, there were some mechanistic differences amongst the hydrolysis reactions by $Cs_8Nb_6O_{19}$. For example, in Sarin and DMMP, the rate-limiting step resulted in a minimum which exhibited a pentacoordinated phosphorus intermediate bound to the niobate. This intermediate then dissociated in a second reaction step. Conversely, an examination of the reaction coordinate for DMCP revealed that the rate-limiting step resulted in scission of the P-Cl bond (along with protonation and nucleophilic addition of the hydroxide), immediately yielding surface-bound chloride and tetrahedral phosphorus products. Finally, the rate-limiting barrier for Sarin was found to be 22.8 kJ/mol, and the analogous barriers were 44.6 kJ/mol and 28.1 kJ/mol, respectively, for DMMP and DMCP. This result advances DMCP as a better candidate to simulate Sarin than DMMP in this case.

Next, we provided an exodus from our studies of reactions at the gas—solid interface by examining the mechanism of hydrolysis of a gas-phase Sarin molecule on the surface of an aqueous $Cs_8Nb_6O_{19}$ solution. Using molecular dynamics, we surrounded the niobate explicitly with water molecules before adsorbing Sarin, causing Cs counterions to dissociate away from the vicinity of Sarin adsorption. By comparing the results from subsequent electronic structure calculations with those for the gas—solid surface reaction, we were able to investigate the key role that interactions between adsorbed species and Cs counterions play on the energetics of reaction. As such, we found that limiting the interactions between adsorbed species and counterions serves to decrease the strength of adsorption to the niobate. Further, decreased

interactions with counterions destabilize the rate-limiting transition state, thereby decreasing the overall rate of reaction.

Finally, we concluded this line of research by completely submerging ourselves into the solution-phase. In this manner, we were able to obtain insight into the role of solvent molecules on the hydrolysis of Sarin by the Lindqvist niobate. We found that, in the absence of nearby counterions, solvent water molecules serve to decrease the rate-limiting barrier of reaction. However, we note that this may be dependent upon the specific orientation of explicit water molecules; future work should consider additional solvent configurations. Also, by examining the rate-limiting barrier for water deprotonation on the surface of the polyoxoniobate in the solution phase both in the presence and absence of a co-adsorbed agent, we suggest that specific base catalysis is likely in solution, with concomitant general base catalysis.

9.2 Future Work

In our atmospherically relevant studies, we examined the reaction of the oxidative gases ozone and nitrate on organic surfaces. For the reaction of multiple ozone molecules with the C_{60} fullerene, we have traced a highly involved reaction pathway to the formation of a stable ketene product. Previous work has shown, however, that prolonged exposure of fullerenes to ozone results in the formation of amorphous polymer substances, suggesting that adjacent fullerene cages become polymerized during reaction.[6] Also, the ultra-high vacuum study by Zhang et al.,[3] and thus our investigation, only probed the initial reaction step of nitrate addition to a vinyl-terminated self-assembled monolayer, leaving a reactive radical species. Over time, this radical may react with adjacent surface chains, leading to agglomeration as noted in other systems.[7] Thus, future work in this area shall expand the surface models implemented to examine large-scale effects after longer times and higher gas exposures.

For the work with agent and simulant hydrolysis, computational investigations of the solution-phase system remain highly relevant. Though we were able to confirm a general base hydrolysis mechanism by the Lindqvist polyoxoniobate at the gas—surface interface, a similar conclusion in the aqueous phase requires further substantiation. Future work will continue to probe this mechanism. This may be best achieved through the use of QM/MM calculations, treating the area around the agent-adsorption site with the higher level of theory. Alternatively,

reactive molecular dynamics, which implement force fields that allow for bond breakage and formation, may be the best approach to this problem.

9.3 References

(1) Davis, E. D.; Wagner, A.; McEntee, M.; Kaur, M.; Troya, D.; Morris, J. R. *The Journal of Physical Chemistry Letters* **2012**, *3*, 3193.

(2) Shang, Z.; Pan, Y.; Cai, Z.; Zhao, X.; Tang, A. *The Journal of Physical Chemistry A* **2000**, *104*, 1915.

(3) Zhang, Y.; Chapleski, R. C.; Lu, J. W.; Rockhold, T. H.; Troya, D.; Morris, J. R. *Physical Chemistry Chemical Physics* **2014**, *16*, 16659.

(4) Kinnan, M. K.; Creasy, W. R.; Fullmer, L. B.; Schreuder-Gibson, H. L.; Nyman, M. *European Journal of Inorganic Chemistry* **2014**, *2014*, 2361.

(5) Guo, W.; Lv, H.; Sullivan, K. P.; Gordon, W. O.; Balboa, A.; Wagner, G. W.; Musaev, D. G.; Bacsa, J.; Hill, C. L. *Angewandte Chemie International Edition* **2016**, *55*, 7403.

(6) Cataldo, F. *Carbon* **2002**, *40*, 1457.

(7) McIntire, T. M.; Scott Lea, A.; Gaspar, D. J.; Jaitly, N.; Dubowski, Y.; Li, Q.; Finlayson-Pitts, B. J. *Physical Chemistry Chemical Physics* **2005**, *7*, 3605.